Analysis of underground rock excavations accounting for uncertainty

Liu, Huaxin

2018

Liu, H. (2018). Analysis of underground rock excavations accounting for uncertainty. Doctoral thesis, Nanyang Technological University, Singapore.

http://hdl.handle.net/10356/73348

https://doi.org/10.32657/10356/73348

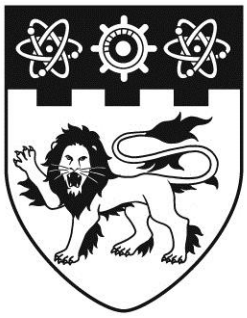

NANYANG TECHNOLOGICAL UNIVERSITY

Analysis of Underground Rock Excavations Accounting for Uncertainty

Liu Huaxin

School of Civil and Environmental Engineering

2018

Analysis of Underground Rock Excavations Accounting for Uncertainty

Liu Huaxin

School of Civil and Environmental Engineering

A thesis submitted to the Nanyang Technological University

in partial fulfilment of the requirements for the degree of

Doctor of Philosophy

2018

Abstract

In engineering practice, widely used methods for the analysis and design of underground projects are deterministic approaches, which overlook the stochastic nature of rock mass properties and in situ stress conditions. Probabilistic analysis is more reasonable since the uncertainties can be considered explicitly. Therefore, the main purpose of this thesis is to investigate the reliability analysis of underground excavation problems.

A simple closed-form solution (the Duncan-Fama solution) for circular tunnels in Mohr-Coulomb grounds is used to illustrate various reliability methods, including the first-order reliability method (FORM), direct Monte Carlo simulation (MCS), Latin Hypercube Sampling (LHS), MCS with importance sampling and polynomial response surface method (RSM), which provides the basis for the content in later chapters. For a special case where the design point is far away from the mean value point, a numerical error problem is encountered for the linear RSM. The problem is caused by sampling in the unrealistic domain of the input parameters. A multiple-step response surface method (RSM) is proposed to solve this numerical error problem.

The reliability analysis of single limit state is then extended to the system reliability evaluation which considers the interaction among different limit states. The iterative solution for a circular tunnel reinforced by end-anchored rockbolts is used to illustrate the system reliability analysis, in which the tensile force of the rockbolt, tunnel convergence and plastic zone size are considered as three performance functions. The bimodal bounds method and the multivariate normal cumulative distribution function (*mvncdf*) method are compared. It is shown that the second-order reliability method (SORM) can be used to refine the reliability indices from FORM and to improve the accuracy of the estimated system probability of failure. The optimal rockbolt installation position corresponds to the smallest system probability of failure. For problems where closed-form solutions are not available, a modified hybrid approach using the linear RSM to locate the design point and artificial neural network (ANN) to approximate the actual limit state surface (LSS) is proposed. Comparison with the

second-order RSM shows that the proposed approach is efficient, accurate and robust for the system reliability evaluation.

How reliability-based design (RBD) can provide insights to the partial factor design approach, such as the Eurocode 7 (EC7), is discussed and illustrated using various tunnelling problems. The first-order second-moment method (FOSM) and the point estimate method (PEM) may produce non-unique reliability indices for different but mathematically equivalent limit state functions. FORM is more consistent than FOSM and PEM and is suggested to be used in RBD. The intuitive expanding ellipsoid perspective and the efficient constrained optimization method for FORM help overcome the conceptual and computational barriers for practitioners. The structurally-controlled failure mechanism including the case of a symmetrical roof wedge and the stress-controlled failure mechanism including the cases of a lined circular tunnel and a rockbolt-reinforced tunnel are used to show the insights from RBD. RBD via FORM can determine the role (resistance or load factor) of input parameters on a case-by-case basis in ways that prescribed partial factors cannot. Besides, different case studies show that RBD can play a complementary role to the partial factor design approach when the correlation of the input parameters should be considered, when uncertainties of geometrical parameters are involved, when the rock parameters that are not covered in the design code are involved and when the same parameter has opposite effects on different performance functions.

A real-life underground excavation project, Jurong Rock Cavern (JRC) in Singapore, is presented to show how reliability analysis is conducted for a real case study. The statistics of rock engineering properties are characterized using the site investigation and laboratory test results. The deterministic analysis using the finite difference software FLAC^{3D} shows that the estimate of the rock mass Young's modulus has a great influence on the cavern displacement. It is shown that the simplified 2D analysis using the stress reduction method can simulate the 3D excavation and support installation process. The longitudinal deformation profile (LDP) from 3D analysis using FLAC^{3D} can be used to determine the stress reduction coefficient for the simplified 2D analysis. For JRC, the support system including fully-grouted rockbolts and shotcrete has limited effect on the cavern displacement because of the late

installation of the support and the good quality of the rock mass. FORM and second-order RSM with cross terms are used to calculate the reliability index and design point for JRC project.

The uniaxial compressive strength (UCS) and elastic modulus (EM) data summarized for JRC sedimentary rocks and some data collected for the igneous rocks are used to characterize the spatial variability of rock properties. The autocorrelation structures are selected using a Bayesian model class selection approach and the scales of fluctuation for these two parameters are estimated using a Bayesian updating method. The results show that the autocorrelation structures for UCS and EM could be described by a single exponential autocorrelation function. The scales of fluctuation for UCS and EM range from 0.3 m to 8.0 m and from 0.3 m to 8.4 m, respectively. These results serve as guidelines for selecting proper autocorrelation functions and autocorrelation distances for rock properties in the reliability analysis and could also be used as prior information for quantifying the spatial variability of rock properties in a Bayesian framework.

Acknowledgements

It has been four years since I started the PhD study in Nanyang Technological University (NTU). Along with this inspiring but challenging journey are the supports from people to whom I would like to express my deepest appreciation.

First and foremost, I would like to express heartfelt gratitude to my supervisor, Associate Professor Low Bak Kong, for his patient guidance, kindness, and continuous encouragement. Prof. Low himself sets a good example for an excellent researcher. His academic rigour and curiosity for knowledge greatly impress and inspire me. Deep thinking and logical writing are two things that he emphasizes from the beginning of my PhD study. What I learned from him is not only helpful to conduct research but will be a lifelong treasure for my future.

Next, special thanks will be given to Mr. U Kar Winn, who is a part-time PhD candidate in NTU. The fact that he has been working as a geologist and a geotechnical engineer for more than 20 years and now is pursuing a PhD degree itself is a very inspiring story. He is always ready to help and considerate of others. The discussions with him about the Jurong Rock Cavern project greatly help me gain some practical rock engineering experience.

Then, I am also thankful to Dr. Zhang Wengang, Dr. Qi Xiaohui and Dr. Ji Jian, who are my seniors but more importantly my friends.

Last but not the least, I would like to express my love to my family members, who have been always supportive and encouraging.

List of published papers

Liu, H. and Low, B. K. (2017), "System reliability analysis of tunnels reinforced by rockbolts", Tunnelling and Underground Space Technology, Vol. 65, pp. 155-166.

Liu, H. and Low, B. K. (2018), "Reliability-based design of tunnelling problems and insights for Eurocode 7", Computers and Geotechnics, Vol. 97, pp. 42-51.

Liu, H. and Qi, X. H. (2017), "Random field characterization of uniaxial compressive strength and elastic modulus for intact rocks", Geoscience Frontiers, doi:10.1016/j.gsf.2017.11.014.

Liu, H. and Low, B. K. (2017). "System reliability analysis of circular tunnels reinforced by end-anchored rockbolts using bimodal bounds method and mvncdf method." 6TH INTERNATIONAL SYMPOSIUM ON GEOTECHNICAL SAFETY AND RISK, Denver, USA.

https://ascelibrary.org/doi/abs/10.1061/9780784480724.059

Table of contents

Abstract ..... **I**

Acknowledgements ..... **IV**

List of published papers ..... **V**

Table of contents ..... **VI**

List of tables ..... **XII**

List of figures ..... **XV**

List of abbreviations and symbols ..... **XX**

Chapter 1 Introduction **1**

1.1 Background 1

1.2 Objectives and scope of research 3

1.3 Outline of the thesis 4

Chapter 2 Literature review **6**

2.1 Introduction 6

2.2 Review of deterministic analysis methods for underground excavations 6

2.2.1 Empirical method 6

2.2.2 Analytical methods 13

2.2.3 Numerical methods 14

2.2.4 Observational method 17

2.3 Review of commonly used reliability methods 18

2.3.1 Fundamentals of probabilistic analysis 18

2.3.2 Probabilistic assessment methods 21

2.3.3 Review of approximate approaches for implicit performance functions 30

2.4 Review of probabilistic analyses of underground excavation problems.. 40

2.5 Summary 43

Chapter 3 Probabilistic analysis of a circular tunnel using various reliability methods 45

3.1 Analytical solutions for circular tunnels in Mohr-Coulomb grounds under hydrostatic in situ stresses 45

3.2 Direct first-order reliability method applied to closed-form solutions 47

3.2.1 Sensitivities of input parameters 49

3.2.2 The effect of negatively correlated random variables..... 49

3.2.3 Reliability-based design 51

3.2.4 Comparison of different FORM algorithms and FOSM 52

3.3 Monte Carlo simulation applied to the Duncan-Fama solution 54

3.3.1 Direct Monte Carlo simulation 54

3.3.2 Latin hypercube sampling and Monte Carlo simulation with importance sampling 55

3.3.3 Subset simulation 58

3.4 Polynomial response surface methods (RSM) 59

3.4.1 Linear and second-order polynomial RSM applied to the Duncan-Fama solution 59

3.4.2 Comparison with the response surface method using interpolation algorithm 62

3.5 Multiple steps for response surface method 63

3.6 Summary 70

Chapter 4 System reliability analysis of tunnels reinforced by rockbolts ...71

4.1 Introduction 71

4.2 System reliability analysis methods 72

4.2.1 Lower and upper bounds method 72

4.2.2 Multivariate normal cumulative distribution function (mvncdf) method 73

4.2.3 Monte Carlo simulation (MCS) based on various surrogate models ... 76

4.3 Deterministic analysis of rockbolt-reinforced tunnels based on Bobet and Einstein (2011) formulations 77

4.4 System reliability analysis of circular tunnels reinforced by rockbolts ... 80

4.4.1 System reliability analysis using bimodal bounds and mvncdf methods 81

4.4.2 Improvement of the system reliability evaluation using the reliability indices from SORM 83

4.4.3 Influence of the correlation coefficient between cohesion and friction angle on the system P_f 84

4.4.4 Effect of the rockbolt installation position on the system P_f 86

4.4.5 Illustrative system reliability-based design of the rockbolt length and spacing 88

4.5 System reliability analysis using RSM and ANN 90

4.5.1 Comparison of linear RSM with the second-order RSM without cross terms 95

4.5.2 Comparison with the second-order RSM with cross terms and the importance sampling technique 96

4.6 Summary and conclusion 101

Chapter 5 Reliability-based design of tunnelling problems and insights for Eurocode 7 103

5.1 Introduction 103

5.2 Eurocode 7 design and FORM-based design 104

5.2.1 Eurocode 7 design 104

5.2.2 FORM and intuitive dispersion ellipsoid perspective 105

5.2.3 FORM analysis of a circular tunnel in Mohr-Coulomb material 107

5.2.4 Tentative design based on Eurocode 7 109

5.2.5 Comparison between RBD and EC7 111

5.3 FOSM, PEM, FORM and SORM 112

5.4 A symmetrical roof wedge above a circular tunnel 118

5.5 A lined circular tunnel under different lateral stress conditions 120

5.6 Reliability analysis of a circular tunnel reinforced by end-anchored rockbolts 123

5.7 Summary and conclusion 126

Chapter 6 Case study: Jurong Rock Cavern (JRC) in Singapore.....128

6.1 Background 128

6.2 Preconstruction investigation 130

6.3 Deterministic and statistical characterization of engineering properties of the rock 132

6.4 Deterministic analysis of JRC project 145

6.5 Monitoring displacement results 150

6.6 Reliability analysis of JRC 154

6.7 Summary 156

Chapter 7 Characterization of the spatial variability of intact rock properties using the Bayesian approach 158

7.1 Introduction 158

7.2 Random field modelling of spatial variability for UCS and EM of intact rocks 159

7.3 Bayesian model class selection and Bayesian updating approach 162

7.3.1 Selection of the most plausible autocorrelation function using Bayesian model class selection method 162

7.3.2 Evaluation of posterior statistics of the random field model parameters using Bayesian updating method 165

7.4 Database of uniaxial compressive strength and elastic modulus for intact rocks 166

7.5 Results for selected autocorrelation model and updated random field parameters for UCS and EM 170

7.5.1 Most plausible autocorrelation models for UCS and elastic modulus 171

7.5.2 Posterior statistics of random field parameters 173

7.6 Summary 176

Chapter 8 Summary and Recommendation 177

8.1 Summary 177

8.2 Recommendations for future research 179

8.2.1 Reliability analysis of structurally-controlled failure problems 180

8.2.2 Influence of the spatial variability of rock properties on the stability of underground rock excavations 180

8.2.3 Transformation uncertainty and model uncertainty 180

Appendix A List of literature on the reliability analysis of underground excavation problems 181

Appendix B Cross-validation of FORM using different methods in Excel and MATLAB 189

Appendix C Iterative closed-form solution for circular tunnels reinforced by rockbolts.....195

Appendix D User-defined subroutine of FLAC^{3D} for JRC project 198

References 202

List of tables

Table 2.1 Rock mass classification and guidelines for supports of 10 m span rock tunnels with RMR system (after Bieniawski, 1989) 8

Table 2.2 Correlation equations between RMR and Q (after Zhang, 2013) 10

Table 2.3 Empirical equations for estimating Young's modulus for rock mass (after Aksoy et al., 2010) 11

Table 3.1 Results for direct MCS (p_i=0) 54

Table 3.2 Results for direct MCS (p_i=0.228 MPa) 55

Table 3.3 Results for LHS (p_i=0.228 MPa) 56

Table 3.4 Results for MCS with importance sampling (p_i=0.228 MPa) 57

Table 3.5 Results for linear and second-order RSM 61

Table 3.6 Results for linear and second-order RSM using interpolation 62

Table 3.7 Input parameters for the numerical error problem 63

Table 3.8 Comparison of three strategies 69

Table 4.1 Statistics of random variables for the rockbolt-reinforced circular tunnel case 80

Table 4.2 Use of SORM reliability indices in system reliability evaluation 84

Table 4.3 Required length and spacing for a target reliability index 2.5 90

Table 4.4 Deterministic analysis results for different rockbolt lengths 90

Table 4.5 FORM results for linear RSM 93

Table 4.6 MCS results for ANN and closed-form solution 94

Table 4.7 FORM results for second-order RSM without cross terms 95

Table 4.8 Coefficients of second-order RSM without cross terms 96

Table 4.9 FORM results for second-order RSM with cross terms 96

Table 4.10 Coefficients for second-order RSM with cross terms 97

Table 4.11 MCS results for second-order RSM without and with cross terms 97

Table 4.12 Results of FORM and MCS for different values of the limiting ratio ... 98

Table 4.13 Importance sampling and MCS results based on RSM, closed-form solution and ANN for g2 ($\varepsilon_{limiting}$=0.8%) 100

Table 4.14 Comparison of the hybrid approach and RSM 101

Table 5.1 Design of support pressure based on EC7 (5/95 Percentile) 110

Table 5.2 Design of support pressure based on EC7 (30/70 Percentile) 110

Table 5.3 Design of support pressure (5/95 Percentile) considering partial factors 111

Table 5.4 Characteristic values for the input random variables 117

Table 5.5 FOSM and PEM results for three definitions of the performance function 117

Table 5.6 Statistics of random variables and FORM results for the circular tunnel reinforced by rockbolts 125

Table 6.1 Summary of the site investigation 131

Table 6.2 List of boreholes and numbers of samples for UCS test 133

Table 6.3 Statistical information of UCS 134

Table 6.4 Statistical information of Young' modulus of the intact rock 137

Table 6.5 Numbers of different laboratory tests 138

Table 6.6 Statistical information for other engineering properties of intact rocks 139

Table 6.7 Global database for sedimentary intact rocks 140

Table 6.8 Statistical information for GSI, E_i and E_{rm} 145

Table 6.9 Input parameters for the deterministic 2D analysis 146

Table 6.10 Different deformation modulus values of rock mass 147

Table 6.11 Input parameters for the rockbolt and shotcrete 150

Table 6.12 Locations of monitoring device and the estimated distances 152

Table 6.13 Statistical inputs for the reliability analysis of JRC 154

Table 6.14 Reliability analysis results for JRC 155

Table 6.15 Coefficients for the second-order response surface with cross terms .. 156

Table 7.1 Logarithms of the evidence for different autocorrelation functions and different sets of UCS data 172

Table 7.2 Logarithms of the evidence for different autocorrelation functions and different sets of EM data 172

Table 7.3 Posterior statistics for the random field parameters of UCS 173

Table 7.4 Posterior statistics for the random field parameters of EM 175

Table A.1 List of literature on reliability analysis of underground excavation problems 180

Table B.1 Characteristic values for input parameters 189

List of figures

Fig. 2.1. Relation between the stand-up time and roof span according to RMR (after Bieniawski, 1989) 8

Fig. 2.2. Support design chart using Q system (after Grimstand and Barton, 1993) 10

Fig. 2.3. General chart for GSI estimation (after Marinos and Hoek, 2000) 12

Fig. 2.4. Sketches for rock masses with different numbers of joints (after Bobet et al., 2009) 16

Fig. 2.5. PDF of load, resistance and safety margin (after Nowak and Collins, 2012) 19

Fig. 2.6. Three-dimensional representation of basic probabilistic concepts (adapted from Haldar and Mahadevan, 2000) 20

Fig. 2.7. Illustration of the reliability index in the plane when c and ϕ are negatively correlated (after Low, 2014) 24

Fig. 2.8. Sampling points shown for axial-point design and two-level factorial design 30

Fig. 2.9. Sampling points shown for central composite design 31

Fig. 2.10. Comparison of UD with random sampling (after Lü et al., 2012) 32

Fig. 2.11. Basic structure of ANN (after Anderson, 2005) 36

Fig. 2.12. Reviewed methods and their relations 43

Fig. 3.1. Illustration of a circular tunnel under hydrostatic in situ stress (after Hoek, 2007) 46

Fig. 3.2. FORM results for the plastic zone size performance function 48

Fig. 3.3. The influence of correlation coefficient between c and ϕ on β and P_f 50

Fig. 3.4. The expanding ellipse plot for the case of two random variables (a) no correlation (b) negative correlation 51

Fig. 3.5. PDF of the performance function (p_i=0) 53

Fig. 3.6. Spreadsheet for the MCS with importance sampling 57

Fig. 3.7. Performance function contours 65

Fig. 3.8. Linear response surface for k=1 65

Fig. 3.9. Linear response surface for different k values 66

Fig. 3.10. Linear response surface based on g(x)=0.0325 m (k=1) 67

Fig. 3.11. Convex and concave performance function curves 68

Fig. 3.12. Performance function curve using Eq. (3.17) 69

Fig. 4.1. Illustration of the Hasofer-Lind β for single limit state 74

Fig. 4.2. Illustration of system reliability analysis for three limit states 75

Fig. 4.3. A circular tunnel with end-anchored rockbolts (after Bobet and Einstein, 2011) 77

Fig. 4.4. Illustration of the stress reduction method (a) first stage (b) second stage 78

Fig. 4.5. (a) Numerical model and (b) finite difference mesh for verifying the closed form solution 79

Fig. 4.6. Illustration of the three performance functions 80

Fig. 4.7. System reliability analysis of a circular tunnel with rockbolts 82

Fig. 4.8. Influence of $\rho_{\phi,c}$ on the system P_f based on FORM reliability indices 85

Fig. 4.9. Influence of $\rho_{\phi,c}$ on the system P_f based on SORM reliability indices 85

Fig. 4.10. Influence of rockbolt installation position on the reliability indices 86

Fig. 4.11. Influence of rockbolt installation position on the system P_f based on FORM reliability indices 87

Fig. 4.12. Influence of rockbolt installation position on the system P_f based on SORM reliability indices 87

Fig. 4.13. Steps for the iterative response surface method 91

Fig. 4.14. Actual LSS and response surfaces for g2 when $\varepsilon_{limiting}$=0.8% 99

Fig. 5.1. Illustration of the intuitive expanding ellipsoid perspective (after Low and Tang, 2004) 106

Fig. 5.2. FORM results for the circular tunnel in Mohr-Coulomb ground 108

Fig. 5.3. Location of the sampling points in PEM for three random variables (after Baecher and Christian, 2003) 114

Fig. 5.4. Illustration of a symmetrical roof wedge above a circular tunnel (after Low and Einstein, 2013) 114

Fig. 5.5. Reliability analysis results for the tunnel roof wedge problem 119

Fig. 5.6. A lined circular tunnel in an elastic ground 121

Fig. 5.7. FORM analysis results for a lined circular tunnel 122

Fig. 5.8. A circular tunnel with end-anchored rockbolts (after Bobet and Einstein, 2011) 124

Fig. 5.9. Illustration of the stress reduction method using coefficient β_σ 124

Fig. 6.1. Location of JRC project (after TriTech, 2007) 128

Fig. 6.2. Layout of the caverns (after JTC, 2010) 129

Fig. 6.3. Generalized vertical geological profile (after Kar Winn, 2016) 129

Fig. 6.4. Location of all boreholes (after JTC, 2010) 132

Fig. 6.5. Lognormal distribution fitted to the UCS data (Site Investigation 2004 and GRI 2007) 136

Fig. 6.6. Lognormal distribution fitted to the UCS data (NTU 2013) 136

Fig. 6.7. Correlation between UCS and E_i 137

Fig. 6.8. Correlation between cohesion and friction angle 139

Fig. 6.9. An example of geological mapping of excavation face (after Kar Winn, 2016) 141

Fig. 6.10. Picture of the excavation face corresponding to the geological map (after Kar Winn, 2016) 142

Fig. 6.11. Correlation between RMR and Q 143

Fig. 6.12. Excavation geometry of the cavern and the finite difference mesh 146

Fig. 6.13. Displacement contours for 2D deterministic analysis 147

Fig. 6.14. Longitudinal deformation profile for the cavern crown 148

Fig. 6.15. Longitudinal deformation profile for the cavern sidewall 149

Fig. 6.16. Distribution of the monitoring points and the estimated distance from monitoring device to excavation face 151

Fig. 6.17. Roof point 3 settlements with time (CS 1-1 60 m) 152

Fig. 7.1. Five autocorrelation functions commonly used in geotechnical practice 161

Fig. 7.2. Collected uniaxial compressive strength data 168

Fig. 7.3. Collected elastic modulus data 170

Fig. 7.4. Variation of the likelihood with scale of fluctuation 174

Fig. B.1 MATLAB code for the Duncan-Fama solution 187

Fig. B.2. MATLAB code for the classical iterative approach 188

Fig. B.3. MATLAB code for the optimization toolbox in MATLAB 189

Fig. B.4 FORM results using Solver in Excel 190

Fig. B.5 MATLAB code for FORM using traditional iteration procedure.....190

Fig. B.6 MATLAB code for FORM using constrained optimization.....191

List of abbreviations and symbols

Abbreviations

ACF	Autocorrelation function
ANN	Artificial Neural Network
ASD	Allowable Stress Design
BEM	Boundary Element Method
BNACF	Binary noise autocorrelation function
BPNN	Back Propagation Neural Network
CCM	Convergence-Confinement Method
CDF	Cumulative Distribution Function
CEACF	Cosine exponential autocorrelation function
DDA	Discontinuous Deformation Analysis
DEM	Distinct Element Method
EC7	Eurocode 7
EM	Elastic modulus
FDM	Finite Difference Method
FEM	Finite Element Method
FORM	First-order Reliability Method
FOSM	First-order Second Moment
FS	Factor of Safety
GACF	Gaussian autocorrelation function
GRC	Ground Reaction Curve
GSI	Geological Strength Index
H-B	Hoek-Brown
JRC	Jurong Rock Cavern
KRSM	Kriging-based Response Surface method
LDP	Longitudinal Deformation Profile
LHS	Latin Hypercube Sampling
LR	Logarithm Regression
LRFD	Load and Resistance Factor Design
LSD	Limit State Design

LSS	Limit State Surface
MARS	Multivariate Adaptive Regression Splines
M-C	Mohr-Coulomb
MCS	Monte Carlo Simulation
mvncdf	Multivariate Normal CDF
NATM	New Austrian Tunnelling Method
NMM	Numerical Manifold Method
PDF	Probability Distribution Function
PEM	Point Estimate Method
PR	Polynomial Regression
Q	Tunneling Quality Index
RBD	Reliability-based design
RMi	Rock Mass index
RMR	Rock Mass Rating
RQD	Rock Quality Index
RSM	Response Surface Method
SCC	Support Characteristic Curve
SEACF	Single exponential autocorrelation function
SLS	Serviceability Limit State
SMACF	Second-order Markov autocorrelation function
SoF	Scale of fluctuation
SORM	Second-order Reliability Method
SRF	Stress Reduction Factor
SRSM	Stochastic Response Surface Method
SVM	Support Vector Machine
TBM	Tunnel Boring Machine
UCS	Uniaxial Compressive Strength
UD	Uniform Design
ULS	Ultimate Limit State

Symbols

a	Unknown coefficient for RSM
	Hoek-Brown constant

A_b	Cross-section area of the rockbolt
b_i	Unknown coefficient for RSM
$\boldsymbol{C}$	Covariance matrix
c	Cohesion
c_i	Unknown coefficient for RSM
D	Disturbance factor in H-B failure criterion
	Distance from installation point to tunnel face
E_b	Young's modulus of the rockbolt
E_i	Young's modulus of the intact rock
E_{rm}	Young's modulus of the rock mass
E_s	Young's modulus of the shotcrete
f_{linear}	Pure linear transfer function
f_{tansig}	Tangential sigmoid transfer function
$f_{transfer}$	Transfer function
$f_X(x)$	PDF of variable X at x
G_{rm}	Shear modulus of the rock mass
$g(x)$	Performance function of input x
$\overline{g}(x)$	Response surface function
$\mathbf{H}_{\text{red}}$	Reduced and transformed Hessian matrix
$I_g(x)$	Importance sampling factor function
	Indicator function
J_a	Joint Alteration Number
J_n	Joint Set Number
J_r	Joint Roughness Number
J_w	Joint Water Reduction Factor
K_0	Lateral stress coefficient
k	Sampling factor
k_n	Normal stiffness of joints
k_s	Shear stiffness of joints
$\mathbf{L}$	Lower Cholesky matrix
m	Number of limit states in a system

	Material constants for H-B rock mass
N	Number of random variables
n	Number of random variables
o	Output of the neural network
P_f	Probability of failure
p_i	Internal support pressure
p_i^{cr}	Critical support pressure
p_0	Hydrostatic in situ stress
$\boldsymbol{R}$	Correlation matrix
r_p	Plastic zone radius
r_0	Tunnel radius
s	Hoek-Brown constant
T	Tensile rockbolt force
$T_{limiting}$	Maximum allowable tensile force
u_{max}	Maximum displacement
w	Weights in the neural network
X	Random variable
α	Direction cosine; apical angle
β	Reliability index
β_{FOSM}	Reliability index of FOSM
β_σ	Stress reduction coefficient
δ	Coefficient of variance
ε_i	A small increment
ε_L	Limiting normalized displacement
$\varepsilon_{limiting}$	Limiting ratio of displacement over radius
ε_{tol}	Tolerance of the difference
ζ	Control factor
κ	Main curvatures
$\lambda_{limiting}$	Limiting ratio of plastic zone over radius
μ_i^N	Mean of the equivalent normal distribution
μ_g	Mean value of performance function

μ_x	Mean value of variable X
ν	Poisson's ratio
$\rho_{\phi c}$	Correlation coefficient between c and ϕ
σ_0	In situ stress
σ_{ci}	UCS of the intact rock
σ_g	Standard deviation of performance function
σ_i^N	Standard deviation of equivalent normal distribution
σ_x	Standard deviation of variable X
Φ(.)	CDF of the standard normal variable
ϕ	Friction angle
ψ_R	Resistance factor
ψ_s	Load factor

Chapter 1 Introduction

1.1 Background

The rapid urbanization and increasing demand for the aboveground space accelerate the development of underground excavations, which makes it possible to enlarge the space humans can use for different purposes. In the past, it was only possible to excavate small tunnels in relatively strong rocks. With the development of construction technologies and support systems, various excavations with gradually increasing sizes have been constructed not only in strong rocks but also in weak grounds.

The factors that contribute to the fast development of underground excavations can be briefly summarized as:

(1) Successfully applied empirical design methods such as the Rock Mass Rating (RMR) and Q system. Since proposed, these empirical methods have been successfully applied to various underground projects around the world. Besides, the evolutionary nature of these empirical methods with the accumulation of experience makes them powerful tools which can be updated along with the development of new techniques.

(2) Relatively mature numerical methods and powerful computational capabilities of computers. Various numerical methods have been proposed and improved since the 1970s, including the Finite Element Method (FEM), Finite Difference Method (FDM), etc. They have become the common practice for the analysis of excavation problems and can play a complementary role to the empirical methods especially when no similar projects have been constructed. Numerical methods make it possible to analyze excavation problems with complex ground-support interactions and various geometries. In addition, parametric studies can be carried out easily using numerical methods to investigate the effects of important parameters on the structural behavior.

(3) Developing construction methods and support systems. The New Austrian Tunnelling Method (NATM) widely enlarged the scope of grounds in which excavation can be constructed. Recently developed Tunnel Boring Machine

(TBM) makes the excavation and support installation an automatic process and greatly reduces the construction time. Along with the development of these excavation techniques is the fast progress in support systems. Rockbolts or cables, shotcrete and liners are commonly used as rock support and reinforcement methods. The high capacity cables and various fibre reinforced shotcrete as well as other support systems further improve the versatility of the support selection. All these developments make excavations possible even in the weak ground.

All these methods are based on the deterministic analysis, in which the uncertainties in the input parameters are considered implicitly. The traditional analysis uses the factor of safety (FS) for the ultimate limit state (ULS) analysis. For serviceability limit state (SLS), the tunnel wall displacement and plastic zone size are compared with critical values to indicate whether the behavior of the rock mass is satisfactory or not. However, uncertainties exist in the field investigation, parameter interpretation, and models used to calculate the output, etc. Not modelling the inherent uncertainty in the analysis may cause failure of the project or uneconomical design. Moreover, it is well recognized that FS is inconsistent to reflect the safety level of a geotechnical structure. The same structure with different definitions of FS will have different FS values. Therefore, these require a more reasonable analysis approach which takes into account of the uncertainties and a more consistent indicator of the safety level.

Probabilistic or reliability analysis explicitly considers the underlying uncertainties in parameters. Instead of calculating FS in the deterministic analysis, the probabilistic analysis uses the reliability index or probability of failure as the indicator of the stability of a structure. The reliability index is a more realistic and consistent indicator of safety than FS. In calculating the probability of failure, the sensitivities of different input parameters are a byproduct whereas, in the deterministic analysis, a series of parametric studies should be conducted in order to study the sensitivity.

Direct evaluation of the probability of failure is not practical due to the difficulty in calculating the joint probability distribution function (PDF) and the multiple integral over the failure domain. Thus, simplified approximate approaches, such as the first-order reliability method (FORM), second-order reliability method (SORM) and Monte Carlo Simulation (MCS), have been proposed to estimate the probability of failure.

These approaches can be applied to problems with explicit closed-form solutions easily. However, for problems in which the solution can only be obtained from the numerical simulation using stand-alone packages, some "bridges" are necessary to link the results from the numerical simulation to probability assessment methods. The "bridges" are called surrogate models or bridging methods, among which stand the Response Surface Method (RSM) and Artificial Neural Network (ANN).

The partial factor design approach has been suggested to replace FS design in geotechnical engineering, for example, the Eurocode 7 (EC7) for the Europe and the Load and resistance factor design (LRFD) for the North America. Singapore has also adopted Eurocode for structural and geotechnical designs. However, these partial factor design codes cover little about the rock engineering principles. Reliability-based design (RBD) can play a useful complementary role to the partial factor design as pointed out by Low and Phoon (2015). In RBD, the partial factors do not need to be specified but are automatically obtained and can reflect the sensitivities, standard deviations, correlation structures and probability distributions in a way that prescribed partial factors cannot. This is desirable, particularly for rock engineering in which some partial factors are not suggested by the design code. It is of great practical importance to show the insights from RBD compared with the partial factor design and to illustrate how RBD can help the evolution of design codes (e.g. EC7) for tunnelling problems.

Reliability analysis can consider the uncertainties explicitly and RBD provides additional insights compared with traditional design approaches. The application of reliability analysis methods to underground rock excavations has not been sufficiently examined. The focus of this thesis is to investigate the reliability analysis of underground excavation problems and to illustrate the insights from RBD for tunnelling problems.

1.2 Objectives and scope of research

The detailed objectives of this thesis are as follows:

(1) To illustrate and compare different reliability analysis methods applied to a benchmark tunnelling problem.

(2) To investigate the system reliability analysis considering the interaction among different limit states, to compare different surrogate models in terms of accuracy, efficiency and robustness, and to propose an efficient and accurate surrogate model for system reliability analysis.
(3) To show the insights from the reliability-based design compared with the partial factor design and to present how reliability-based design can complement EC7 and help the evolution of EC7 for tunnelling problems.
(4) To illustrate how to characterize the statistics of the rock engineering properties from site investigation and laboratory tests and to show how these input parameters can be used to the reliability analysis of a real-life underground project in Singapore.
(5) To characterize the spatial variability of the uniaxial compressive strength and elastic modulus of rocks and to select the most probable autocorrelation functions and to estimate the autocorrelation distances using the Bayesian model class selection method and the Bayesian updating method.

1.3 Outline of the thesis

This thesis consists of eight chapters.

Chapter 1 briefly introduces the background of underground excavations and the merits of the reliability analysis over deterministic approaches. A quick view of the objectives and the general outline of this thesis are also provided.

Chapter 2 presents the literature review which can be divided into three parts. The first part reviews the existing deterministic analysis and design tools for underground excavation problems, including the empirical method, analytical method, numerical method and observational method. The second part is about the basic reliability analysis concepts and commonly used methods, including the methods to estimate the probability of failure, such as FORM, SORM and MCS, and the surrogate models, such as RSM and ANN. The reliability analyses of underground excavation problems are reviewed in the third part.

Chapter 3 illustrates the application of various reliability methods to a benchmark problem in tunnelling engineering, which is the basis for later chapters. For a special case, a numerical error problem occurs and several strategies are proposed to deal with this error problem.

Chapter 4 focuses on the system reliability analysis of tunnelling problems. Different system reliability methods are compared using a circular tunnel reinforced by end-anchored rockbolts. The influence of the rockbolt installation position on the system probability of failure is discussed. A hybrid approach combining the linear polynomial RSM with ANN is proposed to efficiently locate the design point and to approximate the limit state surface (LSS).

Chapter 5 concentrates on the insights from RBD compared with the partial factor design for tunnelling problems. The intuitive expanding ellipsoid perspective and the efficient constrained optimization method for FORM help reduce the conceptual and computational barriers for practitioners. The insights are discussed using various tunnelling problems including structurally-controlled and stress-controlled failure mechanisms.

Chapter 6 contains the analysis of a real-life underground rock excavation project in Singapore. The statistical information of the rock engineering properties is characterized using the site investigation and laboratory test results. FORM and RSM are used to calculate the reliability index for this project.

Chapter 7 characterizes the spatial variability of the uniaxial compressive strength and elastic modulus of sedimentary and igneous rocks. The most probable autocorrelation functions are selected by the Bayesian model class selection method and the autocorrelation distances are estimated by the Bayesian updating method.

Chapter 8 summarizes this thesis with recommendations for future research.

Chapter 2 Literature review

2.1 Introduction

This chapter presents a comprehensive review of research work which is relevant to the deterministic and probabilistic analysis of underground excavations. Deterministic tools and design methods for tunnelling problems are reviewed first in section 2.2. Then, the basic concepts and commonly used reliability analysis methods are revisited in section 2.3. Next, an up-to-date review of the probabilistic analysis of underground excavation problems is provided in section 2.4. Finally, a brief summary of this chapter is presented in section 2.5.

2.2 Review of deterministic analysis methods for underground excavations

2.2.1 Empirical method

Empirical methods are based on engineering judgments and developed with the accumulation of the first-hand experience of engineering practice. Some rules of thumb are generalized for the stability analysis and support system selection. These methods are widely used in engineering practice due to the simplicity for application. The rock mass is a complex material which contains the intact rock and the discontinuities (e.g. joints, faults and bedding planes). The properties of both the intact rock and the discontinuity vary from case to case. Therefore, it is difficult, if not impossible, to describe the quality of rock masses. To quantify the rock mass quality, engineers proposed different classification systems to assign a value to the rock mass based on the site observation. In the field of underground excavation, Rock Mass Rating (RMR) and Q systems are popular empirical methods because they can be used not only to assess the rock mass quality but also to give guidelines about rock support selection. The following paragraphs review these two classification systems.

RMR

The RMR system was first proposed by Bieniawski (1973) and developed through several revisions until the latest 1989 version (Bieniawski, 1989). Five classification parameters listed below are included in the RMR scheme.

(1) Strength of intact rock or uniaxial compressive strength of intact rock (UCS)

(2) Rock Quality Designation (RQD)

(3) Spacing of discontinuities

(4) Condition of discontinuities

(5) Groundwater conditions

For each parameter, a rating value is assigned. The overall RMR value ranging from 0 to 100 is obtained by adding all these five rating values. The influence of the orientation of discontinuities can be accounted for by applying an adjusting value to the overall RMR. All the tables guiding the selection of rating values are given in Bieniawski (1989). The applications of RMR in underground excavations can be summarized as:

(1) Rock mass classification (see Table 2.1)
(2) Estimate of rock mass strength properties
(3) Estimate the stand-up time and the maximum unsupported rock span (see Fig. 2.1)
(4) Preliminary selection of rock supports (see Table 2.1)

Some advantages and disadvantages of the RMR system are:

(1) RMR system takes into account of the rock strength.
(2) The recommendation for tunnel supports is constrained to 10 m span only, which is out of date.
(3) The RQD has limitations in characterizing joints (Milne et al., 1998).

Table 2.1 Rock mass classification and guidelines for supports of 10 m span rock tunnels with RMR system (after Bieniawski, 1989)

Ground mass class	Excavation	Support		
		Rock bolts	Shotcrete	Steel sets
1. Very good RMR:81-100	Full face: 3 m advance	Generally no support required except for occasional spot bolting		
2. Good RMR:61-80	Full face:1.0-1.5 m advance; complete support 20 m from face	Locally bolts in crown, 3 m long, spaced 2.5 m with occasional wire mesh	50 mm in crown where required	None
3. Fair RMR: 41-60	Top heading and bench: 1.5-3 m advance in top heading; commence support after each blast;commence support 10 m from face	Systematic bolts 4 m long, spaced 1.5-2 m in crown and walls with wire mesh in crown	50-100 mm in crown and 30 mm in sides	None
4. Poor RMR: 21-40	Top heading and bench: 1.0-1.5 m advance in top heading; install support concurrently with excavation- 10 m from face	Systematic bolts 4-5 m long, spaced 1-1.5 m in crown and walls with wire mesh	100-150 mm in crown and 100 mm in sides	Light ribs spaced 1.5 m where required
5. Very poor RMR < 21	Multiple drifts: 0.5-1.5 m advance in top heading; install support concurrently with excavation; shotcrete as soon as possible	Systematic bolts 5-6 m long, spaced 1-1.5 m in crown and walls with wire mesh. Bolt invert	150-200 mm in crown, 150 mm in sides, and 50 mm on face	Medium to heavy ribs spaced 0.75 m with steel lagging and forepoling. Close invert

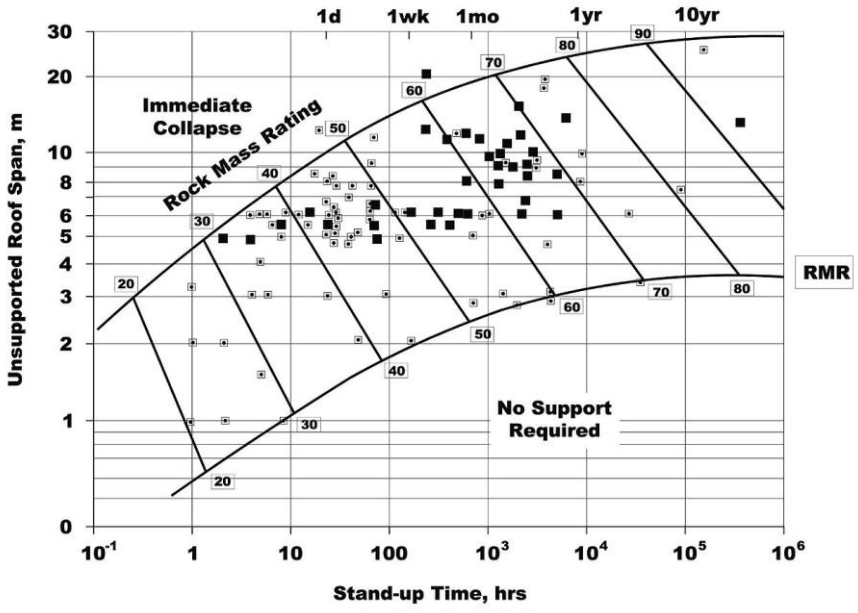

Fig. 2.1. Relation between the stand-up time and roof span according to RMR (after Bieniawski, 1989)

Q system

The Q system was first developed by Barton et al. (1974) initially intended for the support design for tunnels in hard rock. Similar to RMR system, site observations are used to assigned values to different parameters based on which the overall Q value for the rock mass is obtained. Six parameters, which are listed below, can be determined according to the tables provided by Barton (2002).

(1) RQD (Rock Quality Designation)
(2) J_n (Joint Set Number)
(3) J_r (Joint Roughness Number)
(4) J_a (Joint Alteration Number)
(5) J_w (Joint Water Reduction Factor)
(6) SRF (Stress Reduction Factor)

The overall Q value is obtained by

$$Q = \left(\frac{RQD}{J_n}\right) \times \left(\frac{J_r}{J_a}\right) \times \left(\frac{J_w}{SRF}\right) \tag{2.1}$$

The three quotients in Eq. (2.1) represent the block size, joint condition and active stress, respectively. Applications of the Q system can be summarized as:

(1) Rock mass classification (see Fig. 2.2)
(2) Estimate of rock mass strength properties
(3) Selection of underground excavation support (see Fig. 2.2)

Rock mass is divided into seven categories ranging from exceptionally good to exceptionally poor according to Fig. 2.2 and the preliminary design of support can be selected from Fig. 2.2. Some advantages and disadvantages of the Q-system are pointed out by Palmstrom and Stille (2007):

(1) The Q-system works best in ground conditions where block falls are likely.
(2) The application of SRF is unclear for buckling, rock burst and squeezing conditions.
(3) RQD has several limitations in characterising the degree of jointing.

The more detailed comments about uses and misuses of the Q system can be found in Palmstrom and Broch (2006).

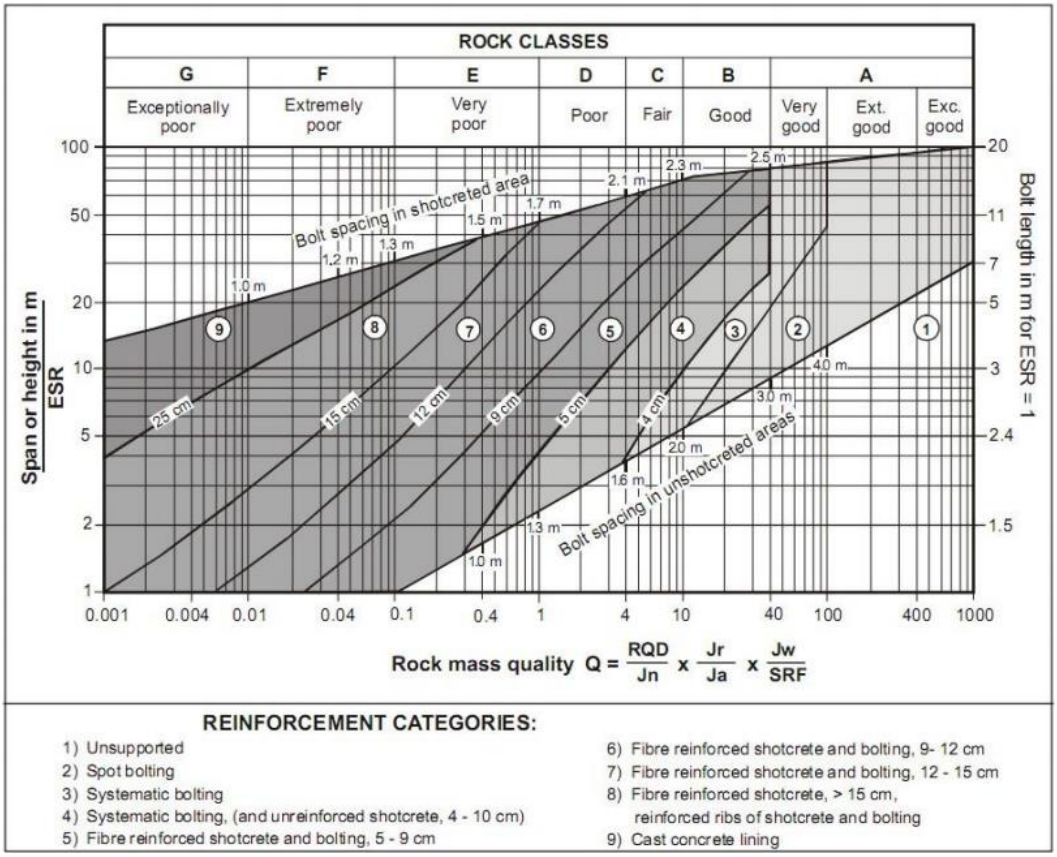

Fig. 2.2. Support design chart using Q system (after Grimstand and Barton, 1993)

Various formulae are proposed to relate RMR to Q system, some of which are given in Table 2.2.

Table 2.2 Correlation equations between RMR and Q (after Zhang, 2013)

Researcher(s)	Correlations
Bieniawski (1984)	$RMR = 9 \ln Q + 44$
Rutledge and Preston (1978)	$RMR = 5.9 \ln Q + 43$
Cameron-Clarke and Budavari (1981)	$RMR = 5 \ln Q + 60.8$
Abad et al. (1984)	$RMR = 10.5 \ln Q + 41.8$
Kaiser and Gale (1985)	$RMR = 8.7 \ln Q + 38$
Al-Harthi (1993)	$RMR = 9 \ln Q + 49$
Barton (1995)	$RMR = 15 \ln Q + 50$
Tugrul (1998)	$RMR = 7 \ln Q + 36$
Kumar et al. (2004)	$RMR = 6.4 \ln Q + 49.6$

Milne et al. (1998) suggested that RMR and Q should be estimated separately. The application of these two systems for estimating rock mass Young's modulus is listed in Table 2.3.

Table 2.3 Empirical equations for estimating Young's modulus for rock mass (after Aksoy et al., 2010)

Researcher(s)	Equation (units GPa)
Bieniawski (1978)	$E_m = 2RMR-100 \quad (RMR > 50)$
Serafim and Pereira (1983)	$E_m = 10^{(RMR-10)/40} \quad (RMR \le 50)$
Nicholson and Bieniawski (1990)	$E_m = E_i[0.0028\ RMR^2 + 0.9\exp(RMR/22.821)]/100$ (E_i = deformation modulus of intact rock)
Verman (1993), Verman et al. (1997)	$E_m = 0.3(H)^{\alpha}10^{(RMR-20)/38a} \quad (H > 50$ m)
Mitri et al. (1994)	$E_m = E_i[0.5(1-\cos(\pi \times RMR/100))]$
Singh (1997)	$E_m = H^{0.2} \cdot Q^{0.36} \quad (Q < 10)$
Barton (2002)	$E_m = 10Q_c^{1/3} \quad (Q_c = Q(\sigma_{ci}/100))$
Hoek et al. (2002)	$E_m = (1-D/2)\ (\sigma_{ci}/100)^{1/2} \cdot 10^{(GSI-10)/40}\ (\sigma_{ci} \le 100$MPa) $E_m = (1-D/2)\ 10^{(GSI-10)/40b} \quad (\sigma_{ci} > 100$ MPa) (σ_{ci} = uniaxial compressive strength of intact rock)
Ramamurthy (2004)	$E_m = E_i\exp[(RMR-100)/17.4]$
Zhang and Einstein (2004)	$E_m = E_i(10^{0.0186RQD-1.91})$
Hoek and Diederichs (2006)	$E_m = E_i[0.02+(1-D/2) / (1+e^{(60+15D-GSI)/11})]$

Besides these two widely used rock mass classification systems, there exist other methods which play equally important role in rock engineering. Palmstrom and Stille (2007) summarized other rock engineering systems, two of which are briefly reviewed.

Other systems

The Geological Strength Index (GSI), proposed by Hoek (1994), estimates the rock mass quality based on the field observation. The rock mass structure type and the surface condition are two descriptive indices for the selection of GSI values, as shown in Fig. 2.3. Although GSI can be used as a classification method, the main application of GSI lies in its role as an important parameter in the Hoek-Brown (H-B) failure criterion (Hoek et al., 2002). A case study to estimate GSI based on the geological observation and its application in H-B failure criterion is shown in Chapter 6.

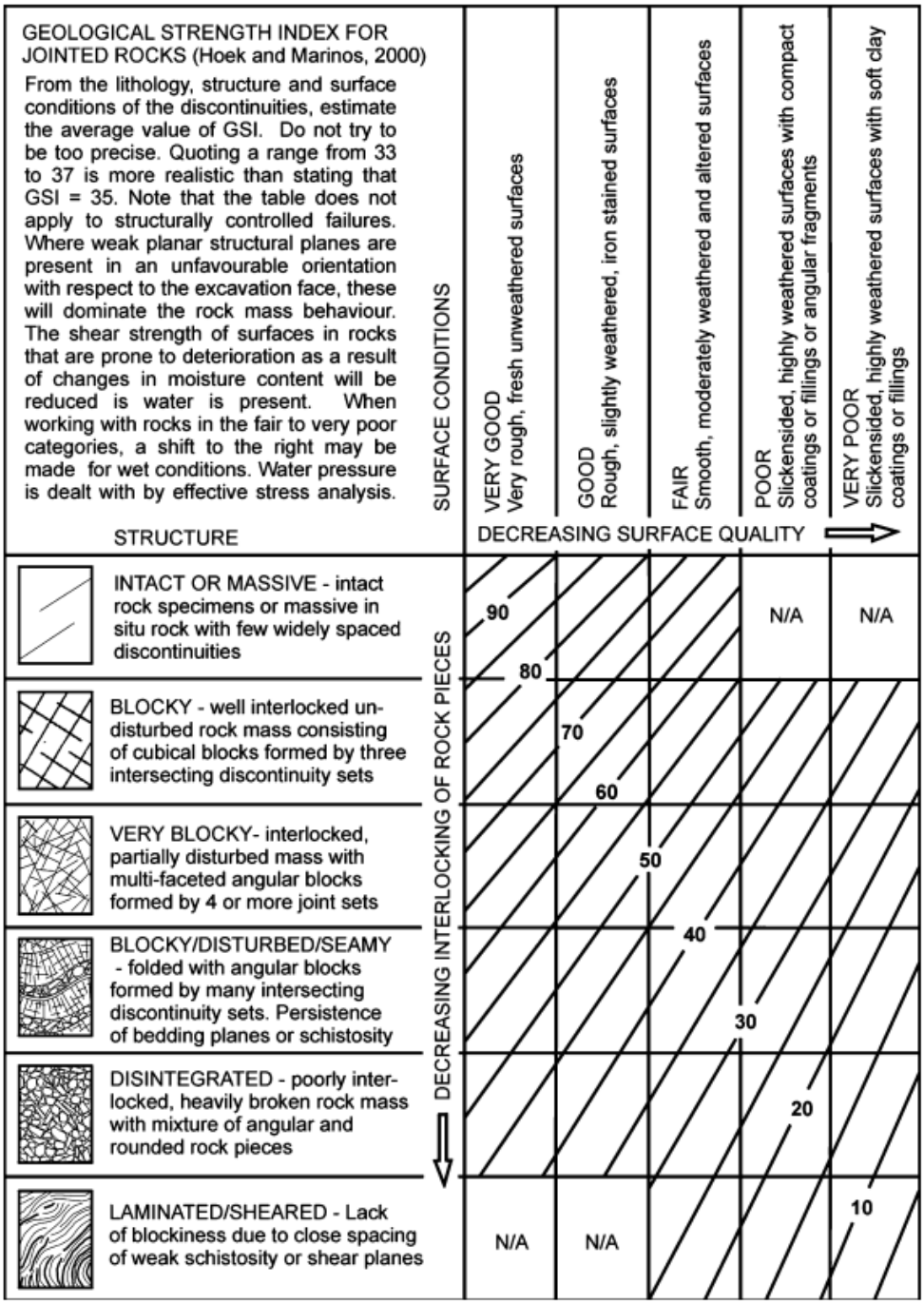

Fig. 2.3. General chart for GSI estimation (after Marinos and Hoek, 2000)

The RMi (Rock Mass index), first developed by Palmstrom (1995), is used to characterize the ground of both massive and jointed rock condition. In addition, it considers the ratio between the block size and tunnel size, adjusted for the joint orientation and the number of joints. One advantage of this method is that it covers rock falls as well as overstressed ground since it provides rock support estimation for the

continuous and discontinuous ground. This method uses more parameters than RMR and Q system and thus is more complicated to use (Palmstrom and Stille, 2007).

In summary, empirical methods or rock mass classification methods have been widely used in rock engineering due to the discontinuous, heterogeneous and anisotropic nature of the rock mass. The merits and demerits are obvious for these methods. They are simple to apply and usually provide safe designs of excavation problems, which have been tested by numerous case studies around the world. However, the support selection relies on a limited number of parameters which cannot entirely characterize the rock mass properties. Moreover, neither the RMR nor the Q system gives any information about how the ground behaviour and failure mechanism are considered in making recommendations for the rock support. Furthermore, structural resistance, serviceability and durability should be considered in the rock engineering design while only the first is addressed in the classification systems.

2.2.2 Analytical methods

Closed-form solutions are derived based on the elastoplasticity theory and various solutions have been proposed for stress and displacement calculations in underground excavation engineering. In this thesis, analytical methods refer to closed-form solutions which can be explicitly expressed and semi-analytical solutions in which some simple iterations may be required. Analytical methods for tunnelling problems date back to a solution for the stress redistribution in a stressed elastic plate containing a circular hole, proposed by Kirsch (1898). Since then, many researchers had proposed analytical solutions for excavations of different shapes and under anisotropic in situ stresses in the elastic ground. A detailed review of these methods can be found in Brown and Bray (1987).

The above-mentioned solutions are for elastic grounds. For elastic-perfectly-plastic grounds, the stress and displacement solutions for a circular excavation in a ground with Mohr-Coulomb (M-C) failure criterion subjected to the hydrostatic in situ stress were given by Duncan Fama (1993). The same problem but for Hoek-Brown failure criterion can be solved using the formulae by Carranza-Torres and Fairhurst (1999) and Carranza-Torres (2004).

Apart from the solutions for tunnels without support, other analytical solutions considering the support are also available. Carranza-Torres (2009) presented stress and displacement solutions for circular excavations reinforced by grouted or anchored rockbolts in the elastic ground. Bobet and Einstein (2011) proposed solutions for continuous and discontinuous coupled rockbolts uniformly distributed around a circular excavation in the elastoplastic ground with M-C criterion subjected to hydrostatic in situ stress. The Duncan-Fama solution and Bobet and Einstein solution are given in later chapters.

The disadvantages of analytical methods are obvious. Analytical solutions only exist in simple problems in which the excavation shape or ground properties or in situ stresses are idealized. Another significant demerit is that many assumptions used in the derivation of these solutions render the problem different from the actual situation in the field. For example, the solutions for rockbolts reinforced circular tunnels proposed by Bobet and Einstein (2011) assume that the rockbolts are uniformly distributed all around a circular tunnel in a homogeneous and isotropic ground subjected to hydrostatic in situ stress, which is seldom the case encountered in an actual excavation project. However, analytical solutions possess advantages with which other methods cannot compare.

(1) They are simple to use, especially when tabulated in the spreadsheet.
(2) They help understand and analyze the response and behavior of the rock mass and the support.
(3) They can be used as verification and calibration case studies for other methods, e.g. the numerical method.

2.2.3 Numerical methods

Most underground excavations have irregular shapes and the in situ stresses as well as the rock properties are more complicated than the case considered in analytical solutions. Consequently, a number of computer-based numerical methods have been developed to deal with complex excavations. Different numerical methods, which can be categorized into three groups, are listed below.

1. Continuum modelling

- Boundary Element Method (BEM)
- Finite Element Method (FEM)
- Finite Difference Method (FDM)

2. Discontinuum modelling
    - Distinct Element Method (DEM)
    - Discontinuous Displacement Analysis (DDA)
3. Coupled modelling
    - Numerical Manifold Method (NMM)
    - BEM+FEM, BEM+DEM, etc.

As the name suggests, the difference between the first two categories lies in the treatment of the problem domain. The continuum modelling treats the whole domain as a continuum and discretizes the domain into numbers of small elements (mesh) for iterative calculations. The widely used continuum methods in rock engineering are the FEM (Zienkiewicz and Morice, 1971) and FDM (Otter et al., 1966). These two methods both discretize the whole domain into small elements but have different methods of calculation. FEM utilizes the stiffness matrix to calculate strains from stresses whereas FDM uses the partial differential equations, in which no stiffness matrix is formed. Joints can be considered explicitly by the joint element or interface in these two methods, but too many joints in a model may be computational time-costly or cause the numerical non-convergence problem. Software used in tunnelling problems includes Phase^2 (www.rocscience.com) using FEM and FLAC or FLAC^{3D} (www.itascacg.com) using FDM.

Unlike the continuum methods, discontinuum modelling treats the problem domain as discrete blocks or particles. Discontinuum modelling is suitable when independent rock block movement must be recognized. Translation and rotation of the rock block can be modelled in this method. Commonly used discontinuum methods are the DEM (Cundall, 1971) and DDA (Shi and Goodman, 1985). Software includes UDEC or 3DEC (www.itascacg.com) using DEM and DDA software.

There are no quantitative guidelines to decide which method should be used (Bobet et al., 2009). However, a general suggestion is shown in Fig. 2.4.

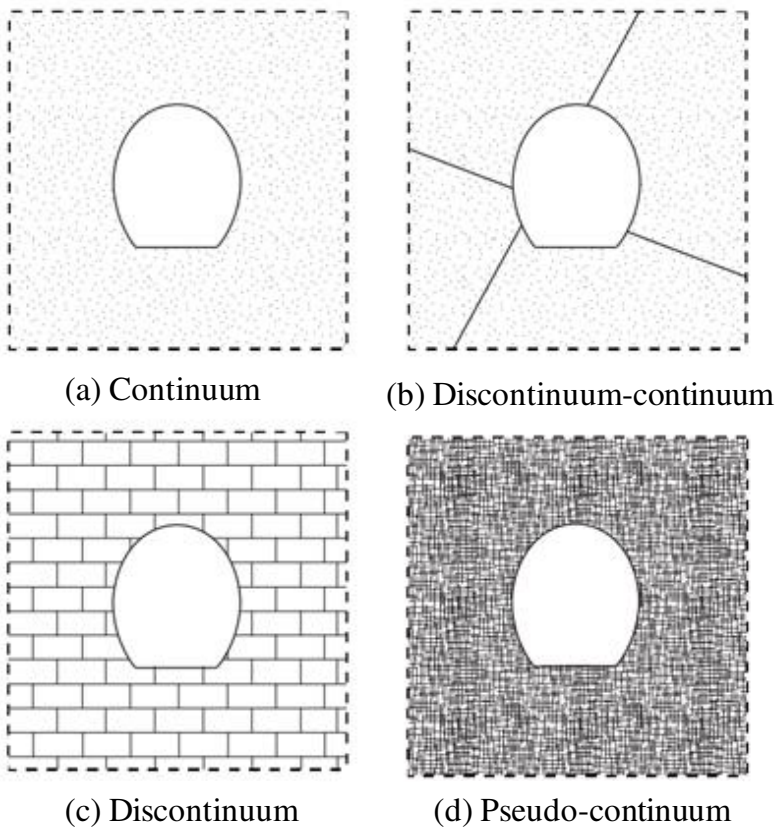

Fig. 2.4. Sketches for rock masses with different numbers of joints (after Bobet et al., 2009)

In Fig. 2.4, (a) represents the rock mass without joints; (b) represents the rock mass with several joints; (c) represents the rock mass with a few joint sets; (d) represents heavily jointed rock mass. Continuous modelling is typically applied to the case (a) and (d) with suitable input parameters for the rock mass. Discontinuous modelling can be applied to the case (b) and (c), although case (b) can also be analyzed using continuum method. Correspondingly, there are two failure mechanisms in tunnelling problems, the stress-controlled and structurally-controlled failure. Stress-controlled failure means the stress exerted on the rock mass exceeds the strength of the rock mass. The rock mass experiences the plastic deformation and the plastic zone develops around the excavation. This may lead to unacceptable large displacements or plastic zone sizes. Structurally-controlled failure means the instability of rock blocks formed by intersecting discontinuities.

The third type of the numerical method is the coupled modelling or hybrid modelling, which combines the other two categories. The coupled modelling can take advantage

of two or more methods. Frequently used coupled modelling includes BEM/FEM (Zienkiewicz et al., 1977), DEM/FEM (Pan and Reed, 1991), etc. The numerical manifold method (NMM) (Shi, 1996) is another combined continuum-discontinuum method, integrating FEM and DDA. The application of NMM to simulate the rock fracture can refer to Wu and Wong (2012) and Wong and Wu (2014).

A detailed review of numerical methods and their applications in geotechnical engineering can refer to Jing and Hudson (2002), Jing (2003) and Bobet et al. (2009), while Bobet et al. (2009) focused on the review of discontinuum modelling.

2.2.4 Observational method

The fast development of numerical methods makes it possible to analyze the behavior of rock masses with excavations of various shapes under complex in situ stress conditions. However, it is well recognized that the actual behavior of the rock mass frequently differs from the prediction of numerical calculations. Field measurements are carried out during and after the construction of engineering projects. The parameters used in the original design can be evaluated against the results of the field measurement, and, if necessary, the original design can be revised. This design method is called the "observational method", which dates back to the "learn-as-you-go" method by Terzaghi and Peck (1948). Unlike the above-mentioned design methods, which predict field behavior in advance, the observational method measures the actual behavior, e.g. the displacement, stress, strain, etc. If the monitored value exceeds the acceptable limit during construction, the construction should be stopped and the pre-defined contingency plans will be triggered (Palmstrom and Stille, 2007). This method provides the most straightforward assessment of the stability of a project. Therefore, the observational method has become a compulsory part of the construction process.

From field measurement data, original design parameters obtained from site investigation can be reassessed. This procedure is the reverse of the traditional design process and thus is called "back analysis", which is an essential tool in the observational method. Sakurai and Takeuchi (1983) used the measured displacement around a tunnel to analyze the stability and to assess the input parameters. The radial and tangential strains from extensometer measurements were checked against the hazard warning levels to determine the stability of a tunnel by Sakurai (1997). As pointed out by Sakurai

et al. (2003), observational methods have evolved from basic visual procedures, constructed on site, to sets of sophisticated procedures using modernized measuring instruments and computer-based back analysis techniques.

2.3 Review of commonly used reliability methods

Due to complex geotechnical processes and in situ stresses, the properties of soils and rocks have great variability. The strength and deformation characteristics of rocks are determined from field or laboratory tests. In field tests, engineering experience and subjective judgment play an important role, while in laboratory tests, samples from the field are more or less disturbed and errors are introduced in measuring and estimating the properties. All these are uncertainties in analyzing geotechnical problems and more detailed summaries were presented by Einstein and Baecher (1983), Baecher and Christian (2003), for example.

Considering the uncertainties in geotechnical engineering, it is necessary to extend the deterministic analysis to probabilistic evaluation. This section first introduces the basic concepts in the probabilistic analysis, followed by the review of the commonly used reliability methods. Then, several surrogate models are presented to deal with problems without explicit performance functions.

2.3.1 Fundamentals of probabilistic analysis

The basic concepts of probabilistic analysis can be easily appreciated through the illustration of the case with two random variables, load (Q) and resistance (R). Unlike the deterministic analysis in which the parameters are deterministic values, the load and resistance are considered as random variables with their probabilistic density functions (PDF) shown in Fig. 2.5.

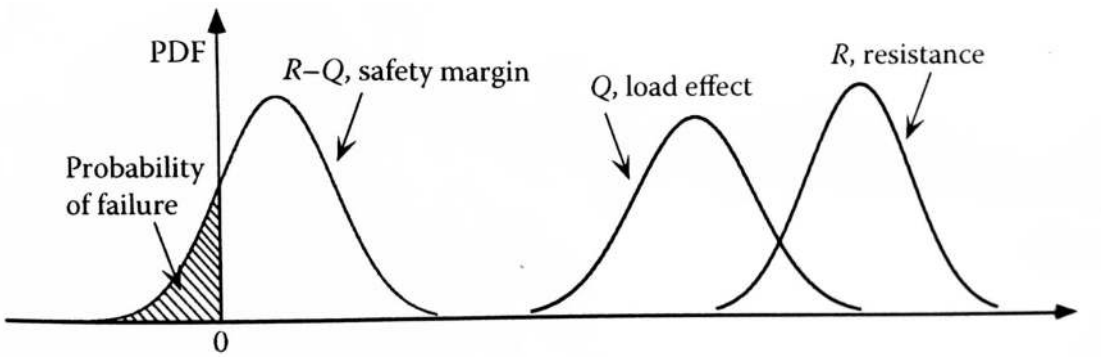

Fig. 2.5. PDF of load, resistance and safety margin (after Nowak and Collins, 2012)

The performance function, which links the input load and resistance parameters to the desired output, can be defined in this case as:

$$g(R, Q) = R - Q \tag{2.2}$$

The limit state, corresponding to the boundary separating the safe domain from the unsafe domain, refers to the situation when $g(R, Q)=0$. If $g>0$, the performance is satisfactory (desired performance) and the area is characterized as a safe domain; if $g<0$, the performance is unsatisfactory (undesired performance) and the area is characterized as an unsafe domain.

In geotechnical engineering, two types of limit states are considered—ultimate limit states (ULS) and serviceability limit states (SLS). ULS is related to the situation when loads exceed the capacity and thus the load-carrying capacity is lost. SLS refers to the situation when excess deformations render the structure unable to fulfil its function.

The probability of failure (P_f), shown by the shaded zone in Fig. 2.5, is defined as the probability that undesired performance or structural failure occurs.

$$P_f = P(R - Q < 0) = P(g < 0) \tag{2.3}$$

The above equation can be rewritten as:

$$P_f = \iint_{g<0} f_{R,Q}(r, q)dqdr \tag{2.4}$$

where $f_{R,Q}(r, q)$ is the joint PDF of the load and resistance.

In general, the probability of failure can be calculated by integrating the joint PDF of R and Q over the failure domain, i.e. $g(R, Q)<0$. These basic concepts, including the joint PDF, safe domain, failure domain, limit state surface (LSS) and probability of failure P_f, are graphically shown in Fig. 2.6.

Reliability index β is a widely used parameter to characterize the safety of a structure. Here, the definition of reliability index is introduced as the shortest distance from the origin to LSS in the uncorrelated standard normal variable space, given by Hasofer and Lind (1974). The nearest point on LSS to the origin is called the design point.

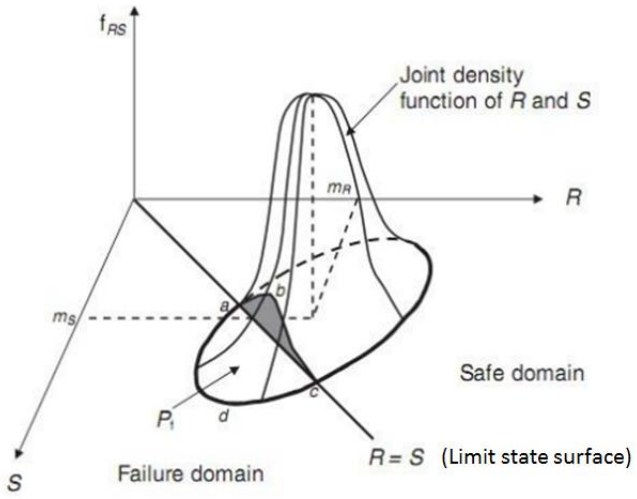

Fig. 2.6. Three-dimensional representation of basic probabilistic concepts (adapted from Haldar and Mahadevan, 2000)

(Note: in this figure, S is in lieu of Q to represent the load effect)

The purpose of the probabilistic analysis is to assess the reliability or the probability of failure of the structure. In geotechnical engineering, performance functions may have complex forms or even cannot be explicitly expressed. Besides, the joint PDF of random variables with various distributions cannot be obtained analytically and the direct integration of joint PDF over the failure domain is impossible for complex problems. All these factors make it difficult to evaluate the probability of failure through Eq. (2.4). However, researchers have proposed various approaches to deal with this problem. Some of the simplified or approximate methods are introduced in the following section.

2.3.2 Probabilistic assessment methods

In this section, three approximate methods and one simulation method, namely, first-order second-moment method (FOSM), first-order reliability method (FORM), second-order reliability method (SORM) and Monte Carlo Simulation (MCS) method, to estimate the probability of failure are introduced.

2.3.2.1 First-order second-moment (FOSM)

First-order second-moment (FOSM) method uses the first-order Taylor expansion of the performance function at the mean value point and the first two moments (i.e. mean value and standard deviation) of the random variables to calculate the reliability index. This method is also named as the mean value first-order second-moment (MVFOSM) method. The detailed formulation and application examples of FOSM can refer to Haldar and Mahadevan (2000) and Baecher and Christian (2003), for example.

FOSM assumes that the performance function is normally distributed such that the reliability index is the distance from the mean value to zero in units of the standard deviation, shown by

$$\beta_{FOSM} = \frac{\mu_g}{\sigma_g} \tag{2.5}$$

where μ_g and σ_g are the mean and the standard deviation of the performance function, respectively. The performance function can be approximated by the first-order Taylor expansion at the mean value point as

$$g(x_1, x_2, ..., x_n) \approx g(\mu_{X_1}, \mu_{X_2}, ..., \mu_{X_n}) + \sum_{i=1}^{n} (x_i - \mu_{X_i}) \frac{\partial g}{\partial x_i} \tag{2.6}$$

where $g(x_1, x_2, ..., x_n)$ is the performance function; x_i is the value of the *i*-th random variable; μ_{X_i} is the mean value for the *i*-th random variable. The mean and standard deviation of the performance function can be estimated by (e.g. Haldar and Mahadevan, 2000; Baecher and Christian, 2003)

$$\mu_g \approx g(\mu_{X_1}, \mu_{X_2}, ..., \mu_{X_n}) \tag{2.7}$$

$$\sigma_g^2 \approx \sum_{i=1}^{n}\sum_{j=1}^{n}\rho_{X_iX_j}\sigma_{X_i}\sigma_{X_j}\frac{\partial g}{\partial x_i}\frac{\partial g}{\partial x_j} \tag{2.8}$$

where σ_{X_i} is the standard deviation of X_i; $\rho_{X_iX_j}$ is the correlation coefficient between two random variables. The mean of the performance function can be approximated by the performance function value calculated with the mean values of input random variables. The estimate of the standard deviation of the performance function can be implemented by the central difference method if the partial derivatives cannot be obtained analytically.

$$\frac{\partial g}{\partial x_i} \approx \frac{1}{2\varepsilon_i}\left[g(\mu_{X_1}, \mu_{X_2},..., \mu_{X_i}+\varepsilon_i,..., \mu_{X_n}) - g(\mu_{X_1}, \mu_{X_2},..., \mu_{X_i}-\varepsilon_i,..., \mu_{X_n})\right] \tag{2.9}$$

where ε_i is a small increment applied to the random variable. FOSM is easy to implement. However, this method suffers from some deficiencies (Haldar and Mahadevan, 2000). FOSM uses the means, standard deviations and correlation coefficients but overlooks the distributions of input random variables. Because the mean and standard deviation of the performance function depend on the formulation, different forms of performance functions would yield different FOSM reliability indices. A similar method called Point Estimate Method (PEM) uses the same definition of the reliability index as FOSM, but estimates the mean and standard deviation of the performance function by using sampling points values around the mean value. The application of FOSM and PEM on tunnelling problems will be illustrated in Chapter 5.

2.3.2.2 First-order reliability method (FORM)

To overcome these deficiencies, the Hasofer-Lind reliability index (Hasofer and Lind, 1974) was proposed and the design point was used instead of the mean value point as the location where the Taylor series expansion was conducted. Unlike the reliability index defined in the FOSM, which is the ratio of the mean over the standard deviation of the performance function, the Hasofer-Lind reliability index is defined in the reduced variable space as the shortest distance from the origin to the nearest point on LSS. This definition overcomes the lack of invariance encountered in FOSM. The matrix formulation of the Hasofer-Lind index is

$$\beta = \min_{\mathbf{x}\in F}\sqrt{(\mathbf{x}-\boldsymbol{\mu})^T\mathbf{C}^{-1}(\mathbf{x}-\boldsymbol{\mu})} \tag{2.10}$$

or

$$\beta = \min_{\mathbf{x}\in F} \sqrt{\left[\frac{x_i - \mu_i}{\sigma_i}\right]^T \mathbf{R}^{-1} \left[\frac{x_i - \mu_i}{\sigma_i}\right]} \tag{2.11}$$

where **x** is a vector of the random variable x_i; **μ** is the vector of the mean value μ_i and σ_i is the standard deviation; **C** is the covariance matrix and **R** is the correlation matrix; F is the failure domain. Eq. (2.11) is suggested to be used instead of Eq. (2.10) since the correlation matrix is easier to set up and conveys the correlation structure more explicitly (Low and Tang, 1997). The search for the design point and corresponding reliability index is through an iterative process by first assuming the tentative design point (usually the mean value point), then obtaining the corresponding direction cosine of the performance function and tentative reliability index, from which new tentative design point can be calculated. This iterative process continues until the reliability index converges. Detailed formulation and procedure of the calculation can be found in Melchers (1999), Haldar and Mahadevan (2000), for example. The final design point and reliability index remain the same no matter how the performance function is formulated. The iterative process to calculate the reliability index and design point is noted as the traditional or classical procedure in this thesis. Practitioners may think this procedure is cumbersome and is not straightforward.

Low and Tang (1997) proposed an expanding ellipsoid perspective to interpret and an efficient method using the Excel Solver to calculate the Hasofer-Line index, as shown in Fig. 2.7.

In Fig. 2.7, the one-sigma-ellipse (1-σ ellipse) and the β-ellipse, tilted for correlated variables or untilted for uncorrelated variables, represent the probability contours of the input variables. With the expanding of the ellipse, the probability decreases. Once the ellipse touches LSS separating the safe domain from the unsafe domain, the point of tangency is the design point or the most probable point of failure. The reliability index β is the distance from the mean value point to the design point in units of the directional standard deviation (*R/r* in Fig. 2.7). To find the design point is graphically equivalent to finding the smallest ellipsoid tangent to LSS. This procedure can be implemented using the Excel optimization tool Solver.

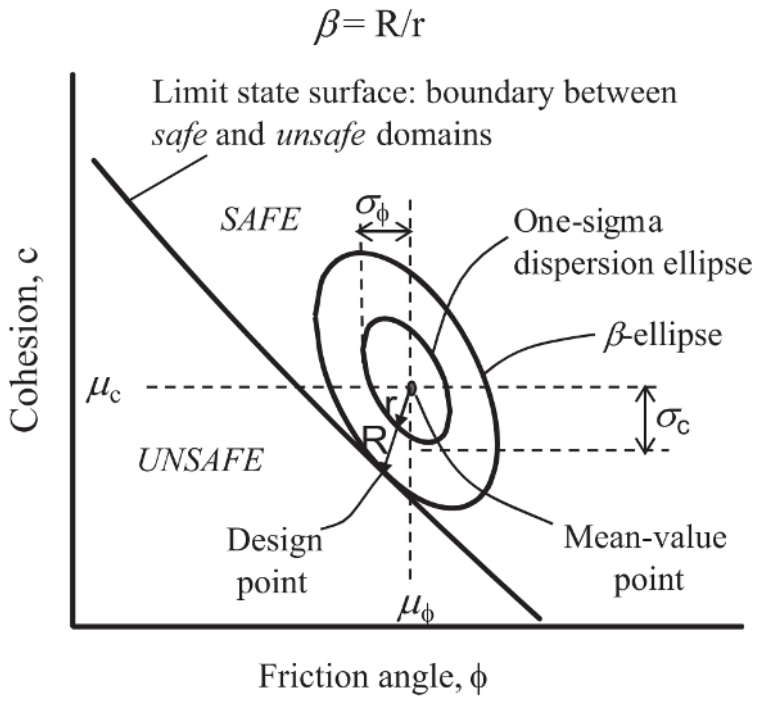

Fig. 2.7. Illustration of the reliability index in the plane when *c* and ϕ are negatively correlated (after Low, 2014)

The Hasofer-Lind index was originally proposed for normal distributions. It can be extended to nonnormal distributions, which is the FORM analysis. When non-normal distributions are involved, equivalent normal mean and standard deviation may be used instead. These equivalent values can be estimated based on the two-parameter equivalent transformation (Rackwitz and Fiessler, 1978) or more complicated three-parameter equivalent transformation (Chen and Lind, 1983; Wu and Wirsching, 1987). The reliability index for FORM is

$$\beta = \min_{\mathbf{x}\in F} \sqrt{\left[\frac{x_i - \mu_i^N}{\sigma_i^N}\right]^T \mathbf{R}^{-1} \left[\frac{x_i - \mu_i^N}{\sigma_i^N}\right]} \tag{2.12}$$

where μ_i^N and σ_i^N are the mean and standard deviation of the equivalent normal random variable. For non-normal variables, Fig. 2.7 still applies except that the mean and standard deviations are replaced by those for the equivalent normal distributions. Eq. (2.12) and the Rackwitz and Fiessler transformation were used in the constrained optimization approach of FORM in Low and Tang (2004).

An alternative procedure to the Low and Tang (2004) approach was presented by Low and Tang (2007) using the following equation for the reliability index:

$$\beta = \min_{\mathbf{x} \in F} \sqrt{\mathbf{n}^T \mathbf{R}^{-1} \mathbf{n}} \tag{2.13}$$

Low and Tang (2004) procedure varies **x** (variable values in the original x-space) whereas Low and Tang (2007) varies **n** (variable values in the correlated standard normal variable space, n-space). Low and Tang (2007) showed that changing the variable values in the n-space had the advantages such as:

(1) Faster, more efficient, robust and succinct
(2) Obviating the need for computations of equivalent normal means and standard deviations
(3) Easy of initialization prior to the constrained optimization

Details of the FORM 2004 and 2007 procedures together with various geotechnical case studies can refer to Low (2008), Low (2014) and Low (2015). The constrained optimization can be easily implemented in the ubiquitous spreadsheet environment using Solver tool. Meanwhile, the constrained optimization toolbox in MATLAB and other software can also be used to conduct this intuitive and transparent method. Through the transformation from non-normal variables to equivalent normal variables, the correlation structure may be changed, which can be considered in the Nataf transformation as shown in Der Kiureghian and Liu (1986) and Melchers (1999). However, for most geotechnical engineering problems, the modified correlation matrix differs insignificantly from the original matrix. Therefore, for the case studies in this thesis, the change of the correlation matrix is ignored for simplicity.

The probability of failure can be estimated through

$$P_f \approx 1 - \Phi(\beta) = \Phi(-\beta) \tag{2.14}$$

where $\Phi(.)$ is the cumulative distribution function (CDF) of the standard normal variable. The equation is exact only when LSS is planar and the variables follow normal distributions. Inaccuracies may arise when LSS is significantly nonlinear. Thus, more refined alternatives have been proposed, for example SORM.

2.3.2.3 Second order reliability method (SORM)

Instead of using first-order Taylor series expansion at the design point in FORM, second-order approximations are adopted in SORM. SORM can capture the nonlinearity of LSS around the design point. It is based on the FORM results (reliability index β and design point) which are the inputs for SORM. Therefore, SORM is an extension of FORM. Widely used SORM approaches attempt to evaluate the curvature of LSS at the design point in the dimensionless and rotated u-space (uncorrelated standard normal random variable space). The probability of failure is estimated as a function of the FORM reliability index and the main curvatures $\boldsymbol{\kappa}$ using established SORM equations of the following form:

$$P_f(SORM) = f(\beta_{FORM}, \boldsymbol{\kappa}) \tag{2.15}$$

Several formulae in the form of the above equation are attributed to Breitung (1984), Hohenbichler and Rackwitz (1988), Tvedt (1989), Tvedt (1990), Köylüoğlu and Nielsen (1994), Hong (1999) and Zhao and Ono (1999). These formulae are summarized in Chan and Low (2012a).

There are two widely used methods to calculate the principal curvatures of LSS at the design point. One is through the eigenvalues of the reduced and transformed Hessian matrix $\mathbf{H}_{\text{red}}$ calculated from the second-order derivatives of LSS at the design point. The detailed formulation and procedure of this method can be found in Haldar and Mahadevan (2000), Choi et al. (2007), Lü and Low (2011), for example. The advantage of this method lies in the fact that the calculated principal curvatures are accurate provided that LSS is exact. However, the disadvantage is the cumbersome and error-prone transformation and calculation procedure.

The other method is the point fitting strategy proposed by Der Kiureghian et al. (1987). This method intends to approximate the actual LSS by a paraboloid which is obtained by fitting $2(n\text{-}1)$ points around the design point for an n random variable case. Since the curvature of a parabola is readily available, these curvatures of the approximate paraboloid are used as the estimate of the curvatures of LSS. This method is comparatively easy to use. Chan and Low (2012a) developed the Excel implementation of this method, in which the complex mathematical operations are relegated to simple

function codes in the Excel platform. The only inaccuracy exists in the approximate nature of the paraboloid to the actual LLS.

It should be emphasized that, though SORM gives a better estimate of the probability of failure for highly nonlinear problems, FORM is the basis of SORM and thus SORM results are useful only when the reliability index and design point from FORM are accurate.

2.3.2.4 Monte Carlo simulation (MCS) method

Instead of approximating the limit state by the first-order or second-order Taylor expansions, Monte Carlo simulation (MCS) involves large numbers of random samplings to artificially simulate experiments to estimate the probability of failure. Typically, MCS is implemented through sampling random variables according to their distributions to obtain samples. Then, each set of samples is treated as the input to calculate the performance function $g(x)$. If $g(x)<0$, it is considered as a failure point. After numbers of such experiments are conducted, the probability of failure can be estimated by

$$P_f \approx \frac{n\left(g(x)<0\right)}{N} \tag{2.16}$$

where N is the total number of experiments and $n\left(g(x)<0\right)$ represents the number of failed experiments. The estimate of the probability of failure can be mathematically demonstrated by rewriting Eq. (2.16) as (Melchers, 1999)

$$P_f = \int_{g(x)<0} I_g(x) f_x(x) dx \approx \frac{1}{N}\sum_{i=1}^{N} I_g(x_i) \approx \frac{n\left(g(x)<0\right)}{N} \tag{2.17}$$

where $I_g(x)$ is an indicator function with regard to $g(x)$ and is defined as

$$I_g(x) = \begin{cases} 0 & \text{if } g(x) \geq 0 \\ 1 & \text{if } g(x) < 0 \end{cases} \tag{2.18}$$

It is clear that the estimate of the probability of failure can be straightforwardly interpreted as the ratio of the number of realizations of **x** which render $g(x_i)<0$ over the total number of realizations. If the maximum error of the probability of failure is e

at confidence 1-α, then the required number of realizations is estimated by (Rubinstein and Kroese, 2011)

$$N = \hat{P}_f (1 - \hat{P}_f) \left(\frac{z_{\alpha/2}}{e} \right)^2 \tag{2.19}$$

where $\hat{P}_f$ is the estimated value of P_f and $z_{\alpha/2}$ is the point of the standard normal distribution satisfying $P(Z > z_{\alpha/2}) = \alpha/2$.

The coefficient of variation of $\hat{P}_f$ can be estimated by

$$\delta_{\hat{P}_f} \approx \sqrt{\frac{(1 - \hat{P}_f)}{N\hat{P}_f}} \tag{2.20}$$

MCS is considered robust and accurate, especially when the number of experiments is large and thus is typically chosen as the verification method for other probabilistic approaches. The advantages lie in its straightforwardness and robustness. However, the computational cost is prohibitive when the performance function is implicit and the probability of failure is small. To overcome such limitations, some more advanced MCS methods have been proposed.

Contrast to the traditional (or crude, or direct) MCS, Latin Hypercube Sampling (LHS) method adopts more efficient sampling tactic to generate random samples, thus reducing the error. LHS first divides the sampling range into N intervals for each random variable. The probability of *x* locating in each interval is 1/N. Then, in each interval, a sample is selected randomly and thus N samples for each random variable are prepared. Finally, arrange all these sampling values randomly into N combinations of all random variables. Some examples show that LHS reduced the coefficient of variation (McKay, 1992). LHS now is widely adopted, for example, the MCS software @RISK (www.palisade.com).

Another widely used advanced MCS is the importance sampling technique. Unlike the LHS to adopt an efficient sampling strategy, importance sampling technique introduces a new sampling function, the PDF of which is noted as $\psi(v)$. For importance sampling, Eq. (2.17) can be modified as (Melchers, 1999)

$$P_f = \int_{g(x)<0} I\big(g(x)<0\big)\frac{\phi(v)}{\psi(v)}\psi(v)dv \approx \frac{1}{N}\sum_{i=1}^{N} I\big(g(x)<0\big)\frac{\phi(v_i)}{\psi(v_i)} \tag{2.21}$$

where $\psi(v)$ is termed as the importance sampling PDF at value v; $\phi(v)$ is the value of PDF of the standard normal distribution at v. Through this transformation, a new sampling PDF can be used instead. Therefore, the problem lies in how to choose the importance sampling function. Harbitz (1986) proposed an importance sampling method based on the design point which contributes most to the probability of failure. This technique samples a larger proportion of points located in the failure domain than the direct MCS and, therefore, requires less sampling points. The importance sampling technique has been used in various geotechnical problems, e.g. Ching et al. (2009) for the slope stability analysis.

A recently popular method of MCS is the subset simulation (Au and Beck, 2001; Au et al., 2007; Au et al., 2010). It uses the idea that an event with a small probability of failure can be expressed as a product of some intermediate events with larger conditional probabilities of failure. Subset simulation converts a problem of a small failure probability to a sequence of more likely events. Therefore, it is most efficient for problems with small probabilities of failure. The first level of sampling is the direct MCS. The following levels of sampling points are selected from the failure domain of previous levels through the Markov Chain Monte Carlo technique. Au et al. (2010) developed the spreadsheet implementation of the subset simulation. This method has been used in the slope stability analysis (Wang et al., 2010b; Wang et al., 2011).

Besides these three advanced MCS stated above, there are other techniques to reduce the variance of MCS, such as the directional simulation method (Bjerager, 1988) and the linear sampling method (Koutsourelakis et al., 2004).

MCS is also widely used in the reliability analysis of underground excavations and typically as a verification method for other approaches, e.g. FORM and SORM. Relevant research can be found in Oreste (2005), Lü and Low (2011), among others.

FOSM, FORM, SORM and MCS reviewed in this section can only be effectively implemented when the explicit expression of the performance function is readily available. However, this requirement can seldom be satisfied in geotechnical

engineering. The difficulty caused by the implicit nature of the performance function can be overcome by using the surrogate models.

2.3.3 Review of approximate approaches for implicit performance functions

When the performance function values cannot be obtained explicitly, the numerical methods, such as FEM and FDM, are used to calculate the response of a model. Under such circumstances, surrogate models or bridging methods are needed to approximate the implicit performance functions. Sampling points together with the corresponding output values from numerical simulations are necessary to construct surrogate models. In this section, various sampling strategies typically used in the literature are reviewed first. Then, the surrogate models or bridging methods, including the polynomial response surface method (RSM) and artificial neural network (ANN), are revisited and a summary of other methods is provided.

2.3.3.1 Sampling Strategy

Axial-point Design

One central point and two sampling points on each random variable axis are included in the axial-point design method. If there are n random variables, the total number of sampling points is $2n+1$. This method can be graphically illustrated by a two-variable case shown in Fig. 2.8.

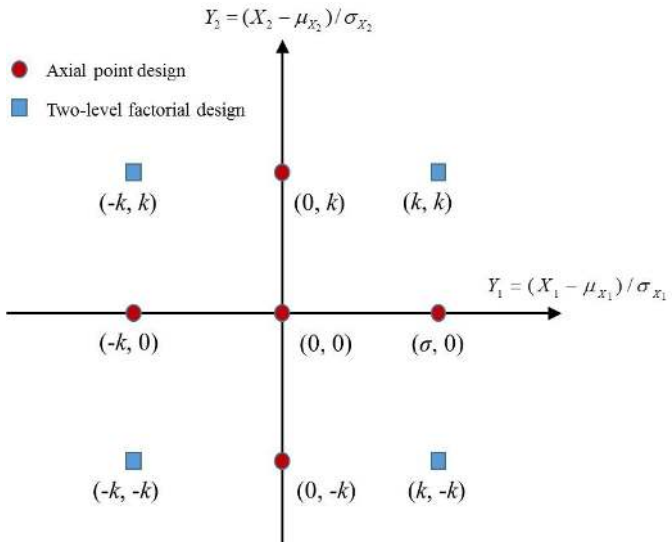

Fig. 2.8. Sampling points shown for axial-point design and two-level factorial design

The axial sampling points can be expressed as $x_i = x_c \pm k\sigma_i$, where x_c is the value for the central point; k is the sampling factor controlling the sampling range; σ_i is the standard deviation. The axial-point design method is widely used in the polynomial response surface method, e.g. Tandjiria et al. (2000), Xu and Low (2006).

Two-level Factorial Design

In this design, two values are selected for each random variable, typically one value (+k) above the central point value and the other value (-k) below the central point value. All combinations of these values for all random variables are chosen as the sampling points (Myers, 1971). This can be illustrated using a two-variable case in Fig. 2.8. If n random variables are concerned, the two-level factorial design generates 2^n sampling points. Unlike the axial-point design, which generates points on the axes, the two-level factorial design uses sampling points at corners. This design approach is typically used in the point estimate method but seldom used in the surrogate models.

Central Composite Design

The central composite design (Box and Wilson, 1951), made up of the central point, the axial points and points at all corners, is a combination of the sampling points in the axial-point design and the two-level factorial design. Thus, the total number of sampling points is 2^n+2n+1 for an n random variable case. This method is shown in Fig. 2.9 for a three-variable example.

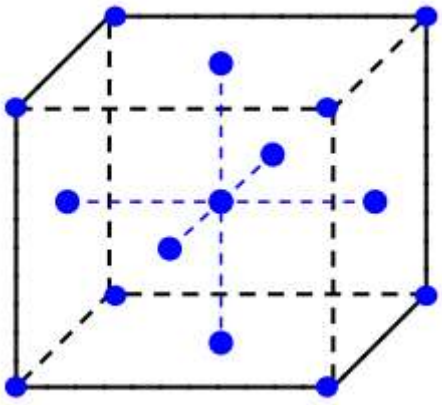

Fig. 2.9. Sampling points shown for central composite design

Uniform Design (UD)

Different from the above sampling methods which focus on the surrounding of the central point, UD tries to distribute the sampling points over the domain of interest uniformly. First proposed by Fang (1980), UD is able to randomly select the sampling points in a uniform manner. For example, in Fig. 2.10, 25 sampling points selected by UD in the range of [-1,1] for two random variables are uniformly distributed in a 5-by-5 lattice with each sampling point located in one sub-lattice. For comparison, the sampling points by random selection are also shown in the same figure. Random selection cannot guarantee that the sampling points are uniformly distributed. Thus, some parts of the domain may be crowded with more sampling points while other parts may contain few points.

The merit of UD lies in that it can produce samples with high representativeness of the whole domain and thus it is suitable when the accuracy of the approximation in the entire domain is of concern. Another point should be pointed out is that there is no restriction on the number of sampling points in UD. In principle, the number of sampling points required to accurately approximate LLS should be determined on a case-by-case basis. It is influenced by the number of random variables and the nonlinearity of the problem considered.

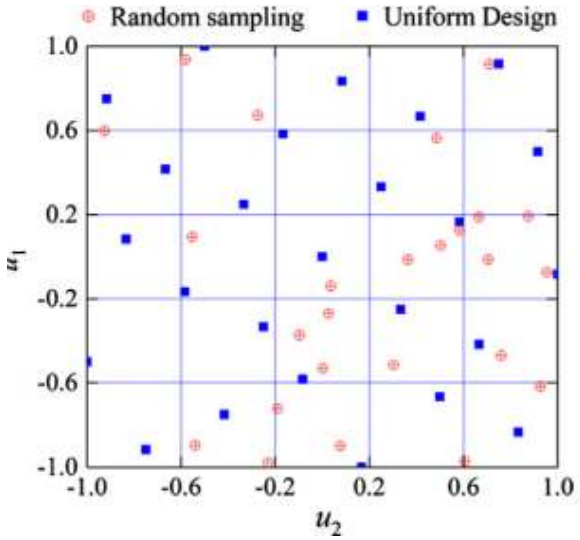

Fig. 2.10. Comparison of UD with random sampling (after Lü et al., 2012)

Other sampling methods for global sampling includes the Latin Hypercube Sampling widely used in the MCS. The collocation-based sampling used for the stochastic response surface method (Tatang et al., 1997).

2.3.3.2 Response surface method

One of the widely used surrogate models is the RSM. In the general meaning, RSM refers to any method that uses prescribed expressions, such as polynomials and exponential functions, to approximate LSS. In this thesis, only the polynomial RSM is considered. Although the forms of the expression are prescribed, the coefficients are unknown. To approximate LSS is to determine the unknown coefficients using the sampling points. Previous research about RSM can be summarized in the following four aspects.

1. Selection of the forms of response function

   Linear and quadratic polynomial response functions are typically adopted because of their simplicity. Higher orders of polynomial functions may lead to ill-conditioned systems of equations and erratic system behaviour (Melchers, 1999) and thus are not widely used. Other forms of response functions are rare in the literature, such as the inverse polynomials (Nelder, 1966) and reciprocal functions (Tandjiria et al., 2000).

2. Determination of the unknown coefficients

   If the number of sampling points equals that of the unknown coefficients, the coefficients can be determined by solving a series of linear equations. For example, the second-order polynomial RSM uses the following expression

$$\bar{g}(x) = a + \sum_{i=1}^{n} b_i x_i + \sum_{i=1}^{n} c_i x_i^2 \tag{2.22}$$

   where $\bar{g}(x)$ is the response function; a, b_i and c_i are unknown coefficients that should be determined; x_i is the random variable value; n is the number of random variables. Bucher and Bourgund (1990) suggested the axial-point design scheme could be used to obtain $2n+1$ sampling points by

$$x_i = x_c \pm k\sigma_i \tag{2.23}$$

where x_i is the sampling point value; x_c is the value of centre sampling point; σ_i is the standard deviation; k is a user defined sampling factor. This sampling strategy effectively uses the probabilistic characteristics (mean value and standard deviation) of the random variables.

If the number of sampling points exceeds the number of unknown coefficients, the least square method has to be used to determine the coefficients. For example, in the two-level factorial design, the total number of experiments increases exponentially with the number of the random variables. The number of sampling points is greater than the unknown coefficients and the least square method should be used (Wong et al., 2005). RSM determined by the least square method cannot guarantee that the response surface passes through every sampling point but is a best-fit to all the sampling points.

3. Iteration strategy

Bucher and Bourgund (1990) introduced an efficient iterative strategy to make the response function gradually approach the actual LSS around the design point. After the construction of the first tentative response surface, the estimate of the design point is obtained as $\bar{x}_D$. Then the new center point x_M is calculated by the linear interpolation between $\bar{x}_D$ and the previous center point $\bar{x}$ by

$$x_M = \bar{x} + (\bar{x}_D - \bar{x})\frac{g(\bar{x})}{g(\bar{x}) - g(\bar{x}_D)} \tag{2.24}$$

This iteration strategy requires that one more evaluation of the performance function at the tentative design point. Later, a more general expression for the iteration strategy was given by Muzeau and Lemaire (1997) as

$$x_M = (1-\zeta)\bar{x} + \zeta\bar{x}_D \tag{2.25}$$

where ζ is the arbitrary controlling factor. ζ=1 represents that the tentative design point is chosen as the sampling central point for the next iteration. This iteration strategy does not require one more evaluation of the performance function and has been widely applied to reliability analyses of various geotechnical problems, e.g.

Mollon et al. (2009b), Lü and Low (2011), Chan and Low (2012b) and Ji and Low (2012).

4. Convergence criterion

   The widely used convergence criterion is to compare the reliability index in current iteration *i* and that in the previous iteration *i*-1 (Muzeau and Lemaire, 1997), as given below.

$$\left|\beta_i - \beta_{i-1}\right| < \varepsilon_{tol} \tag{2.26}$$

   Typically, the tolerance ε_{tol} is selected between 10^{-4} and 10^{-2}.

Several research papers focused on the improvement of the RSM. Rajashekhar and Ellingwood (1993) pointed out that reducing the sampling factor *k* during the iteration would increase the accuracy. However, if the process was repeated infinitely with progressively smaller k values, at some stage, one would get an ill-conditioned system of equations. Guan and Melchers (2001) used some assumed performance functions to study the effect of the sampling factor on the probability of failure. The results showed that the accuracy of the reliability index depended on the sampling factor. However, there were no guidelines for selecting the sampling factor. Wong et al. (2005) encountered a numerical error problem in which the reliability index could not converge using RSM. In their study, the non-smoothness of the performance function was considered to cause the non-convergence problem.

The research mentioned above is concerned with the polynomial RSM. Recently, more sophisticated RSM, with similar concepts but different expressions, have been developed and applied to geotechnical engineering problems. One of such method is the Stochastic Response Surface Method (SRSM). SRSM adopted a similar expression as the third-order polynomial RSM. The purpose of the SRSM is to yield a relatively accurate representation of the performance function in a larger random variable space, whereas RSM only approximates the performance function in the neighbourhood of the design point. The cost of the global approximation is that a large number of sampling points should be experimented. The application of this method can be found in Li et al. (2011) for a slope stability analysis and Mollon et al. (2013) for a tunnel face stability

problem. Another recently developed method is called Kriging-based Response Surface Method (KRSM), which is similar in the idea with the SRSM. KSRM, like SRSM, does not need the iteration procedure but requires a huge number of sampling points to approximate the performance function in the whole random variable space. Zhang et al. (2013a) used this method to analyze a layered soil slope and to estimate the probability of failure.

2.3.3.3 Artificial Neural Network (ANN)

Artificial neural network (ANN), which simulates the human brain structure, is a universally used regression and prediction model due to its powerful learning ability. ANN is an information processing technique based on the biological nerve systems. This technique has the ability to respond to input stimuli and to adapt to the changing environment by learning from experience (Hykin, 1999). Fig. 2.11 is an illustration of a typical three-layer ANN, which is used to explain the basic structure.

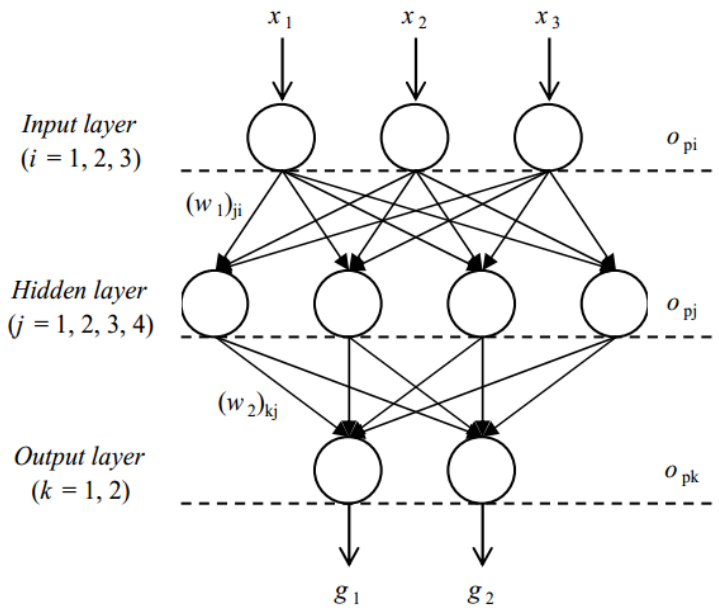

Fig. 2.11. Basic structure of ANN (after Anderson, 2005)

In Fig. 2.11, there are three layers, namely, the input layer, the hidden layer and the output layer. Each element represented by a circle in the hidden layer is named as a neuron (four neurons in the figure). Although there is no restriction on the number of hidden layers, it has been demonstrated that ANN with a typical three-layer structure (i.e. single hidden layer) can approximate any function, provided that sufficient hidden

neurons are available (Hornik et al., 1989). Thus, this three-layer structure is widely adopted in ANN analysis. The connection between the input layer and the hidden layer and that between the hidden layer and output layer are through weights $(w_1)_{ji}$, $(w_2)_{kj}$ and transfer functions. The output from the hidden layer o_{pj} is to apply a transfer function to the weighted sum of the outputs from the input layer o_{pi}:

$$o_{pj} = f_{transfer}\left(\sum_i (w_1)_{ji} o_{pi} + (w_1)_{bias}\right) \tag{2.27}$$

where $(w_1)_{ji}$ is the weight between the input node i and the hidden node j; $(w_1)_{bias}$ is the bias between input and hidden layers; $f_{transfer}$ is the transfer function.

The output from the output layer o_{pk} is the outcome of applying a transfer function to the weighted sum of the outputs from the hidden layer o_{pj}:

$$o_{pk} = f_{transfer}\left(\sum_j (w_2)_{kj} o_{pj} + (w_2)_{bias}\right) \tag{2.28}$$

where $(w_2)_{kj}$ is the weight between hidden node j and output node k ; $(w_2)_{bias}$ is the bias between hidden and output layers; $f_{transfer}$ is the transfer function.

Typically used transfer functions for the hidden layer are the log-sigmoid function and tan-sigmoid function because of their simple, continuous and differentiable nature whereas the pure linear transfer function is preferred for the output layer.

The most widely used ANN is the feed-forward back propagation neural network (BPNN), which consists of two passes of data transfer, namely, the forward pass and the backward pass. The input data propagates forward through the network while the error between the network output and the target value is propagated backwards to adjust the weights and biases within the network, which is a self-learning process. Due to this robust error-correction capability, BPNN gains its popularity in solving curve-fitting, prediction and classification problems. The adjustment of the weights within the network is called the training process, during which the error is progressively reduced. There are various error reduction methods ranging from simple to complex such as the gradient descent, gradient descent with momentum, Levenberg-Marquardt, Bayesian regularization, etc. Detailed of these learning algorithms can refer to Hagan et al. (1996).

The advantages of ANN or BPNN are

(1) There is no constraint on the number of the sampling points to train ANN but, in theory, more sampling points yield better results.
(2) Powerful learning ability makes ANN can approximate almost any kind of performance functions.
(3) The main structure of ANN can be applied to different problems without much modification.

The disadvantages are

(1) There are no general guidelines for choosing the number of hidden neurons and some parameters needed in the training algorithms. The best selection of these values depends on the problem considered.
(2) It is well recognized that ANN is better at interpolation than extrapolation, which requires that the sampling points should cover the whole domain of interest.
(3) The over-fitting problem, which means ANN performs poorly outside the sampling domain, is a common obstacle encountered. Different strategies, such as the cross-validation, can be used to obviate this problem.

ANN has been extensively applied to geotechnical engineering problems. Shahin et al. (2001) reviewed the application of ANN, including foundation, slope, liquefaction, tunnels and underground opening, etc. Later, Shahin et al. (2008) extended their review with special focus on the modelling procedures about ANN. Some of the representative papers are reviewed here. Goh (1994) and Goh (2002) assessed the liquefaction potential using ANN. Juang and Chen (1999) and Juang et al. (1999) analyzed the liquefaction resistance based on the cone penetration test using ANN. ANN was used together with FORM to calculate the probability of failure for a beam case and a shallow tunnel case by Goh and Kulhawy (2003) and for a braced retaining wall problem by Goh and Kulhawy (2005). Chan and Low (2012b) used ANN to approximate LLS for a laterally loaded pile.

For underground excavations, ANN is also widely adopted to approximate performance functions. Soroosh et al. (2006) used 170 tunnel convergence results obtained from FEM analyses to train ANN and the network was used to predict the convergence before the support was installed. Goh and Zhang (2012) related the factor of safety to geometry

parameters and rock mass Q values through ANN and drew some design charts for preliminary design. Lü et al. (2012) studied the ground-support interaction for a deep rock tunnel through the convergence-confinement method (CCM) using ANN and uniform design. In their study, SORM was also conducted to obtain a more accurate probability of failure based on the first-order and second-order derivatives of ANN proposed by Deng (2006).

2.3.3.4 Other surrogate models

All the approximate methods are called surrogate models in reliability analysis to substitute the implicit performance functions. Generally speaking, any kind of model, which has the ability to map the relation between inputs and outputs, can be used as the bridging method. Besides RSM and ANN, researchers also applied other methods to geotechnical engineering problems.

One category is the regression method including polynomial regression (PR) and logarithmic regression (LR). Zhu et al. (2008) studied the displacements of sidewalls for an underground hydropower project and proposed a polynomial regression formula based on numerical simulation results. Multiple regression models were conducted to assess the relationship between the support pressure, depth and tunnel deformation for rock masses with different strength properties by Basarir (2008). Zhang and Goh (2012) related the global factor of safety and percent strain of a horseshoe-shaped tunnel to the deformation modulus, strength parameters and in situ stress conditions using the polynomial regression model, based on which FORM was conducted to calculate the probability of failure.

Unlike the regression method, which presumes the form of the expression, multivariate adaptive regression splines (MARS) use a series of piecewise linear segments with different gradients to model the nonlinear response. The detailed explanation and procedure of the MARS can be found in Friedman (1991). Zhang and Goh (2013) illustrated the applicability of MARS to various geotechnical problems including seismic liquefaction, surface settlement induced by tunnelling and collapse potential of the compacted soil. Zhang and Goh (2014) approximated the serviceability limit state of a twin-cavern using MARS.

Due to the development of computers, artificial intelligence algorithms, among which stands ANN, have been through fast development. These algorithms endow the computer the capability of learning by itself from numerous data sets. Thus, using such algorithms for data mining is also called machine learning. Besides ANN, another machine learning method used as the surrogate model in geotechnical engineering is the support vector machine (SVM) (Vapnik et al., 1997), which was first proposed as a method for classification. Some of the applications of SVM in geotechnical engineering can refer to Goh and Goh (2007) for a seismic liquefaction problem, Zhao (2008) for a slope stability problem and Samui (2008) for a shallow foundation problem. SVM has also successfully been applied to underground excavation analysis. A set of data of monitored displacements of a tunnel was used to train SVM and to estimate the nonlinear relationship between soil parameters and the tunnel convergence (Mahdevari et al., 2013). Zhao et al. (2014) used FORM and least square SVM, which is a modified SVM model proposed by Suykens and Vandewalle (1999), to calculate the probability of failure for circular and horseshoe-shaped tunnels.

It is impossible to review all the available surrogate models. Instead of listing all these methods, two or three methods will be focused on and used in this thesis.

2.4 Review of probabilistic analyses of underground excavation problems

The above sections review the general deterministic analysis methods for underground excavation problems and the commonly used reliability methods. The literature review of the probabilistic analysis of underground excavation problems is presented in this section. The reliability analysis of geotechnical problems is abundant such as the pile and foundation problems (e.g. Zhang et al., 2001; Zhang et al., 2005) or the slope stability problem (e.g. Li et al., 2011; Ji and Low, 2012). However, the reliability analysis of underground rock excavation problems is limited in the literature. A detailed list of the journal papers regarding the probabilistic analyses of underground excavation problems is shown in Appendix A. Some observations of the literature can be summarized as follows.

The closed-form solution was commonly used to verify different probabilistic methods or surrogate models. For closed-form solutions, MCS can be directly applied without

much computational effort and the MCS results are regarded as the benchmark for comparison of other methods. For example, the Duncan-Fama solution, first extended to the probabilistic analysis by Hoek (1998), has been used by various researchers. Li and Low (2010) applied FORM to this solution and discussed the influence of the distribution on the reliability index. Lü and Low (2011) applied FORM, SORM and polynomial RSM to the Duncan-Fama solution for M-C grounds and the Carranza-Torres solution for H-B grounds. The Duncan-Fama solution has been used to illustrate other surrogate models, e.g. Zhao et al. (2014) used the least square SVM, Wang et al. (2016a) adopted the augmented radial basis function and Li et al. (2016) illustrated SVM combined with uniform design. From the literature, it can be seen that the Duncan-Fama solution has become a benchmark tunnelling problem for the probabilistic analysis. It can be used as a good starting point of this thesis to illustrate the reliability analysis of tunnelling problems (Chapter 3). Practitioners may not be familiar with the probabilistic analysis concepts and detailed procedures. In Chapter 3, widely used probabilistic methods are illustrated using the benchmark problem to help overcome the conceptual and computational barriers for practitioners.

The convergence-confinement method (CCM), which combines the longitudinal deformation profile (LDP), the ground reaction curve (GRC) and the support characteristic curve (SCC), can be considered as a simplified method to analyze the ground-support interaction for circular tunnels. This method has been used to illustrate FOSM and PEM (Laso et al., 1995), to illustrate FORM and RSM (Lü et al., 2011), to show ANN with uniform design (Lü et al., 2012), to investigate the system reliability analysis by Lü et al. (2013), Zeng and Jimenez (2014) and to elucidate the moving least square RSM (Lü et al., 2017).

Most reliability analyses of tunnelling problems concern the estimate of the probability of failure and the surrogate models are used to approximate the limit state surface locally around the design point, e.g. Mollon et al. (2009b). However, some researchers intended to approximate the performance function globally, meaning not in the vicinity of the design point but in a larger domain. Mollon et al. (2011) used SRSM to analyze the tunnel face stability problem. A global response surface method (GRSM), which is similar to SRSM, was used to approximate the damage depth and displacement of a

tunnel by Langford and Diederichs (2015). SRMS was also used by Wang and Li (2017) to approximate the distribution of the tunnel displacement.

There are two limit states, including ULS and SLS, in tunnelling problems. Most of the previous research focuses on the analysis of one limit state or two limit states separately, e.g. Zhang and Goh (2012) and Zhang and Goh (2014). The system reliability analysis, which considers the interaction among all limit states, should be further investigated. A more detailed review of the system reliability analysis will be given in Chapter 4.

Although some literature discussed RBD of tunnels, e.g. Low and Einstein (2013) and Langford and Diederichs (2013). Detailed discussions about the similarities and differences between RBD and the traditional design approach (FS design and the partial factor design) should be investigated. The insights from RBD compared with the partial factor design approach for tunnelling problems will be illustrated in Chapter 5.

Apart from the research in which closed-form solutions were used to illustrate different methods, some papers presented reliability analyses of real-life underground excavation problems, e.g. Su et al. (2011), Cai (2011) and Su et al. (2017). However, the characterization of the statistical input parameters from the site investigation or laboratory test results were seldom covered. Thus, there is a need to show how the statistical information can be characterized from in situ and laboratory test results and how the characterized parameters can be used in the reliability analysis of a real-life project, which will be shown in Chapter 6.

The spatial variability is a major source of uncertainties associated with rock properties. In the literature, there rarely exist any studies quantifying the scale of fluctuation and autocorrelation structure of rock properties. As commented by Hsu and Nelson (2006), very little work had been done on characterizing the spatial variability of rock properties. One of the possible reasons is that the extraction of rock samples is difficult and costly, resulting in limited rock data (Aladejare and Wang 2017). Therefore, the rock properties collected in Chapter 6 can be used to characterize the spatial variability of rocks. The Bayesian method is able to select the most plausible model with a high fitting capacity as well as robustness (Cao and Wang 2013; Wang and Aladejare 2015). The Bayesian model selection method is used to determine the most probable

autocorrelation functions and to estimate the autocorrelation distances of the rock properties in Chapter 7.

2.5 Summary

In this chapter, a literature review was presented mainly in three parts: deterministic analysis approaches, basic probabilistic analysis methods and the reliability analysis of underground excavations. For the deterministic analysis, commonly used design and analysis tools, namely, the empirical method using rock mass classifications, analytical method using closed-form solutions, numerical modelling using FEM, FDM, DEM, etc., and observational method using field measuring data, are reviewed. In later chapters, the analytical solution and numerical modelling will be used.

In the review of basic reliability methods, several critical concepts concerning the reliability analysis are reviewed first. FOSM, FORM, SORM and MCS, which are common methods for estimating the probability of failure, are reviewed next. For problems without explicit performance functions, surrogate models are needed to connect FORM and SORM with the results from stand-alone numerical software. Thus, the bridging methods or surrogate models are revisited. Through the combination of FORM, SORM, MCS, surrogate models and numerical simulations, the reliability index and probability of failure of complex problems can be obtained. The reviewed methods and their relations are shown in Fig. 2.12.

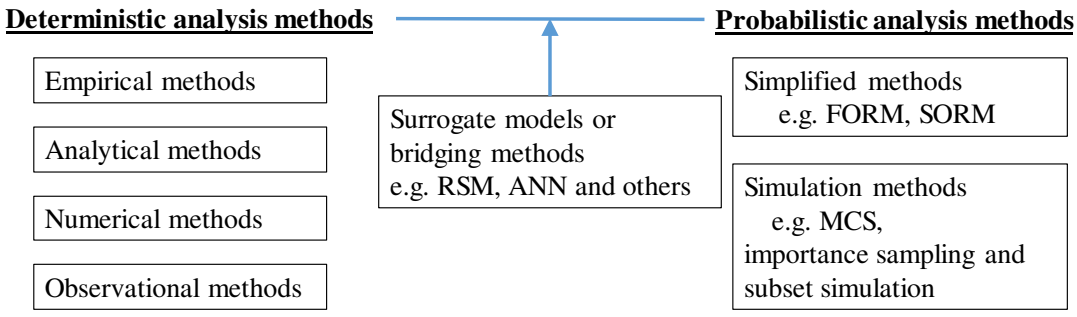

Fig. 2.12. Reviewed methods and their relations

A detailed list of the reliability evaluation of underground excavation problems is provided in Appendix A. Some observations of the literature include: the Duncan-Fama solution is a benchmark problem and can be used as a good starting point to show and compare different reliability methods, which will be presented in Chapter 3; the system reliability analysis considering the interaction among different limit states needs further investigation, which will be shown in Chapter 4; the insights from reliability-based design and how it can complement the partial factor design approach should be discussed and illustrated for tunnelling problems, which will be displayed in Chapter 5; the statistical characterization of the rock engineering properties and how the statistical inputs can be used in the reliability analysis can be best explained by an actual underground excavation project, which will be illustrated in Chapter 6. The spatial variabilities of the uniaxial compressive strength and elastic modulus are characterized using the Bayesian method in Chapter 7.

Chapter 3 Probabilistic analysis of a circular tunnel using various reliability methods

Analytical solutions are valuable in understanding the rock mass behavior and in testing numerical models. Therefore, analytical solutions are a good starting point for the underground excavation analysis. Since the surrounding rock mass seldom remains elastic after the tunnel is excavated, the elastic solutions for the stress and displacement calculation, such as the Kirsch solution (Kirsch, 1898), will not be studied here. As pointed out in Chapter 2, the Duncan-Fama solution (Duncan Fama, 1993) for circular tunnels in elastic-perfectly-plastic Mohr-Coulomb grounds under hydrostatic in situ stresses has been widely used by different researchers to verify various probabilistic analysis approaches and surrogate models. The Duncan-Fama solution has become a benchmark problem for the reliability analysis of tunnelling problems. Therefore, this starting chapter is intended to show and compare different reliability methods and surrogate models using the Duncan-Fama solution. The content in this chapter is the basis for later chapters.

In this chapter, the first-order reliability method (FORM) is first applied to the Duncan-Fama solution. Then, the results are compared with those from the first-order second-moment method (FOSM), Monte Carlo simulation (MCS) with and without importance sampling and subset simulation. Next, surrogate models or bridging methods, including the first- and second-order polynomial response surface methods (RSM), are illustrated. A numerical error problem is encountered in the application of the linear RSM to problems in which the reliability index β is large. This numerical error problem is investigated in detail and a multiple-step solution is proposed to solve this problem. In the next section, the Duncan-Fama solution is presented.

3.1 Analytical solutions for circular tunnels in Mohr-Coulomb grounds under hydrostatic in situ stresses

The Duncan-Fama solution describes the displacement and stress distribution around a circular tunnel in a homogeneous and isotropic ground, which obeys the Mohr-

Coulomb failure criterion, under the hydrostatic in situ stress condition. The problem is illustrated in Fig. 3.1.

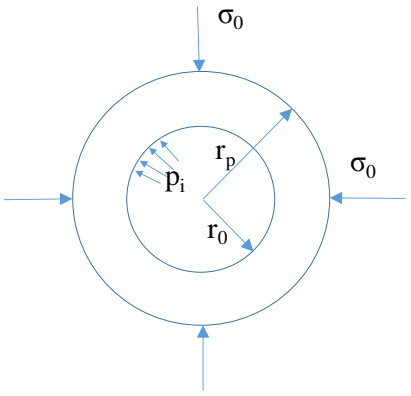

Deterministic parameters:

Tunnel radius: $r_0 = 2.5$ m
Poisson's ratio: $\nu = 0.3$

Probabilistic parameters:

Young's modulus E (MPa): Normal $\mu = 373$ $\sigma = 48$
Cohesion c (MPa): Normal $\mu = 0.23$ $\sigma = 0.068$
Friction angle ϕ (°): Normal $\mu = 22.85$ $\sigma = 1.31$
In situ stress σ_0 (MPa): Normal $\mu = 2.5$ $\sigma = 0.25$

Fig. 3.1. Illustration of a circular tunnel under hydrostatic in situ stress (after Hoek, 2007)

In Fig. 3.1, σ_0 is the hydrostatic in situ stress; p_i is the internal support pressure; r_0 is the tunnel radius; r_p is the plastic zone radius. The critical support pressure p_i^{cr}, below which the plastic zone starts to develop around the tunnel, is calculated from:

$$p_i^{cr} = \frac{2\sigma_0 - \sigma_{cm}}{1+k} \tag{3.1}$$

$$k = \frac{1+\sin\phi}{1-\sin\phi}, \quad \sigma_{cm} = \frac{2c\cos\phi}{1-\sin\phi} \tag{3.2}$$

where ϕ is the friction angle and c is the cohesion of the rock mass. If the internal support pressure is greater than p_i^{cr}, no plastic zone appears and the inward radial displacement of the tunnel wall is

$$u_r^e = \frac{r_0(\sigma_0 - p_i)}{2G}, \quad G = \frac{E}{2(1+\nu)} \tag{3.3}$$

where G and E are the shear modulus and Young's modulus of the rock mass and ν is the Poisson's ratio. If p_i is less than p_i^{cr}, plastic yielding occurs and the radius of the plastic zone is given by

$$r_p = r_0\left[\frac{2(\sigma_0(k-1)+\sigma_{cm})}{(k+1)((k-1)p_i+\sigma_{cm})}\right]^{\frac{1}{k-1}} \tag{3.4}$$

The inward radial displacement of the excavation boundary is calculated from:

$$u_r^{pl} = \frac{r_0}{2G}\left[2(1-\nu)(\sigma_0 - p_i^{cr})\left(\frac{r_p}{r_0}\right)^2 - (1-2\nu)(\sigma_0 - p_i)\right] \tag{3.5}$$

Above equations are applicable for non-associated flow rules (dilation angle=0).

3.2 Direct first-order reliability method applied to closed-form solutions

The input parameters for the analysis, shown in Fig. 3.1, are adopted from Hoek (1998) and Li and Low (2010). Based on the equations given above, the Duncan-Fama solution calculates the plastic zone radius and tunnel wall convergence. The acceptability of the tunnel behavior can be assessed through the following two performance functions.

$$g_1(x) = \lambda_{\text{limiting}} - \frac{r_p}{r_0} \tag{3.6}$$

$$g_2(x) = \varepsilon_{\text{limiting}} - \frac{u}{r_0} \tag{3.7}$$

where u is the tunnel wall convergence and calculated by Eq. (3.5) for the case with plastic zones; $\lambda_{\text{limiting}}$ and $\varepsilon_{\text{limiting}}$ are the limiting ratios with respect to r_p / r_0 and u / r_0 respectively.

The first performance function concerns the plastic zone size developed around the excavation whereas the second considers the maximum inward displacement of the tunnel. The selection of the limiting ratios is based on the experience of engineers. In this case, $\lambda_{\text{limiting}}$ is chosen to be 3 while $\varepsilon_{\text{limiting}}$ is 0.01. In the analysis by Li and Low (2010), c, ϕ, E are regarded as random variables. However, it is well known that the in situ stress can be hardly measured precisely and has a significant influence on the tunnel behavior. Thus, four parameters including σ_0 are treated as random variables while other input parameters are deterministic values for this case. The statistical inputs are shown in Fig. 3.1. The four random variables are assumed to be normally distributed. Typically, the cohesion and friction angle are likely to be negatively correlated, i.e. the

cohesive strength usually drops as the friction angle increases and vice versa. Therefore, -0.5 is used as the correlation coefficient between the cohesion and friction angle.

The expression for the FORM reliability index is (Low and Tang, 2007):

$$\beta = \min_{g(x)<0} \sqrt{\mathbf{n}^T \mathbf{R}^{-1} \mathbf{n}} \tag{3.8}$$

where ***n*** represents the random variable values in the correlated standard normal space. Fig. 3.2 shows the FORM results with respect to the first performance function based on the Duncan-Fama solution.

	A	B	C	D	E	F	G
1	r_p/r_0	Indicator	$\lambda_{limiting}$	$\varepsilon_{limiting}$	*PerFunc*	β	P_f
2	3.000	1	3	0.01	0.000	0.6655	25.3%
3	Variable	x_i*	Correlation matrix R				n_i
4	ϕ (°)	22.998	1	-0.5	0	0	0.113
5	c (MPa)	0.189	-0.5	1	0	0	-0.598
6	E (MPa)	373.0	0	0	1	0	0.000
7	σ_0 (MPa)	2.549	0	0	0	1	0.197

Fig. 3.2. FORM results for the plastic zone size performance function

In Fig. 3.2, cell B2 is the indicator whether performance function 1 or performance function 2 is concerned; cell E2 is the performance function value which is based on the indicator value; cells C2:D2 are limiting values for the two performance functions. For the Low and Tang (2007) method, the n_i column (cells G4:G7) is initially set to zero and the corresponding performance function value is 0.37, showing that the mean value point is in the safe domain and the reliability index is positive. The Solver is used to minimize the reliability index (cell F2), by changing the n_i column (cells G4:G7), subject to the constraint that the performance function (cell E2) equals zero. The design point in the n-space is automatically located and shown in the n_i column (cells G4:G7). The corresponding design point values in the original random variable space are shown in the x_i^* column (cells B4:B7). For this case where the internal support pressure is zero, the reliability index is 0.6655, corresponding to a probability of failure P_f of 25.3%. P_f is estimated by

$$P_f \approx 1 - \Phi(\beta) \tag{3.9}$$

where $\Phi(.)$ is the cumulative distribution function (CDF) of standard normal distribution.

3.2.1 Sensitivities of input parameters

The sensitivity is a by-product of the FORM analysis and is reflected by the absolute values in the n_i column. This is an advantage since repeated parametric studies required in the deterministic analysis are obviated. The n-value for E is zero, meaning that the performance function is not influenced by this parameter. This is expected as the plastic zone radius is not a function of Young's modulus. Among the four parameters, the cohesion is the most influential factor while the result is less sensitive to the friction angle. The increase of the in situ stress and the decrease of the cohesion will lead to the enlargement of the plastic zone. Thus, it is reasonable that the design point value of the in situ stress is higher than the mean value whereas for the cohesion the design point value is lower than the mean value. However, the friction angle is slightly increased from 22.85 to 23.00. This is due to the negative correlation between the cohesion and the friction angle. When the cohesion drops, the friction angle is more likely to increase. Because the result is more sensitive to the cohesion, the design point value for the friction angle is slightly greater than the mean value.

3.2.2 The effect of negatively correlated random variables

The cohesion and friction angle are negatively correlated since cohesion and friction are not mobilized simultaneously: cohesion decreases as friction increases. This is because the peak strength is produced due to interlocking and friction among particles and not due to the chemistry of the bonds. The interlocking resistance can be mobilized at low normal stresses and then lost, while the frictional strength component is proportional to the normal confining stress (e.g. Martin, 1997; Kaiser et al., 2000; Hajiabdolmajid et al., 2002).

In the above case study, the correlation coefficient between the cohesion and friction angle $\rho_{\phi c}$ is assumed to be -0.5. To further investigate the influence of the negative correlation on the reliability index and probability of failure, several values of $\rho_{\phi c}$

ranging from -1 to 0 are used to conduct the parametric study for $p_i = 0$ MPa. The results are shown in Fig. 3.3. It is clear from the plot that the reliability index decreases while the probability of failure increases as $\rho_{\phi c}$ changes from -1 to 0.

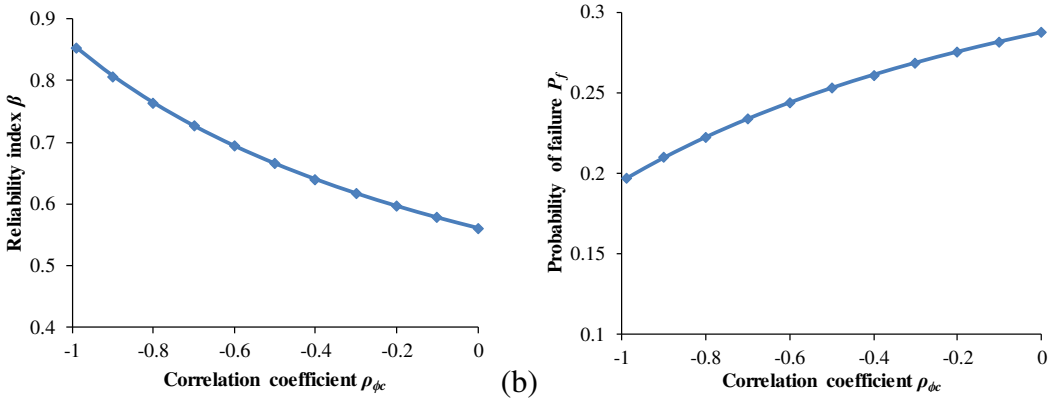

(a) (b)

Fig. 3.3. The influence of correlation coefficient between c and ϕ on β and P_f

The negative correlation means that smaller cohesion values tend to appear with larger values of the friction angle. The chance of having smaller values for both parameters is smaller than the case where the correlation is ignored. Therefore, the reliability decreases and the probability of failure increases with the negative correlation coefficient changing from -1 to 0.

The influence of the negative correlation on the design point and the reliability index can also be explained by the expanding ellipsoid perspective. Although the expanding hyper-ellipsoid plot for four random variables can only be conceived in the mind's eyes, the expanding ellipse plot (Fig. 3.4) for two random variables can be used to illustrate the influence of the negative correlation on the design point and the reliability index.

In Fig. 3.4, the ellipse represents the contour of the joint probability distribution. For uncorrelated random variables, e.g. Fig. 3.4 (a), the ellipse is untilted. When the expanding ellipse touches the limit state, the design point values for both parameters are below their mean values. However, for negatively correlated random variables, the ellipse is tilted towards the negatively inclined direction. The negatively correlated c-ϕ dispersion ellipse will expand more (larger reliability index) than the uncorrelated c-ϕ dispersion ellipse to touch LSS. As an example shown in Fig. 3.4 (b), the design point value for the friction angle may be greater than the mean value. Note that Fig. 3.4 is a qualitative explanation in the original space (x-space). The effects of the negative

correlation between the cohesion and friction angle were also discussed in Low (2007), Li and Low (2010), Lü and Low (2011), among others.

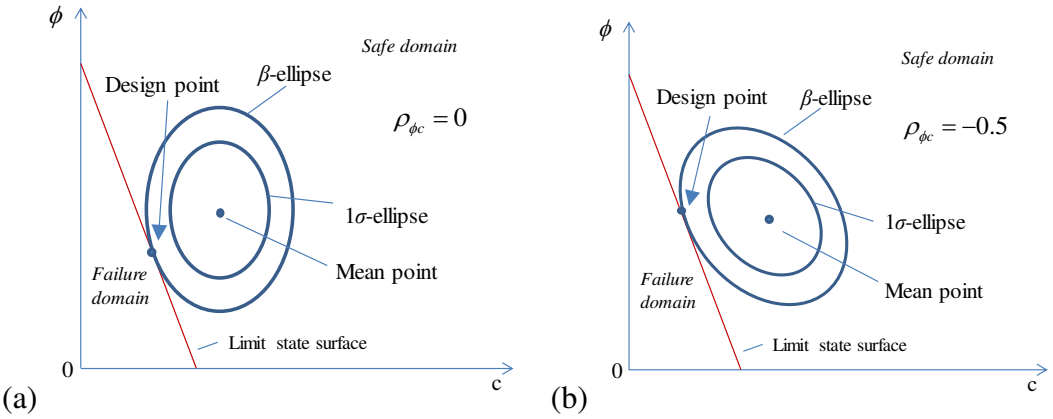

Fig. 3.4. The expanding ellipse plot for the case of two random variables (a) no correlation (b) negative correlation

3.2.3 Reliability-based design

As shown in Fig. 3.2, the probability of failure 25.3% for the first performance function, when the internal support pressure is zero, is unacceptably high. For design purposes, the engineers should find proper internal support pressure to reduce the probability of failure to an acceptable level. A reliability index of 2.5, which corresponds to a P_f of 0.62%, is used in this case study. Since this problem only involves one design parameter, i.e. the internal support pressure, the value can be determined through trial and error and it is found to be 0.228 MPa to yield a reliability index 2.5.

For the second performance function, the ratio of the tunnel wall displacement over the tunnel radius is 0.036 at the mean value point when $p_i = 0$. The ratio exceeds the limiting value 0.01, which means that the mean value point already lies in the failure domain and the reliability index should be regarded as negative, as discussed in Low (2008). Calculation results show that p_i is 1.073 MPa to achieve a target reliability index of 2.5 for the second performance function. If both performance functions are concerned, 1.073 MPa is the design value since the second criterion is more critical than the first one.

3.2.4 Comparison of different FORM algorithms and FOSM

FORM using the constrained optimization method is easily applicable and robust. This method can be cross-validated using the classical iterative procedure in the uncorrelated standard normal random variable space (u-space) as shown in many textbooks (e.g. Ang and Tang, 1984; Melchers, 1999; Haldar and Mahadevan, 2000). For this case, the orthogonal transformation (shown in Ang and Tang, 1984) is used to transform the correlated variables to uncorrelated variables. The MATLAB implementation for this case is shown in Appendix B. Another approach is to use the constrained optimization function *fmincon* in MATLAB, which is also shown in Appendix B. Three FORM algorithms, namely, FORM using Solver in Excel, FORM using the classical iterative procedure and FORM using MATLAB optimization toolbox, obtain the same results, reliability index β=0.666 and design point (23.00°, 0.19MPa, 373 MPa and 2.55MPa) for this case. Comparison shows that the classical iterative procedure is the most cumbersome. The transformation or rotation of the axes of the correlated random variables may be conceptually difficult for practitioners. The optimization method obviates the transformation process. The optimization function in MATLAB may be difficult for engineers to use since the objective function and the linear or nonlinear constraints should be coded using separate user-defined functions. Excel presents the data straightforwardly and the Solver can be easily set up. Therefore, FORM using Excel Solver is the most user-friendly approach. The advantage of MATLAB lies in its capabilities of conducting complex matrix calculations for more advanced probabilistic analyses.

Apart from FORM, another widely used approach to calculate the reliability index is FOSM as shown in Chapter 2. FOSM assumed that the performance function is normally distributed and the reliability index is $\beta_{FOSM} = \mu_g / \sigma_g$, where μ_g and σ_g are the mean and standard deviation of the performance function. FOSM has been widely used because of its simplicity, such as Orr and Breysse (2008) for the reliability-based design of a foundation and Laso et al. (1995) and Chen (2012) for tunnelling problems.

When p_i=0, the mean and standard deviation of the first performance function are 0.216 and 0.840 from MCS with 10,000 runs. The corresponding FOSM reliability index is 0.257, which is different from 0.666 from FORM. The PDF of the performance function

is shown in Fig. 3.5. MCS yields a probability of failure of 25.7% for this case, verifying that the FORM reliability index is accurate. The inaccuracy of FOSM reliability index is caused by the fact the performance function is not normally distributed. For the FOSM reliability index 0.257, the corresponding probability of failure is 39.9% from Eq. (3.9). If FOSM is used for this case, the probability of failure will be greatly overestimated.

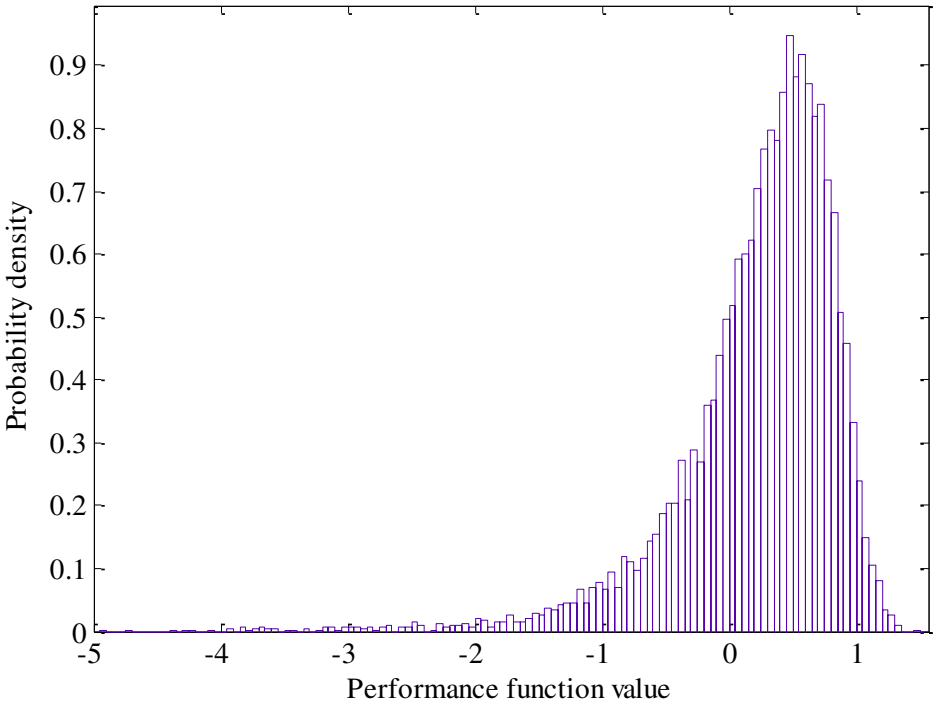

Fig. 3.5. PDF of the performance function (p_i=0)

When p_i=0.228 MPa, the mean and standard deviation are 0.961 and 0.281 from MCS with 100,000 runs and the FOSM reliability index is 3.42 (corresponding P_f=0.03%). For comparison, the FORM reliability index is 2.5 and corresponding P_f=0.62%. MCS yields a probability of failure of 0.66% for this case, verifying that the FORM reliability index is accurate.

The above comparison shows that FOSM reliability index may be erroneous for performance functions which are not normally distributed. Moreover, for problems without closed-form solutions, the estimate of the mean and standard deviation of the performance function cannot be readily obtained from MCS and the estimate from the numerical method (such as the central difference method shown in Chapter 2) may

deviate from the true values. Another drawback of FOSM is the dependency of the FOSM reliability index on the formulation of the performance function, which will be illustrated in Chapter 5.

3.3 Monte Carlo simulation applied to the Duncan-Fama solution

3.3.1 Direct Monte Carlo simulation

MCS has been ubiquitously adopted as the verification method for other reliability analysis methods including FORM due to the robustness. Six simulations, each of which consists of 20,000 and 100,000 runs, are performed using the software @RISK (www.palisade.com) to verify P_f obtained from FORM. The results shown in Table 3.1 are based on the case when the support pressure is zero and the first performance function is concerned.

Table 3.1 Results for direct MCS (p_i=0)

No. of Simulations	1	2	3	4	5	6
P_f (20,000 runs)	25.64%	25.43%	25.77%	25.54%	26.19%	25.28%
P_f (100,000 runs)	25.53%	25.70%	25.82%	25.69%	25.77%	25.87%

For the case where each simulation consists of 20,000 runs, the average value is 25.64% and the standard deviation is 0.0032. For the case where each simulation consists of 100,000 runs, the average value of P_f is 25.73% and the standard deviation is 0.0012. The mean value compares well with the probability of failure 25.3% obtained from FORM. The coefficient of variation (COV) of MCS results can be estimated by $\sqrt{(1-P_f)/(NP_f)}$ (e.g. Haldar and Mahadevan, 2000), where N is the number of runs in each simulation. The corresponding COV is 0.0120 and 0.0054 for 20,000 and 100,000 runs, respectively. Six simulations show that the COV is 0.0124 and 0.0046 respectively, which agree well with the COV estimated from $\sqrt{(1-P_f)/(NP_f)}$. Comparison of these two MCS results shows that increasing the number of runs can reduce the variation of the result but at the cost of more time consumed.

Since the probability of failure is high for this case, the results of the six simulations vary within a narrow range around the mean value. However, if the probability of failure is low, more runs of MCS are needed to obtain more accurate results and to reduce the variance. When the design support pressure 0.228 MPa is applied, the reliability index is 2.5 with a probability of failure of 0.62% for the first performance function. The results from the direct (or crude) MCS are shown in Table 3.2.

Table 3.2 Results for direct MCS (p_i=0.228 MPa)

No. of Simulations	1	2	3	4	5	6
P_f (20,000 runs)	0.690%	0.745%	0.565%	0.680%	0.620%	0.610%
P_f (100,000 runs)	0.652%	0.652%	0.689%	0.604%	0.623%	0.641%

As can be seen from the results, the variance of the six simulations greatly increases compared with Table 3.1. For the case where each simulation consists of 20,000 runs, the average value is 0.652% and the standard deviation is 0.0007. For the case where each simulation consists of 100,000 runs, the average value is 0.644% and the standard deviation is 0.0003. The COV is 0.1 and 0.045 for 20,000 and 100,000 runs respectively, compared with 0.087 and 0.039 from the COV estimated using $\sqrt{(1-P_f)/(NP_f)}$. Clearly, the COV increases for problems with small P_f. Although MCS with more runs reduces the COV, the efficiency of direct MCS is not satisfactory. Direct MCS is not efficient for problems with low probabilities of failure. Therefore, several advanced methods have been proposed in the literature. Latin Hypercube Sampling (LHS), MCS with importance sampling and subset simulation are the most widely used approaches.

3.3.2 Latin hypercube sampling and Monte Carlo simulation with importance sampling

As pointed out in Chapter 2, Latin hypercube sampling (LHS) adopted a more efficient sampling strategy to reduce the variance of the results and is the default choice in @RISK to conduct MCS. The results of LHS for this case are shown in Table 3.3.

Table 3.3 Results for LHS (p_i=0.228 MPa)

No. of Simulations	1	2	3	4	5	6
P_f (20,000 runs)	0.735%	0.630%	0.705%	0.700%	0.660%	0.710%
P_f (100,000 runs)	0.661%	0.665%	0.654%	0.654%	0.677%	0.656%

The COV of LHS results is 0.055 and 0.013 for 20,000 and 100,000 runs respectively, which are smaller than those for the direct MCS. The ranges of the six simulation results are also smaller for LHS, indicating that LHS can improve the efficiency and reduce the variation compared with the direct MCS.

For the direct MCS, few sampling points will fall into the failure domain when the probability of failure is low. The main idea of importance sampling is to sample around the design point instead of the mean value point. Therefore, the importance sampling method can guarantee sufficient sampling points in the failure domain. The procedure for the importance sampling is explained below.

The formula for the importance sampling is (Melchers, 1989)

$$P_f = \int_{g(x)<0} I\big(g(x)<0\big)\frac{\phi(v)}{\psi(v)}\psi(v)dv \approx \frac{1}{N}\sum_{i=1}^{N} I\big(g(x)<0\big)\frac{\phi(v_i)}{\psi(v_i)} \tag{3.10}$$

The meaning of the symbols is given in Chapter 2. Fig. 3.6 shows the spreadsheet set-up for the implementation of MCS with importance sampling based on Chan (2012). The design point values in the uncorrelated standard normal space (u-space) $\mathbf{u}^*$ are calculated from $\mathbf{u}^*=\mathbf{L}^{-1}\mathbf{n}^*$, where $\mathbf{L}$ is the lower Cholesky matrix and $\mathbf{L}^{-1}$ is the inverse matrix of $\mathbf{L}$. The lower Cholesky matrix is obtained from the correlation matrix $\mathbf{R}$. The column vector $\mathbf{u}$ contains random variables following the standard normal distribution. Column v is obtained by $\mathbf{v}=\mathbf{u}+\mathbf{u}^*$ and column n is from $\mathbf{n}=\mathbf{L}\mathbf{u}$. The column ϕ (v) computes the value of the probability density distribution (PDF) of the standard normal distribution N(0,1) at v_i. The column ψ(v) computes the value of the PDF of the standard normal distribution N(u_i*,1) at v_i. The cell g(x) is the performance function value for x and I(g(x)<0) is an indicator function defined such that I(.)=1 if g(x)<0 and I(.)=0 if otherwise. A(x,v) contains the formula $I(g(\mathbf{x})<0)[\Pi\phi(\mathbf{v})/\Pi\psi(\mathbf{v})]$. The column u

is generated according to the uncorrelated standard normal distribution and the average value of A(**x**,**v**) is the estimate of the probability of failure.

Lower Cholesky Matrix L				L^{-1}				I(g(x)<0)
1	0	0	0	1	0	0	0	1
-0.5	0.866	0	0	0.577	1.155	0	0	g(x)
0	0	1	0	0	0	1	0	-0.288
0	0	0	1	0	0	0	1	A(x,v)
								0.015

Variable	n*	u*	u	v	n	x	ϕ(v)	ψ(v)
ϕ (°)	0.221	0.221	1.016	1.237	1.237	24.470	0.186	0.238
c (MPa)	-2.170	-2.378	0.039	-2.339	-2.644	0.050	0.026	0.399
E (MPa)	0.000	0.000	0.100	0.100	0.100	377.801	0.397	0.397
σ_0 (MPa)	0.740	0.740	1.271	2.011	2.011	3.003	0.053	0.178

Fig. 3.6. Spreadsheet for the MCS with importance sampling

The results for MCS with importance sampling are shown in Table 3.4. For the case where each simulation consists of 20,000 runs, the average value is 0.648% and the standard deviation is 4×10^{-5}. For the case where each simulation consists of 100,000 runs, the average value of is 0.645% and the standard deviation is 3×10^{-5}. The COV is 0.0068 and 0.0044 for 20,000 and 100,000 runs respectively. Obviously, the variance in MCS results is significantly reduced if importance sampling is used. Even with 20,000 runs in each simulation, the results from importance sampling are more consistent than those obtained from MCS without importance sampling using 100,000 runs in each simulation. Comparisons among direct MCS, LHS and MCS with importance sampling show that the importance sampling is the most efficient method but it requires the design point known in advance.

Table 3.4 Results for MCS with importance sampling (p_i=0.228 MPa)

No. of Simulations	1	2	3	4	5	6
P_f (20,000 runs)	0.644%	0.645%	0.650%	0.654%	0.644%	0.652%
P_f (100,000 runs)	0.644%	0.645%	0.646%	0.640%	0.647%	0.648%

3.3.3 Subset simulation

The subset simulation was proposed for problems with small probabilities of failure and to effectively approximate the tail PDF of the performance function (Au and Beck, 2001). The subset simulation uses the conditional probability to express an event with a small probability as a sequence of intermediate events with larger probabilities as:

$$P_f = P(F_m) = P(F_1)\prod_{i=2}^{m} P(F_i \mid F_{i-1}) \tag{3.11}$$

where $P(F_m)$ is the probability of the target event; $P(F_i)$ is the probability of intermediate events; $P(F_i \mid F_{i-1})$ is the probability of the event i conditioned on the event i-1. A specified value of the conditional probability p_0 is selected (p_0=0.1 is found to be a good choice, e.g. Au and Beck, 2007). For example, for a problem with the probability of failure 10^{-4}, only 4 levels are needed to accurately estimate the probability of failure. With the decrease of the probability, the advantage of the subset simulation over the direct MCS becomes more obvious. The first level of the subset simulation is the direct MCS in which N samples are generated. Among these samples, p_0N samples are the starting samples to generate other $(1-p_0)N$ samples in the next level using the Markov Chain Monte Carlo (MCMC) simulation (e.g. Au and Beck, 2001). Altogether, a m-level subset simulation will generate $N+(m-1)(1-p_0)N$ samples. More details can refer to Au et al. (2010) and Wang et al. (2011).

For the case when p_i=0.228 MPa, the conditional probability p_0 is selected to be 0.1 and 4 levels of subset simulation each of which has 5000 runs are selected. Six simulations yield the probability of failure as 0.667%, 0.608%, 0.642%, 0.618%, 0.728% and 0.592%. The average value is 0.643% with a COV of 0.077. Subset simulation selects more samples from the failure domain than the direct MCS and therefore is more efficient than the direct MCS. With the increase of levels, more sampling points will locate in the failure domain. For comparison, the importance sampling directly samples around the design point. The variation of the subset simulation results is greater than that of importance sampling for this case. However, subset simulation does not require the location of the design point, which is needed in the importance sampling. The advantage of the subset simulation lies in that a problem with a small probability of failure can be estimated with a small number of sampling points. For example, 3 levels

of the subset simulation each of which consists of 1000 runs give a probability of failure of 0.699% for this case.

From the above calculations, a comparison of the FORM, FOSM and MCS can be made as follows. FOSM is simple in concept. However, the assumption that the performance function is normally distributed may not be true for all problems, as shown in Fig. 3.5. For the Duncan-Fama solution when there is no support, the FOSM reliability index is 0.257 and corresponding P_f is 39.9%, which are erroneous. Furthermore, the FOSM reliability index is dependent on the formulation of the performance function. FOSM may yield different reliability indices and probabilities of failure for different but mathematically equivalent limit state functions, as will be illustrated in Chapter 5. With the constrained optimization method and the expanding ellipsoid perspective, FORM is easy to implement and to understand. FORM is more robust and accurate than FOSM. For this case, the FORM reliability index is 0.666 with a P_f of 25.3% which agrees with the MCS result (P_f=25.7%). However, FORM may not be accurate for problems with obvious curvatures of the limit state surface at the design point. The result from MCS is accurate if the solution is in closed-form. Therefore, the MCS result is widely used as the benchmark to verify and compare the results from other methods. However, MCS is not efficient since the performance function should be evaluated by a large number of sampling points. The efficiency of direct MCS can be improved by importance sampling and subset simulation.

3.4 Polynomial response surface methods (RSM)

3.4.1 Linear and second-order polynomial RSM applied to the Duncan-Fama solution

FORM can be conducted directly if the closed-form solution is available. However, for underground excavation problems where the ground is seldom homogeneous and isotropic and the excavation shape is hardly regular, no analytical solution exists. Under such circumstances, reliability methods can only be applied via some bridging methods or surrogate models. Linear and second-order RSM are widely used in geotechnical engineering, e.g. Tandjiria et al. (2000), Xu and Low (2006), Mollon et al. (2009b).

The case study presented in the above sections is used here to illustrate the implementation of RSM and to compare the FORM results based on the linear and second-order RSM. Linear and second-order RSM without cross terms use the following two expressions respectively.

$$\bar{g}(x) = a + \sum_{i=1}^{n} b_i x_i \tag{3.12}$$

$$\bar{g}(x) = a + \sum_{i=1}^{n} b_i x_i + \sum_{i=1}^{n} c_i x_i^2 \tag{3.13}$$

where $\bar{g}(x)$ is the response function; a, b_i and c_i are unknown coefficients that should be determined; x_i is the random variable value; n is the number of random variables.

If the number of variables is n, the numbers of unknown coefficients for the linear and second-order RSM without cross terms are $n+1$ and $2n+1$, respectively. The same number of sampling points and corresponding performance function values are needed to determine the unknown coefficients. The procedure for conducting the iterative RSM can be summarized as follows.

(1) Prepare the sampling points and evaluate the performance function at these sampling points. For the first trial, the sampling central points is chosen at the mean value point μ_i and other sampling points are determined by $x_i = \mu_i - k\sigma_i$ for the linear RSM and $x_i = \mu_i \pm k\sigma_i$ for the second-order RSM. For this case, n=4 and there are 5 sampling points for the linear RSM and 9 for the second-order RSM in each iteration. k is the sampling factor controlling the sampling range and equal to one in this case. σ_i is the standard deviation.

(2) Calculate the unknown coefficients. From the sampling points and corresponding performance function values, the unknown coefficients can be calculated by solving a set of linear equations. This step yields a tentative response surface $\bar{g}(x)$.

(3) Perform FORM on the tentative response surface using Low and Tang (2007) algorithm to obtain a tentative design point and a tentative reliability index.

(4) Repeat steps (1) -(3) until the tentative reliability index converges. In this case, the difference between two successive reliability indices smaller than 0.005 is considered as convergence. From the second iteration, the new sampling central

point is chosen as the last tentative design point.

(5) Once the results converge, the final reliability index and design point can be determined.

The final converged results for the Duncan-Fama solution are shown in Table 3.5. Four cases are presented, i.e. p_i =0, p_i =0.228 MPa for performance function 1 and p_i=0, p_i=1.073 MPa for performance function 2. Although the second-order RSM requires more sampling points in each iteration, the number of iterations needed to reach convergence is smaller. Through the comparison with the results obtained from direct FORM, the reliability index and the design point values are more accurate for the second-order RSM than the linear RSM. Therefore, the second-order RSM is preferred for the case at hand since it is more accurate. Because the mean value point for performance function 2 when p_i =0 lies in the failure domain, the reliability index obtained should be regarded as negative.

Table 3.5 Results for linear and second-order RSM

Performance Function 1						
p_i=0	Iteration	β	ϕ (°)	c (MPa)	E (MPa)	σ_0 (MPa)
Direct FORM		0.666	22.998	0.189	373.000	2.549
Linear RSM	7	0.672	23.093	0.186	373.000	2.533
Second-order RSM	4	0.666	23.034	0.188	373.000	2.544
p_i=0.228 MPa	Iteration	β	ϕ (°)	c (MPa)	E (MPa)	σ_0 (MPa)
Direct FORM		2.500	23.140	0.082	373.000	2.685
Linear RSM	11	2.541	23.646	0.067	373.000	2.614
Second-order RSM	5	2.498	23.435	0.075	373.000	2.653
Performance Function 2						
p_i=0	Iteration	β	ϕ (°)	c (MPa)	E (MPa)	σ_0 (MPa)
Direct FORM		-3.643	22.303	0.346	430.161	1.762
Linear RSM	8	-3.686	22.075	0.374	437.691	1.837
Second-order RSM	4	-3.644	22.264	0.350	431.022	1.774
p_i=1.073 MPa	Iteration	β	ϕ (°)	c (MPa)	E (MPa)	σ_0 (MPa)
Direct FORM		2.501	22.631	0.207	300.834	2.983
Linear RSM	7	2.523	22.652	0.205	287.987	2.929
Second-order RSM	6	2.500	22.641	0.207	298.630	2.974

3.4.2 Comparison with the response surface method using interpolation algorithm

The procedure for conducting RSM summarized in the previous section uses the tentative design point as the sampling central point in the next iteration. This procedure is widely adopted, e.g. Mollon et al. (2009b) and Lü and Low (2011). In Chapter 2, it was mentioned that Bucher and Bourgund (1990) proposed an interpolation algorithm to find the next sampling central point using

$$x_M = \bar{x} + (\bar{x}_D - \bar{x}) \frac{g(\bar{x})}{g(\bar{x}) - g(\bar{x}_D)} \tag{3.14}$$

The new tentative design point is $\bar{x}_D$ and its performance function value is $g(\bar{x}_D)$. Then, the new center point x_M is obtained from the linear interpolation between $\bar{x}_D$ and the previous center point $\bar{x}$. Other steps are the same as stated in the previous section. This method is noted as RSM using interpolation (shown in Table 3.6) and the results of the reliability analysis are compared with those using RSM without interpolation.

Table 3.6 Results for linear and second-order RSM using interpolation

Performance Function 2						
p_i=0	Iteration	β	ϕ (°)	c (MPa)	E (MPa)	σ_0 (MPa)
Direct FORM		-3.643	22.303	0.346	430.161	1.762
Linear RSM	7	-3.686	22.074	0.374	437.676	1.837
Second-order RSM	4	-3.644	22.260	0.350	431.612	1.773
p_i=1.073 MPa	Iteration	β	ϕ (°)	c (MPa)	E (MPa)	σ_0 (MPa)
Direct FORM		2.501	22.631	0.207	300.834	2.983
Linear RSM	6	2.523	22.652	0.205	288.000	2.929
Second-order RSM	4	2.500	22.649	0.207	298.328	2.972

Comparison of Table 3.6 with Table 3.5 shows that the numbers of iterations are slightly reduced except for the case using the second-order RSM when p_i =0. The accuracies of the reliability index and the design point are almost the same. However, note that the RSM with interpolation needs one more evaluation of the performance function in each iteration. Therefore, for this case, RSM with interpolation does not

show any advantage over RSM without interpolation in terms of accuracy and efficiency. A detailed check of the iteration procedure shows that the interpolation algorithm is most efficient in the first few iterations when the sampling points are far away from the design point. With the response surface approaching the limit state surface, the difference between RSM with and without interpolation is negligible.

3.5 Multiple steps for response surface method

The case study in the above section illustrates the combination of RSM and FORM to calculate the reliability index and the design point. Simple and easy to understand, RSM has been widely used in the reliability analysis of geotechnical engineering. However, the polynomial RSM may encounter some non-convergence problems as presented in Mollon et al. (2009b) and Lü and Low (2011). Besides, the numerical error problems may occur for some special case studies. One such case is elaborated as follows.

This case study again uses the Duncan-Fama solution for a circular tunnel with uniform internal pressure, subjected to hydrostatic in situ stress. All input parameters for this case are listed in Table 3.7. The parameters are similar to those for the quasi-circular tunnel case in Lü and Low (2011).

Table 3.7 Input parameters for the numerical error problem

c (MPa)	ϕ (°)	σ_0 (MPa)	p_i (MPa)	r_0 (m)
0.287	21	16	7	5

Parameter	Distribution	Mean	Standard Deviation
E (GPa)	Lognormal	2.095	0.419
ν	Lognormal	0.25	0.02

Two parameters are regarded as uncorrelated random variables, Young's modulus of the rock mass E and Poisson's ratio ν, with lognormal distributions. Here, only two parameters are regarded as random variables because the problem can be graphically explained using two-dimensional plots.

The performance function is

$$g(x) = 0.1 - u \tag{3.15}$$

where 0.1 m is the maximum allowable displacement which is 2% of the tunnel radius; u is the tunnel convergence. The reliability index β is 5.224 obtained from FORM applied directly to the Duncan-Fama solution using Low and Tang (2004) algorithm. Then the linear RSM is used to testify its feasibility and accuracy for this case. Unlike the case in above sections where sampling points and RSM are in n-space in accordance with the Low and Tang (2007) method, the response surface is constructed in the original space (x-space) for this case study corresponding to the Low and Tang (2004) approach. The sampling factor k is selected to be 1. The first construction of the tentative LSS, based on the three sampling points at and around the mean value, is

$$0.0325 + 0.0215E - 0.05\nu = 0 \tag{3.16}$$

When the Excel Solver is invoked to obtain the tentative design point based on the above trial LSS, a problem is encountered during the search process. Based on Eq. (3.16), E is negative when v is in the range of 0 to 0.5. In the analytical solution of the displacement, E appears in the denominator, which means E=0 is a point of discontinuity for the displacement expression and the first-order derivative of the displacement with respect to E does not exist at this point. Obviously, this situation will cause the error during the search process when E goes from positive to negative values as the Solver uses the Newton-Raphson method to search for the solution.

Since the analytical solution for the displacement is available, the exact LSS, i.e. $g(x)$=0, and several performance function contours ($g(x)$=0.01 m, 0.02 m, 0.03 m, 0.04 m, 0.05 m) are plotted in Fig. 3.7.

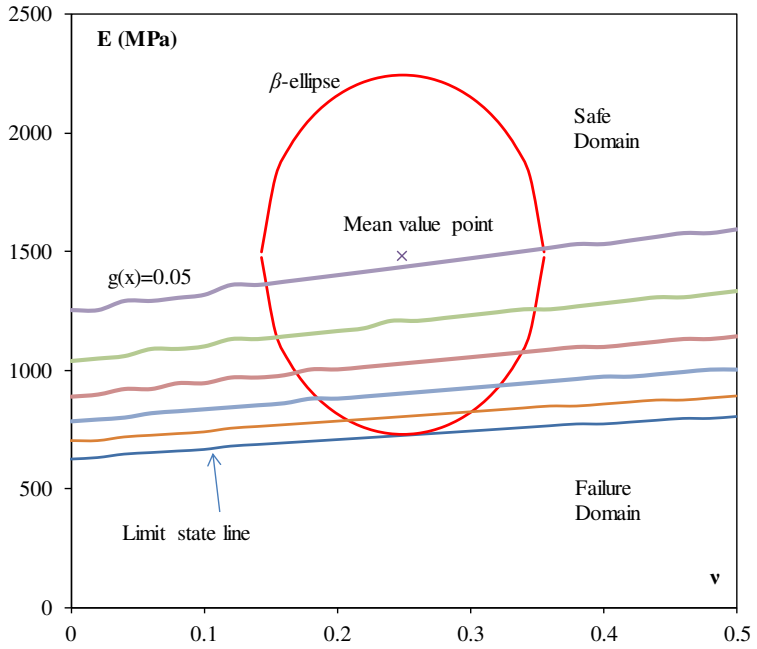

Fig. 3.7. Performance function contours

It is clear that the contours become denser near the limit state line, meaning that the slope of the performance function is comparatively gentle around the mean value point but becomes steeper around the design point. Since Poisson's ratio has little effect on the performance function as illustrated in Fig. 3.7, the performance function is plotted against E while keeping ν=0.25 to show the variation of the performance function with E, as displayed in Fig. 3.8.

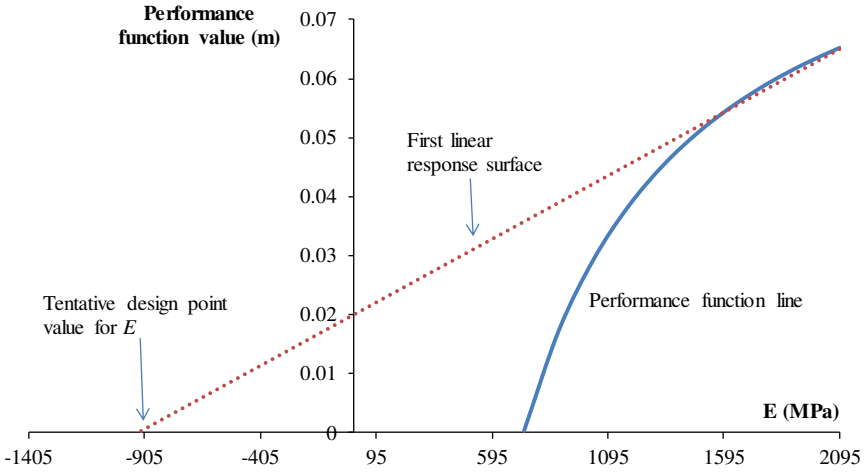

Fig. 3.8. Linear response surface for k=1

When constructed using sampling points around the mean value (k=1), the linear response surface will intersect the horizontal axis at E = -930 MPa. When E goes into the negative domain, the Solver will encounter a numerical problem. Next, the sampling range is enlarged to check whether a larger k value can resolve this problem. The results are plotted in Fig. 3.9.

Strategy 1

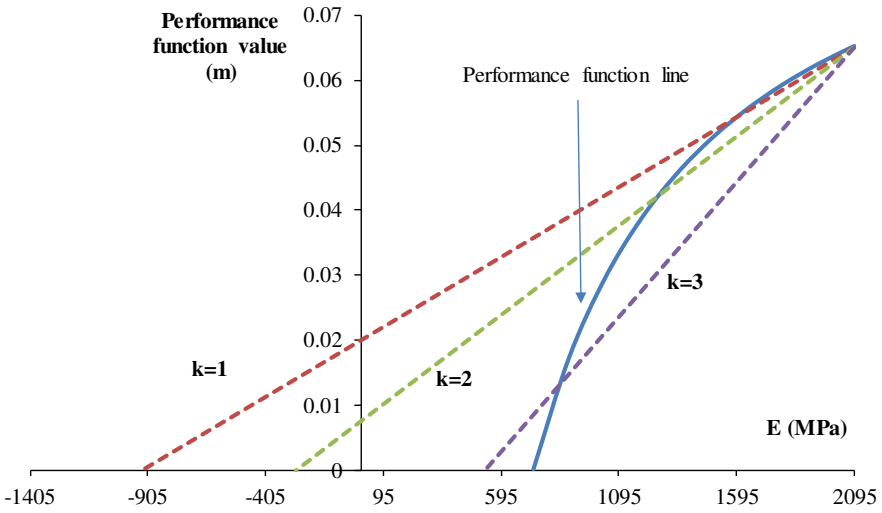

Fig. 3.9. Linear response surface for different *k* values

When k=3, the linear response surface intersects the horizontal axis at 524 MPa, which means that a greater value for the sampling factor k can solve the numerical problem. The Solver finds the first tentative design point and the reliability index converges after 9 iterations at 5.209. compared with 5.224 from the direct FORM.

Strategy 2

An alternative strategy to deal with the Solver error problem in this case is to construct the tentative LSS based on $g(x)=c$ instead of based on $g(x)=0$ directly. c is a constant between 0 and $g(\mu_x)$. In this case, $g(\mu_x)$ is the performance function value 0.065 m at the mean value point. The main idea of this strategy is to target at multiple intermediate performance function values instead of targeting at the limit state function in one step. The reason why this method can overcome the numerical problem is that

the intersection point of the trial response surface and $g(x)=c$ (c is assumed as 0.0325 m, half of 0.065 m for this case) locates in the positive domain as illustrated in Fig. 3.10.

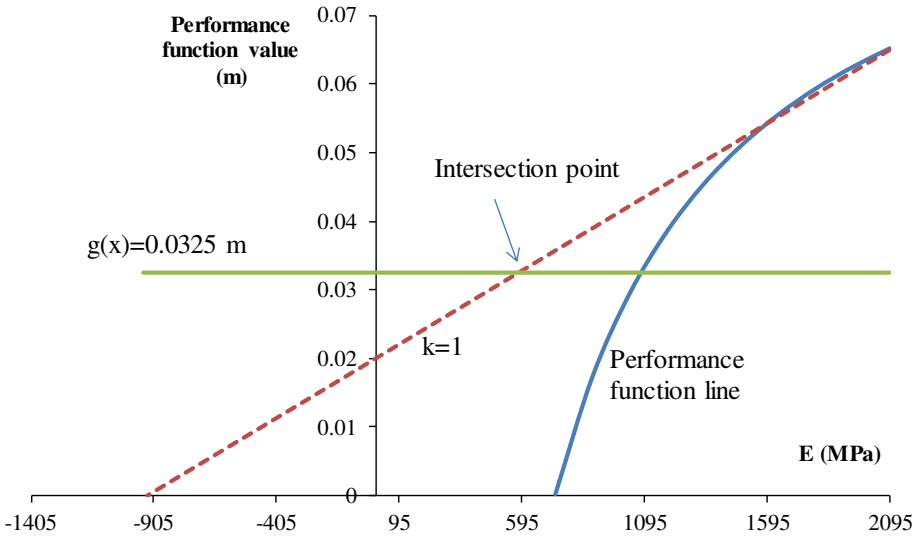

Fig. 3.10. Linear response surface based on g(x)=0.0325 m (*k*=1)

After the first construction of the trial response surface, the tentative design point based on $g(x)$=0.0325 m is obtained as E=692 MPa and v=0.3. Note that the tentative design point value is slightly different from the intersection point shown in Fig. 3.10 because the plot shows the change of the performance function with E while v=0.25, and is not in the E-v space. Then, iterations can be conducted until the design point based on $g(x)$=0.0325 m is determined. Next, in the second step, $g(x)$=0.0325 m is replaced by $g(x)=0$ and the converged reliability index is found to be 5.222 after seven iterations. A more efficient approach is that, instead of conducting iterations based on the intermediate step $g(x)$=0.0325 m until β converges, the tentative design point can be chosen as the sampling central point and $g(x)=0$ replaces $g(x)$=0.0325 m from the second iteration.

This strategy to overcome the numerical error problem is called the multiple-step method which is to approximate limit state surfaces in several steps instead of in one step. $g(x)=c$, where c is a constant between 0 and $g(\mu_x)$, is used in lieu of $g(x)=0$ in the first step. Then $g(x)=c$ is set back to $g(x)=0$ in the second step.

Strategy 3

For this case, the value of the performance function is positive at the mean value point and is approaching zero with the random variables getting closer to the design point. This forms a downward performance function curve. The Solver error problem exists only when the performance function curve is convexly downward. Conversely, if the performance function curve is concavely downward, this problem will disappear, which is illustrated in Fig. 3.11.

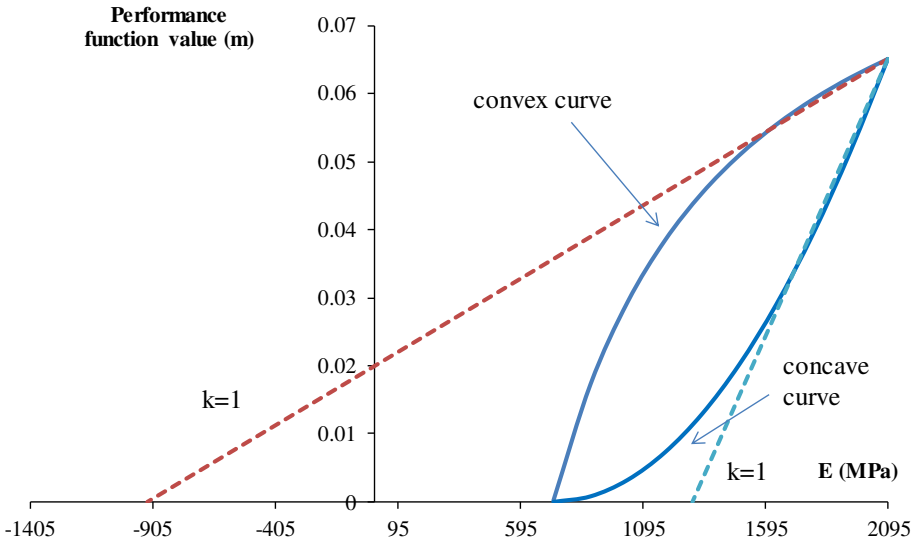

Fig. 3.11. Convex and concave performance function curves

If the performance function curve is concave, all the tentative design points fall in the valid range of the variables (positive range for E). This suggests that the form of the performance function will influence the location of the tentative design point. Another different but mathematically equivalent expression is tested.

$$g(x)=\frac{1}{u}-10 \tag{3.17}$$

Eq. (3.17) is equivalent to Eq. (3.15) in terms of the limit state, i.e. $g(x)=0$. LSS is identical so the reliability index obtained from the direct FORM is the same. RSM is conducted based on this performance function and β converges at 5.211 after only four iterations for k=1. The performance function curve is shown in Fig. 3.12.

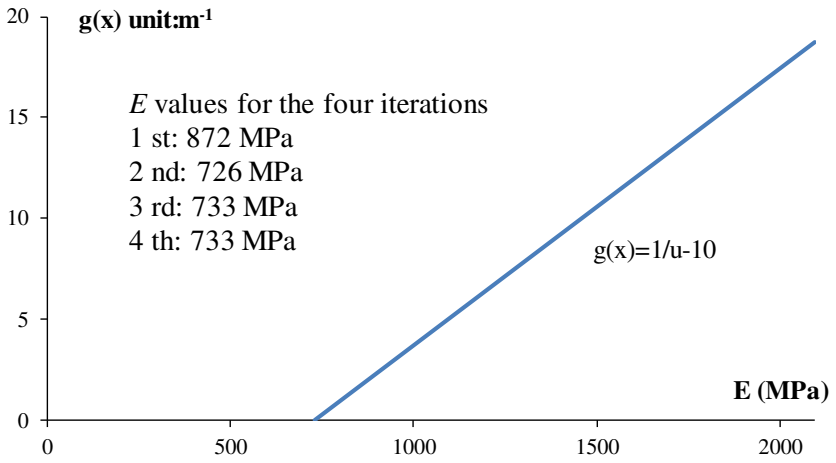

Fig. 3.12. Performance function curve using Eq. (3.17)

When Eq. (3.17) is used, the performance function curve is a linear function of *E*. Therefore, it is reasonable that the reliability index converges rapidly using the linear RSM.

To sum up, three different strategies are tried to solve the numerical error problem encountered in a special case. The comparison of these three strategies is shown in Table 3.8.

Table 3.8 Comparison of three strategies

	Accuracy	Efficiency	Versatility
Strategy 1	Good	Fair	Fair
Strategy 2	Good	Fair	Good
Strategy 3	Good	Good	Poor

All these methods are feasible to obtain a relatively accurate reliability index. However, trial-and-error is necessary for all these three strategies for different case studies. In the first method by enlarging the sampling range, the *k* value should be determined. In the second method by multiple steps to approach the limit state surface, the number of steps and the constant c values in $g(x)=c$ should be tried. In the last method, alternative expressions for the performance function should be tested to check whether they are feasible or not. When the design point is far away from the mean value point, even a larger sampling range may not work. For situations when many random variables are

involved and the relation between the performance function and the random variables is not explicit, to choose a proper expression for the performance function may be difficult. However, the second strategy, i.e. the multiple steps towards the limit state surface method, is more versatile and flexible for different problems. Therefore, the multiple-step approach for the response surface method is recommended to deal with the numerical error problem.

3.6 Summary

Analytical solutions are important to understand the rock mass behavior around an excavation. The Duncan-Fama solution for circular tunnels in Mohr-Coulomb grounds has become a benchmark problem to verify and compare different reliability methods and surrogate models. In this chapter, different approaches have been applied to this closed-form solution, including the direct FORM, FOSM, MCS with and without importance sampling, subset simulation and polynomial response surface methods. In a special case where the tentative response surface may lead to invalid values for the random variables, a numerical error occurs. Three different strategies are proposed to solve the error problem. It is found that the multiple-step approach is versatile and can be used to problems where the design point is far away from the mean value or many iterations are needed to obtain a converged reliability index. This chapter illustrates the fundamental approaches of reliability analysis and may serve as the basis for following chapters.

Chapter 4 System reliability analysis of tunnels reinforced by rockbolts

4.1 Introduction

As pointed out in Chapter 2, from literature, most of the reliability analysis of underground rock excavations considers one limit state or two limit states separately. However, for tunnelling problem, both the ultimate limit state (ULS) including the structural failure and the serviceability limit state (SLS) including the displacement are not independent but are correlated to each other. The design based on one limit state may not satisfy the requirement of other limit states. Therefore, it requires system reliability analysis which can consider each limit state and the interaction among various limit states. In the literature, rare are system reliability evaluations of tunnelling problems (e.g. Lü et al., 2013; Zeng and Jimenez, 2014). Lü et al. (2013) evaluated the ground-support interaction of a circular tunnel using the convergence-confinement method (CCM) and estimated the system P_f by giving the lower and upper bounds. Zeng and Jimenez (2014) used the same case study as in Lü et al. (2013) but with a linearization approach. The probabilities of failure estimated in these two papers are close to each other.

In order to investigate the application of the system reliability analysis on tunnelling problems, this chapter first reviews the commonly used methods for the system reliability assessment. Next, the bimodal bounds method and the multivariate normal cumulative distribution function (**mvncdf)** method are applied to an iterative closed-form solution for a circular tunnel reinforced by rockbolts, which was proposed by Bobet and Einstein (2011). It is shown that SORM can be used to refine the reliability indices and to improve the accuracy of the estimated system P_f. The influence of the correlation coefficient between the cohesion and the friction angle of the rock mass, and that of the rockbolt installation position on the system P_f are discussed. Then, a modified hybrid approach is proposed to approximate LSS for problems without explicit performance functions. The proposed method is compared in detail with traditional second-order RSM without and with cross terms. In the next section, commonly used approaches for the system reliability analysis are examined.

4.2 System reliability analysis methods

A system can be categorized into series or parallel systems. There are many parallel and mixed systems in geotechnical engineering. But in this chapter, series systems are of concern since any failure mode will cause the unsatisfactory performance of the system. Commonly used methods for the system reliability analysis are summarized below.

4.2.1 Lower and upper bounds method

The unimodal bounds method (Cornell, 1967) estimates the bounds for the system P_f using the P_f of the individual limit state while overlooking the correlation among different limit states. Since the bounds are often too wide for practical uses, they are seldom used in the system reliability analysis. The bimodal bounds method (Ditlevsen, 1979) considers the correlation structure among different limit states and gives a narrower bound range than the unimodal bounds method. Besides, the results from FORM (reliability index and design point) can be directly used as inputs in this method. Therefore, the bimodal bounds method is widely applied to geotechnical engineering problems. Low et al. (2011) applied this method to the system reliability analysis of a retaining wall and a layered soil slope and discussed the contribution of different slip surfaces to the system P_f. Lü et al. (2013) estimated the system P_f of a circular tunnel using the bimodal bounds method and investigated the influence of the support installation position on the system P_f. For problems where LSS is highly nonlinear, the results from FORM may not be accurate. For this situation, SORM can be used to improve the accuracy of estimating the lower and upper bounds.

For the bimodal bounds method, the system P_f can be estimated by

$$\begin{aligned}&\left\{P(E_1)+\sum_{i=2}^{m}\max\left[P(E_i)-\sum_{j=1}^{i-1}P(E_iE_j),0\right]\right\}\le P_{F,sys}\\&\le\left\{P(E_1)+\sum_{i=2}^{m}\left\{P(E_i)-\max\left[\underset{j<i}{P}(E_iE_j)\right]\right\}\right\}\end{aligned}\tag{4.1}$$

where $P(E_i)$ is the failure probability of the i-th failure mode; $P_{F,sys}$ is the system P_f; $P(E_iE_j)$ is the probability that the i-th and j-th limit state functions are violated

simultaneously; m is the number of limit states. $P(E_i)$ can be assessed by FORM, SORM and others. $P(E_iE_j)$ can be estimated by

$$\max[a,b] \le P(E_iE_j) \le a+b \text{, for } \rho_{ij} \ge 0 \tag{4.2a}$$

$$0 \le P(E_iE_j) \le \min[a,b] \text{, for } \rho_{ij} < 0 \tag{4.2b}$$

where a and b are defined as

$$a = \Phi(-\beta_i)\Phi\left(-\frac{\beta_j - \rho_{ij}\beta_i}{\sqrt{1-\rho_{ij}^2}}\right) \tag{4.3a}$$

$$b = \Phi(-\beta_j)\Phi\left(-\frac{\beta_i - \rho_{ij}\beta_j}{\sqrt{1-\rho_{ij}^2}}\right) \tag{4.3b}$$

where β_i and β_j are the reliability indices for limit state i and j respectively; ρ_{ij} is the correlation coefficient between limit state i and j; $\Phi(.)$ is the cumulative distribution function of the standard normal distribution. Substituting the bounds of $P(E_iE_j)$ into Eq. (4.1), the upper and lower bounds of $P_{F,sys}$ can be estimated. Note that different permutations of all limit states may yield slightly different bounds. The limit state with the highest probability of failure is typically regarded as the first limit state in Eq. (4.1) (Ang and Tang, 1984).

4.2.2 Multivariate normal cumulative distribution function (mvncdf) method

The Hasofer-Lind index and FORM uses the first-order Taylor series approximation of the performance function linearized at the design point to replace the actual nonlinear LSS. Hasofer and Lind (1974) defined the reliability index β as the shortest distance from the origin to LSS in the uncorrelated standard normal random variable space as shown in Fig. 4.1.

The P_f can be estimated by

$$P_f \approx 1 - \Phi(\beta) \tag{4.4}$$

In Fig. 4.1, u_1 and u_2 are two uncorrelated random variables with standard normal distributions; the solid line is the actual LSS; the dashed line is the linearized LSS at

the design point. $1-\Phi(\beta)$ estimates the P_f based on the shaded area in Fig. 4.1. Note that the shaded area is just an approximation of the actual failure domain, which is represented by the area above LSS.

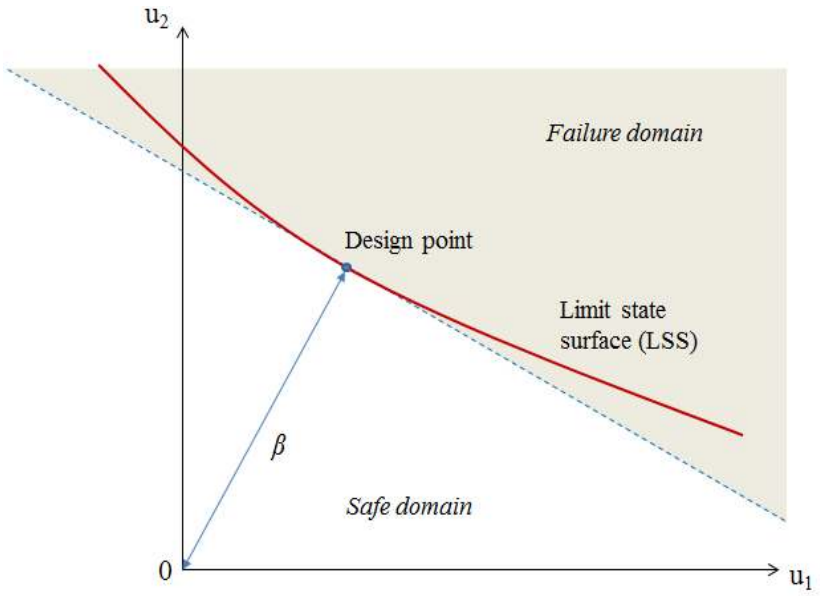

Fig. 4.1. Illustration of the Hasofer-Lind *β* for single limit state

This linearization can be extended to the system reliability analysis. Hohenbichler and Rackwitz (1982) showed that LSS could be linearized at design points and the system P_f could be estimated through the complementary of the intersection of safe domains, which is graphically shown in Fig. 4.2.

$$P_f = P\left(\bigcup_{i=1}^{n}\left\{g_i(\mathbf{X})\le 0\right\}\right)\approx P\left(\bigcup_{i=1}^{n}\left\{I_i(\mathbf{U})\le 0\right\}\right)=1-P\left(\bigcap_{i=1}^{n}\left\{-\boldsymbol{\alpha}_i\mathbf{U}<\beta_i\right\}\right)=1-\Phi_n(\boldsymbol{\beta};\boldsymbol{\rho}) \quad (4.5)$$

where $g_i(\mathbf{X})$ is the *i*-th performance function in the original space; *n* is the number of limit states; $I_i(\mathbf{U})$ is the linearized performance function in the uncorrelated standard normal space; $\boldsymbol{\alpha}$ is the vector of direction cosines; $\boldsymbol{\beta}$ is the vector of reliability indices; $\boldsymbol{\rho}$ is the correlation matrix of the limit states; $\Phi_n(.)$ represents the standard multinormal cumulative distribution function.

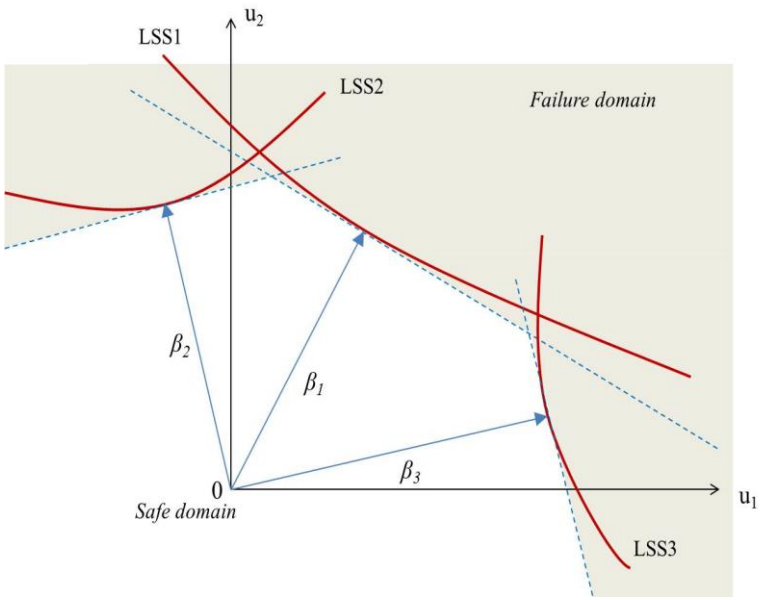

Fig. 4.2. Illustration of system reliability analysis for three limit states

Through Eq. (4.5), the estimate of the system P_f relegates to the calculation of the standard multinormal cumulative distribution function. Comparison between Eq. (4.4) and Eq. (4.5) shows that the reliability analysis of a single limit state problem can be easily extended to the system reliability analysis by replacing $\Phi(\beta)$ with $\Phi_n(\boldsymbol{\beta};\boldsymbol{\rho})$. The calculation of $\Phi_n(\boldsymbol{\beta};\boldsymbol{\rho})$ can be conducted by multiple integrals as shown in Eq. (4.6), which can be implemented in platforms such as Excel.

$$\Phi_n(\boldsymbol{\beta};\boldsymbol{\rho}) = \int_{-\infty}^{\beta_n} \cdots \int_{-\infty}^{\beta_2} \int_{-\infty}^{\beta_1} \frac{1}{\sqrt{(2\pi)^n |\boldsymbol{\rho}|}} \exp\left(-\frac{1}{2}\mathbf{z}^T \boldsymbol{\rho}^{-1} \mathbf{z}\right) dz_1 dz_2 \cdots dz_n \tag{4.6}$$

Besides, $\Phi_n(\boldsymbol{\beta};\boldsymbol{\rho})$ can be simply implemented by the **mvncdf** function in MATLAB. Since the **mvncdf** function in MATLAB is the simplest approach to calculate $\Phi_n(\boldsymbol{\beta};\boldsymbol{\rho})$, the estimate of the system P_f by Eq. (4.5) is referred to as **mvncdf** method in this chapter. Zeng and Jimenez (2014) also used this method but named it as the linearization approach. SORM can be used to refine the reliability indices, which are the inputs for estimating the system P_f.

4.2.3 Monte Carlo simulation (MCS) based on various surrogate models

When closed-form solutions are available, the above two methods, namely the bimodal bounds method and the **mvncdf** method, can be used directly. However, for problems with implicit performance functions, surrogate models have to be used first to approximate limit state functions. Surrogate models include polynomial RSM, machine learning methods (e.g. ANN, support vector machines) and others. Once response surfaces for different limit states are obtained, MCS can be conducted easily based on the closed-form response surfaces. The details regarding the construction of RSM and ANN are given in Chapter 2. What should be mentioned here is that once the response surfaces are obtained, the bimodal bounds method and the **mvncdf** method can also be used based on these approximate LSS. However, direct MCS based on the response surface is the most straightforward method for problems without closed-form solutions.

Zhang et al. (2011) and Zhang et al. (2013b) used the second-order RSM to replace the actual LSS for representative slip surfaces selected among thousands of potential ones and obtained the system P_f by MCS. Li and Chu (2015) also used the second-order RSM and similar methods as in Zhang et al. (2011) to choose representative slip surfaces but considered the spatial variability of soil properties. Zhang et al. (2013a) adopted the kriging-based RSM as the surrogate model and compared the results for two slope case studies with previous literature. The same case studies were used and compared by Jiang et al. (2014) using collocation-based stochastic RSM and by Kang et al. (2015) using Gaussian process regression.

For problems without explicit performance functions, the surrogate models are necessary and the third method (MCS based on surrogate models) has the advantage that direct MCS can be applied without using FORM or SORM. The accuracy of estimating the system P_f depends on the accuracy of the surrogate model. In this study, a modified hybrid approach is proposed and compared in detail with the widely used second-order RSM for a circular tunnel case.

4.3 Deterministic analysis of rockbolt-reinforced tunnels based on Bobet and Einstein (2011) formulations

Bobet and Einstein (2011) proposed an iterative closed-form formulation for a circular tunnel reinforced by end-anchored rockbolts in homogeneous and isotropic elastoplastic ground with the Coulomb failure criterion as shown in Fig. 4.3 in which σ_0 is the in situ stress, σ_i is the internal support pressure, r_0 is the tunnel radius, and S_θ is the circumferential distance between two adjacent rockbolts. This 2D formulation also considers the 3D supporting effect of the tunnel face by the stress reduction method where it is assumed that the unreinforced opening prior to rockbolt installation is subjected to an internal support pressure $\beta_\sigma \sigma_0$. The detailed formulae regarding this solution are given in Appendices A and B1 in Bobet and Einstein (2011) and summarized in Appendix C in this thesis.

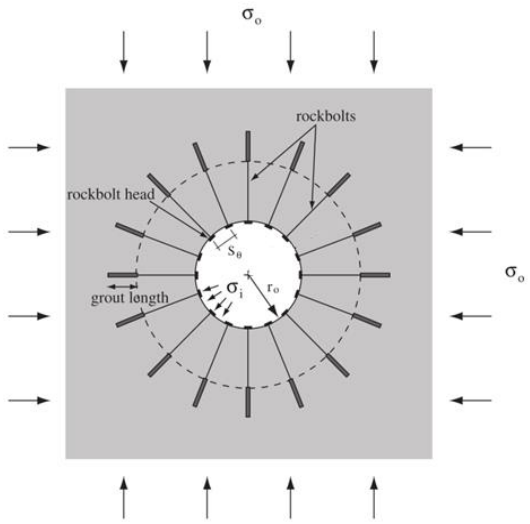

Geometry:
Tunnel radius: r_0= 3 m
Rockbolt length: L= 3 m
Rockbolt:
Rockbolt spacing in the axial direction: S_z= 1 m
Rockbolt spacing in the circumferential direction: S_θ= 1 m
Diameter of rockbolts: d_b= 25 mm
Young's modulus of rockbolts: E_b= 210 GPa
Poisson's ratio of rockbolts: ν_b= 0.3
Rock mass properties:
Young's modulus of ground: E= 500 MPa
Poisson's ratio of ground: ν= 0.2
Peak and residual internal friction angles: $\phi_p = \phi_r$= 30°
Dilation angle: ψ= 0.5 ϕ_p
Peak and residual cohesion: $c_p = c_r$= 0.1 MPa
Stress conditions:
In situ stress: σ_0= 1 MPa
3D excavation effect parameter: β_σ= 0.3
Post-construction internal support pressure: σ_i= 0

Fig. 4.3. A circular tunnel with end-anchored rockbolts (after Bobet and Einstein, 2011)

During the construction of a tunnel, the support such as the rockbolts and shotcrete is not installed immediately after the excavation but at some distance from the tunnel excavation face. Thus, when the support is installed, there is already some deformation of the rock mass. With the advance of the tunnel face, the support and the rock mass will deform together. The excavation and support installation are a three dimensional problem. In order to consider this delayed installation effect in the 2D analysis, various

simplified approaches have been proposed, as summarized by Möller (2006). Among these simplified 2D methods, the stress reduction method is widely used. This method is implemented in two stages as shown in Fig. 4.4. In the first stage, the rock mass inside the tunnel is removed and a uniform support pressure $\beta_\sigma \sigma_0$ is applied to the excavation boundary. The stress reduction coefficient β_σ should be selected such that, after equilibrium, the displacement of the tunnel wall corresponds to the initial displacement before the support is installed. In the second stage, the support pressure is removed and the support (rockbolts, shotcrete and liner) is installed.

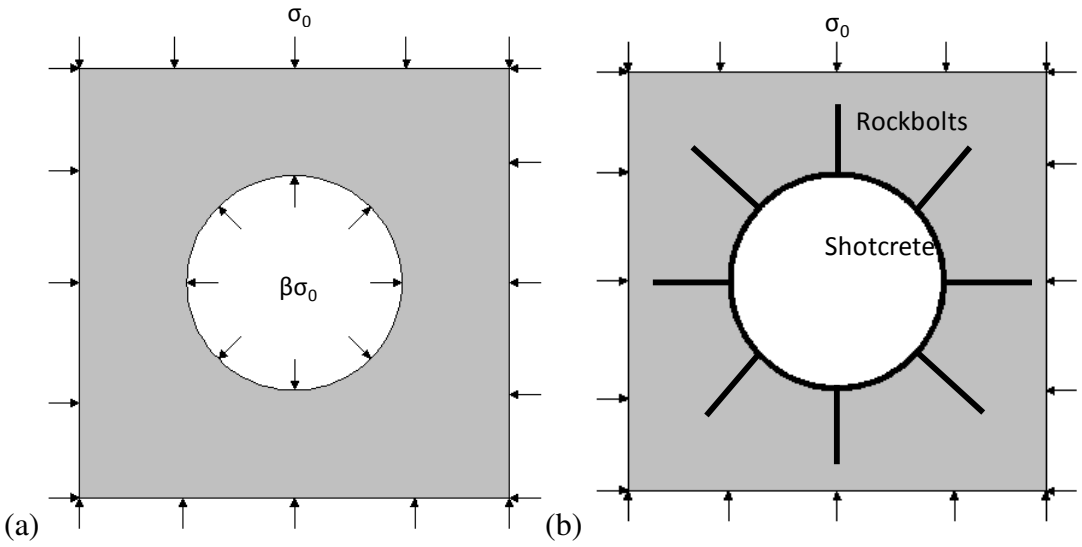

Fig. 4.4. Illustration of the stress reduction method (a) first stage (b) second stage

The Bobet and Einstein (2011) formulation can be verified using numerical software such as FLAC^{3D} (www.itascacg.com). The numerical model and mesh used for this case are shown in Fig. 4.5. The input parameters are the same as those in Fig. 4.3 except that the rockbolt spacing in the circumferential direction S_θ is 1.57 m. This value is used because the number of rockbolts will be an integer. The two-stage implementation is also used in the numerical simulation. The result for the first stage can be checked by the Duncan-Fama solution as shown in Chapter 3. The displacement of the tunnel wall is 5.5 mm by FLAC^{3D}, which agrees well with the Duncan-Fama solution result 5.5 mm. After the second stage, the final displacement is 13.8 mm from FLAC^{3D}, compared well with the Bobet and Einstein solution which gives 12.9 mm displacement.

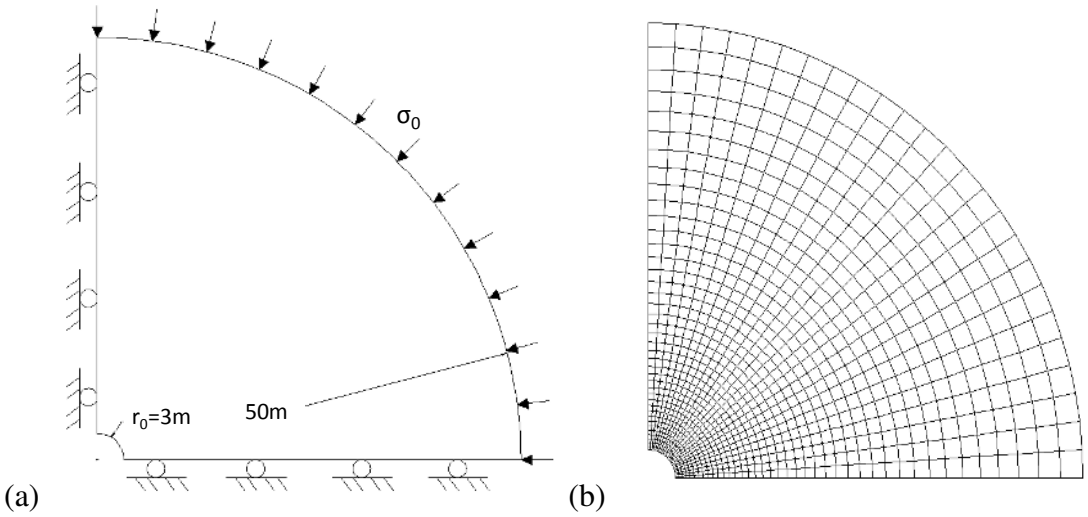

Fig. 4.5. (a) Numerical model and (b) finite difference mesh for verifying the closed form solution

Low and Einstein (2013) first extended the Bobet and Einstein solution to reliability evaluation by FORM and SORM considering one single limit state, i.e. the tensile rupture of the rockbolt. In this chapter, three limit states, including an ultimate and two serviceability limit states, will be of concern. The performance functions for the system are given as:

$$g_1(x) = T_{\text{limiting}} - T \tag{4.7}$$

$$g_2(x) = \varepsilon_{\text{limiting}} - \frac{u}{r_0} \tag{4.8}$$

$$g_3(x) = \lambda_{\text{limiting}} - \frac{r_p}{r_0} \tag{4.9}$$

where T_{limiting} (170 kN in this case) is the maximum allowable tensile force; T is the mobilized tensile force in the rockbolt; $\varepsilon_{\text{limiting}}$ (0.5% in this case) is the limiting ratio of u / r_0; u is the tunnel wall displacement; $\lambda_{\text{limiting}}$ (2.0 in this case) is the limiting ratio of r_p / r_0; r_p is the radius of the plastic zone. Three failure modes are graphically shown in Fig. 4.6.

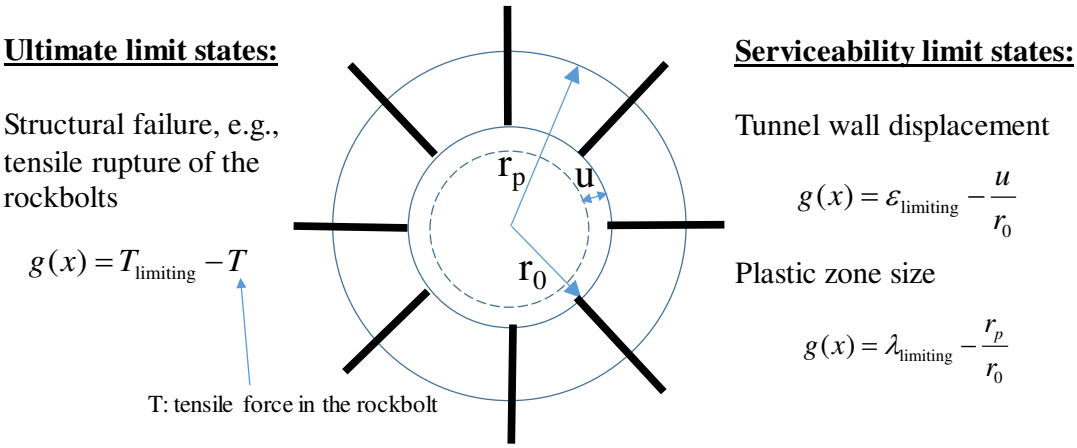

Fig. 4.6. Illustration of the three performance functions

These three performance functions consider the mobilized tensile force in the rockbolt, the maximum displacement and the plastic zone size, respectively. Other input parameters are the same as those in Low and Einstein (2013) and are shown in Fig. 4.3. For the following probabilistic analysis, the random variables and corresponding probabilistic characteristics (means and standard deviations) are shown in Table 4.1. The friction angle and the cohesion of the rock mass are considered to be negatively correlated with a correlation coefficient -0.5.

Table 4.1 Statistics of random variables for the rockbolt-reinforced circular tunnel case

Distribution	Variables	Mean μ	StD σ
Lognormal	β_σ	0.3	0.05
Lognormal	ϕ (°)	30	4
Lognormal	c (MPa)	0.1	0.01
Lognormal	E (MPa)	500	100

4.4 System reliability analysis of circular tunnels reinforced by rockbolts

This section compares the bimodal bounds method with the **mvncdf** method and shows that the reliability index from SORM can be used to improve the estimate of the system

probability of failure. Also discussed are the influence of the correlation coefficient between the cohesion and friction angle and the influence of the rockbolt installation position on the system probability of failure.

4.4.1 System reliability analysis using bimodal bounds and mvncdf methods

System reliability analysis using the bimodal bounds method and the **mvncdf** method involves the calculation of reliability indices for each limit state and the correlation matrix of all limit states. Since the closed-form solution is available, the Low and Tang (2007) approach can be directly applied to obtain the reliability indices (β_i) and corresponding design points ($\mathbf{n}_i^*$) in the correlated standard normal random variable space. The relation between $\mathbf{n}_i^*$ and $\mathbf{x}_i^*$ (design point in the original random variable space) is shown by Eq. (4.10), where $\boldsymbol{\mu}_x$ and $\boldsymbol{\sigma}_x$ are the vectors of mean values and standard deviations of the random variable $\mathbf{x}$.

$$\mathbf{n}_i^* = \frac{\mathbf{x}_i^* - \boldsymbol{\mu}_x^N}{\boldsymbol{\sigma}_x^N} \tag{4.10}$$

where $\boldsymbol{\mu}_x^N$ and $\boldsymbol{\sigma}_x^N$ are the equivalent mean and standard deviation of the random variables for non-normal distributions.

The correlation matrix $\boldsymbol{\rho}$ of a system composed of m limit states can be assembled as (e.g. Ang and Tang, 1984):

$$\mathbf{A} = \left[\frac{\mathbf{n}_1^*}{\beta_1}, \frac{\mathbf{n}_2^*}{\beta_2} ..... \frac{\mathbf{n}_m^*}{\beta_m} \right] \tag{4.11}$$

$$\boldsymbol{\rho} = \mathbf{A}^T \mathbf{R}^{-1} \mathbf{A} \tag{4.12}$$

where $\mathbf{R}$ is the correlation coefficient matrix for the input random variables.

Given the reliability indices and correlation matrix of all limit states, the bimodal bounds method can be simply implemented using the user-defined Excel function given by Low et al. (2011). Meanwhile, for the **mvncdf** method, the MATLAB function **mvncdf** is used and the system P_f can be estimated based on Eq. (4.5). The FORM results along with the system P_f obtained from these two methods are shown in Fig. 4.7.

For comparison, MCS is performed to estimate the system P_f, which is regarded as the benchmark for comparison.

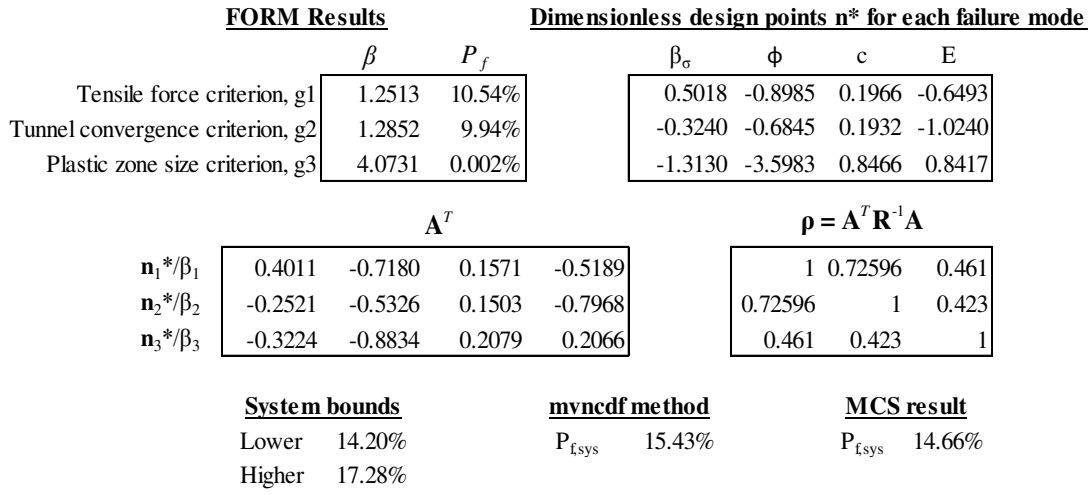

Fig. 4.7. System reliability analysis of a circular tunnel with rockbolts

For this case study, the following points are the detailed explanation of the results in Fig. 4.7.

(a) The probabilities of failure from FORM analysis for each limit state are 10.54%, 9.94% and 0.002%, respectively, indicating that the third limit state is almost unlikely. The system failure is mainly contributed by the first two limit states.

(b) The design points for each limit state show the influence of different random variables on the performance functions. The β_σ value represents the supporting effect of the tunnel excavation face and is related to the distance from the rockbolt installation position to the tunnel face. The greater the distance, the less the supporting effect from the tunnel face and the smaller β_σ values. Therefore, smaller β_σ values correspond to greater distances, and vice versa. For the rockbolt tensile force criterion (limit state 1), the positive dimensionless n* value for β_σ indicates that a greater β_σ value leads to a larger tensile force in the rockbolts. If the rockbolts are installed at a closer location from the tunnel excavation face (greater β_σ value), with the advance of the tunnel face, more stress will be carried by the rockbolt, yielding a larger tensile force in the rockbolts. However, for limit state 2 and 3, the

n* values for β_σ are negative. This is also expected because late installation of the support will cause a larger tunnel wall displacement and plastic zone size.

(c) These three limit states are positively correlated and the correlation matrix is shown by **ρ**.

(d) For the bimodal bounds method, the lower bound of the system P_f is 14.20% while the upper bound is 17.28% with a range of 3.08%. For this system with three limit states, all possible permutations of the three limit states give almost identical system P_f bounds.

(e) The **mvncdf** method gives a system P_f of 15.43%, which lies within the range set by the bimodal bounds method. As mentioned in section 4.2.2, the system P_f estimated by Eq. (4.5) can also be evaluated through the multiple integral shown by Eq. (4.6).

(f) Three MCS, each of 250,000 runs, are performed based on the closed-form solution to obtain the system P_f using the commercial software @risk. The average value is 14.66% (14.64%, 14.65%, 14.68%), which is smaller than the P_f obtained by the **mvncdf** method. The coefficient of variation (COV) of the MCS can be estimated by $\sqrt{(1-P_f)/(NP_f)}$, where N is the number of runs in each simulation. For this case, the COV of MCS is about 0.48%.

4.4.2 Improvement of the system reliability evaluation using the reliability indices from SORM

As noted in Fig. 4.7, the system P_f obtained by the **mvncdf** method is greater than that from MCS. This inaccuracy is mainly caused by the use of reliability indices from FORM. The FORM is accurate only when the input random variables are normally distributed and LSS is planar. However, the first limit state has significant curvatures at the design point and thus the P_f estimated from FORM is not precise. SORM is widely used to improve the results from FORM by considering the curvatures of LSS at the design point. Chan and Low (2012a) developed the spreadsheet implementation of SORM based on the approximating paraboloid method proposed by Der Kiureghian et al. (1987) and this approach is adopted in this study. Table 4.2 shows the results for the system reliability evaluation using the SORM reliability indices.

Table 4.2 Use of SORM reliability indices in system reliability evaluation

	β_{FORM}	$P_{f,FORM}$	β_{SORM}	$P_{f,SORM}$	$P_{f,MCS}$	System P_f	
g1	1.251	10.54%	1.345	8.93%	8.87%	Lower bound	13.38%
g2	1.285	9.94%	1.271	10.18%	10.23%	Upper bound	16.13%
g3	4.073	0.0023%	4.089	0.0022%	0.0022%	mvncdf	14.50%

For the first limit state, the P_f from SORM ($P_{f,\,SORM}$) is 8.93%, which is close to the P_f of 8.87% from the MCS ($P_{f,\,MCS}$). The SORM reliability index β_{SORM} is calculated from Eq. (4.13) and is used in lieu of β_{FORM} for the system reliability evaluation.

$$\beta_{SORM} = -\Phi^{-1}(P_{f,SORM}) \tag{4.13}$$

The system bounds using the bimodal bounds method and system P_f of 14.50% using **mvncdf** method agree well with the MCS result (14.66% in Fig. 4.7).

4.4.3 Influence of the correlation coefficient between cohesion and friction angle on the system P_f

Fig. 4.7 shows the results when the correlation coefficient $\rho_{\phi,c}$ between the friction angle ϕ and the cohesion c of the rock mass is -0.5. When $\rho_{\phi,c}$ changes from -0.9 to 0, the influence of $\rho_{\phi,c}$ on the system P_f is shown in Fig. 4.8, in which the system P_f is calculated using FORM reliability indices. It is clear that the system P_f increases as $\rho_{\phi,c}$ changes from -0.9 to 0 and the range set by the lower and upper bounds slightly increases. For comparison, the system P_f obtained from MCS based on the closed-form solution is also shown in Fig. 4.8. The MCS results are close to the lower bounds but different from the results for the **mvncdf** method. As mentioned in section 4.4.2, SORM reliability indices can be used to refine the system P_f estimated from the bimodal bounds method and the **mvncdf** method. The system P_f results based on the SORM reliability indices are shown in Fig. 4.9. If SORM reliability indices are used, the results from the **mvncdf** method agree well with the MCS results. From both Fig. 4.8 and Fig. 4.9, the system P_f obtained by the **mvncdf** method always lies within the lower and upper bounds by the bimodal bounds method.

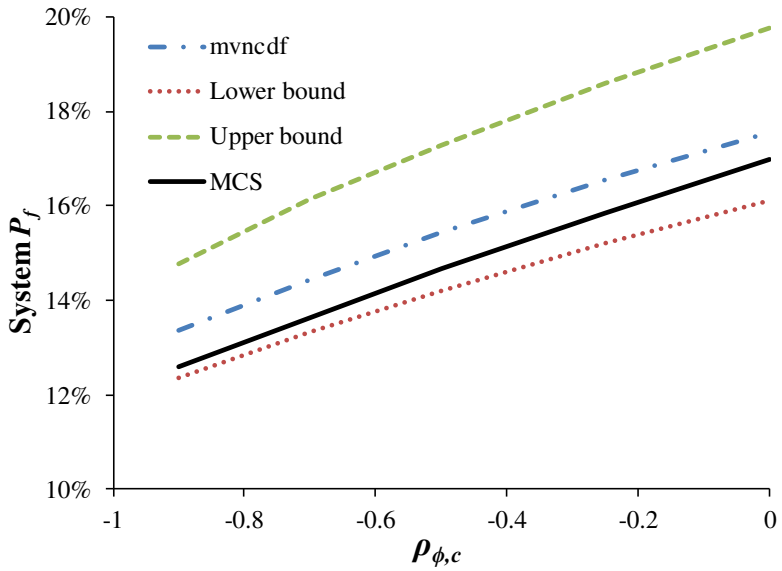

Fig. 4.8. Influence of $\rho_{\phi,c}$ on the system P_f based on FORM reliability indices

The reason why the system P_f increases when the $\rho_{\phi,c}$ changes from -0.9 to 0 can be explained as follows. A negative correlation means that a smaller value of ϕ tends to appear with a larger value of c and thus the chance of c and ϕ having both low values is smaller compared with the situation where there is no correlation. Therefore, the P_f is lower for the case with negative correlations.

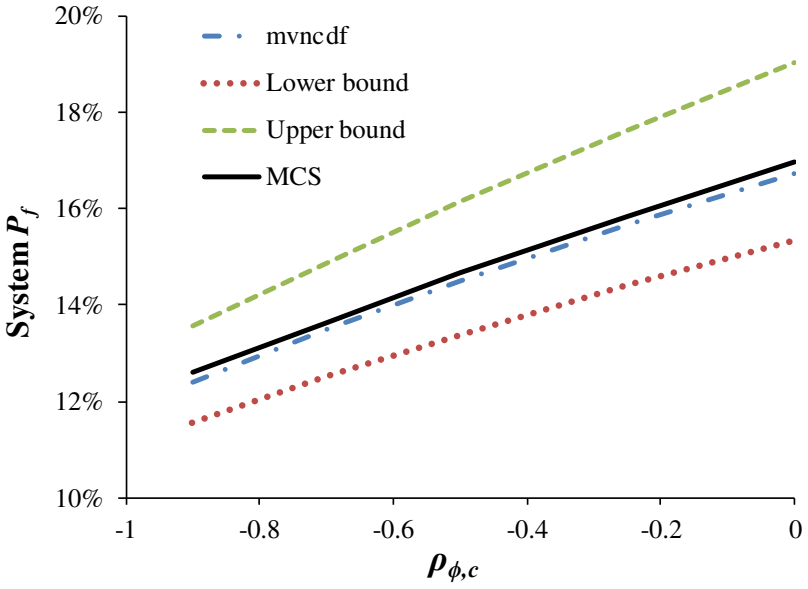

Fig. 4.9. Influence of $\rho_{\phi,c}$ on the system P_f based on SORM reliability indices

4.4.4 *Effect of the rockbolt installation position on the system* P_f

As explained in point (b) in section 4.4.1, the β_σ value is related to the rockbolt installation position. A smaller β_σ value corresponds to a greater distance from the installation position to the tunnel face, and vice versa. The influence of the mean value of β_σ on the reliability indices corresponding to the three limit states of Eq. (4.7)-Eq. (4.9) is shown in Fig. 4.10.

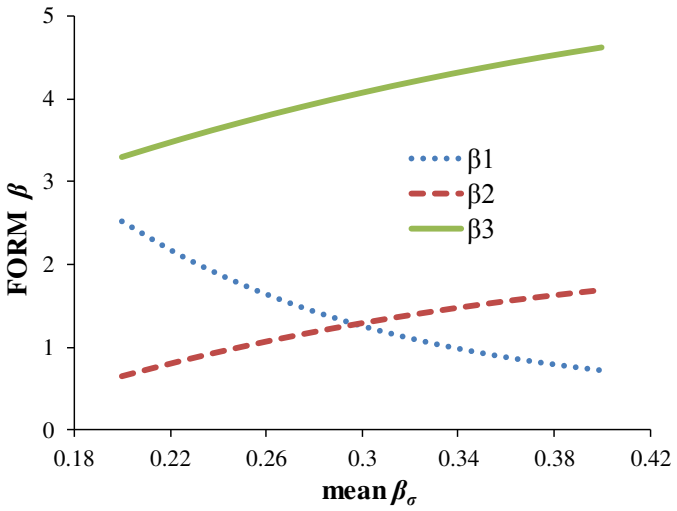

Fig. 4.10. Influence of rockbolt installation position on the reliability indices

In this case, the COV of β_σ is fixed at 0.05/0.3=0.167. β_1 decreases while β_2 increases as the mean of β_σ becomes larger, which can be explained as follows. A larger β_σ value means the rockbolts are installed at a shorter distance from the advancing tunnel face. Therefore, with further advance of the tunnel, a greater portion of the stress is carried by the rockbolts (smaller β_1) and the tunnel final convergence is smaller (larger β_2). A smaller β_σ value means "delay" in placing the rockbolts and thus leads to smaller tensile forces and larger tunnel convergences.

Single limit state analysis may overlook the influence of input parameters on the system probability of failure. Fig. 4.11 shows the change of system P_f obtained from the bimodal bounds method and the **mvncdf** method with the mean value of β_σ. The system P_f is calculated based on FORM reliability indices. For comparison, MCS results based on the closed-form solution are also shown. When the mean β_σ is greater than 0.3, there is a significant discrepancy between the MCS results and the system P_f from the

bimodal bounds method and the **mvncdf** method. Again, the SORM reliability indices are used to improve the accuracy of the estimated system P_f and the results are shown in Fig. 4.12. The refined system P_f is in good agreement with MCS results.

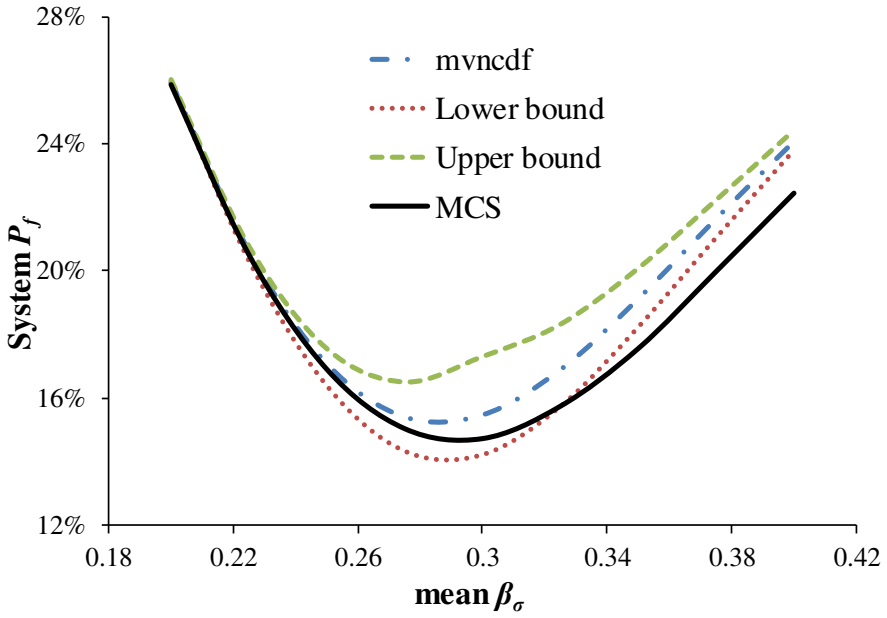

Fig. 4.11. Influence of rockbolt installation position on the system P_f based on FORM reliability indices

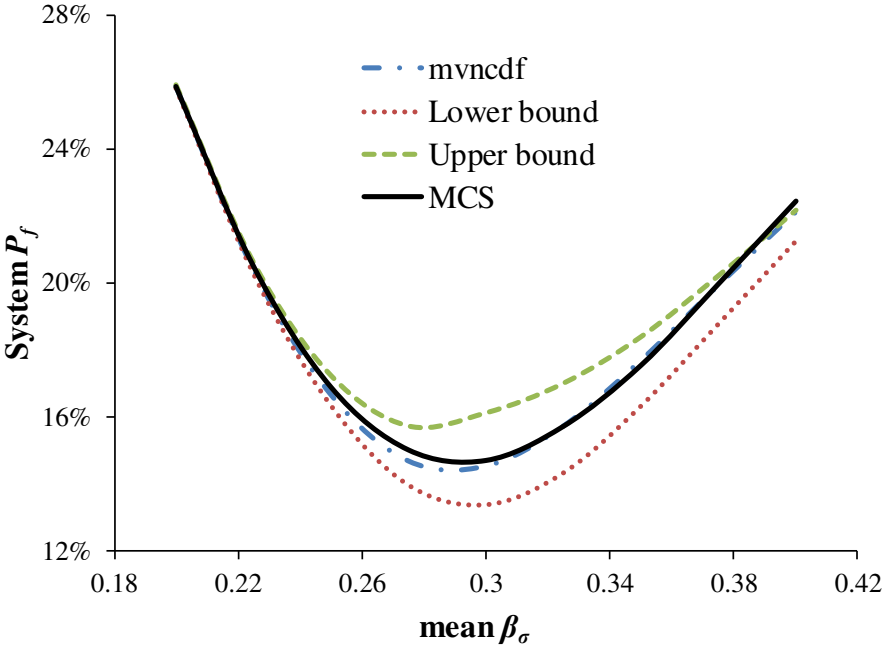

Fig. 4.12. Influence of rockbolt installation position on the system P_f based on SORM reliability indices

From Fig. 4.12, when the mean value of β_σ is about 0.3, the system P_f obtains its smallest value which is 14.50% by the **mvncdf** method. The system P_f first decreases and then increases as the mean of β_σ increases. This can be explained by the results in Fig. 4.10. Before the minimum system P_f value point, the system failure is controlled by the second performance function (displacement) and thus the system P_f decreases (β_2 increases) as the mean of β_σ increases. After the minimum system P_f value point, the system failure is dominated by the first performance function (tensile force) and thus system P_f increases (β_1 decreases) as the mean of β_σ increases. This phenomenon indicates that if the support is too close to the excavation face, rockbolts may fail due to the large stress it carries. However, if the support is installed too far away from the excavation face, the final convergence of the tunnel may be unacceptably large. The system reliability analysis result based on the probabilistic evaluation is in agreement with engineers' knowledge.

4.4.5 Illustrative system reliability-based design of the rockbolt length and spacing

It has been shown in the above discussions that the **mvncdf** method with reliability indices calculated from SORM can estimate the system P_f accurately. However, the system P_f (about 15%) is unacceptably high when the rockbolt length (L) is 3 m and the spacing is 1 m in both radial and normal directions (S_z and S_θ). One can design the length and spacing of the rockbolts so as to achieve a more adequate reliability index, for example β = 2.5 corresponding to a P_f of 0.62%. For projects of which the failure consequence is severe, higher reliability index values can be specified (e.g. β = 3.0). In this section, the length (L) and spacing ($S_z = S_\theta$) of the rockbolts are designed to achieve a target system reliability index (β = 2.5). Since the third limit state has little influence on the system failure, only the first two performance functions are considered in this system reliability-based design problem.

The procedure for the system reliability-based design can be summarized as follows. First, choose a design value for the rockbolt length (e.g. 3 m) and a trial value for the spacing. Next, FORM is conducted based on the two performance functions and $\beta_{1,FORM}$, $\beta_{2,FORM}$ as well as the correlation matrix for the limit states are obtained. Then, SORM

is conducted in order to refine the reliability indices to $\beta_{1,SORM}$ and $\beta_{2,SORM}$. The SORM reliability indices and the correlation matrix for the limit states are used as inputs for the **mvncdf** method to estimate the system P_f and the reliability index β_{system}. At the first trial, β_{system} may not be equal to the target reliability index. Thus, different values for the spacing are tried until $\beta_{system} = 2.5$.

Three rockbolt length values are selected (the first column in Table 4.3) and the required spacing values shown in column 2 of Table 4.3 are found through trial and error to achieve a target system reliability index 2.5. The system P_f (column 3 of Table 4.3) is estimated by the **mvncdf** method and the corresponding reliability indices are close to 2.5. In order to check the accuracy of the **mvncdf** method, three MCS each of which consists of 200,000 runs are conducted and the results are shown in the last four columns of Table 4.3. Comparison between column 3 and 8 shows that the **mvncdf** method results agree well with the MCS results and the design solution for the rockbolt length and spacing can achieve a target system P_f and a target reliability index. For the design values of the rockbolt length and spacing in this case study, the system failure is controlled by the second limit state (the maximum displacement) while the reliability indices for the first limit state are in the range of 6 to 7. With the increase of the length from 2 m to 4 m, the tensile force in the rockbolt actually decreases and thus the displacement increases. Therefore, in order to achieve the same reliability index 2.5, the design value for the spacing decreases with longer rockbolts. The fact that longer rockbolts yield larger displacements for this case can be illustrated by the deterministic analysis. The input parameters are shown in Fig. 4.3 except that the in-plane spacing of the rockbolts is 1.57 m. The results from the closed-form solution and from FLAC^{3D} are shown in Table 4.4. The results show that indeed the tensile force becomes smaller and the tunnel wall displacement becomes larger with longer rockbolts. The change of the displacement is insignificant for this case. In engineering practice, the design of the end-anchored rockbolts should consider the plastic zone radius or the excavation damage zone for the stress-controlled failure. The anchored end point should be located in the stable rock mass. For the structurally-controlled failure, the rockbolt should be long enough to anchor the largest unstable rock block.

Table 4.3 Required length and spacing for a target reliability index 2.5

Length (m)	Required spacing for β=2.5 (m)	System P_f (%)	β_{system}	System P_f three MCSs (%)			Average MCS P_f (%)
2	0.58	0.617	2.502	0.614	0.618	0.619	0.617
3	0.52	0.617	2.502	0.637	0.603	0.629	0.623
4	0.48	0.613	2.505	0.629	0.615	0.637	0.627

Table 4.4 Deterministic analysis results for different rockbolt lengths

	Closed-form solution		FLAC^{3D}	
Rockbolts length (m)	Tensile force (kN)	Tunnel wall displacement (mm)	Tensile force (kN)	Tunnel wall displacement (mm)
2	209	12	198	13.1
3	177	12.9	178	13.8
4	156	13.6	162	14.5
6	129	14.8	137	15.7

4.5 System reliability analysis using RSM and ANN

The above system reliability analysis is based on the situation where the closed-form solution exists. However, for problems with implicit performance functions, which are often the case for tunnelling problems, various surrogate models should be used to approximate the actual LSS as pointed out in section 4.2.3. Among all the available surrogate models, polynomial RSM is widely adopted due to its efficiency in locating the design point via the iterative strategy. The basic idea of the iterative RSM is to gradually approximate the actual LSS using polynomial functions $\overline{g}(x)$ as shown in Chapter 2 and 3. The unknown coefficients of the polynomial function are determined by solving a linear equation set using a small number of sampling points. The iterative procedure is shown in Fig. 4.13 and can be described as follows. First, the mean value point is chosen as the sampling central point and the first tentative response surface is determined. Next, FORM is conducted based on the tentative response surface and the tentative design point and reliability index are calculated. Then, the tentative design point is selected as the next sampling central point and a new tentative response surface

and reliability index are obtained. The iteration continues until the difference between two consecutive reliability indices is acceptably small. This iterative polynomial RSM has been successfully applied to various geotechnical problems (e.g. Xu and Low, 2006; Lü et al., 2011). Since fewer sampling points are required for the linear RSM, it will be used to gradually approach the actual LSS.

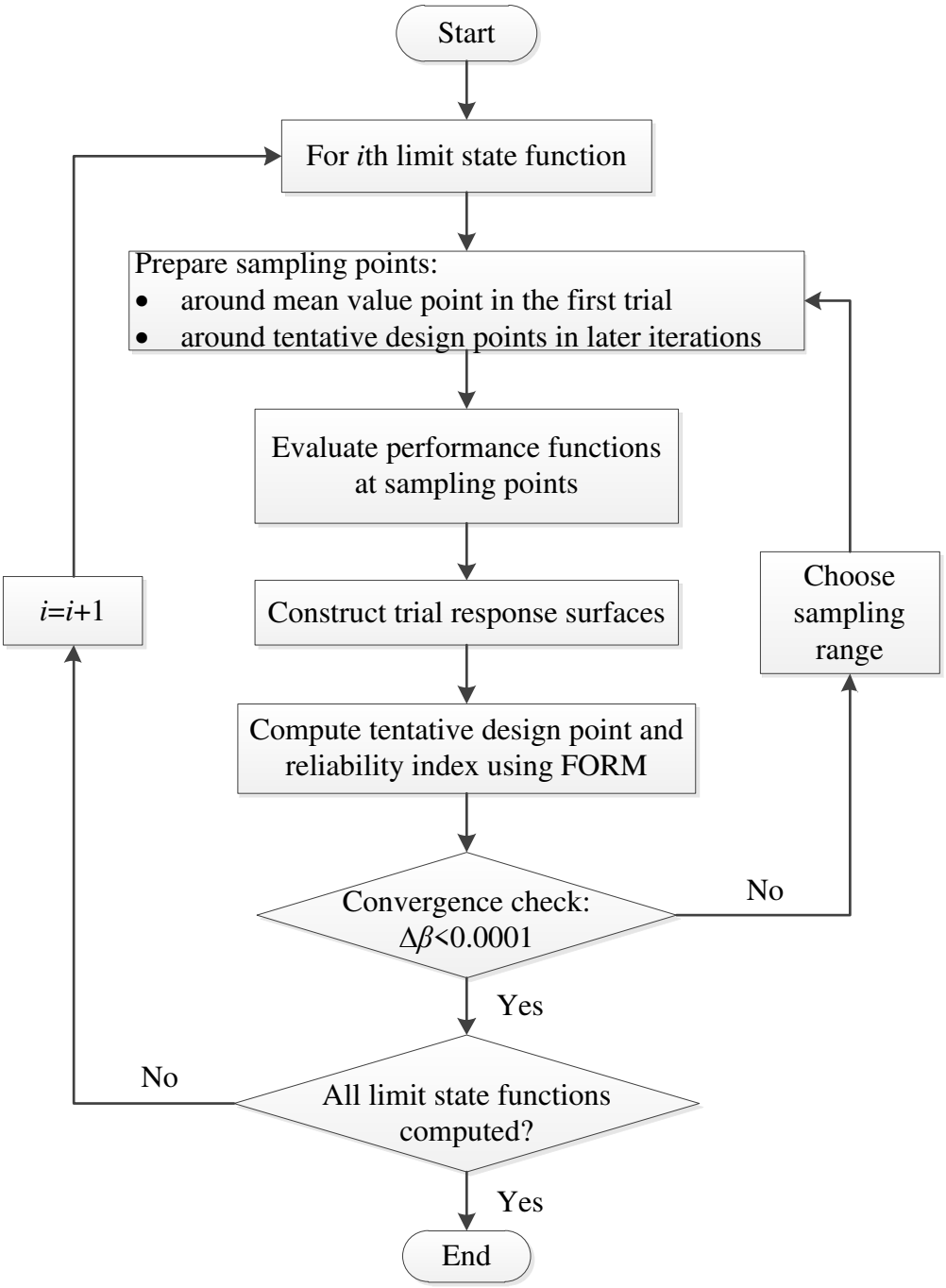

Fig. 4.13. Steps for the iterative response surface method

Although the linear RSM is efficient in locating the design point, it suffers from the fact that nonlinearity of the actual LSS cannot be approximated. In order to consider the curvature of the actual LSS around the design point, Chan and Low (2012b) suggested that a new set of sampling points around the design point can be used to construct ANN whereas Lü et al. (2013) used the second-order polynomial function to approximate the LSS around the design point. However, all these methods require additional sampling points around the design point. A modified method is used in this study. Instead of building ANN based on a set of new sampling points, all the sampling points during the iteration when the linear response surface is gradually approaching the actual LSS are used to train the neural network. Therefore, there is no "waste" of the sampling points which contribute to locating the design point. Besides, compared with other methods, this approach can approximate the performance function not only around the design point but in a larger domain from the mean value point to the design point. Once ANN is constructed, direct MCS can be used based on the response of ANN without much computational efforts. The accuracy and efficiency of this proposed approach can be illustrated through the same case study of a circular tunnel reinforced by rockbolts as mentioned in the above sections but assuming that the performance functions are not known in closed-form.

First, the iterative linear RSM with the expression shown by Eq. (4.14) is applied to obtain the design point.

$$\overline{g}(x) = a + \sum_{i=1}^{n} b_i x_i \tag{4.14}$$

where $\overline{g}(x)$ is the response function; a and b_i are unknown coefficients that should be determined; x_i is the random variable value.

There are n+1 sampling points in each iteration. Therefore, one central point u and n sampling points ($u - k\sigma$) around the central point are selected (k is the sampling range factor and σ is the standard deviation). Constant sampling factor k=0.5 is used throughout the iteration. The sampling points are prepared in the correlated standard normal space (n-space) corresponding to the Low and Tang (2007) algorithm. The converged results are shown in Table 4.5. For performance function 1 and 2, where reliability indices are between 1.2 and 1.3, only five iterations are needed to get the converged reliability index. For performance function 3, where the reliability index is

large, 7 iterations are needed. The numbers of total sampling points are calculated via multiplying the number of iterations by five (five sampling points in each iteration). The reliability indices obtained from the linear RSM agree with those from direct FORM shown in Fig. 4.7, verifying that the linear RSM is accurate in locating the design point.

Table 4.5 FORM results for linear RSM

	Number of iterations	Total sampling points	$\beta_{LinearRSM}$
g1	5	25	1.2515
g2	5	25	1.2852
g3	7	35	4.0735

Next, all the sampling points obtained during the iterations are used to train ANN, i.e. 25, 25 and 35 points are used for the three limit states respectively. Hornik et al. (1989) demonstrated that ANN with a typical three-layer structure can approximate any function provided that sufficient hidden neurons are available. Thus, a 4-10-1 network (four input random variables, 10 hidden neurons and one output) is adopted in this study. The basic structure of ANN is shown in Fig. 2.11 (Chapter 2). The transfer function between the input layer and the hidden layer is the tangential sigmoid function, which is shown by Eq. (4.15), and the transfer function between the hidden layer and output layer is the pure linear function.

$$f(x) = \frac{2}{(1+e^{-2x})} - 1 \tag{4.15}$$

Before training ANN, sampling points are normalized to the range of [-1, 1] as shown by Eq. (4.16) in order to eliminate the influence of magnitudes of different variables.

$$u_i^N = \frac{2(u_i - u_{\min})}{u_{\max} - u_{\min}} - 1 \tag{4.16}$$

where u_i^N is the normalized value; u_i is the original value; $u_{\max}$ and $u_{\min}$ are the maximum and minimum values.

When samples are ready, the training process is implemented by adjusting the weights between adjacent layers. The Bayesian regularization algorithm minimizes a linear combination of square errors of the sampling points and is shown to have good generalization qualities (e.g. McKay, 1992; Cheng and Li, 2009). Therefore, this

algorithm is used to find the optimum values for the weights and biases in ANN. After the training process, the optimum weights and biases can be used to calculate the output of ANN through Eq. (4.17). The detailed formulation and calculation of ANN can be found in textbooks, e.g. Anderson (2005).

$$Y = f_{linear}\left\{b_0 + \sum_{k=1}^{h}\left[w_k f_{\tan sig}\left(b_{hk} + \sum_{i=1}^{m} w_{ik} X_i\right)\right]\right\} \tag{4.17}$$

in which b_0 is the bias at the output layer; w_k is the weight between hidden layer neuron k and output layer single neuron; b_{hk} is the bias at neuron k in the hidden layer; w_{ik} is the weight between input neuron i and hidden layer neuron k; X_i is the random variable; f_{linear} is the pure linear transfer function and $f_{\tan sig}$ is the tangential sigmoid transfer function.

Eq. (4.17) can be regarded as a closed-form expression for ANN and MCS can be conducted based on this expression. Results for the individual limit state and the system failure are compared with those from MCS based on the closed-form solution, which are shown in Table 4.6.

Table 4.6 MCS results for ANN and closed-form solution

	P_f(Closed-form)	P_f(ANN)			
		Simulation 1	Simulation 2	Simulation 3	Average
P_f (g1)	8.87%	8.97%	9.01%	8.91%	8.96%
P_f (g2)	10.23%	10.22%	10.25%	10.14%	10.20%
P_f(system)	14.66%	14.48%	14.53%	14.48%	14.50%

To obtain the P_f for limit state 1, 2 and the system P_f, three MCS each of which consists of 200,000 runs are conducted. The average values of MCS on ANN agree well with MCS results based on the closed-form solution, demonstrating that the proposed method is accurate in approximating the actual LSS. For the third limit state, since the P_f is relatively low (2×10^{-5} from FORM analysis), it has almost no effect on the system P_f.

4.5.1 Comparison of linear RSM with the second-order RSM without cross terms

The above analysis uses the linear RSM. In the literature, second-order polynomial RSM without cross terms is widely used to approximate the LSS. In this section, second-order polynomial RSM without cross terms is used and the results are compared with those from linear RSM. The expression of the second-order RSM without cross terms is shown by Eq. (4.18).

$$\bar{g}(x) = a + \sum_{i=1}^{n} b_i x_i + \sum_{i=1}^{n} c_i x_i^2 \tag{4.18}$$

where $\bar{g}(x)$ is the response function; a, b_i and c_i are unknown coefficients that should be determined; x_i is the random variable value.

Since there are $2n+1$ unknown coefficients, the axial-point design (shown in Chapter 2) using one central point u and $2n$ points ($u \pm k\sigma$) can be used. For comparison, the sampling factor is still kept at 0.5 during the iteration. The iteration procedure is the same as that used in the linear RSM and the results for second-order RSM without cross terms are shown in Table 4.7 and Table 4.8. Table 4.8 displays the coefficients for the final second-order RSM without cross terms. The coefficients together with Eq. (4.18) can be used to establish the closed-form response surface. In this case, since the sampling points are prepared in the correlated standard normal random variable space, n_i values instead of x_i values in Eq. (4.18) are used to obtain the response surface.

Table 4.7 FORM results for second-order RSM without cross terms

	Number of iterations	Total sampling points	β_{SecOrd}
g1	4	36	1.2513
g2	4	36	1.2852
g3	8	72	4.0731

The total number of sampling points is calculated by multiplying the number of iterations by 9 (9 sampling points in each iteration). For all three limit states, the numbers of sampling points are larger compared with the linear RSM although the numbers of iterations are almost the same. For all three limit states, the reliability

indices obtained from the second-order RSM without cross terms (β_{SecOrd} in Table 4.7) agree with the results from direct FORM based on the closed-form solution.

Table 4.8 Coefficients of second-order RSM without cross terms

	g1	g2	g3
a	31.4230	1.12E-03	0.6068
b_1	-10.8756	2.19E-04	0.0537
b_2	21.6344	5.02E-04	0.1029
b_3	6.5746	1.44E-04	0.0602
b_4	12.7372	6.24E-04	-0.0380
c_1	0.9604	-2.61E-05	-0.0035
c_2	0.2900	-5.10E-05	-0.0138
c_3	0.2328	1.94E-06	0.0003
c_4	-0.0820	-6.05E-05	-0.0014

4.5.2 Comparison with the second-order RSM with cross terms and the importance sampling technique

The second-order RSM with cross terms uses the expression shown by Eq. (4.19).

$$\bar{g}(x) = a + \sum_{i=1}^{n} b_i x_i + \sum_{i=1}^{n} c_i x_i^2 + \sum_{1 \le i < j \le n} d_k x_i x_j \tag{4.19}$$

where d_k is the unknown coefficient for the cross terms, $1 \le k \le n(n-1)/2$.

In each iteration, $(n^2+3n+2)/2$ (15 in this case) sampling points are needed. For comparison, the sampling factor is kept at 0.5 during the iteration. The iteration procedure is the same and the results for the second-order RSM with cross terms are shown in Table 4.9 and Table 4.10.

Table 4.9 FORM results for second-order RSM with cross terms

	Number of iterations	Total sampling points	$\beta_{SecOrdCross}$
g1	3	45	1.2513
g2	3	45	1.2852
g3	4	60	4.0731

Table 4.10 Coefficients for second-order RSM with cross terms

	g1	g2	g3
a	29.6681	1.03E-03	0.5667
b_1	-7.6848	9.00E-05	-0.0095
b_2	20.1550	3.99E-04	0.0871
b_3	5.7816	8.80E-05	-0.0205
b_4	11.5956	5.54E-04	-0.0264
c_1	0.9607	-2.61E-05	-0.0034
c_2	0.2900	-5.10E-05	-0.0138
c_3	0.2328	1.94E-06	0.0003
c_4	-0.0821	-6.05E-05	-0.0014
d_1	2.6203	-1.04E-04	-0.0208
d_2	0.4632	-2.99E-05	-0.0095
d_3	1.4244	-6.28E-05	-0.0044
d_4	-0.6654	-4.73E-05	-0.0185
d_5	-0.4650	-7.68E-05	0.0052
d_6	0.0571	-1.37E-05	0.0019

Compared with the linear RSM, the numbers of iterations for all three limit states are smaller and the reliability indices agree better with those from direct FORM. However, the total numbers of sampling points are greater due to the fact that 15 points are needed in each iteration. MCS is applied to the converged second-order RSM with and without cross terms. The probabilities of failure are displayed in Table 4.11.

Table 4.11 MCS results for second-order RSM without and with cross terms

	Second-order RSM without cross terms			Second-order RSM with cross terms		
	g1	g2	System P_f (g1,g2)	g1	g2	System P_f (g1,g2)
1	9.76%	11.67%	16.05%	8.81%	10.07%	14.54%
2	9.70%	11.62%	16.03%	8.83%	10.12%	14.56%
3	9.81%	11.62%	16.06%	8.90%	10.07%	14.67%
Average	9.76%	11.64%	16.05%	8.88%	10.09%	14.59%

Three MCS each comprising 200,000 runs are conducted based on the response surfaces for the first two limit states. The system P_f is based on the first and second limit states

and thus is noted as System P_f(g1, g2) in Table 4.11. MCS results based on the closed-form solution are shown in Table 4.6 and regarded as the benchmark for comparison. For the third limit state, since P_f is relatively low, MCS with 10^7 runs based on ANN, second-order RSM with and without cross terms gives a P_f of almost zero, verifying that the third limit state has no influence on the system P_f.

For the P_f of the first and the second limit state, the results for the second-order RSM with cross terms are more accurate than those for RSM without cross terms. So are the results for the system P_f(g1, g2). This comparison shows that the second-order RSM with cross terms is more accurate in approximating the LSS than the RSM without cross terms. The proposed method using linear RSM and ANN has similar accuracy as the second-order RSM with cross terms but costs fewer sampling points.

However, for some cases, direct MCS based on the second-order RSM with cross terms may yield erroneous results. If the limiting ratio ($\varepsilon_{limiting}$) of the tunnel displacement over the tunnel radius increases from 0.5% to 1%, the results from the direct FORM based on the closed-form solution and from MCS based on the second-order RSM with cross terms are shown in Table 4.12. For limiting ratios from 0.5% to 0.7%, the FORM results and the MCS results are in the same order of magnitude. However, for ratios from 0.8% to 1%, the MCS results are erroneous since the P_f should decrease with increasing limiting ratios. Next, the case when limiting ratio is 0.8% is used to illustrate this problem.

Table 4.12 Results of FORM and MCS for different values of the limiting ratio

Limiting ratio $\varepsilon_{limiting}$	0.5%	0.6%	0.7%	0.8%	0.9%	1.0%
β	1.285	2.239	3.010	3.648	4.187	4.651
P_f (FORM)	9.94%	1.26%	0.13%	0.013%	0.0014%	0.0002%
P_f (MCS based on RSM)	10.08%	1.24%	0.13%	0.18%	1.30%	5.00%

The false MCS result based on the second-order RSM with cross terms is caused by the special characteristics of the second-order polynomials. A graphical apprehension of the discrepancy is presented in Fig. 4.14, which shows the actual LSS and the second-order response surface in the correlated standard normal space of E and ϕ while the other two random variables (β_σ and c) are kept at their design point values.

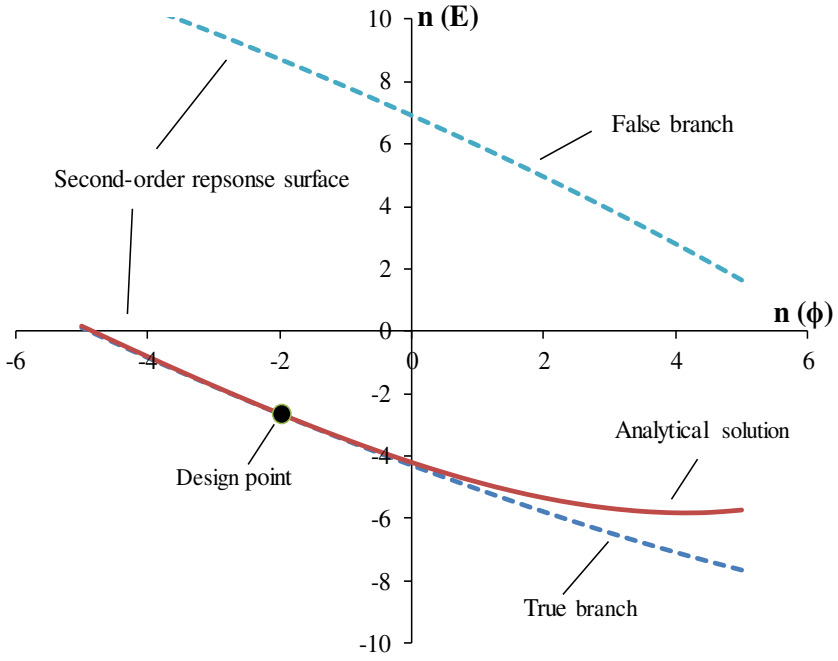

Fig. 4.14. Actual LSS and response surfaces for g2 when $\varepsilon_{limiting}$=0.8%

It can be seen from Fig. 4.14 that the second-order response surface with cross terms has two branches, represented by the dashed lines. One branch is close to the actual LSS obtained from the analytical solution whereas the other branch lies on the opposite side. The branch close to the actual LSS is useful in delimitating the boundary between the safe and unsafe domains and thus is called the "true branch". The other branch is named as the "false branch" since sampling points outside the false branch will be wrongly classified into the unsafe domain. This false branch causes the error in estimating the P_f by MCS. Note that Fig. 4.14 is an illustrative plot showing LLS and RSM in the two-random-variable space. For the problem, the true LSS and RSM are in the four-random-variable space. To further verify that the erroneous result is caused by the false branch problem, 200,000 runs of MCS based on RSM is conducted. Among these 200,000 sampling points, 350 points are failure points based on RSM. The corresponding P_f is 0.175% which agrees with 0.18% from Table 4.12. If these 350 points are evaluated by the closed-form solution, only 28 points are true failure points, meaning that other 322 points are wrongly classified as failure points by RSM. The true P_f is 28/200000=0.014% which agrees with 0.013% from FORM in Table 4.12. The erroneous MCS result based on the second-order RSM was also observed and explained

by Chan and Low (2012b) and Lü et al. (2012) but solutions for such problems were not provided.

In direct MCS, samples are taken around the origin shown in Fig. 4.14. Thus, a number of the sampling points will lie outside the false branch resulting in the erroneous result. Importance sampling can alter the sampling probability density function. Harbitz (1986) suggested shifting the sampling center from the origin to the design point which contributes most to the probability of failure. This technique samples a large portion of the points located in the failure domain and hence the number of wrongly classified sampling points could be greatly reduced. The importance sampling implementation in the spreadsheet environment, which was used in Chan (2012), is adopted in this study. Three importance sampling simulations each comprising 5,000 runs are conducted based on the second-order RSM with cross terms and the closed-form solution for the second limit state g2 when $\varepsilon_{limiting}$=0.8%. The results are shown in Table 4.13.

Table 4.13 Importance sampling and MCS results based on RSM, closed-form solution and ANN for g2 ($\varepsilon_{limiting}$=0.8%)

P_f (%)	1	2	3	Average
Importance sampling based on second-order RSM	0.0119	0.0124	0.0125	0.0123
Importance sampling based on closed-form solution	0.0128	0.0127	0.0123	0.0126
Importance sampling based on ANN	0.0128	0.0124	0.0124	0.0126
Direct MCS based on ANN	0.0125	0.0123	0.0126	0.0125

The average P_f from RSM is close to that from the closed-form solution, indicating that the importance sampling technique can indeed reduce the error caused by the false branch of the second-order RSM with cross terms. In order to show the advantage of the proposed approach, direct MCS and MCS with importance sampling are applied to ANN and the results are shown in Table 4.13. For the direct MCS based on ANN, each MCS comprises 2×10^6 runs. The results of direct MCS based on ANN are almost the same as those based on closed-form solution. The above comparison shows that direct MCS can be applied to ANN but the false branch problem may render the second-order RSM with cross terms less robust for the direct MCS. Table 4.13 shows the results when the limiting ratio is 0.8%, the importance sampling can also solve the false branch problem for the case when the limiting ratio is 0.9% and 1%. When $\varepsilon_{limiting}$=0.9%, 5000

runs of importance sampling gives a probability of failure of 0.0013% based on RSM compared well with the direct FORM result (0.0014% in Table 4.12) based on the closed-form solution. When $\varepsilon_{\text{limiting}}$=1%, 5000 runs of importance sampling gives a probability of failure of 1.53×10^{-6} based on RSM, compared well with the direct FORM result (2×10^{-6} in Table 4.12) based on the closed-form solution.

In this section, detailed comparisons among the proposed method using linear RSM and ANN, the second-order RSM without and with cross terms have been presented for the case of a circular tunnel reinforced by rockbolts. The comparison is shown in Table 4.14.

Table 4.14 Comparison of the hybrid approach and RSM

	Accuracy	Efficiency	Robustness
Hybrid approach	Good	Good	Good
RSM without cross terms	Fair	Fair	Fair
RSM with cross terms	Good	Fair	Fair

The MCS results based on the second-order RSM without cross terms are less accurate. Therefore, the second-order RSM without cross terms is not suggested for this case study. Although the second-order RSM with cross terms can accurately locate the design points, it suffers from the low efficiency and the false branch problem which may render the direct MCS result erroneous for some cases. It is shown in this study that the importance sampling technique can replace the direct MCS to reduce the error caused by the false branch. The proposed method which uses the linear RSM to locate the design point and ANN to approximate the LLS is shown to be robust, accurate and efficient and thus is preferable to be adopted for the system reliability analysis.

4.6 Summary and conclusion

This chapter begins by reviewing the commonly used system reliability methods including the bimodal bounds method, the **mvncdf** method using the multivariate normal cumulative distribution function and the MCS based on the approximate LSS. The first two methods can be directly applied if closed-form solutions exist. For

problems with implicit performance functions, direct MCS based on approximate response surfaces is straightforward for the system reliability analysis.

The first two methods are applied to the iterative closed-form solution for a circular tunnel with rockbolts proposed by Bobet and Einstein (2011). The system P_f estimated from the **mvncdf** method always lies within the lower and upper bounds set by the bimodal bounds method for the same input reliability indices and correlation matrix of the limit states. Also discussed are the influence of the correlation coefficient between the cohesion and the friction angle and the influence of the rockbolt installation position on the system P_f. It is also presented that the SORM can be used to refine reliability indices and to improve the accuracy of the estimated system P_f.

A modified hybrid approach is proposed in this study. First, the linear RSM is used to locate the design point through the iterative algorithm. Then, ANN is adopted to approximate the LSS using the sampling points obtained during the iteration. Finally, the MCS is conducted based on ANN to estimate the system P_f. The proposed method is compared in detail with second-order RSM without and with cross terms regarding the robustness, efficiency and accuracy. The second-order RSM without cross terms may be inaccurate and inefficient whereas the false branch problem may render the direct MCS result erroneous for the second-order RSM with cross terms. It is also shown in this chapter that the importance sampling technique can reduce the error caused by the false branch problem. Comparison shows that the proposed hybrid method of linear RSM followed by ANN requires fewer sampling points and the MCS results based on this method are satisfactory. Therefore, it is suggested that the hybrid approach be used in the system reliability analysis.

This chapter may help to have a better understanding of different approaches for the system reliability analysis and of the advantages and potential problems associated with these methods.

Chapter 5 Reliability-based design of tunnelling problems and insights for Eurocode 7

Chapter 3 and 4 focus on the reliability analysis which is used to estimate the probability of failure of a given problem or system. For practical engineers, what is more important is how the probabilistic approach could be used in the design process. From April 2015, Singapore started to use the partial factor design standard Eurocode as the only prescribed design code. Eurocode 7 is related to geotechnical engineering, but with little coverage of the rock engineering design. This chapter presents how reliability-based design (RBD) can provide insights which can help the evolution of the partial factor design approach for rock tunnelling problems.

5.1 Introduction

The factor of safety design approach had long been dominating the geotechnical engineering although it cannot reflect how safe a geotechnical structure really is. This approach attempts to ensure that the loadings on a structure do not exceed the allowable limit and is, in some textbooks, called the allowable stress design (ASD), e.g. Baecher and Christian (2003). The uncertainties associated with material properties and in situ conditions are considered implicitly by a single factor of safety. A better alternative to ASD is the limit state design (LSD) which is based on predictions about how the design performs near failure. For example, the Eurocode 7 (EC7) (EN1997-1, 2004) for the European countries and the load and resistance factor design (LRFD) (AASHTO, 2012) for the North America. Both codes use the characteristic values factored by partial factors to check the limit states. With the development of the probabilistic analysis, RBD has become popular recently due to the fact that it is robust and the uncertainties are treated explicitly. Most commonly used reliability analysis methods include the first-order second-moment method (FOSM), point estimate method (PEM), first-order reliability method (FORM), second-order reliability method (SORM) and Monte Carlo simulation (MCS).

The partial factor design has been successfully applied to various geotechnical problems. However, these design codes cover little about the rock engineering

principles and rock engineers struggle with the application of the partial factor design to rock engineering problems. All the specifications in such design codes are pertaining to and calibrated by soil engineering problems. Rock engineering principles seem to be neglected in EC7 as pointed out by Harrison (2014). This may be due to historical reasons that less emphasis has been placed on the rock engineering during the preparation of the EC7 draft and due to the fact that the discontinuous, heterogeneous and anisotropic nature of the rock mass requires a great deal of empiricism be involved (Lamas et al., 2014). A committee on the evolution of EC7 has been formed to develop EC7 with regard to rock engineering design. On the other hand, Low and Phoon (2015) and Low (2017a) illustrated that RBD can play a complementary role to the partial factor design using some soil engineering problems. In this chapter, some tunnelling problems are used to show that RBD, more specifically FORM based design, is helpful in the evolution of EC7 for rock engineering. First, the difference between the partial factor design approach and the RBD is illustrated by a circular tunnel in a Mohr-Coulomb ground. Then, different reliability analysis approaches (FOSM, PEM, FORM and SORM) are compared using a symmetrical roof wedge problem. Next, three case studies are employed to show the insights from RBD compared with the partial factor design. Finally, how RBD can complement the partial factor design for tunnelling problems is summarized.

5.2 Eurocode 7 design and FORM-based design

5.2.1 Eurocode 7 design

For the partial factor design, the design should satisfy the following condition (EN1997-1, 2004):

$$\sum \frac{R_{C,i}}{\psi_{R,i}} \geq \sum \psi_{S,j} S_{C,j} \tag{5.1}$$

where ψ_R is the resistance factor; R_C is the characteristic value of the resistance; ψ_S is the load factor; S_C is the characteristic value of the load.

The characteristic value of the resistance and load should be selected, based on Clause 2.4.5.2(2)P in EC7, as ‘a cautious estimate of the value affecting the occurrence of the

limit state' and can be selected by the statistical method if the distribution of this parameter is known based on Clause 2.4.5.2(10). The characteristic value for the resistance is lower than its mean value and, for the load, the characteristic value is higher than the mean value.

All partial factors specified by EC7 are greater than one and therefore, through factoring, the resistance is diminished and the action amplified. Three sets of partial factors are specified for actions, material properties, and resistances. These three sets of partial factors are not applied simultaneously but there are three design approaches combining different sets of partial factors (Bond and Harris, 2008).

- Design approach 1 (DA1): (Combination 1) factoring actions only; (Combination 2) factoring materials only
- Design approach 2 (DA2): factoring actions and resistance but not materials
- Design approach 3 (DA3): factoring structural actions and materials (geotechnical actions from the soil are unfactored)

According to Eq.(5.1), the factored resistance (design value of resistance) is required to be greater than or equal to the factored load (design value of load).

5.2.2 FORM and intuitive dispersion ellipsoid perspective

Although elaborated in previous chapters, the FORM analysis is reiterated here focusing on the intuitive expanding ellipsoid perspective to reduce the conceptual barriers for the practitioners. The matrix formulation of the Hasofer-Lind reliability index (Hasofer and Lind, 1974) is

$$\beta = \min_{\mathbf{x}\in F} \sqrt{(\mathbf{x}-\boldsymbol{\mu})^T \mathbf{C}^{-1} (\mathbf{x}-\boldsymbol{\mu})} \tag{5.2}$$

where $\mathbf{x}$ is a vector of the input random variables; $\boldsymbol{\mu}$ is a vector of the mean values of $\mathbf{x}$; $\mathbf{C}$ is the covariance matrix; F represents the failure domain. The Hasofer-Lind reliability index was originally proposed for correlated normal random variables. For non-normal distributions, the formulation for FORM β is shown by (Low and Tang, 2004):

$$\beta = \min_{\mathbf{x}\in F} \sqrt{\left[\frac{x_i - \mu_i^N}{\sigma_i^N}\right]^T \mathbf{R}^{-1} \left[\frac{x_i - \mu_i^N}{\sigma_i^N}\right]} \tag{5.3}$$

where **R** is the correlation matrix; μ_i^N and σ_i^N are the mean and standard deviation of the equivalent normal distribution of the random variable x_i and can be calculated through the transformation by Rackwitz and Fiessler (1978). The classical approach to calculate the FORM reliability index involves the rotation of the axes of the original random variables and an iterative scheme to approximate the design point. Low and Tang (2004) proposed an intuitive dispersion ellipsoid perspective for FORM analysis as shown in Fig. 5.1.

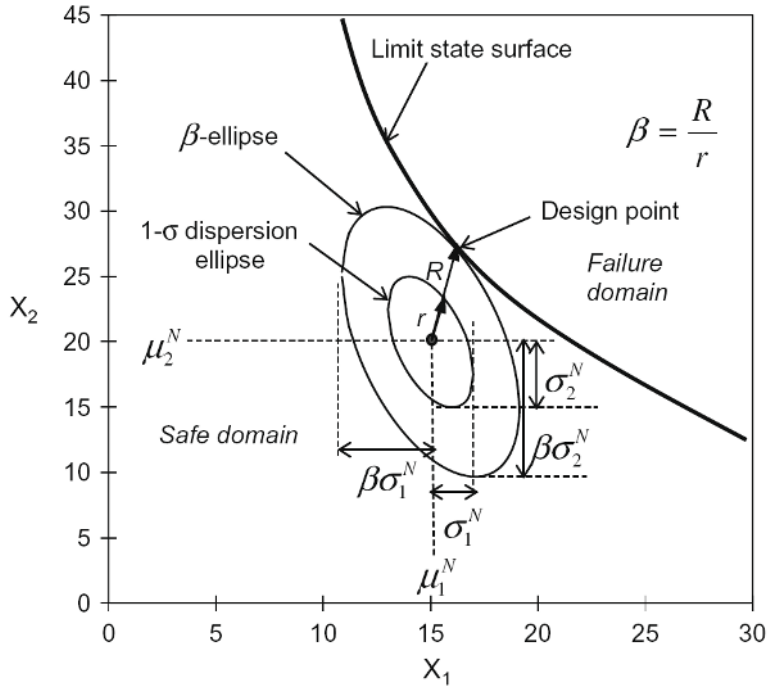

Fig. 5.1. Illustration of the intuitive expanding ellipsoid perspective (after Low and Tang, 2004)

The FORM analysis can be described as follows. An ellipse (for the two-random-variable case), tilted for correlated random variables or untilted for uncorrelated random variables, represents the contour line of the joint distribution of two random variables. Finding the design point is equivalent to expanding the ellipse until it touches the limit state surface (LSS) separating the safe domain from the unsafe domain. This tangent point is the design point which is the most probable combination of values of input

random variables on LSS. The reliability index β is calculated by *R/r*, where *R* is the directional distance from the mean value point to the β-ellipse and *r* is the distance to the 1σ-ellipse as shown in Fig. 5.1. To obtain the reliability index means maximizing the value of the multivariate normal probability density function and is graphically equivalent to finding the smallest ellipse tangent to LSS. This optimization procedure can be implemented in the ubiquitous Excel platform or other software such as MATLAB as shown in Chapter 3. An alternative to Eq. (5.3) is given in Low and Tang (2007) as

$$\beta = \min_{\mathbf{x} \in F} \sqrt{\mathbf{n}^T \mathbf{R}^{-1} \mathbf{n}} \tag{5.4}$$

where $\mathbf{n}$ represents the dimensionless vector of $(x_i - \mu_i^N)/\sigma_i^N$. The constrained optimization method by varying random variables in *n*-space (correlated standard normal space) is used to calculate the reliability index β and the probability of failure P_f can be estimated from

$$P_f \approx 1 - \Phi(\beta) \tag{5.5}$$

where $\Phi(.)$ is the cumulative distribution function (CDF) of the standard normal distribution. For more details of the Low and Tang (2007) procedure, readers may refer to Low (2008) and Low (2015). Next, the Duncan-Fama solution for a circular tunnel excavated in the Mohr-Coulomb elastic-perfectly-plastic ground is used to illustrate the RBD via FORM, the partial factor design based on EC7 and the difference between RBD and the partial factor design.

5.2.3 FORM analysis of a circular tunnel in Mohr-Coulomb material

The analytical solution of the plastic zone size and displacement of the tunnel can be found in Hoek (2007) and is presented in Chapter 3. Four input parameters, namely, friction angle ϕ, cohesion *c*, Young's modulus *E* and the hydrostatic in situ stress p_0 are treated as random variables while the radius of the tunnel is a deterministic value r_0=2.5 m, Poisson's ratio ν =0.3 and the dilation angle 0 for the rock mass in this case. Normal distributions with mean values denoted by *Mean* and standard deviations denoted by *StD* in Fig. 5.2 are assigned to the four parameters as suggested by Hoek (1998). The four input random variables are assumed to be independent first (scenario 1) with the

correlation matrix being the identity matrix. The uniform internal support pressure p_i is the target design parameter and the performance function denoted by *PerFunc* in Fig. 5.2 is

$$g(\mathbf{X}) = \varepsilon_{\text{limiting}} - \frac{u}{r_0} \tag{5.6}$$

where $\varepsilon_{\text{limiting}}$ is the maximum allowable ratio ($\varepsilon_{\text{limiting}}$= 2% in this case) of the tunnel convergence u over the radius r_0.

Deterministic input parameters

r_0 (m)	2.5
ν	0.3

PerFunc **FORM results**

PerFunc	β	P_f
0.000	3.000	0.13%

Probabilistic input parameters

Distribution	Parameter	Mean	StD
Normal	ϕ (°)	22.85	1.31
Normal	c (MPa)	0.23	0.068
Normal	E (MPa)	373	48
Normal	p_0 (MPa)	2.5	0.25

Scenario 1

x_i*	Correlation Matrix [**R**]				n_i*	**Design parameter**
21.59	1	0	0	0	-0.965	p_i (MPa)
0.129	0	1	0	0	-1.488	0.725
306	0	0	1	0	-1.393	**MCS results**
3.00	0	0	0	1	1.980	P_f=0.16%

Scenario 2

x_i*	Correlation Matrix [**R**]				n_i*	**Design parameter**
22.56	1	-0.5	0	0	-0.225	p_i (MPa)
0.162	-0.5	1	0	0	-1.002	0.683
293	0	0	1	0	-1.674	**MCS results**
3.03	0	0	0	1	2.123	P_f=0.15%

Fig. 5.2. FORM results for the circular tunnel in Mohr-Coulomb ground

An initial value ($0 < p_i < p_0$) for the support pressure p_i is selected and then the Solver in Excel is invoked to obtain the minimum value of β by varying the values in n_i^* column under the constraint that $g(\mathbf{X})$=0. Through trial and error, a support pressure yielding a target reliability index (β = 3.0 in this case) will be found as shown in Fig. 5.2. The values in the x_i^* column represent the design point which is the most probable point of failure on LSS separating the safe domain from the unsafe domain. The n_i^*

value for each random variable reflects the sensitivity of the input variables. For this case, the in situ stress is the most influential factor to the tunnel convergence. The sensitivity information is a by-product of FORM analysis and cannot be reflected by the EC7 approach using fixed partial factors.

The strength parameters c and ϕ are usually negatively correlated, meaning lower values of c tend to appear with higher values of ϕ, and vice versa. The correlation structure among input parameters can be readily incorporated into the FORM analysis and the results are shown as scenario 2 in Fig. 5.2 with the correlation coefficient between c and ϕ being -0.5. Because of the negative correlation between these two resistance factors, the chance of having both lower values for c and ϕ becomes smaller and therefore, the tunnel is safer. Thus, the required support pressure to achieve the same β of 3.0 is slightly smaller. The influence of c and ϕ on the tunnel convergence significantly decreases due to the negative correlation (refer to the n_i^* values for c and ϕ). MCS with 200,000 runs gives similar P_f as those estimated by FORM for both scenarios.

5.2.4 Tentative design based on Eurocode 7

As Harrison (2014) noted, it seemed that the development of EC7 had no explicit input from the rock engineering community and the application of EC7 to rock engineering problems is still under discussion and development. The general philosophy of EC7 for soil engineering will be tentatively applied to rock engineering problems and partial factors not covered in EC7 will be assumed and discussed in the light of the RBD approach.

Clause 2.4.8.(2) in EC7 (EN1997-1, 2004) states that "Values of partial factors for serviceability limit states (SLS) should normally be taken equal to 1.0", which is due to the fact that the ultimate limit states (ULS) are more critical than SLS in soil engineering such as the failure of a foundation or a retaining wall. However, for tunnelling problems, SLS is of great concern such as the tunnel convergence.

First, the partial factors are taken as 1.0 as suggested in EC7 and only the conservative characteristic values for the input parameters are considered. There are no specifications for choosing the characteristic values but the statistical methods may be

used, for example, the 5/95 percentile for resistance and load parameters. The design values are calculated by factoring the selected characteristic values. The value of the design parameter is chosen such that Eq. (5.1) has an equal sign. The results of the design based on EC7 design approach 1 (DA1) are shown in Table 5.1.

Table 5.1 Design of support pressure based on EC7 (5/95 Percentile)

EC7 DA1	5/95 Percentile	Partial Factor	Design value	Design parameter
tan ϕ	0.378	1.00	0.378	p_i (MPa)
c (MPa)	0.118	1.00	0.118	1.17
E (MPa)	294	1.00	294	
p_0 (MPa)	2.91	1.00	2.91	

The tanϕ instead of ϕ is factored in line with EC 7 specifications. Since the partial factors are ones, there is no difference between DA 1 combination 1 (factoring actions only) and combination 2 (factoring materials only). For this case, design values are fully dependent on the selection of the percentile values. For comparison, the reliability index from FORM is 5.169 for uncorrelated random variables. The results for the case if 30/70 percentile is selected are shown in Table 5.2.

Table 5.2 Design of support pressure based on EC7 (30/70 Percentile)

EC7 DA1	30/70 Percentile	Partial Factor	Design value	Design parameter
tan ϕ	0.408	1.00	0.408	p_i (MPa)
c (MPa)	0.194	1.00	0.194	0.76
E (MPa)	347.7	1.00	347.7	
p_0 (MPa)	2.63	1.00	2.63	

For the 30/70 percentile case, the reliability index from FORM is 3.194 which is different from 5.169 for the 5/95 percentile case. Comparison shows that the selection of the characteristic values will significantly influence the design parameter values (1.17 MPa vs 0.76 MPa). This is a potential drawback of EC7 since there is no specific guidance on characteristic values and designers may have different preferences for selecting these values.

Because the SLS is critical for most underground excavation problems, the statement that partial factors should be taken as ones is debatable in rock engineering. If the partial factors (not equal to one) are used, the design results are shown in Table 5.3. Note that

the partial factors are tentatively used with the same values given in EC7 for soils. For the evolution of EC7, those partial factors should be carefully calibrated for rock engineering problems.

Table 5.3 Design of support pressure (5/95 Percentile) considering partial factors

EC 7 DA1 C1	5/95 Percentile	Partial Factor	Design value	Design parameter
tan ϕ	0.378	1.00	0.378	p_i (MPa)
c (MPa)	0.118	1.00	0.118	1.92
E (MPa)	294	1.00	294	
p_0 (MPa)	2.91	1.35	3.93	

EC 7 DA1 C2	5/95 Percentile	Partial Factor	Design value	Design parameter
tan ϕ	0.378	1.25	0.302	p_i (MPa)
c (MPa)	0.118	1.25	0.094	1.35
E (MPa)	294	1.00	294	
p_0 (MPa)	2.91	1.00	2.91	

Since the partial factor for Young's modulus is not specified in EC7, in this case, 1.0 is used for illustrative purposes. For DA1 C1, the reliability index is 6.510 whereas for DA1 C2, the reliability index is 5.739. Comparison of Table 5.1 and Table 5.3 indicates that the design values for p_i are larger if the partial factors (not equal to one) are used. Besides, more support pressure is required for DA1 C1 than for DA1 C2 by virtue of the larger partial factor for the load p_0 and the fact that the displacement is more sensitive to the in situ stress than the strength parameters in this case.

5.2.5 Comparison between RBD and EC7

The same β value for different problems indicates the same safety level and therefore, the design based on the reliability index or probability of failure is consistent across various problems. In contrast, for the design based on EC7 or other partial factor design codes, different designers may select different characteristic values for the inputs and different sets of partial factors (DA1, 2 and 3) may be used. Thus, the design may result in inconsistent safety levels with different reliability indices.

As shown in Fig. 5.2, the correlation structure among the input random variables can be directly considered in RBD. However, the design remains the same by EC7 whether the correlation is involved or not.

The design point values (x_i* column) and the design point indices (n_i^* column) reflect the most probable point of failure together with the sensitivity automatically and vary from case to case in a way that fixed partial factors cannot. Even in the same design problem where different reliability levels are targeted, the influence of the input parameters will be different, which can be clearly indicated by RBD.

RBD is helpful for parameters that are not covered in EC7 (e.g. Young's modulus and in situ stress) or parameters specified in EC7 for soil engineering but not calibrated for rock engineering (e.g. cohesion and friction angle). Note that the back-calculated partial factors from RBD strongly depend on the chosen characteristic values and vary for different problems.

5.3 FOSM, PEM, FORM and SORM

There are various reliability analysis approaches including FOSM, PEM, FORM, SORM and MCS. Some methods are inconsistent and some may be computational time costly for practitioners. This section discusses advantages and drawbacks of different reliability methods and suggests which method is the most applicable to complement the partial factor design approach.

Unlike the FORM reliability index, FOSM assumes that the performance function is normally distributed such that the reliability index is the distance from the mean value to zero in units of the standard deviation, shown by

$$\beta_{FOSM} = \frac{\mu_g}{\sigma_g} \tag{5.7}$$

where μ_g and σ_g are the mean and the standard deviation of the performance function, respectively. The mean and standard deviation of the performance function can be estimated by (e.g. Haldar and Mahadevan, 2000; Baecher and Christian, 2003):

$$\mu_g \approx g(\mu_{X_1}, \mu_{X_2}, ..., \mu_{X_n}) \tag{5.8}$$

$$\sigma_g^2 \approx \sum_{i=1}^{n}\sum_{j=1}^{n}\rho_{X_iX_j}\sigma_{X_i}\sigma_{X_j}\frac{\partial g}{\partial x_i}\frac{\partial g}{\partial x_j} \tag{5.9}$$

where $g(x_1, x_2,...,x_n)$ is the performance function; x_i is the value of the *i*-th random variable; μ_{X_i} is the mean value for the *i*-th random variable; σ_{X_i} is the standard deviation of X_i; $\rho_{X_iX_j}$ is the correlation coefficient between two random variables. The mean of the performance function can be approximated by the performance function value calculated with the mean values of input random variables. The estimate of the standard deviation of the performance function can be implemented by the central difference method if the partial derivatives cannot be obtained analytically.

$$\frac{\partial g}{\partial x_i} \approx \frac{1}{2\varepsilon_i}\left[g(\mu_{X_1}, \mu_{X_2},..., \mu_{X_i}+\varepsilon_i,..., \mu_{X_n}) - g(\mu_{X_1}, \mu_{X_2},..., \mu_{X_i}-\varepsilon_i,..., \mu_{X_n})\right] \tag{5.10}$$

where ε_i is a small increment applied to the random variable. FOSM uses the means, standard deviations and correlation coefficients but overlooks the distributions of input random variables. Because the mean and standard deviation of the performance function depend on the formulation, different forms of performance functions would yield different FOSM reliability indices.

Another approach to estimate the mean and standard deviation of the performance function is the point estimate method (PEM) (Rosenblueth, 1975). PEM uses symmetrical sampling points around the mean value point to estimate the moments of the performance function. Fig. 5.3 shows the sampling points for the case with three random variables. If the number of random variables is *N*, the total number of sampling points in PEM is 2^N. *P* in Fig. 5.3 represents the weight for each sampling point. If all sampling points have the same distance from the mean value point and the random variables are uncorrelated, $P=1/2^N$. If the input random variables are correlated, the weight can be calculated by (e.g. Baecher and Christian, 2003):

$$P_{(s_1s_2..s_n)} = \frac{1}{2^n}\left[1+\sum_{i=1}^{n-1}\sum_{j=i+1}^{n}(s_i)(s_j)\rho_{ij}\right] \tag{5.11}$$

where s_i and s_j represent the indicator whether the value of the *i*-th or *j*-th variable is above (+1) or below (-1) the mean value; ρ_{ij} is the correlation coefficient between two random variables. PEM uses the same definition of the reliability index as Eq. (5.7).

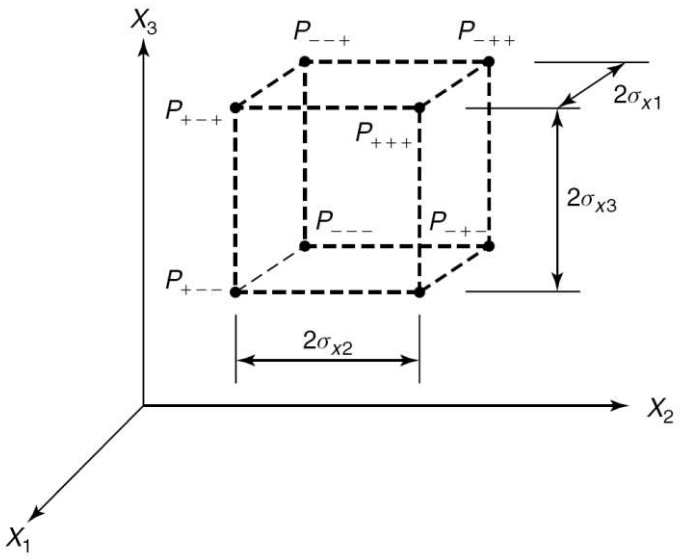

Fig. 5.3. Location of the sampling points in PEM for three random variables (after Baecher and Christian, 2003)

To illustrate the differences among these reliability methods, the stability of a symmetrical roof wedge above a circular tunnel is analyzed. The tunnel together with the roof wedge is shown in Fig. 5.4.

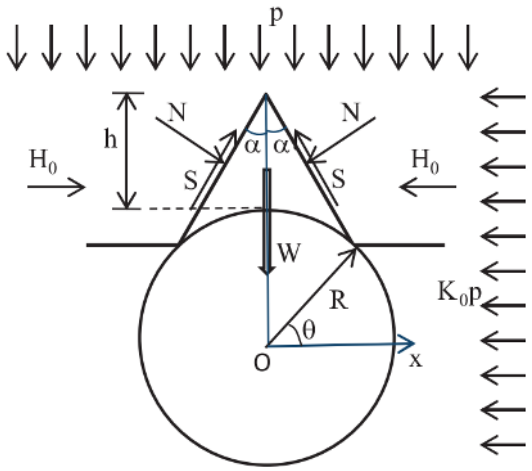

Fig. 5.4. Illustration of a symmetrical roof wedge above a circular tunnel (after Low and Einstein, 2013)

This problem was analyzed deterministically in Sofianos et al. (1999), Brady and Brown (2006) and extended to the probabilistic analysis by Low and Einstein (2013).

In Fig. 5.4, a circular tunnel with a radius R and a symmetrical roof wedge with central height h and apical angle 2α are subject to a vertical in situ stress p and a horizontal stress K_0p. The confining lateral force H_0 acting on the discontinuities can be calculated by the two-stage relaxation method presented in Brady and Brown (2006) as:

$$H_0 = \frac{1}{2} pR\left[(1+K_0)C_{H1} - (1-K_0)C_{H2}\right] \tag{5.12}$$

$$C_{H1} = \left(\frac{h}{R}+1\right) - \frac{1}{(h/R+1)},\ C_{H2} = \left(\frac{h}{R}+1\right) - \frac{1}{(h/R+1)^3} \tag{5.13}$$

and the weight of the roof wedge is

$$W = \gamma R^2\left[\cos^2\theta\left(\tan\theta + \cot\alpha\right) - \pi/2 + \theta\right] \tag{5.14}$$

$$\theta = \cos^{-1}\left[\left(\frac{h}{R}+1\right)\sin\alpha\right] + \alpha \tag{5.15}$$

where γ is the unit weight of the rock and θ is the angle from the horizontal direction to the point where the discontinuity cuts through into the tunnel as shown in Fig. 5.4. The normal (N) and shear (S) forces on the two discontinuities are

$$N = \frac{H_0(k_s\cos^2\alpha + k_n\sin^2\alpha)\cos\phi}{k_s\cos\alpha\cos\phi + k_n\sin\alpha\sin\phi} \tag{5.16}$$

$$S = \frac{H_0(k_s\cos^2\alpha + k_n\sin^2\alpha)\sin\phi}{k_s\cos\alpha\cos\phi + k_n\sin\alpha\sin\phi} \tag{5.17}$$

$$S = N\tan\phi \tag{5.18}$$

where ϕ is the friction angle of the discontinuity; k_n and k_s are the normal and shear stiffness of the discontinuity. It is obvious that the normal and shear forces are dependent on the ratio of k_n and k_s. Sofianos et al. (1999) defined the factor of safety as the ratio of pull-out resistance over the actual weight of the wedge. However, Asadollahi and Tonon (2010) used the factor of safety as the ratio of the upward resistant force over the downward driving force. These two definitions would result in significantly different factors of safety for the same case and this inconsistency can be reconciled by using the FORM analysis as explained by Low and Einstein (2013).

The performance function of this problem is shown by Eq. (5.19), which is the upward resistant force deducted by the downward driving force.

$$g_1(\mathbf{X}) = 2N\tan\phi\cos\alpha + T - 2N\sin\alpha - W \tag{5.19}$$

where T is the upward supporting force and is the design parameter. Apart from this definition, other mathematically equivalent formulations of the limit state (when the performance function is equal to zero) can be defined using the factor of safety as:

$$g_2(\mathbf{X}) = FS_1 - 1 = \frac{\text{Limiting wedge weight}}{\text{Actual wedge weight}} - 1 = \frac{2N\tan\phi\cos\alpha + T - 2N\sin\alpha}{W} - 1 \tag{5.20}$$

$$g_3(\mathbf{X}) = FS_2 - 1 = \frac{\text{Upward resisting force}}{\text{Downward driving force}} - 1 = \frac{2N\tan\phi\cos\alpha + T}{W + 2N\sin\alpha} - 1 \tag{5.21}$$

The first performance function is defined as the safety margin which is the difference between the resistance and the load. The other two performance functions use two different definitions of the factor of safety. For g1, the FOSM reliability index is calculated by Eq. (5.7) while, for g2 and g3, the FOSM reliability index can be calculated by

$$\beta_{FOSM} = \frac{\mu_{FS} - 1}{\sigma_{FS}} \tag{5.22}$$

where μ_{FS} and σ_{FS} are the mean and standard deviation of the factor of safety. Note that the following kinematic condition should be satisfied to form a symmetrical roof wedge:

$$\alpha \le \sin^{-1}\left(\frac{1}{1 + h/R}\right) \tag{5.23}$$

However, in the process of searching for the design point using the constrained optimization or MCS, a few points may not satisfy this condition. Under such circumstances, no wedge could be formed and the performance function should be set to positive values, indicating the wedge is stable. This is important since otherwise, a calculation error may occur.

Three parameters are treated as deterministic values: R = 6 m; h/R = 0.85; γ = 0.027 MN/m^3. The other parameters are normally distributed random variables with their mean values and standard deviations shown in Table 5.4. No correlation is included in the five random variables. These values follow those used by Low and Einstein (2013) for illustrative purposes.

Table 5.4 Characteristic values for the input random variables

Distribution	Parameter	Mean	STD
Normal	α (°)	25	2
Normal	ϕ (°)	35	3
Normal	k_s/k_n	0.1	0.025
Normal	p (MPa)	0.5	0.05
Normal	K_0	0.5	0.125

Through trial and error, a design value for the upward supporting force T is found to be 0.479 MN to achieve a target reliability index 3.0 by FORM analysis. If this design value is used and other reliability approaches (FOSM and PEM) are evaluated for different definitions of the performance function, the results are shown in Table 5.5.

Table 5.5 FOSM and PEM results for three definitions of the performance function

T=0.48 MN	FOSM g1	FOSM FS1	FOSM FS2	PEM g1	PEM FS1	PEM FS2
Mean	0.607	2.723	1.464	0.595	2.737	1.472
STD	0.236	0.777	0.185	0.240	0.799	0.184
β	2.571	2.216	2.511	2.480	2.173	2.566
P_f	0.51%	1.33%	0.60%	0.66%	1.49%	0.51%

It is clear that the reliability indices for both FOSM and PEM methods depend on the formulation of the performance function. The reliability indices are different even though the formulations of the limit state are mathematically equivalent, which means that β obtained from FOSM or PEM is not unique but depends on the formulation of the limit state function. For comparison, FORM yields the same reliability index no matter which formulation of the performance function is evaluated. FOSM and PEM gain popularity for geotechnical practitioners because of their simplicity in concept. For example, Orr and Breysse (2008) used the FOSM to design a foundation and compared with the EC7 design. For tunnelling problems, different researchers adopted PEM to conduct reliability analysis or reliability-based design (e.g. Park et al., 2012; Langford and Diederichs, 2013; Napa-García et al., 2017). However, from the case study shown above, FORM is superior to FOSM and PEM in terms of consistency for different formulations of the limit state function.

FORM estimates P_f based on the assumption that the limit state surface is linearized at the design point. More complicated methods that take into account of the curvatures of the limit state surface at the design point include SORM (Der Kiureghian et al., 1987). For geotechnical problems, the limit state surfaces are usually planar or with small curvatures, as shown by numerous FORM analyses (e.g. Li and Low, 2010; Low and Phoon, 2015). Moreover, the target reliability index for a design scenario is typically equal to or greater than 3.0 which corresponds to a P_f smaller than 0.13%. Even with a relative error of 30% for FORM compared with MCS or SORM, the true probability of failure is within 0.1% to 0.18%. The purpose of RBD is not to estimate the probability of failure as accurate as possible, but to ensure that the geotechnical structure is safe with a sufficiently small probability of failure (Low, 2017b). In this regard, FORM can be used in designs to indicate unacceptable high probabilities of failure. Besides, the expanding ellipsoid perspective with the constrained optimization method in the ubiquitous Excel platform makes it easy to implement for practitioners. Therefore, FORM is suggested to be used in geotechnical design problems as a complementary tool to the partial factor design approach.

Next, three case studies analyzed by FORM are discussed to show the insights from RBD compared with the partial factor design, including the same roof wedge problem as shown above, a lined circular tunnel with different lateral stress conditions and a circular tunnel reinforced by end-anchored rockbolts considering multiple failure modes.

5.4 A symmetrical roof wedge above a circular tunnel

The same case study shown in Fig. 5.4 is analyzed with two scenarios, first without the supporting force and then with a designed supporting force (T=0.479 MN) to achieve a target reliability index (β=3.0). The results are shown in Fig. 5.5, in which the column x_i* represents the vector of design point values in the original random variable space and n_i* represents the vector of design point values in the correlated standard normal random variable space.

Scenario 1 T =0 MN

Parameter	x_i*	n_i*	β	0.572
α (°)	25.59	0.295	$P_{f,\ FORM}$	28.4%
ϕ (°)	34.12	-0.294	$P_{f,\ SORM}$	33.7%
k_s/k_n	0.100	-0.001	$P_{f,\ MCS}$	33.6%
p (MPa)	0.495	-0.100		
K_0	0.453	-0.379		

Scenario 2 T =0.479 MN

Parameter	x_i*	n_i*	β	3.000
α (°)	29.04	2.019	$P_{f,\ FORM}$	0.13%
ϕ (°)	28.36	-2.213	$P_{f,\ SORM}$	0.14%
k_s/k_n	0.100	-0.001	$P_{f,\ MCS}$	0.14%
p (MPa)	0.502	0.049		
K_0	0.520	0.157		

Fig. 5.5. Reliability analysis results for the tunnel roof wedge problem

For the first scenario when the supporting force is zero, FORM yields a reliability index 0.572 corresponding to a P_f of 28.4%. From the n_i^* column, the most influential factor is the lateral stress coefficient K_0, followed by the apical angle α and friction angle ϕ. MCS with 100,000 realizations gives a P_f of 33.7%. There is an approximate 16% relative error for FORM, which arises because of the curvatures of the limit state surface at the design point. The accuracy of FORM can be improved by using the second-order reliability method (SORM) which is an extension of FORM. For this case, the fitting paraboloid method proposed by Der Kiureghian et al. (1987) and implemented in Excel platform (Chan and Low, 2012a) is used to improve the accuracy of the estimate of P_f (shown by the $P_{f,SORM}$ in Fig. 5.5) which agrees well with the MCS result.

For the second scenario, the supporting force (0.479 MN) is found through trial and error to achieve a target reliability index 3.0. The P_f estimated from FORM, SORM and MCS are close to each other. For the design scenario, the difference between FORM and SORM is insignificant. The most influential factor is α, followed by ϕ. The sensitivity of the random variable is different from the first scenario.

An interesting observation is that, for scenario 1, the design point values for p and K_0 are below their mean values, indicating that these two parameters are similar to "resistance factors", while, for scenario 2, the design point values are above the mean

values meaning that they are "load factors". This phenomenon can be explained as follows. For scenario 1, α is smaller than ϕ at the design point and the resultant force of N and S in the vertical direction is upward (see Eq. (5.16) and Eq. (5.17)). The larger the p and K_0, the greater the resultant upward resistance force. Therefore, these two parameters are "resistance factors". However, for scenario 2, $\alpha > \phi$ at the design point. The resultant force of N and S is downward. With the increase of p and K_0, the roof wedge becomes more unstable and thus these two parameters are "load factors". It is evident from the above discussions that the in situ stress may play opposite roles (resistance or action) depending on the roof geometry. RBD via FORM can detect and reflect the opposite effects of the input parameters under different circumstances automatically, which is a desired feature that prescribed partial factors do not possess.

5.5 A lined circular tunnel under different lateral stress conditions

The second case study is based on the closed-form solution proposed by Einstein and Schwartz (1979) for a lined circular tunnel in an elastic ground with anisotropic stresses. The purpose of the reliability analysis of this case is to investigate the effect of the lateral stress coefficient on the probability of failure and the insights from RBD compared with the partial factor design method.

A circular tunnel with a radius R is excavated in an elastic ground under a vertical stress p and lateral stress $K_0 p$ as shown in Fig. 5.6. The tunnel is lined with shotcrete and the interaction between the rock mass and the shotcrete is represented by σ_R (normal stress) and $\tau_{R\theta}$ (shear stress). The elastic ground and shotcrete are characterized by Young's modulus (E for the ground and E_s for the shotcrete) and Poisson's ratio (ν for the ground and ν_s for the shotcrete). The thickness of the shotcrete is t. The support is assumed to be installed immediately after excavation. The displacement of the tunnel wall is calculated by the following equations assuming that there is no slip between the rock mass and the shotcrete (Einstein and Schwartz, 1979).

$$\begin{aligned} u_s &= \frac{PR(1+\nu)}{E}\left\{\frac{1}{2}(1+K)A_1 + \frac{1}{2}(1-K)\left[4(1-\nu)A_2 - 2A_3\right]\cos 2\theta\right\} \\ v_s &= \frac{PR(1+\nu)}{E}\left\{-(1-K)\left[A_3 + (1-2\nu)A_2\right]\sin 2\theta\right\} \end{aligned} \tag{5.24}$$

$$
\begin{aligned}
A_1 &= \frac{B_1 B_2 (1-\nu)}{B_1 + B_2 + B_1 B_2 (1-\nu)} \\
A_2 &= \frac{B_1 (1-\nu)}{2\left[B_1 (1-\nu) + 4\nu - 6A_4 - 3A_4 B_1 (1-\nu)\right]} \\
A_3 &= A_2 A_4 \\
A_4 &= \frac{(6+B_2) B_1 (1-\nu) + 2B_2 \nu}{3B_2 + 3B_1 + 2B_1 B_2 (1-\nu)}
\end{aligned}
\tag{5.25}
$$

$$
\begin{aligned}
B_1 &= \frac{ER(1-\nu_S^2)}{E_s A_s (1-\nu^2)} \\
B_2 &= \frac{ER^3 (1-\nu_S^2)}{E_s I_s (1-\nu^2)}
\end{aligned}
\tag{5.26}
$$

$$
\begin{aligned}
A_s &= t \\
I_s &= \frac{t^3}{12}
\end{aligned}
\tag{5.27}
$$

where u_s and v_s are the radial and tangential displacements; θ is shown in Fig. 5.6; A_s is the average cross-sectional area of the shotcrete per unit length of the tunnel; I_s is the moment of inertia of the shotcrete per unit length of the tunnel; B_1 and B_2 are the compressibility and flexibility ratios respectively.

The input parameters for this case study are shown in Fig. 5.6. The parameters p, K_0 and E are treated as random variables since the properties of the support (E_s and v_s) show less variability than the in situ stress (p, K_0) and the properties of the rock mass (E). p, K_0 and E are assumed to be uncorrelated lognormal random variables.

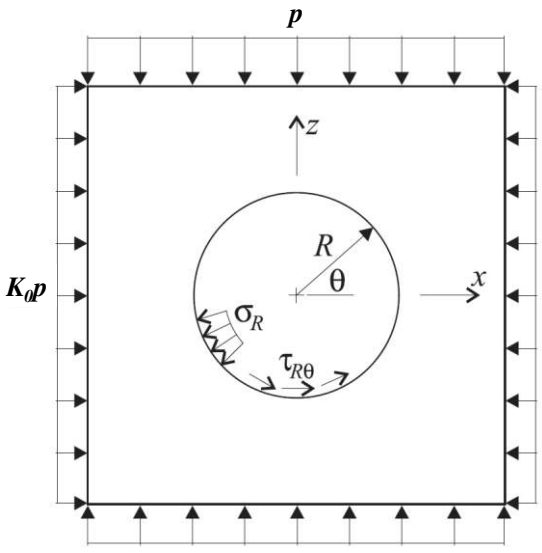

Deterministic input parameters:

R = 5 m
E_s = 25000 MPa
ν_s = 0.15
ν = 0.34

Probabilistic input random variables:

p (MPa) Lognormal μ = 0.6 σ = 0.06
K_0 Lognormal μ = 0.5 σ = 0.1
E (MPa) Lognormal μ = 48 σ = 4.8

Fig. 5.6. A lined circular tunnel in an elastic ground

The performance function is

$$g(x) = \varepsilon_{\text{limiting}} - \frac{u_{\max}}{R} \tag{5.28}$$

where $\varepsilon_{limiting}$ (1% in this case) is the maximum allowable ratio of the maximum tunnel wall convergence (u_{max}) over the tunnel radius R. The thickness of the shotcrete t is the design parameter and is found through trial and error to achieve a target reliability index 3.0. The FORM analysis results are shown in Fig. 5.7.

		Scenario 1					Scenario 2		
μ_K	0.5	Parameter	x_i*	n_i*	μ_K	1.5	Parameter	x_i*	n_i*
σ_K	0.1	p (MPa)	0.716	1.828	σ_K	0.3	p (MPa)	0.653	0.898
t (m)	0.3	K_0	0.343	-1.807	t (m)	0.66	K_0	2.586	2.850
P_f(MCS)	0.120%	E (MPa)	40.84	-1.569	P_f(MCS)	0.124%	E (MPa)	45.93	-0.391

Fig. 5.7. FORM analysis results for a lined circular tunnel

When the lateral stress coefficient K_0 is smaller than 1 (scenario 1), the maximum tunnel convergence occurs at the tunnel crown and if K increases towards 1, the downward displacement at the tunnel crown decreases. Therefore, the lateral stress coefficient is a resistance parameter for this case, as indicated by the negative value (-1.807) in the n* column in Fig. 5.7. However, if the mean value of K_0 is greater than 1.0, for example 1.5, and the COV is kept as 0.2, t is found to be 0.66 m to achieve a target reliability index 3.0. The FORM results are shown as scenario 2 in Fig. 5.7. MCS with 200,000 runs is conducted for both scenarios and P_f agrees with the target reliability index. When the lateral stress coefficient K_0 is greater than 1, the maximum tunnel convergence occurs at the tunnel sidewall and if K_0 increases, the horizontal displacement at the tunnel sidewall increases. Therefore, the lateral stress coefficient is a load parameter for this case, as indicated by the positive value (2.85) in the n* column. For this circular tunnel under anisotropic stress conditions, the role of the lateral stress coefficient (whether it is a resistant or loading parameter) in the tunnel convergence will change from case to case and cannot be reflected by the partial factor design approach.

The tunnel roof wedge problem shows that whether the vertical stress and the lateral stress coefficient are resistance or load factors is dependent on the relative magnitude of the friction angle of discontinuities and the apical angles. The lined circular tunnel problem shows that the role of the lateral stress coefficient for the same circular geometry will change for different stress coefficient values. From these two case studies, it is clear that the role of the vertical stress and the lateral stress coefficient should be determined on a case-by-case basis.

5.6 Reliability analysis of a circular tunnel reinforced by end-anchored rockbolts

The case study shown in Chapter 4 is used to illustrate the opposite roles of the same parameter for different limit states. Bobet and Einstein (2011) proposed an iterative closed-form formulation for a circular tunnel reinforced by end-anchored rockbolts in homogeneous and isotropic elastoplastic ground with the Coulomb failure criterion as shown in Fig. 5.8 in which σ_0 is the in situ stress, σ_i is the internal support pressure, r_0 is the tunnel radius, and S_θ is the circumferential distance between two adjacent rockbolts. This 2D formulation also considers the 3D supporting effect of the tunnel face by the stress reduction method using a reduction coefficient β_σ. It is assumed that the unreinforced opening prior to rockbolt installation is subjected to an internal support pressure $\beta_\sigma \sigma_0$, as shown in Fig. 5.9. U_{max} represents the final displacement of the tunnel section which is far away from the excavation face. D is the distance from the rockbolt installation position to the excavation face.

In this chapter, two limit states, including an ultimate and a serviceability limit state, will be of concern. The performance functions for the system are given as:

$$g_1(x) = T_{\text{limiting}} - T \tag{5.29}$$

$$g_2(x) = \varepsilon_{\text{limiting}} - \frac{u}{r_0} \tag{5.30}$$

where T_{limiting} (170 kN in this case) is the maximum allowable tensile force; T is the mobilized tensile force in the rockbolt; $\varepsilon_{limiting}$ (0.5% in this case) is the limiting ratio of u/r_0; u is the tunnel wall displacement. Note that the limiting ratio value used in this

case is different from the values used in Eq. (5.6) ($\varepsilon_{limiting}$ = 2%) and (5.28) ($\varepsilon_{limiting}$ =1%). Different values are selected to show that the limiting value is not a fixed value but should be carefully selected based on the requirement of different tunnels. If the tunnel has a stringent requirement on the convergence or the consequence of the tunnel failure is severe, smaller limiting values should be used. The insights provided by the reliability analysis are not dependent on the selection of the limiting values.

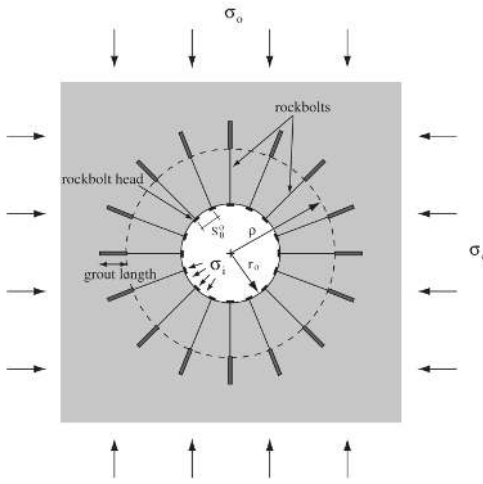

Geometry:
Tunnel radius: r_0= 3 m
Tunnel radius plus rockbolt length: ρ= 6 m
Rockbolt:
Rockbolt spacing in the axial direction: S_z= 1 m
Rockbolt spacing in the circumferential direction: S_0= 1 m
Diameter of rockbolts: d_b= 25 mm
Young's modulus of rockbolts: E_b= 210 GPa
Poisson's ratio of rockbolts: ν_b= 0.3
Rock mass properties:
Young's modulus of ground: E= 500 MPa
Poisson's ratio of ground: ν= 0.2
Peak and residual internal friction angles: $\phi_p = \phi_r$= 30°
Dilation angle: ψ= 0.5 ϕ_p
Peak and residual cohesion: $c_p = c_r$= 0.1 MPa
Stress conditions:
In situ stress: σ_0= 1 MPa
3D excavation effect parameter: β_σ= 0.3
Post-construction internal support pressure: σ_i= 0

Fig. 5.8. A circular tunnel with end-anchored rockbolts (after Bobet and Einstein, 2011)

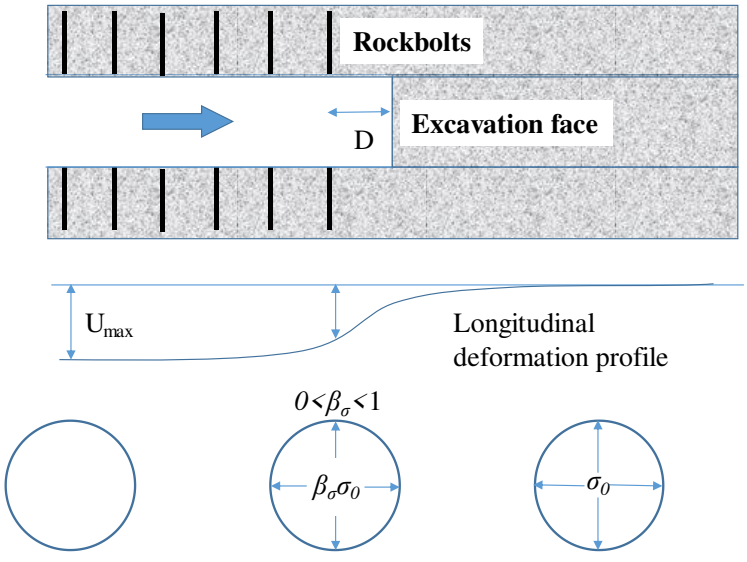

Fig. 5.9. Illustration of the stress reduction method using coefficient β_σ

These two performance functions consider the mobilized tensile force in the rockbolt and the maximum displacement, respectively. Other input parameters are the same as

those in Low and Einstein (2013) and are shown in Fig. 5.8. For probabilistic analysis, the random variables and corresponding probabilistic characteristics (means and standard deviations) are shown in Table 5.6. The friction angle and the cohesion of the rock mass are considered to be negatively correlated with a correlation coefficient -0.5.

Table 5.6 Statistics of random variables and FORM results for the circular tunnel reinforced by rockbolts

Distribution	Variables	Mean μ	StD σ	n* (g1)	x* (g1)	n* (g2)	x* (g2)
Lognormal	β_σ	0.3	0.05	0.502	0.32	-0.324	0.28
Lognormal	ϕ (°)	30	4	-0.898	26.39	-0.684	27.15
Lognormal	c (MPa)	0.1	0.01	0.197	0.101	0.193	0.101
Lognormal	E (MPa)	500	100	-0.649	431	-1.024	400

FORM is conducted for these two performance functions and the results are shown in Table 5.6. The reliability index for the first performance function (β_1) is 1.25 corresponding to a P_f of 10.54%, whereas the reliability index for the second performance function (β_2) is 1.29 with a P_f of 9.94%. MCS with 100,000 runs gives P_f of 8.87% and 10.23% for these two performance functions. Again, the design point values in the n-space (labelled n* in Table 5.6) reflect the sensitivity information of the input random variables. For the first performance function (g1), the design point value (labelled x*) for β_σ is greater than the mean value, meaning β_σ is a load factor. However, for g2, the design point value is smaller than the mean value, meaning β_σ is resistance factor. The influence of β_σ on the two performance functions can be explained by Fig. 5.9. β_σ represents the supporting effect from the tunnel excavation face and is related to the distance D from the excavation face to the rockbolt installation position. If the rockbolts are installed at closer locations from the face (smaller D), the effect of the excavation face is more significant (greater β_σ). Therefore, after equilibrium, more loads will be carried by the rockbolts, resulting in greater tensile forces in the rockbolt and smaller final displacements of the tunnel. Thus, increasing β_σ will decrease β_1 but increase β_2. This explains why β_σ plays opposite roles for the two performance functions.

Similar situations exist for other parameters, for example Young's modulus of the rockbolts (E_b). If stiffer steels (greater E_b) for the rockbolts are used, after equilibrium, the mobilized tensile force becomes larger and the final displacement smaller. E_b also exhibits opposite effects on different performance functions. This phenomenon may

appear for other geotechnical problems and it is difficult for the design code to specify that one parameter should be factored up for one performance function and factored down for the other performance function. RBD via FORM can determine the role of the input parameter automatically and on a case-by-case basis. In this regard, RBD can complement partial factor design codes for a better understanding of the effects of the input parameters. Furthermore, RBD through the system reliability analysis can investigate not only the individual limit state but also the interaction among all limit states (see Chapter 4).

5.7 Summary and conclusion

In this chapter, the differences between RBD via FORM and the partial factor design approach are presented first. Then, different reliability analysis methods including FOSM, PEM and FORM are compared using a roof wedge stability problem with three definitions of the limit state. Results show that FORM is consistent and, with the intuitive expanding ellipsoid perspective, it is easy to understand and implement for practitioners. Next, three different tunnelling problems including stress-controlled and structurally-controlled failure mechanisms are presented to show that RBD via FORM can play a complementary role to the partial factor design approach and help the evolution of EC7 for rock engineering problems.

To sum up, RBD via FORM can complement partial factor design approaches for rock engineering problems when

- rock parameters which are not covered in the design code are involved;
- the correlation and spatial correlation of the input parameters should be considered;
- the parameter sensitivities vary from case to case;
- the uncertainties of geometrical parameters are involved;
- the role of the same parameter as a resistance or load factor may change from case to case;
- the same parameter has opposite effects on different performance functions.

In rock engineering, the role of the input parameter whether it is resistance or load factor may be case-specific. For example, the in situ stress, seemingly a load parameter, may exhibit resistant behavior for different problems. The change of roles from case to case cannot be specified by the prescribed partial factors. Therefore, RBD via FORM can provide insights which may be overlooked by the partial factor design approach and, thus, can complement EC7 and help the evolution of EC7 for rock engineering.

In the above case studies, analytical solutions or iterative closed-form solutions are used so that readers can readily replicate these examples. In geotechnical practice, problems are complex and require numerical methods such as the finite element method or finite difference method. For this situation, RBD via FORM can still be applied with the help of surrogate models as a bridge connecting FORM and numerical software (see Chapter 3 and 4). Although RBD can play a complementary role to the partial factor design approach as shown by different case studies, it is not intended to suggest replacing the partial factor design approach with RBD. Practitioners are used to design a structure based on the specifications of design codes and may not be familiar with the concept in RBD. The sensitivities of the input parameters vary from case to case and the back-calculated partial factors from RBD are not fixed but may change significantly. Therefore, calibration of rock parameters using RBD may not be practical.

Previous chapters illustrate the reliability analysis and reliability-based design using closed-form or iterative closed-form solutions. Next, a real-life rock excavation project in Singapore is analyzed in Chapter 6.

Chapter 6 Case study: Jurong Rock Cavern (JRC) in Singapore

Previous chapters concern the reliability analysis method and reliability-based design. Closed-form or iterative closed-form solutions are used to illustrate the approach and simple case studies are used to show the insights from the reliability-based design compared with the partial factor design approach. This chapter focuses on how to characterize the statistical information of rock engineering properties from in situ and laboratory tests and how to conduct the reliability analysis of a complex problem without closed-form solutions, illustrated by a real-life underground rock excavation project.

6.1 Background

Jurong Rock Cavern (JRC) is Southeast Asian's first underground facility for oil products storage and is Singapore's first large-scale commercial underground project. It is located at about 130 m below the Banyan Basin on Jurong Island, a partially reclaimed island to the southwest of Singapore mainland (refer to Fig. 6.1).

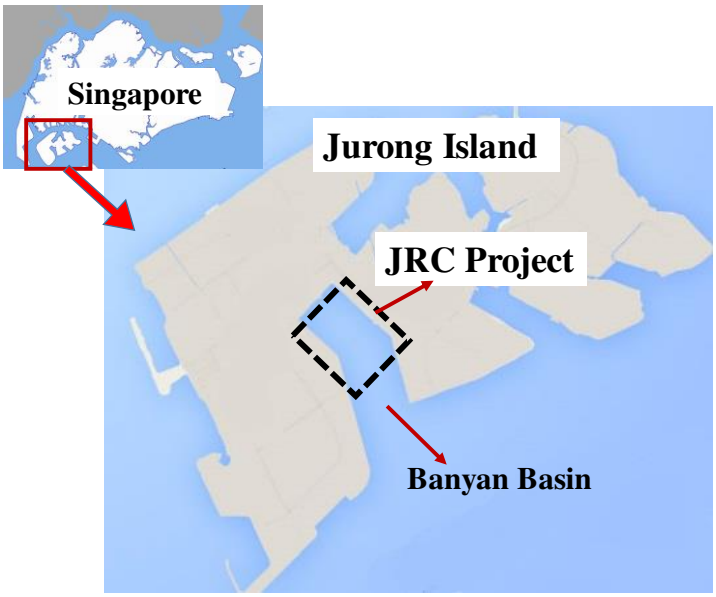

Fig. 6.1. Location of JRC project (after TriTech, 2007)

The ground-breaking ceremony of JRC was in February 2007 and the opening ceremony in September 2014. During this period, Phase 1 of JRC project was excavated with a total excavation volume about 3 million m^3 and a storage capacity of 1.5 million m^3. The 3D view of the JRC project is given in Fig. 6.2.

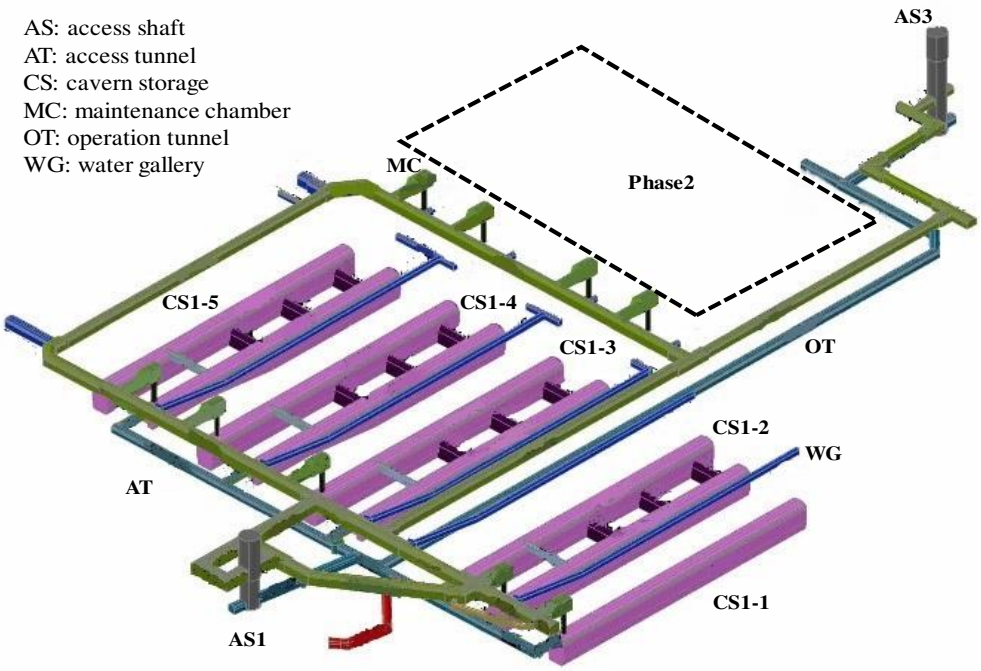

Fig. 6.2. Layout of the caverns (after JTC, 2010)

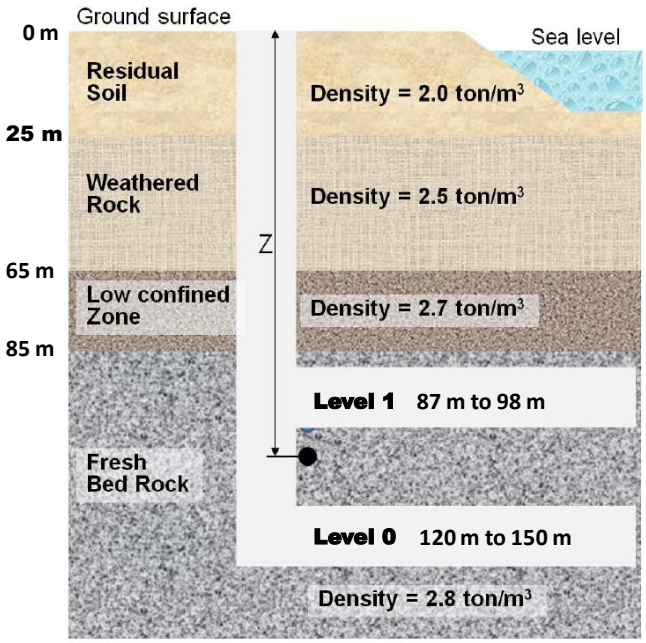

Fig. 6.3. Generalized vertical geological profile (after Kar Winn, 2016)

There are two vertical shafts (AS1 and AS3) connecting the underground facilities to the above-ground. Phase 1 of JRC consists of 9 storage caverns, each of which is 340 m long, and associated access tunnels and operation tunnels which are 8 km in length. The 9 caverns can be divided into one single cavern (CS1-1) and four twin caverns (CS1-2, CS1-3, CS1-4 and CS1-5). Phase 2 remains unexcavated and is used for future extension of Phase 1. The water gallery is located at level 1 and 9 caverns are located at level 0, as shown in Fig. 6.3. The 9 caverns have the same excavation geometry with a height of 27 m and a span of 20 m.

6.2 Preconstruction investigation

Before the construction started, extensive site investigations and laboratory tests had been conducted to investigate the underground conditions. The exploration work can be divided into three stages including the Soil Investigation (SI, 2001-2002), Geological and Rock Investigation (GRI, 2003-2004) and Complementary Site Investigation (CSI, 2006-2007). The first stage was not directly related to JRC project and the information collected is limited. Therefore, only the data from GRI and CSI is focused on and summarized in the next section. All the information regarding the preconstruction stage of JRC project is obtained from the reports listed below.

- TriTech (2004), Geological and Rock Investigation at Jurong Island. Factual results, Volumes I, II, III and IV. (Tritech, 2004)
- TriTech (2007), Final Report of Complementary Site Investigation at Banyan Basin, Jurong Island, Volumes I, II and III. (Tritech, 2007)
- Jurong Town Corp. (2007), Geotechnical Baseline Report. (JTC, 2007)
- Jurong Town Corp. (2008), Geotechnical Data Report. (JTC, 2008)
- Jurong Town Corp. (2010), Geotechnical Design Report. (JTC, 2010)

Nanyang Technological University (NTU) conducted research about JRC project from 2007 to 2012. Some more rock samples retrieved during excavation were tested by the NTU research team. The test results are included in the following research report. Some research test results were published by Li et al. (2012), Li and Wong (2013) and Wong et al. (2013).

- NTU (2013), Final report of the 2007-2012 Jurong Rock Cavern research. (NTU, 2013)

During the site investigation, boreholes were used to carry out in situ tests and the rock core samples from boreholes were used for laboratory tests. The investigation work is summarized in Table 6.1. During CSI, the geophysical survey using refraction seismic method was conducted to clarify the geological conditions under Banyan Basin. Physical properties, such as the temperature and electrical resistivity, were surveyed by the geophysical wireline logging. For all three stages of site investigations, 32 boreholes were drilled and used for different site investigation purposes. The locations of these boreholes and their relative positions with the JRC project are shown in Fig. 6.4. The straight lines associated with some of the inclined boreholes indicate the borehole direction.

Table 6.1 Summary of the site investigation

Investigation		Methodology	Purpose or outcome
In situ tests	Geophysical survey	Refraction seismic survey	Geological conditions under Banyan Basin
	Hydrogeological in situ test	Single and multiple well test	Hydraulic conductivity and transmissivity
	Geophysical wireline logging	Borehole televiewer (BHTV)	Orientation and spacing of discontinuities
	In situ stress test	Hydraulic fracturing method	In situ stresses
Lab tests	Thin section test		Rock type and mineralogy
	Rock test	Point Load Test, Uniaxial Compression Test, Triaxial Test, Brazilian Tensile Test	Engineering properties
	Compatibility test		Interaction among rock, water and the product

The rocks under the Banyan Basin belong to the Jurong Formation, sedimentary rocks widely distributed on the western part of Singapore. The sedimentary rocks extracted from exploring boreholes include mudstone, siltstone and sandstone. The differences among these three rock types lie in the grain size and colour. The grain size gradually

increases and the colour becomes lighter for the mudstone, siltstone and sandstone. These rocks always appear interbedded. The main rock type is the sandstone.

Igneous rocks are only found in dykes and sills, which are composed mainly of quartz and feldspar. As a result, localized contact metamorphism exists in the vicinities of the dykes. Another metamorphism is the regional metamorphism which hardens the sedimentary rocks. These metamorphisms make the sedimentary rock stronger and an ideal material for cavern construction.

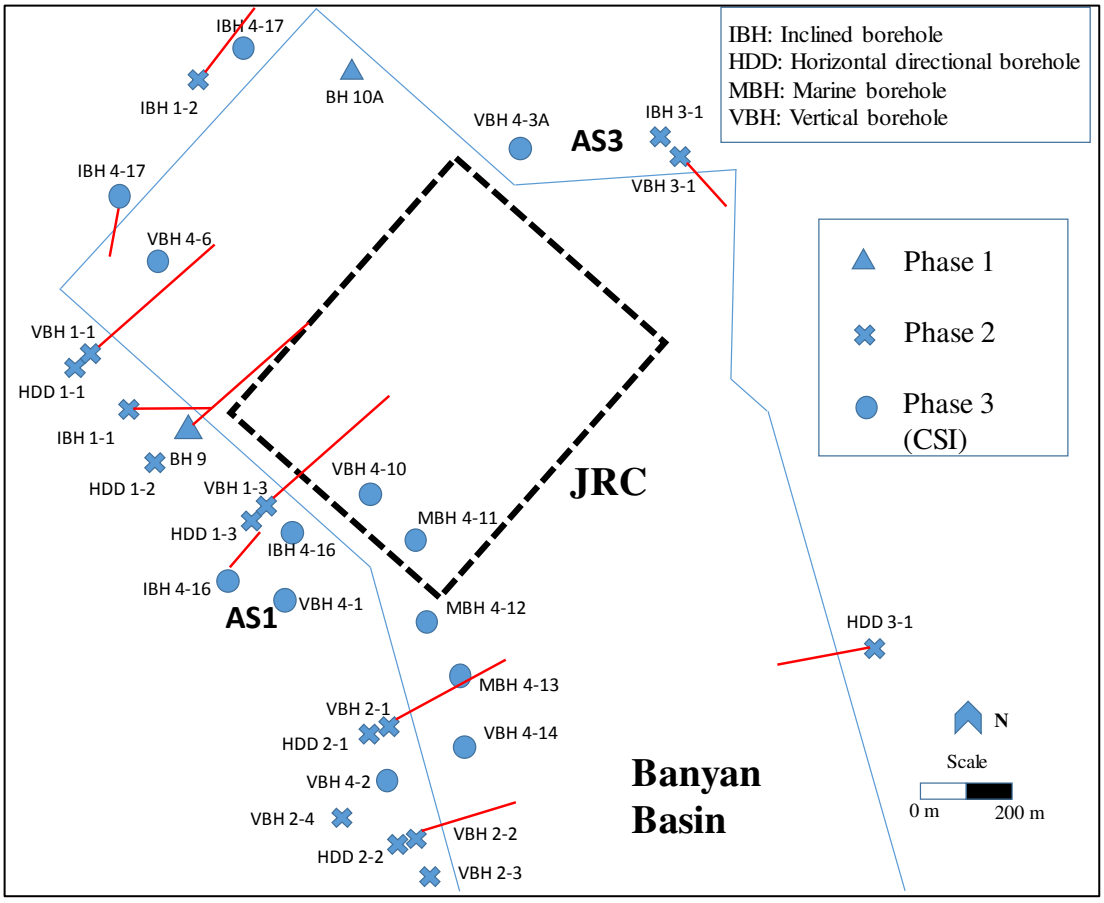

Fig. 6.4. Location of all boreholes (after JTC, 2010)

6.3 Deterministic and statistical characterization of engineering properties of the rock

Uniaxial compression test is an important laboratory experiment to determine the uniaxial compressive strength (UCS) as well as the elastic properties including the

Young's modulus for the intact rock. Therefore, a large number of UCS tests were conducted on the rock core samples retrieved from boreholes during the site investigation, including 103 tests for GRI 2004 and 49 tests for CSI 2007. In addition, during construction, 80 samples from the excavated rock in the operation tunnel were used by the NTU research team. The details of rock samples are listed in Table 6.2.

Table 6.2 List of boreholes and numbers of samples for UCS test

Site Investigation	Total Number of tests	Borehole	Number of tests	Depth range (m)
GRI 2004	103	VBH 1-1	10	53-99
		VBH 1-3	10	52-100
		VBH 2-1	10	86-135
		VBH 2-2	2	73-77
		VBH 2-3	5	31-94
		VBH 3-1	8	22-98
		HDD 1-1	10	92-398
		HDD 1-2	8	116-400
		HDD 1-3	9	99-398
		HDD 2-1	7	137-393
		HDD 2-2	3	132-186
		HDD 3-1	9	120-396
		IBH 1-1	3	41-93
		IBH 1-2	3	154-199
		IBH 3-1	6	99-197
CSI 2007	49	VBH 4-1	15	69-181
		VBH 4-2	11	93-194
		VBH 4-3	21	51-193
		MBH 4-12	1	29
		MBH 4-13	1	48
NTU 2013	80	Sandstone	56	100
		Conglomerated sandstone	4	100
		Conglomerate	12	100
		Limestone	8	100

The location of each borehole can refer to Fig. 6.4. Rock samples from 15 boreholes were used for the UCS test during GRI 2004. These boreholes were widely distributed around the Banyan Basin and intended to give a general description of the rock properties in this area. On the other hand, although only three boreholes were used during the CSI 2007, these boreholes were closer to JRC, especially VBH 4-1 and 4-3,

which are directly located at two vertical shafts. The depth of the retrieved rock cores (CSI 2007) was in accordance with the depth of JRC which was about 100-150 m below the ground. NTU research team conducted 80 tests for different types of rocks. These samples were retrieved from the blocky rocks from the excavation adjacent to AS3 on Level 1. The statistical characterization of UCS values is conducted and a summary of the results is shown in Table 6.3.

Table 6.3 Statistical information of UCS

Site Investigation	Statistical Information	Borehole	Mean (MPa)	STD (MPa)	COV
SI 2004	Mean=100.9 Min=14.9 Max=258.6 STD=58.6 COV=0.58	VBH 1-1*	71.03	37.12	0.52
		VBH 1-3*	122.23	70.81	0.58
		VBH 2-1*	86.15	38.96	0.45
		VBH 2-2	33.59		
		VBH 2-3	97.33		
		VBH 3-1	42.18	25.05	0.59
		HDD 1-1*	109.13	80.98	0.74
		HDD 1-2	101.52	44.40	0.44
		HDD 1-3	144.09	63.62	0.44
		HDD 2-1	145.27	48.43	0.33
		HDD 2-2	70.60		
		HDD 3-1	117.50	65.42	0.56
		IBH 1-1	92.59		
		IBH 1-2	131.53		
		IBH 3-1	91.37	40.29	0.44
CSI 2007	Mean=95.8 Min=27.2 Max=221.2 STD=41.3 COV=0.43	VBH 4-1*	82.20	35.95	0.44
		VBH 4-2*	104.02	40.39	0.39
		VBH 4-3*	103.85	45.25	0.44
		MBH 4-12	58.07		
		MBH 4-13	79.42		
NTU 2013	Mean=199.1 Min=86.2 Max=381.9 STD=65.8 COV=0.33	Sandstone*	209.92	68.60	0.33
		Conglomerated sandstone	192.93		
		Conglomerate*	191.55	58.03	0.30
		Limestone	137.59	27.11	0.20

*Note: * means more than ten rock cores were tested in this borehole*

The mean, standard deviation (STD) and coefficient of variation (COV) values for each borehole and for all samples from different site investigations are provided in Table 6.3.

Note that only a few boreholes labelled by * in the table have more than 10 samples retrieved and the average COV for these boreholes is 0.50. This value may help engineers have a general idea about the variation of UCS in one borehole. For other boreholes, the STD and COV values may be meaningless due to not enough data points. The STD and COV values for boreholes with less than 5 samples are ignored. The average UCS values (about 100 MPa) are similar for GRI 2004 and CSI 2007. The variation of the UCS values is significant since boreholes cover a large area and different depths. Various sedimentary rock samples, ranging from fresh to slightly weathered and from uniform to interbedded, were tested and the results are expected to display great variation. Compared with GRI 2004 and CSI 2007, the UCS values are greater and the variation is smaller for rock samples tested by the NTU research team. This may be caused by several reasons.

- Disturbance to the rock samples. For the site investigation, the rock cores were retrieved from long boreholes under high in situ stress conditions whereas, for NTU research, the rock samples were obtained from blocky rocks excavated during construction. The damage caused by the borehole drilling may yield the lower strength values.
- Selection of rock samples. The rock cores from boreholes were tested regardless of the weathering and interbedded conditions for the site investigation. However, the samples for NTU research were highly selective to represent different rock types such as the fresh homogeneous sandstone. Therefore, the variation of UCS values obtained for the site investigation is more significant.
- Carefulness and proficiency of the staff. Different groups of staffs might be assigned to conduct the UCS test during the site investigation and the proficiencies are different. NTU research team, however, conducted the test more cautiously and the entire procedure was well recorded.

A lognormal distribution is found to best describe the UCS data obtained from the site investigation and during construction as shown in Fig. 6.5 and Fig. 6.6.

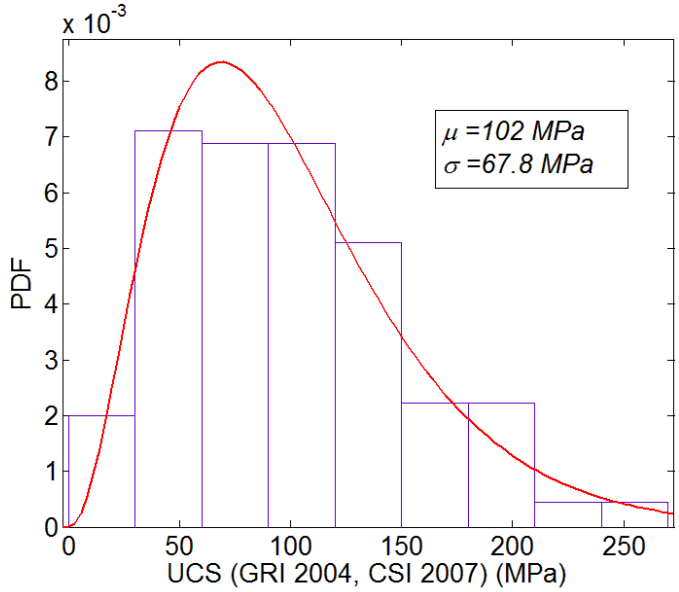

Fig. 6.5. Lognormal distribution fitted to the UCS data (Site Investigation 2004 and GRI 2007)

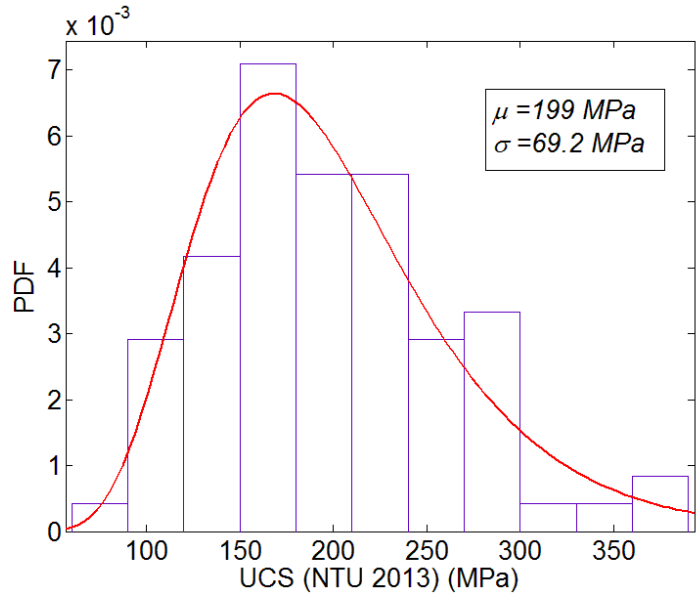

Fig. 6.6. Lognormal distribution fitted to the UCS data (NTU 2013)

Similarly, the mean, STD and COV of the Young's modulus E_i for the intact rock can be obtained and are shown in Table 6.4. For borehole MBH 4-12 and 4-13, the Young's modulus was not recorded in the report. The COV ranges from 0.14 to 0.78. For boreholes with more than ten tests, the average COV is around 0.4. Apart from the statistical information of E_i, the correlation coefficient between UCS and E_i can be calculated as shown in the last column in Table 6.4. If all the test values for UCS and E_i are calculated, the correlation coefficient is 0.53, as shown in Fig. 6.7.

Table 6.4 Statistical information of Young' modulus of the intact rock

Site Investigation	Statistical Information	Borehole	Mean (GPa)	STD (GPa)	COV	Correlation Coefficient
GRI 2004	Mean=49 Min=1.4 Max=138 STD=23.1 COV=0.47	VBH 1-1*	33.53	13.38	0.40	0.60
		VBH 1-3*	42.50	16.37	0.39	0.92
		VBH 2-1*	53.42	23.80	0.45	0.60
		VBH 2-2	22.55			1.00
		VBH 2-3	41.18			0.35
		VBH 3-1	39.23	30.53	0.78	0.45
		HDD 1-1*	42.78	22.12	0.52	0.70
		HDD 1-2	61.53	20.12	0.33	0.45
		HDD 1-3	66.79	30.88	0.46	0.60
		HDD 2-1	68.20	18.32	0.27	0.25
		HDD 2-2	31.81			0.95
		HDD 3-1	54.49	10.65	0.20	0.59
		IBH 1-1	30.21			0.99
		IBH 1-2	45.27			-0.59
		IBH 3-1	63.04	8.85	0.14	-0.54
CSI 2007	Mean=57.4 Min=26.6 Max=90 STD=16.6 COV=0.29	VBH 4-1*	63.97	17.61	0.28	0.57
		VBH 4-2*	53.77	18.41	0.34	0.58
		VBH 4-3*	54.54	14.22	0.26	0.61
		MBH 4-12				
		MBH 4-13				

*Note: * means more than ten rock cores were tested in this borehole*

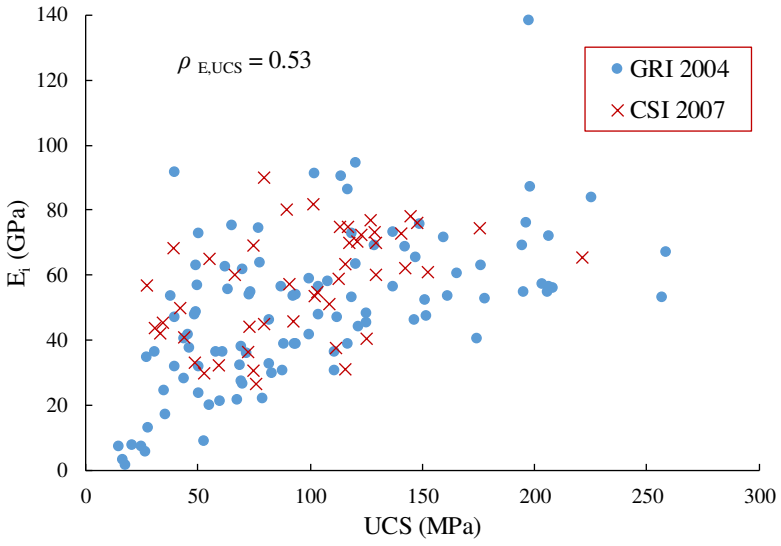

Fig. 6.7. Correlation between UCS and E_i

The positive correlation is expected since stiffer rock cores tend to have higher compressive strengths. Poisson' ratio ν can be obtained together with the Young's modulus in the UCS test. Because ν shows less variation and it has little effect on the tunnel displacement, it is regarded as a deterministic value with the mean value 0.25.

Apart from the uniaxial compression test in which UCS and E_i are obtained, other laboratory tests were conducted during site investigation and construction. The numbers of various tests are summarized in Table 6.5. For the triaxial tests, four to six rock core samples are compressed at different confining pressures. The strength parameters cohesion c and friction angle ϕ are determined based on the best-fit failure envelope. During the test, some samples failed along the existing discontinuities with unpredictable low strength values. These test results were abandoned. Therefore, although 109 triaxial tests were conducted for GRI 2004, only 16 (shown in the parenthesis in Table 6.5) pairs of c and ϕ values were obtained. For the triaxial compression test and the Brazilian tensile test, the NTU research group focused on the influence of the water on the sedimentary rock strength not on estimating the rock strength for JRC project. The rock core samples were dried or saturated before the test. This action rendered the rock cores different from the original ones. Therefore, the test results were not analyzed in this chapter.

Table 6.5 Numbers of different laboratory tests

	Uniaxial compression test	Triaxial compression test	Brazilian Tensile Test	Density
GRI 2004	103	109 (16)	102	105
CSI 2007	49	193 (39)	48	47
NTU 2013	80	70	88	-

The statistical information of c and ϕ from the triaxial test, the tensile strength σ_t from the Brazilian tensile test and the bulk density ρ_B from the density test is presented in Table 6.6. As expected, the bulk density shows less variation and typically is not modelled as a random variable. While the COV of the cohesion and tensile strength is around 0.4 to 0.5, the variation of the friction angle of the intact rock is less significant. For all the cohesion and friction angle values obtained, the correlation coefficient is -

0.37, as shown in Fig. 6.8. Similar to the soil properties, the cohesion and friction angle of intact rocks show a negative correlation.

Table 6.6 Statistical information for other engineering properties of intact rocks

		Cohesion c (MPa)	Friction angle ϕ (°)	Tensile strength (MPa)	Bulk density (g/cm^3)
GRI 2004	Mean	19.6	51.0	10.9	2.6
	Min	8.3	41.1	0.8	2.2
	Max	30.7	62.8	25.0	2.8
	STD	6.9	5.9	5.6	0.12
	COV	35.1%	11.6%	51.9%	4.6%
CSI 2007	Mean	27.8	48.2	11.8	2.7
	Min	6.6	32.8	1.9	2.5
	Max	54	62.0	24.2	2.8
	STD	12.5	7.3	5.0	0.05
	COV	44.8%	15.1%	42.2%	1.8%
Random variable	Distribution	Lognormal	Normal	Lognormal	
	Mean	25.6	49.0	11.5	
	STD	13.3	7.0	7.6	

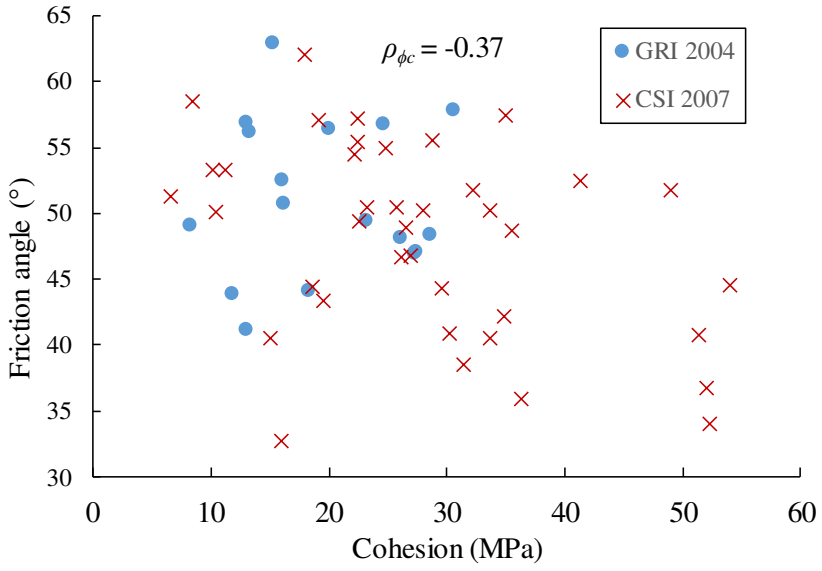

Fig. 6.8. Correlation between cohesion and friction angle

Aladejare and Wang (2017) summarized the variation range of the engineering properties for igneous, sedimentary and metamorphic rocks. Here, the ranges for the

sedimentary rocks (shown in Table 6.7) are used to compare the results from JRC project. The mean values of the properties for the JRC sandstone lie within the range of the mean values (third row in Table 6.7). The COV values for the JRC sandstone agree well with the mean COV from the global database, verifying that the COV values calculated for the JRC sandstone represent the typical variations of engineering properties of the sedimentary rock.

Table 6.7 Global database for sedimentary intact rocks

	Bulk density (g/cm^3)	UCS (MPa)	E_i (GPa)	Cohesion c (MPa)	Friction angle ϕ (°)	Tensile strength (MPa)
1. Mean value	2.7	62.8	23.7	21.23	41.71	7.9
2. Range of mean	1.73-3.00	4.4-264	0.6-73.2	2.6-31.8	24.9-58.3	1.2-17
3. Mean COV(%)	1.2	42.8	43	42.8	14.1	31.5
4. COV range(%)	0.4-13.0	0.4-109.6	7-128	15.7-79.0	3.9-30.6	1.6-59.3

In engineering practice, the rock mass classification systems, such as the RMR, Q and GSI, are of great importance since the support design is mainly based on the empirical charts for different systems as shown in Chapter 2. These systems require a value estimated based on the face mapping to indicate the quality of the rock mass. For example, one of the face mapping logged during the excavation of JRC is shown in Fig. 6.9 and the corresponding photo of the excavation face shown in Fig. 6.10. Altogether, more than 300 face mappings were conducted during the construction of CS1-1. Q and RMR values were estimated independently based on the mappings. The results are shown in Fig. 6.11. The correlation function is in agreement with those presented in Table 2.2 (Chapter 2). The RMR values can be described by a normal distribution with mean 69 and standard deviation 5.6. The Q values can be described by a lognormal distribution with mean 21 and standard deviation 14.

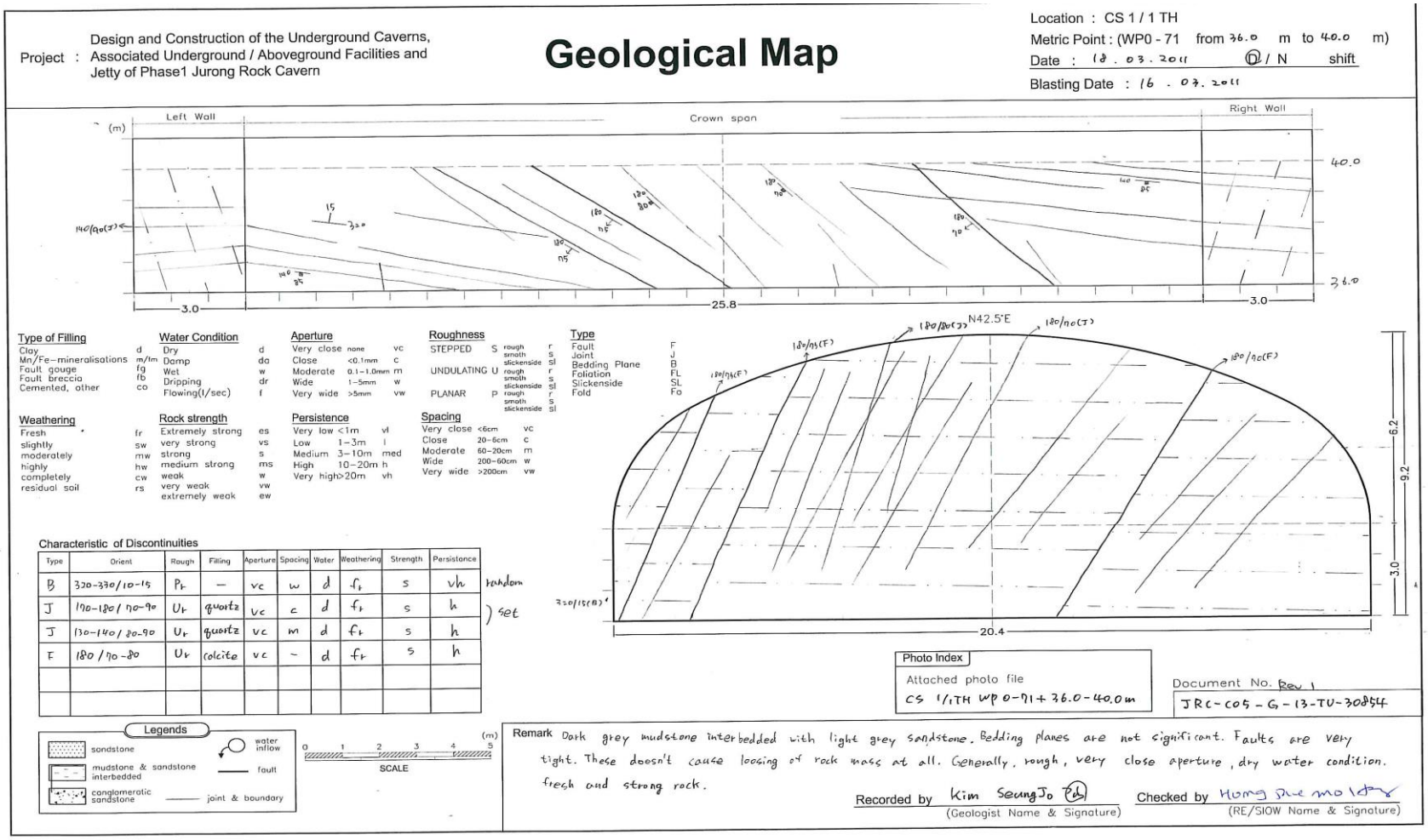

Fig. 6.9. An example of geological mapping of excavation face (after Kar Winn, 2016)

Fig. 6.10. Picture of the excavation face corresponding to the geological map (after Kar Winn, 2016)

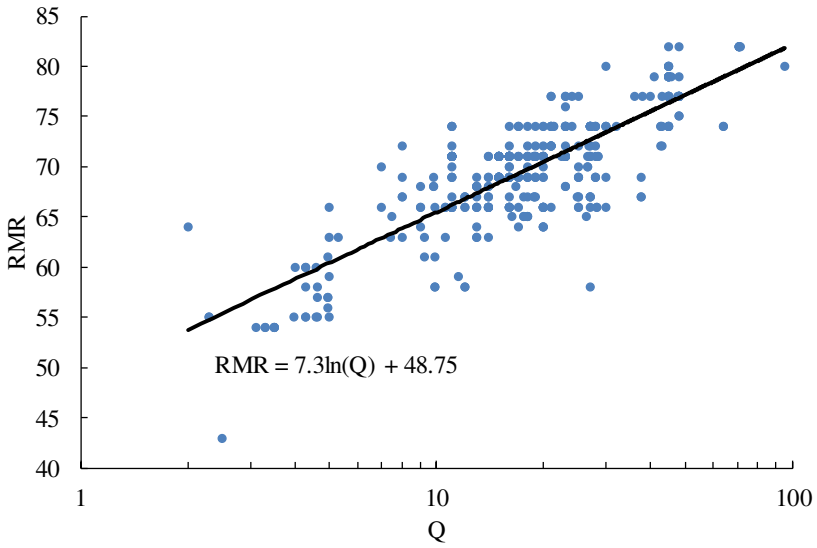

Fig. 6.11. Correlation between RMR and Q

The GSI values were not estimated during excavation but it is the most important parameter for the Hoek-Brown failure criterion which is widely used in the numerical simulation. Hoek and Brown (1997) used the following equation to convert RMR to GSI values for RMR>23

$$GSI = RMR - 5 \tag{6.1}$$

Based on this equation, GSI would have the same STD as RMR. The mean value of GSI would be 64. However, Kar Winn (2016) pointed out that GSI values should be lower than 64 based on the chart to estimate GSI. The chart is shown in Fig. 2.3 in Chapter 2. Based on the geological mapping, the rock mass is very blocky and the surface condition is fair to good. Therefore, the average value of GSI should be 40 to 60. In this chapter, the GSI is modelled as a normal random variable with a mean of 50 and a STD of 5.6 (same STD with RMR).

In the numerical simulation, rock mass properties instead of intact rock properties are required. Hoek and Brown proposed a nonlinear failure criterion (Hoek et al., 2002) for the rock mass together with a series of equations to estimate the rock mass properties.

$$\sigma_1 = \sigma_3 + \sigma_{ci}\left(m_b \frac{\sigma_3}{\sigma_{ci}} + s\right)^a \tag{6.2}$$

$$m_b = m_i \exp\left(\frac{GSI - 100}{28 - 14D}\right) \tag{6.3}$$

$$s = \exp\left(\frac{GSI - 100}{9 - 3D}\right) \tag{6.4}$$

$$a = \frac{1}{2} + \frac{1}{6}\left(e^{-GSI/15} - e^{-20/3}\right) \tag{6.5}$$

where σ_1 and σ_3 are the maximum and minimum principal stresses at failure; m_i is the Hoek-Brown material constant for the intact rock; m_b is a reduced value of m_i for the rock mass; s and a are constants for the rock mass; σ_{ci} is the UCS of the intact rock; D is factor depending on disturbance to the rock mass by blast damage and stress relaxation. It varies from 0 for undisturbed rock mass to 1 for very disturbed rock mass. For intact rocks, s =1 and a =0.5. Therefore, the Hoek-Brown failure criterion for intact rocks becomes

$$\sigma_1 = \sigma_3 + \sigma_{ci}\left(m_i \frac{\sigma_3}{\sigma_{ci}} + 1\right)^{0.5} \tag{6.6}$$

$$(\sigma_1 - \sigma_3)^2 = (m_i \sigma_{ci})\sigma_3 + \sigma_{ci}^2 \tag{6.7}$$

Based on Eq. (6.7), the m_i values can be determined based on the triaxial test results. 50 values for m_i are calculated using the software RocData (www.rocscience.com). The mean value is 21 and STD is 13 with a COV of 0.6. Aladejare and Wang (2017) collected two groups of m_i data (6 test values) and gave a mean of 18.83 and COV of 0.23. Because the data collected from literature is limited, the COV is smaller compared to that calculated based on JRC triaxial test data. The m_i can be modelled by a lognormal distribution with mean 21 and STD 14.

The deformation modulus of the rock mass can be estimated with GSI, E_i (for intact rock) and D as (Hoek and Diederichs, 2006):

$$E_{rm} = E_i\left(0.02 + \frac{1 - D/2}{1 + \exp\left((60 + 15D - GSI)/11\right)}\right) \tag{6.8}$$

The disturbance factor D is regarded as 0 for the JRC project. With the statistical information calculated for GSI and E_i, the distribution of E_{rm} can be readily determined by Monte Carlo simulation. The results are shown in Table 6.8.

Table 6.8 Statistical information for GSI, E_i and E_{rm}

	GSI	E_i (GPa)	E_{rm} (GPa)
Distribution	Normal	Normal	Lognormal
Mean	50	51.6	16.36
STD	5.6	21.5	8.8

In the in situ test report, there is no mention about the variation of the measured in situ stresses. Only the equation for estimating the in situ stress is provided. The vertical stress can be estimated by

$$\sigma_v(MPa) = 2.04 + 0.028\left(Z - 85\right) \tag{6.9}$$

where Z (m) is the depth below the ground. The lateral stress ratio is suggested to be $\sigma_H : \sigma_h : \sigma_v = 2.2 : 1.8 : 1$ at the depth of 100 m below the ground. σ_H and σ_h are the maximum and minimum horizontal stresses. The lateral stress ratio is in accordance with the typical value displayed by the world stress map for Southeast Asia, as shown in Kar Winn (2016).

6.4 Deterministic analysis of JRC project

FLAC^{3D} (www.itasca.com), which is a finite difference method software, is used to model the excavation of the cavern and to estimate the displacement. The 2D excavation geometry and the finite difference mesh are shown in Fig. 6.12. For the numerical simulation model, all four boundaries are roller boundaries preventing movement in the normal directions of the boundaries.

The top heading was excavated first from one end to the other, followed by bench 1 and bench 2 excavation. First, the support is not added in the 2D analysis. All the

input parameters follow the mean values, as shown in Table 6.9. K_0 is the lateral stress coefficient.

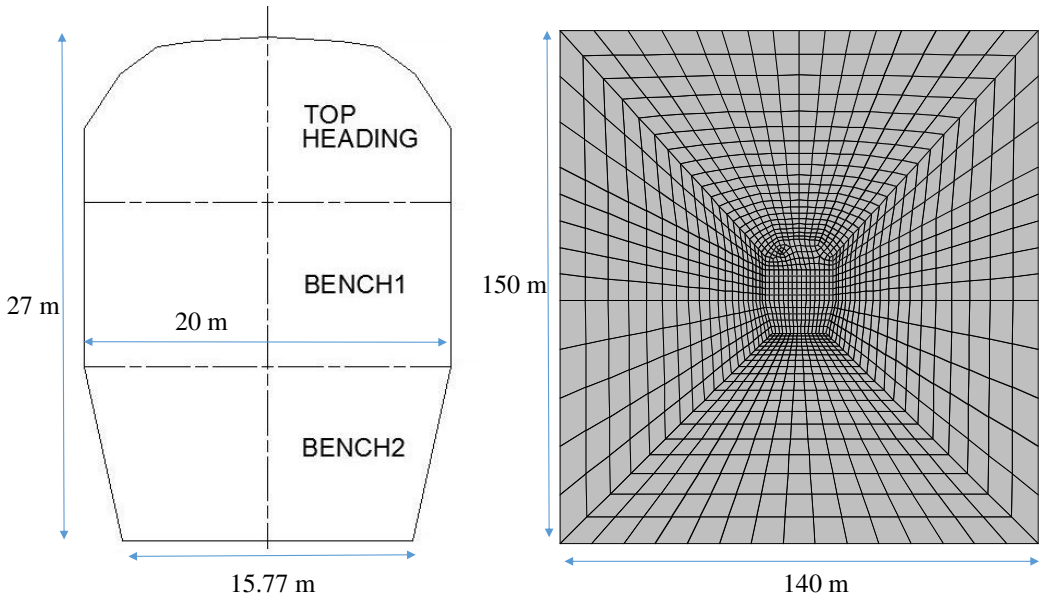

Fig. 6.12. Excavation geometry of the cavern and the finite difference mesh

Table 6.9 Input parameters for the deterministic 2D analysis

GSI	E_{rm} (GPa)	m_i	σ_c (MPa)	K_0	σ_v (MPa)	ν	ρ_B (g/cm^3)
50	16.36	21	102	2.2	3.3	0.25	2.8

After the excavation, the maximum vertical displacement is around 3 mm at the crown of the cavern while the maximum horizontal displacement is 11 mm at the sidewall. The displacement contours are shown in Fig. 6.13.

The most influential factor of the displacement is the deformation modulus of the rock mass, which is a function of GSI and E_i. The selection of GSI is subjective based on the Hoek's table. For this case, the mean value is selected to be 50. Others with the same face mapping may select 40 or 60. Furthermore, the empirical equation to estimate E_{rm} is not unique. For example, Hoek et al. (2002) used another equation

$$E_{rm}\ (GPa) = \left(1 - \frac{D}{2}\right) \cdot 10^{((GSI-10)/40)} \tag{6.10}$$

The E_{rm} values calculated with different GSI values and empirical equations are presented in Table 6.10. If GSI=40 and Hoek 2002 equation is used, the estimated E_{rm} is 5.6 GPa. The corresponding displacement at the crown is 8 mm and at the sidewall is 30 mm. Obviously, the estimate of E_{rm} has a significant influence on the cavern displacement.

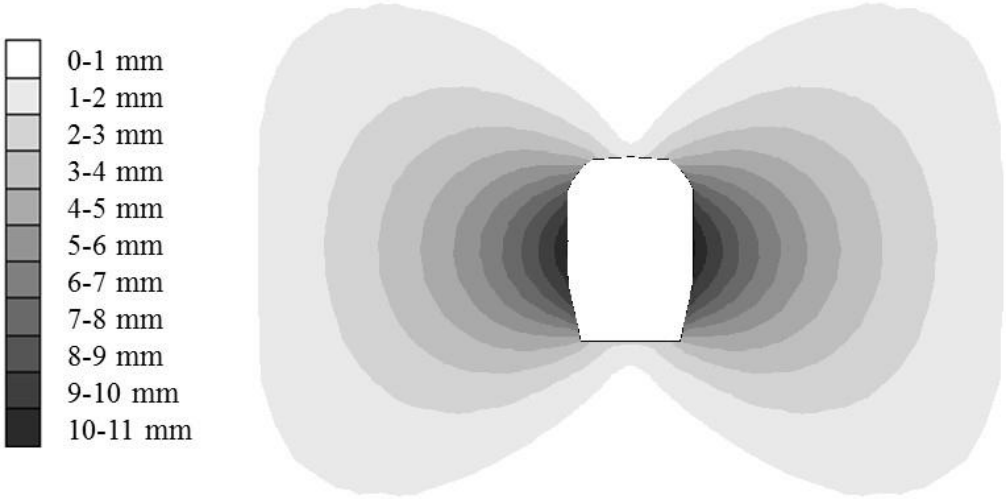

Fig. 6.13. Displacement contours for 2D deterministic analysis

Table 6.10 Different deformation modulus values of rock mass

GSI	Equation	E_i (GPa)	E_{rm} (GPa)
40	Hoek 2002	51.6	5.6
	Hoek 2006	51.6	8.2
50	Hoek 2002	51.6	10.0
	Hoek 2006	51.6	15.9
60	Hoek 2002	51.6	17.8
	Hoek 2006	51.6	26.8

For JRC, the shotcrete and the rockbolts were installed as the rock support. The support cannot be installed immediately after excavation. After mucking out of rock debris, the shotcrete was applied first, followed by the installation of rockbolts. The support was installed about 5 to 10 m behind the excavation face. In reality, the cavern

excavation is a three-dimensional problem. The delayed installation of support can be modelled in the simplified 2D analysis by the stress reduction method as mentioned in Chapter 4 and 5. In order to determine the displacement which has occurred before the installation of support, the longitudinal deformation profile (LDP) is required from the 3D analysis.

The 2D model shown in Fig. 6.12 is extended to 3D with a length of 200 m in the normal direction. The length is long enough to cover the range of the influence of the excavation face. The mean values shown in Table 6.9 are used. The LDP for the cavern crown after the excavation of the top heading is displayed in Fig. 6.14. The negative displacement value means the crown deforms downward.

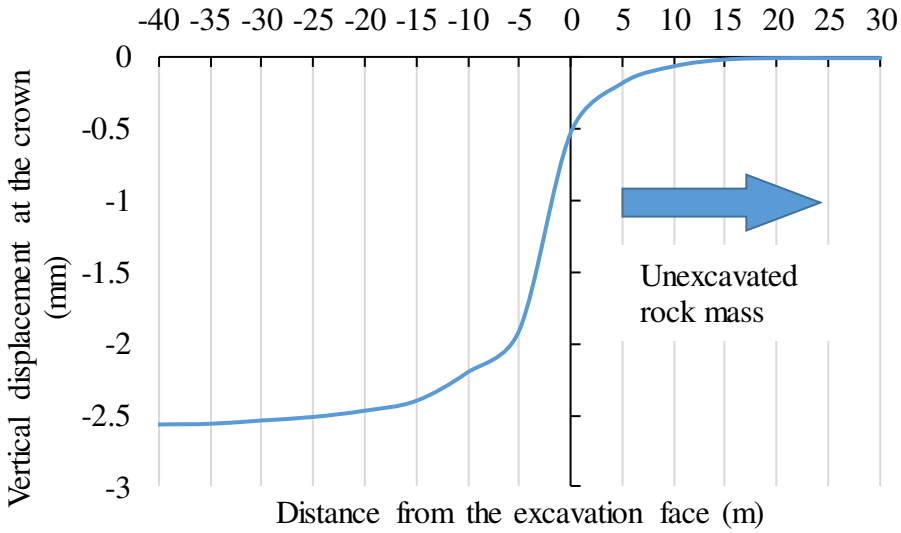

Fig. 6.14. Longitudinal deformation profile for the cavern crown

At 5 m and 10 m behind the tunnel face, the displacement is about 70% and 85% of the final displacement. This shows that the support will have limited effect on reducing the displacement compared with the case without support for the cavern roof. The influence of the excavation face covers from about 15 m ahead of the tunnel face to 30 m behind the face.

For the horizontal sidewall displacement, the LDP is shown in Fig. 6.15. The negative sidewall displacement means that the rock mass deforms towards the inside of the

cavern. Unlike the LDP for the crown which converges to zero displacement ahead of the tunnel, the LDP for the sidewall converges to about 1 mm displacement. This is because the sidewall of the unexcavated part has already moved due to the top heading excavation. At 5 m and 10 m behind the tunnel face, the displacement is 75% and 88% of the final displacement which is about 8 mm after bench 1 excavation. With the excavation of bench 2, the sidewall displacement will increase to 11 mm as shown in Fig. 6.13.

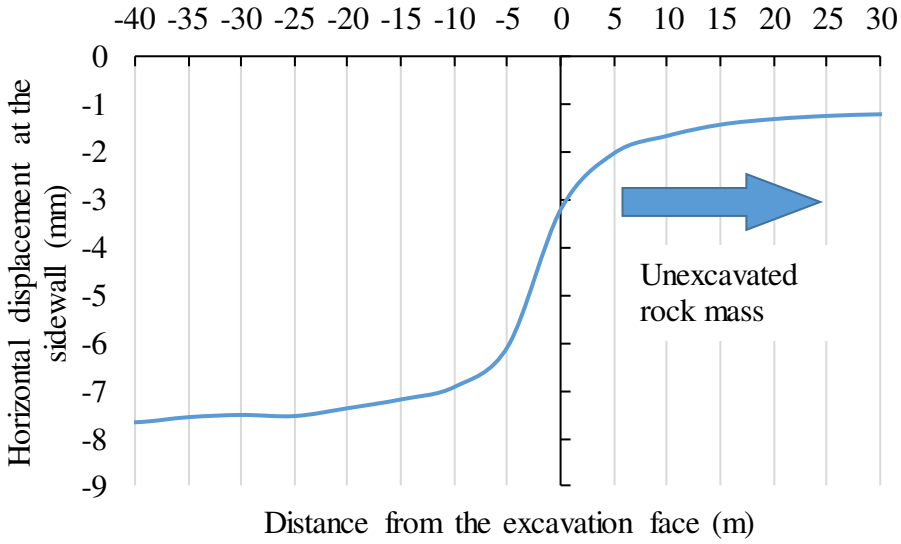

Fig. 6.15. Longitudinal deformation profile for the cavern sidewall

The stress reduction method used in the numerical simulation can be conducted in two steps. First, apply a support pressure to the excavation boundary and run the program until equilibrium. Second, remove the pressure, install the rock support and run the program until equilibrium. Based on the result from LDP, the stress reduction coefficient β_σ can be determined through trial and error to match the displacement before support installation. The input parameters for the rock support are shown in Table 6.11. The rockbolt is the fully grouted glass fibre reinforced polymer bolts. The first three parameters are the Young's modulus, Poisson's ratio and the thickness of the elastic shotcrete. The other parameters are for the rockbolts, including the length (L_{bolt}), in plane spacing (S_θ), out of plane spacing (S_z), Young's modulus (E_{bolt}), tensile strength ($T_{limiting}$), the circular grouting area and others. The support is only slightly

stiffer than the rock mass. The effect of the support on reducing the displacement is limited.

Table 6.11 Input parameters for the rockbolt and shotcrete

E_s (GPa)	v_s	t (m)	L_{bolt} (m)	S_θ (m)	S_z (m)
20	0.15	0.08	5	2.2	2.2
E_{bolt} (GPa)	$T_{limiting}$ (MN)	Area (mm^2)	Bond strength (MN/m)	Bond shear stiffness (MN/m/m)	
50	0.35	380	0.188	100	

The stress reduction method is implemented by using the built-in programming language in FLAC^{3D}, shown in Appendix D. For the top heading excavation, the stress reduction coefficient β_σ =0.2 is found to achieve a displacement of 2 mm while the final displacement is the same as that in Fig. 6.14, verifying that the support has limited effect on the roof displacement. For the sidewall displacement, the same value 0.2 for the stress reduction coefficient is found and the corresponding horizontal displacement is 6 mm.

With the reduction coefficient determined and the statistical information summarized, the reliability analysis of the cavern can be conducted, which will be shown in the probabilistic analysis section.

6.5 Monitoring displacement results

The above section discussed the displacement calculated from the numerical simulation. For an actual project, it is important to use the monitoring data to verify the simulation result and to calibrate the input parameters. However, for the JRC project, the monitoring data cannot be used for such purposes. In this section, the monitoring data is presented and the reason why the data cannot be used is explained.

After excavation, monitoring devices using glass prisms were installed at selected cross sections along each cavern to record the displacements of the cavern boundary. The total station was used to record the coordinates of the glass prisms. The readings for each glass prism from the total station represent the 3D coordinates of each monitoring point. When the prisms were first installed, the initial readings were

recorded as the original location. Later, the coordinates of each monitoring point were logged regularly. The difference between later readings of the coordinate and the initial reading is taken as the displacement for each point.

For each cavern, there is a benchmark point in the connection tunnel for calculating the global coordinates of the monitoring points. Although most total stations are capable of measuring distances longer than 1 kilometre, several temporary relay points were set in the cavern to connect the benchmark point to the monitoring points which are far away, due to the poor light conditions and the duct in the cavern.

There are three cross sections selected for the CS 1-1 cavern. At each cross section, 9 monitoring points, covering the roof arch and two sidewalls, distribute symmetrically as shown in Fig. 6.16. The positive displacement means the rock moves upward or to the right.

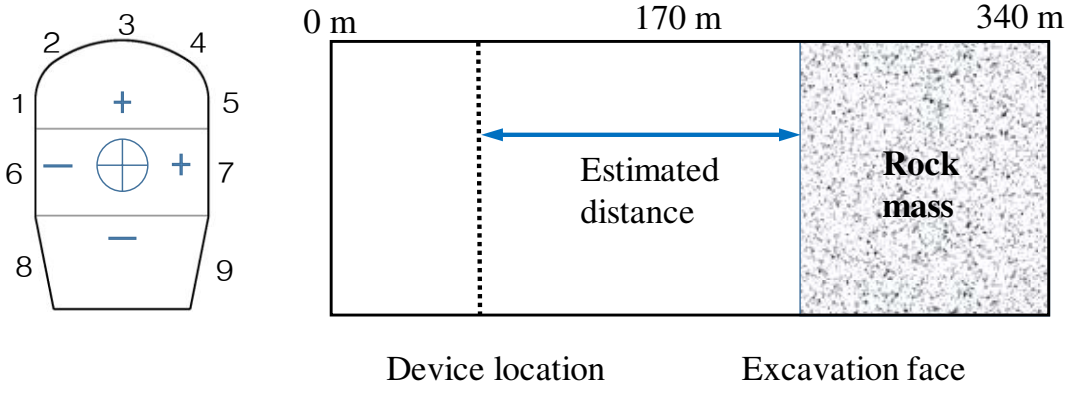

Fig. 6.16. Distribution of the monitoring points and the estimated distance from monitoring device to excavation face

The original data only contains the date when each monitoring device was installed and the recorded displacement with time. What is missing of the data is the distance from the device installation point to the excavation face. In order to estimate the distance indirectly, the time of installing the monitoring device and the excavation progress at this time should be known, as shown in Fig. 6.16. The former is available from the monitoring data and the latter can be acquired from the construction schedule. The estimated distances for CS 1-1 are shown in Table 6.12. First two

columns contain the information from the monitoring data (the location of each cross section and the date when the monitoring device was installed). The location of the excavation face in the third column is obtained based on the date shown in the second column together with the construction schedule. As a result, the distance from the excavation face to the monitoring device is the difference between the first and third column.

Table 6.12 Locations of monitoring device and the estimated distances

Monitoring device location (m)	Date of instrument installation	Excavation face location (m) on the date of starting monitoring	Distance from excavation face to monitoring location (m)
30	05-04-2011	70	40
60	23-04-2011	120	60
200	11-06-2011	240	40

As seen from Table 6.12, the monitoring device was installed far away from the excavation face. From LDP, the monitoring device installed more than 30 m away from the excavation face will record almost zero displacement. The roof displacements with time for the second cross section of CS 1-1 are shown in Fig. 6.17.

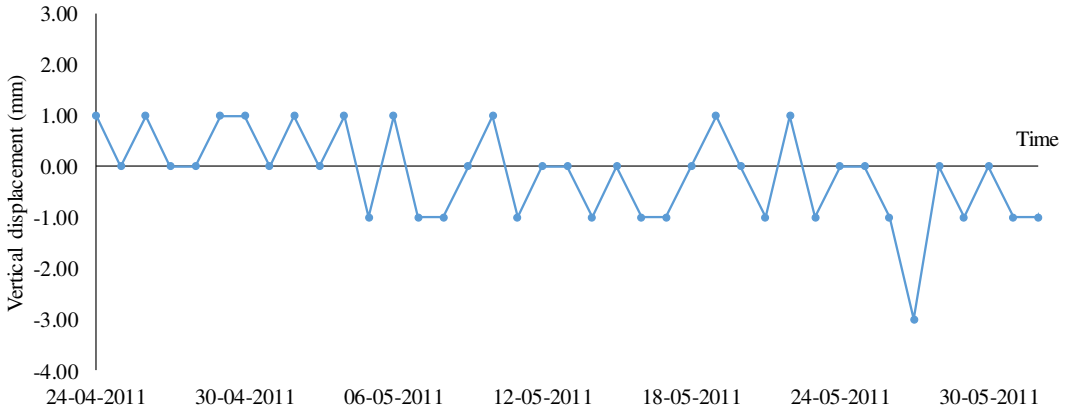

Fig. 6.17. Roof point 3 settlements with time (CS 1-1 60 m)

Most readings are within ±2mm but show an obvious undulating pattern. The same phenomenon exists for other monitoring data. The monitoring device is far away from the excavation face and cannot capture the immediate displacement due to excavation. That's why almost zero displacement is recorded. The up-and-down change of the monitoring displacement is odd and may attribute to the errors listed below.

- The measurement error caused by the total station can be expressed by

$$e_t = \pm(a\ mm + b\ ppm \times D) \tag{6.11}$$

  where a is the constant error; b is the proportional error with distance D; ppm means part per million. For example, if $e_t = \pm(2\ mm + 1\ ppm \times D)$ and $D < 1$ km, the error caused by the total station is within ±3 mm.
- The benchmark location in the connection tunnel and the relay points in the cavern are assumed to be fixed. However, the location may slightly move due to the excavation.
- The drill-and-blast may cause the relative movement and rotation of the glass prism with respect to the rock and thus may render the measurement erroneous.
- Human factors may also cause the error.

As shown above, the monitoring data for JRC cannot be used directly to compare with numerical analysis and to calibrate or back-calculate the input parameters. This does not impair the importance of the monitoring device in the safe construction. For an actual project like JRC, the monitoring device is only used to make in time warnings about unpleasant or unfavorable behavior that may cause serious consequences. This observation technique used during construction is a core principle of the New Austrian Tunnelling Method.

Apart from the observational technique using total stations and glass prisms, the instrument technique using borehole extensometers is also widely used in monitoring the tunnel displacement. The borehole extensometer is more accurate (resolution 0.01 mm) but with the limitation that the measuring range is smaller compared with the observational method. More detailed descriptions of the methods for monitoring

displacements can be found in Brady and Brown (2006). Recently developed technique for monitoring displacement is the fiber optic sensor which was used in a trial test in the operation tunnel of JRC by the NTU research team. The resolution for this technique is as high as 1 μ strain (NTU, 2013). The trial test result shows that the monitoring displacement by the fiber optic sensor is stable without the undulating behavior shown by the observational method.

6.6 Reliability analysis of JRC

The purpose of the reliability analysis of JRC is to show that FORM can be applied to problems without closed-form solutions via surrogate models. In this section, the second-order polynomial response surface method (RSM) with cross terms is used. The iterative procedure is similar to that presented in Fig. 4.10 for the system reliability analysis except that only one performance function is considered in this case for illustrative purposes. The reliability index is considered to reach convergence when the difference between two successive reliability indices is smaller than 0.01. The probabilistic input parameters are shown in Table 6.13, which are based on the calculation in previous sections. These random variables are assumed to be independent. A COV of 30% is assumed for the lateral stress coefficient for this case. Other deterministic input values are presented in previous sections such as the support properties and the stress reduction coefficient.

Table 6.13 Statistical inputs for the reliability analysis of JRC

Distribution	Parameter	Mean	STD
Normal	GSI	50	5.6
Lognormal	m_i	21	14
Lognormal	σ_{ci} (MPa)	102	67.8
Lognormal	E_{rm} (MPa)	16360	8800
Normal	K_0	2.2	0.66

The performance function concerns the maximum sidewall displacement, shown by

$$g(x) = \varepsilon_{\text{limiting}} - \frac{u_{\max}}{0.5S} \tag{6.12}$$

in which $\varepsilon_{limiting}$ is the maximum allowable ratio (0.5% in this case); u_{max} is the maximum sidewall displacement; S is the span of the cavern (S=20m).

The second-order polynomial response surface with cross terms uses the following expression to approximate the performance function.

$$\overline{g}(x) = a + \sum_{i=1}^{n} b_i x_i + \sum_{i=1}^{n} c_i x_i^2 + \sum_{1 \le i < j \le n} d_k x_i x_j \tag{6.13}$$

where a, b_i, c_i and d_k are the unknown coefficients; x_i and x_j are sampling values for the random variables; n is the number of random variables. In each iteration, $(n^2+3n+2)/2$ sampling points (21 points in this case) are needed. The sampling point values in the correlated standard normal random variable space (n-space) are used in accordance with the Low and Tang (2007) method. The iterative results are displayed in Table 6.14, in which k is the sampling factor controlling the sampling range. First, k=2 is used to cover a large random variable space. Then, k=1 is selected until convergence. The values shown are the design point values in the n-space. After convergence, the coefficients of the second-order polynomial RSM are shown in Table 6.15. Other surrogate models can also be used. However, for this case, the second-order polynomial RSM without cross terms cannot converge. The same situation was presented in Lü and Low (2011).

Table 6.14 Reliability analysis results for JRC

Iteration	k	β	GSI	m_i	σ_{ci} (MPa)	E_{rm} (MPa)	K_0
1	2	2.49	-0.077	-0.143	-0.267	-2.070	1.343
2	1	2.48	-0.040	-0.120	-0.137	-2.192	1.141
3	1	2.47	-0.022	-0.128	-0.141	-2.208	1.107

The results show that the rock mass Young's modulus is the most influential factor, followed by the lateral stress coefficient. This is in agreement with engineers' experience that Young' modulus has a significant effect on the displacement. GSI has negligible influence on the reliability index because the variation of GSI for this case is small.

Table 6.15 Coefficients for the second-order response surface with cross terms

a_1	b_1	b_2	b_3	b_4	b_5	c_1
0.016402	-0.00269	-0.00378	-0.00471	-0.01329	0.008714	-0.00033
c_2	c_3	c_4	c_5	d_1	d_2	d_3
-0.00053	-0.00099	-0.00658	-0.00044	-0.0009	-0.00119	-0.00039
d_4	d_5	d_6	d_7	d_8	d_9	d_{10}
0.001631	-0.00154	-0.00118	0.00209	-0.00133	0.002673	0.009156

Note that the reliability analysis presented in this section is to demonstrate the applicability of FORM via iterative RSM on a complex problem without closed-form solutions. The purpose is not to estimate the reliability index or probability of failure accurately. Clearly, the reliability of this problem depends on the selection of the limiting ratio. If a loose criterion is used, e.g. $\varepsilon_{limiting}$=2%, the reliability index will be much higher. For this case, all the data collected from the site investigation are used to estimate the variation of the properties. However, as shown in Fig. 6.4, the boreholes cover a much larger space than JRC. Therefore, the variation estimated may be greater than the variation of the rock mass surrounding the excavation. Moreover, there lacks a reliable way to estimate the Young's modulus of the rock mass, which is the most influential factor to the displacement. Selection of another empirical formula to estimate E_{rm} will result in different reliability indices.

6.7 Summary

In this Chapter, an actual underground rock excavation project is presented to show how the statistical information can be estimated from the site investigation. The mean values and the standard deviations of the rock properties for JRC are compared with the global database summarized by Aladejare and Wang (2017). The variations of properties agree well with the global database. Next, the deterministic analysis of one cavern is presented and it shows that the support has little effect on limiting the displacement because of the good rock quality and the late installation of the support. The stress reduction coefficient for the simplified 2D analysis is determined based on the longitudinal deformation profile obtained from the 3D analysis. Unfortunately, the monitored displacement data cannot be used to verify the deterministic analysis results and to calibrate the input parameters. Finally, the reliability analysis using

FORM and second-order polynomial response surface method with cross terms is conducted for the single cavern problem.

For JRC project, because a large number of in situ and laboratory tests were conducted, there is a sufficient number of data to characterize the variability of the rock properties. Therefore, the frequentist approach is used. However, this may not be the case for other geotechnical problems, for which the data is usually limited. Under such circumstances, the Bayesian approach can be used to integrate the prior knowledge and the observation data in a systematic manner. The Bayesian method has been proven to be useful in geotechnical characterization including the soil properties (Wang et al., 2010a; Wang and Cao, 2013; Cao and Wang, 2014; Wang et al., 2016b) and the rock properties (Wang and Aladejare, 2015; Wang and Aladejare, 2016a; Wang and Aladejare, 2016b).

This chapter mainly focuses on the uncertainty associated with the rock properties. It is shown that the selection of the Young's modulus of the rock mass has a significant effect on the displacement. However, there is no reliable method to choose a proper value for E_{rm}. The uncertainty associated with the process from a field parameter to a design parameter is called the transformation uncertainty (Ching et al., 2015). The uncertainties associated with the predictions from empirical correlations can be reduced as shown in Zhang et al. (2004). This transformation uncertainty, although beyond the scope of this thesis, can be a future research direction.

Chapter 7 Characterization of the spatial variability of intact rock properties using the Bayesian approach

7.1 Introduction

Rocks undergo complex geological processes such as sedimentation, metamorphism, weathering, and tectogenesis. The properties of the rock may vary from a location to another, which is called the spatial variability. The spatial variability is a major source of uncertainties associated with rock properties (e.g. Dasaka and Zhang, 2012; Zhu and Zhang, 2013; Aladejare and Wang, 2017). In previous chapters, reliability evaluations treated the rock properties as random variables, which may mask the spatial information. It is more realistic to model the rock property as a random field rather than a random variable to consider the spatial variability. The rock property at each point can be regarded as a random variable and these random variables in space form the random field. These random variables are not independent but correlated, which is referred to as the spatial correlation or autocorrelation (e.g. Baecher and Christian, 2003). The autocorrelation function describes how the autocorrelation coefficient of a geotechnical property varies with the separation distance between two points (e.g. Phoon et al., 2003). In geotechnical practice, more than one autocorrelation function is commonly used to characterize the autocorrelation structure of geotechnical properties. Li et al. (2015) showed that different autocorrelation structures of geotechnical properties may lead to different reliabilities of geotechnical structures. The most important input parameter for the autocorrelation function is the scale of fluctuation or autocorrelation distance, which provides an indication of the distance within which the properties show relatively strong autocorrelation (Phoon and Kulhawy, 1999). However, most of the existing studies conducted the reliability analysis based on assumed autocorrelation functions and scales of fluctuation of rock properties rather than values inferred from real data (e.g. Gravanis, 2014). As commented by Hsu and Nelson (2006), little work had been done on characterizing the spatial variability of rock properties. One of the possible reasons is that the extraction of rock samples is difficult and costly, resulting in

limited rock data (Aladejare and Wang, 2017). In Chapter 6, the rock data from JRC is collected and summarized. A large number of uniaxial compression tests were conducted and the data can be used to characterize the spatial variability of the uniaxial compressive strength (UCS) and elastic modulus (EM) of the intact sedimentary rock. In view of the limited studies on the spatial variability characterization of rock properties, this chapter evaluates the most probable autocorrelation structures and quantifies the scales of fluctuation for UCS and EM. A Bayesian model class selection approach is used to select the most suitable autocorrelation function because the approach is able to select the most plausible model with a high fitting capacity as well as robustness (Cao and Wang 2013; Wang and Aladejare, 2015). The scales of fluctuation for UCS and EM are subsequently quantified using a Bayesian updating method. The results provide a guideline on selecting reasonable autocorrelation functions and scales of fluctuation for UCS and EM of intact rocks.

7.2 Random field modelling of spatial variability for UCS and EM of intact rocks

The spatial variabilities of UCS and EM of rocks are modeled by random fields. Lognormal distributions are selected to describe the probabilistic distribution of the two parameters to avoid negative values. A lognormally distributed random field $Y(z)$ (z is the depth below ground surface) is used with the mean given by a linear trend function in Eq. (7.1) and a constant standard deviation, σ.

$$t(z) = az + b \tag{7.1}$$

where $t(z)$ is the mean trend; a and b are two regression coefficients. It can be easily deduced that the logarithm of $Y(z)$, $\ln(Y(z))$, is a normally distributed random field with the mean $\mu_N(z)$ and standard deviation $\sigma_N(z)$ given by Eq. (7.2) (e.g. Phoon et al., 2003).

$$\begin{cases} \mu_N(z) = \ln(t(z)) - 0.5\ln(1+(\dfrac{\sigma}{t(z)})^2) \\ \sigma_N(z) = \sqrt{\ln(1+(\dfrac{\sigma}{t(z)})^2)} \end{cases} \tag{7.2}$$

The autocorrelation structure of a random field is usually represented by an autocorrelation function. Five autocorrelation functions commonly used in geotechnical practice (see Eq. 7.3) are considered in this study, i.e. single exponential autocorrelation function (SEACF), Gaussian autocorrelation function (GACF), binary noise autocorrelation function (BNACF), second-order Markov autocorrelation function (SMACF) and cosine exponential autocorrelation function (CEACF) (Phoon et al. 2003). These five autocorrelation functions are represented by $M_1, M_2, \cdots,$ and M_5.

$$\text{SEACF } (M_1):\ \rho(\Delta z) = \exp(-\frac{2|\Delta z|}{\theta}) \tag{7.3a}$$

$$\text{GACF } (M_2):\ \rho(\Delta z) = \exp[-\pi(\frac{\Delta z}{\theta})^2] \tag{7.3b}$$

$$\text{BNACF } (M_3):\ \rho(\Delta z) = \begin{cases} 1-\dfrac{|\Delta z|}{\theta} & \text{for } |\Delta z| \le \theta \\ 0 & \text{otherwise} \end{cases} \tag{7.3c}$$

$$\text{SMACF } (M_4):\ \rho(\Delta z) = (1+4\frac{|\Delta z|}{\theta})\exp(-\frac{4|\Delta z|}{\theta}) \tag{7.3d}$$

$$\text{CEACF } (M_5):\ \rho(\Delta z) = \exp(-\frac{|\Delta z|}{\theta})\cos(\frac{\Delta z}{\theta}) \tag{7.3e}$$

where $\rho(\Delta z) = \rho(z_i - z_j)$ is the autocorrelation coefficient between two standard normal random variables $[\ln(Y(z_i)) - \lambda(z_i)]/\xi(z_i)$ and $[\ln(Y(z_j)) - \lambda(z_j)]/\xi(z_j)$; z_i and z_j are vertical coordinates of the two points associated with $Y(z_i)$ and $Y(z_j)$; θ is the scale of fluctuation (SoF) in the vertical direction. The autocorrelation coefficients for the five autocorrelation functions are plotted in Fig. 7.1.

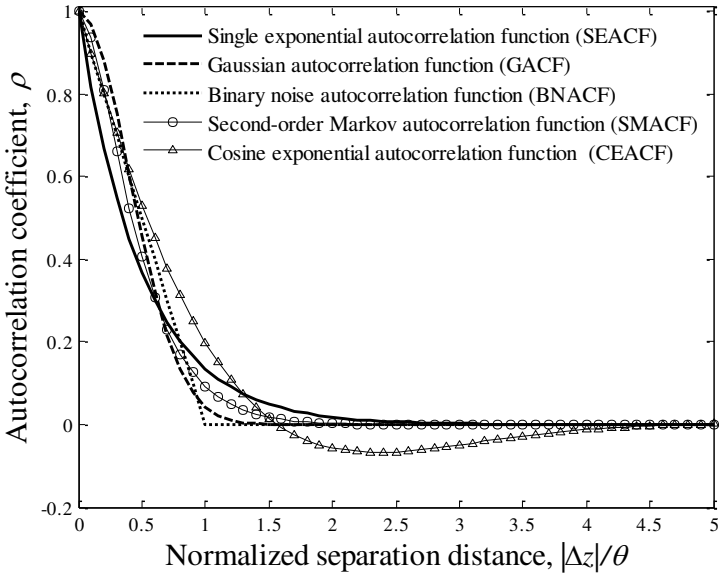

Fig. 7.1. Five autocorrelation functions commonly used in geotechnical practice

With Eq. (7.3), it is easy to evaluate the autocorrelation matrix, R^{M_i}, for a random vector $[\xi(z_1), \xi(z_2), \cdots, \xi(z_n)]$, where $\xi(z_k) = [\ln(Y(z_k)) - \lambda(z_k)]/\xi(z_k)$. The ($k$, l)-th entry of R^{M_i}, $R_{kl}^{M_i}$ represents the autocorrelation coefficient between $\xi(z_k)$ and $\xi(z_l)$ and for the autocorrelation model M_i. $R_{kl}^{M_i}$ is equal to $\rho(z_k - z_l)$ evaluated from the corresponding autocorrelation function in Eq. (7.3). Furthermore, the covariance matrix, C^{M_i}, for the random vector $[\ln(Y(z_1)), \ln(Y(z_2)), \cdots, \ln(Y(z_n))]$ can be obtained based on the relation between the covariance and correlation coefficient. The (k, l)-th entry of C^{M_i}, $C_{kl}^{M_i}$ represents the covariance between $\ln(Y(z_k))$ and $\ln(Y(z_l))$, and is given by Eq. (7.4).

$$C_{kl}^{M_i} = R_{kl}^{M_i} \sigma_N(z_k) \sigma_N(z_l) \tag{7.4}$$

where $\sigma_N(z_k)$ and $\sigma_N(z_l)$ are the standard deviations of $\ln(Y(z_k))$ and $\ln(Y(z_l))$ respectively, and are evaluated by Eq. (7.2).

Let $\hat{Y} = [\hat{Y}(z_1), \hat{Y}(z_2), \cdots, \hat{Y}(z_n)]^T$ be a set of observations of Y at depth $[z_1, z_2, \cdots, z_n]^T$. Based on the definition of multivariate normal distribution, the likelihood of the observations conditional on the random field parameters a, b, σ, θ, and autocorrelation function M_i is given by Eq. (7.5).

$$p(\hat{Y} \mid a, b, \sigma, \theta; M_i) = \frac{\exp[-\frac{1}{2}(\ln(\hat{Y}) - \mu_{N,n})^T (C^{M_i})^{-1} (\ln(\hat{Y}) - \mu_{N,n})]}{\sqrt{(2\pi)^n \mid C^{M_i} \mid}} \tag{7.5}$$

where $\mid C^{M_i} \mid$ is the determinant of C^{M_i}, and $\mu_{N,n}$ is the mean of the random vector $[\ln(Y(z_1)), \ln(Y(z_2)), \cdots, \ln(Y(z_n))]^T$, which is calculated Eq. (7.2).

7.3 Bayesian model class selection and Bayesian updating approach

7.3.1 Selection of the most plausible autocorrelation function using Bayesian model class selection method

Since more than one autocorrelation function could be used to represent the autocorrelation structure of UCS and EM, it is of interest to evaluate which function is the most suitable one. The Bayesian model class selection approach is a well-known model selection method which is capable of determining the optimal model with a high fitting capacity as well as robustness. The robustness means that the model has a low prediction error in the presence of model error and measurement noise. The approach is widely used to select models in geotechnical engineering (e.g. Cao and Wang, 2013; Wang and Aladejare, 2015). This Bayesian model selection approach is also used in this study to select the autocorrelation functions of UCS and EM.

In the framework of Bayesian model class selection, the plausibility of a given model is measured by the probability of the model conditioned on given data. For this case, there are N_{ACF} (N_{ACF} = 5 in this study) autocorrelation models, $M_1, M_2, \cdots, M_{N_{ACF}}$.

Based on the Bayesian theorem, the probability of each model conditional on the measured data $\hat{Y}$ is given by Eq. (7.6).

$$P(M_i \mid \hat{Y}) = \frac{P(\hat{Y} \mid M_i)P(M_i)}{P(\hat{Y})} \tag{7.6}$$

where $P(\hat{Y})$ is the probability of the occurrence of $\hat{Y}$ and it is a normalizing constant independent of M_i; $P(\hat{Y} \mid M_i)$ is the evidence for the model class M_i provided by the data $\hat{Y}$, which expresses the likelihood of the data if the model class M_i is used, and $P(M_i)$ is the prior plausibility of the model class M_i, which reflects the user's judgement on the initial plausibility of the model M_i. The sum of the prior plausibility should be equal to 1 (Yuen 2010). In the case where the users have no clear information of the prior plausibility, the $P(M_i)$ is commonly set to be $1/N_{ACF}$, i.e. the prior plausibility for various candidate models being equal. For this case, the plausibilities of the models are determined by the evidence. The model class with the maximum evidence is regarded as the most suitable model.

Evaluation of the evidence

Based on the law of total probability, the evidence for M_i provided by the data $\hat{Y}$ could be expressed by Eq. (7.7).

$$P(\hat{Y} \mid M_i) = \int_{\Theta_i} p(\hat{Y} \mid a,b,\sigma,\theta;M_i)\, p(a,b,\sigma,\theta \mid M_i) da db d\sigma d\theta \tag{7.7}$$

where Θ_i is the parameter space of the parameter vector $[a,b,\sigma,\theta]$, and $p(a,b,\sigma,\theta \mid M_i)$ is the prior probability density function (PDF) of the parameter vector $[a,b,\sigma,\theta]$. $p(a,b,\sigma,\theta \mid M_i)$ reflects the user's prior knowledge of the random field parameters in the absent of site-specific data. In this study, the four random field parameters, a,b,σ, and θ are assumed to be independent and uniformly distributed. The joint prior PDF of the random vector $[a,b,\sigma,\theta]$ is given by Eq. (7.8).

$$p(a,b,\sigma,\theta \mid M_i) = \frac{1}{(a_{\max} - a_{\min})(b_{\max} - b_{\min})(\sigma_{\max} - \sigma_{\min})(\theta_{\max} - \theta_{\min})} \quad (7.8)$$

The above equation is valid when a, b, σ and θ are within the bounds, i.e. $a \in [a_{\min}, a_{\max}], b \in [b_{\min}, b_{\max}], \sigma \in [\sigma_{\min}, \sigma_{\max}], \theta \in [\theta_{\min}, \theta_{\max}]$ and $p(a,b,\sigma,\theta \mid M_i) = 0$ if otherwise. $a_{\min}$, $b_{\min}$, $\sigma_{\min}$, and $\theta_{\min}$ are the minimum values of $a, b, \sigma,$ and θ respectively. $a_{\max}$, $b_{\max}$, $\sigma_{\max}$, and $\theta_{\max}$ are the maximum values of $a, b, \sigma,$ and θ respectively. The values for the lower and upper bounds of the four random field parameters could be determined based on the physical meaning of the parameters and users' experience. For example, the standard deviation and scale of fluctuation can only take positive values and their lower bounds could be set to small positive values such as 0.01. The evaluation of the evidence in Eq. (7.7) involves an integration of the product of the likelihood and prior PDF of random field parameters. When only a few random variables are involved, direct integration could be conducted through some numerical integration techniques. For cases with a number of random variables, direct numerical integration of the evident is computationally prohibitive and advanced techniques such as Markov Chain Monte Carlo simulation can be used (Wang and Cao 2013). In this study, the direct numerical integration method is used because only four parameters are involved. The range of each parameter is partitioned into a number of intervals and the evidence is the sum of the product of the integrand and the interval widths for each parameter as shown by Eq. (7.9).

$$P(\hat{Y} \mid M_i) \approx \sum_{j,k,l,m} p(\hat{Y} \mid a_j, b_k, \sigma_l, \theta_m) p(a_j, b_k, \sigma_l, \theta_m \mid M_i) \Delta a_j \Delta b_k \Delta \sigma_l \Delta \theta_m \quad (7.9)$$

where $p(\hat{Y} \mid a_j, b_k, \sigma_l, \theta_m)$ and $p(a_j, b_k, \sigma_l, \theta_m \mid M_i)$ are the values of the likelihood function and prior PDF for $[a_j, b_k, \sigma_l, \theta_m]$; $a_j, b_k, \sigma_l,$ and θ_m are the median values of the j-th interval of a, k-th interval of b, l-th interval of σ, and m-th interval of θ. $\Delta a_j, \Delta b_k, \Delta \sigma_l,$ and $\Delta \theta_m$ respectively are the width of j-th interval of a, k-th interval of b, l-th interval of σ, and m-th interval of θ. Note that a sufficient number of intervals is required for an accurate evaluation of the integration. The number of intervals could be determined by parametric studies, i.e. by gradually increasing the number of intervals until a steady integration result is obtained.

7.3.2 Evaluation of posterior statistics of the random field model parameters using Bayesian updating method

The Bayesian updating method is well known to be able to consider the prior knowledge of geotechnical parameters and is widely used in geotechnical engineering (Wang and Cao, 2013; Wang and Aladejare, 2016b). In this study, the posterior knowledge (posterior mean and posterior standard deviation) of the random field model for UCS and EM is also determined using the Bayesian updating method. For this method, the posterior statistics can be obtained by the approximate solutions. The approximation method enables a fast evaluation of the posterior knowledge of random field parameters and is used in this study. The basic idea of the method is to approximate the posterior PDF with a Gaussian PDF with a mean vector equal to the most probable value (MPV) of the posterior PDF, $[a^*, b^*, \sigma^*, \theta^*]$ and covariance given by the inverse of a Hessian matrix, $H(a^*, b^*, \sigma^*, \theta^*)$. The Hessian matrix is defined by the second-order derivation of an object function, $J(a,b,\sigma,\theta)$ (Yuen, 2010):

$$J(a,b,\sigma,\theta) = -\ln[p(\hat{Y} \mid a,b,\sigma,\theta;M_{opt})p(a,b,\sigma,\theta \mid M_{opt})] \tag{7.10}$$

where M_{opt} is the selected optimal model. The (i, j) component of the Hessian matrix is given by Eq. (7.11).

$$H_{ij} = \frac{\partial^2}{\partial\omega_i\partial\omega_j} J(\omega)\big|_{\omega=\omega^*} \tag{7.11}$$

where $\omega = [\omega_1, \omega_2, \omega_3, \omega_4] = [a, b, \sigma, \theta]$ and $\omega^* = [a^*, b^*, \sigma^*, \theta^*]$. The most probable random field parameters could be obtained using an optimization method, such as *fminsearch* function in the MATLAB platform while the Hessian matrix could be evaluated using a finite difference method. Details of the evaluation could be found in Wang et al. (2010a) and Yuen (2010).

7.4 Database of uniaxial compressive strength and elastic modulus for intact rocks

In this study, the UCS and EM data in Chapter 6 for JRC project is used to represent the sedimentary rock properties. Boreholes with more than ten tested rock cores (labelled in Table 6.3) are used to characterize the spatial variability. For comparison, some data for the igneous rocks are collected from the boreholes on the southeast of the Forsmark nuclear power plant, Sweden and the associated rock type is granite. The UCS and EM values from four boreholes are available in the laboratory test reports (downloaded from www.skb.com/publications/). Details of the UCS and EM data are plotted in Fig. 7.2 and Fig. 7.3.

The data in each set in Fig. 7.2 and Fig. 7.3 are from the same borehole and belong to the same rock type. As shown in Fig. 7.2 and Fig. 7.3, 11 sets of data are available for both UCS and EM and the number of data points in each data set ranges from 10 to 21. As noted in the introduction section, the rock data in practice are limited because of the high cost of core drilling. However, the Bayesian model class selection method is capable of dealing with limited data. As shown by Cao and Wang (2014), the Bayesian model class selection method could determine the right model even though the data are sparsely located. In the next section, it is shown that the most probable autocorrelation model selected by the Bayesian method is strikingly consistent for different rock types and data sets.

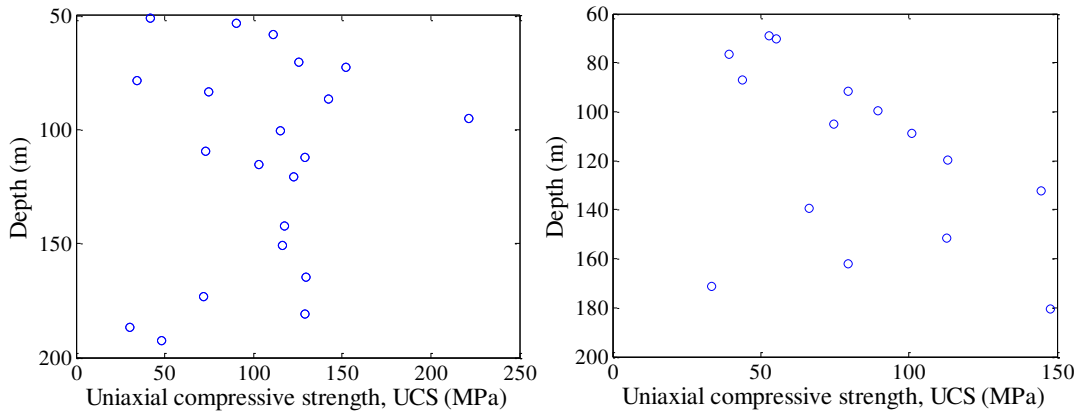

(a) set 1 (sedimentary rock VBH4-3) (b) set 2 (sedimentary rock VBH4-1)

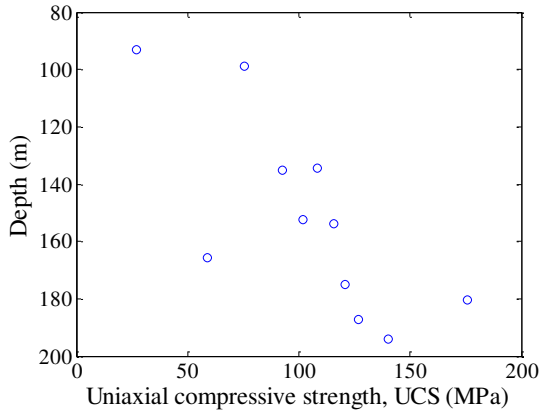

(c) set 3 (sedimentary rock VBH4-2)

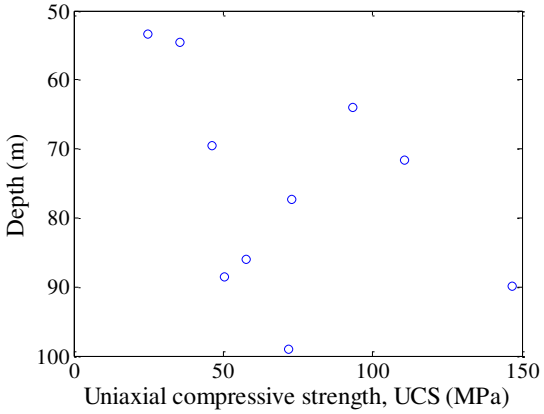

(d) set 4 (sedimentary rock VBH1-1)

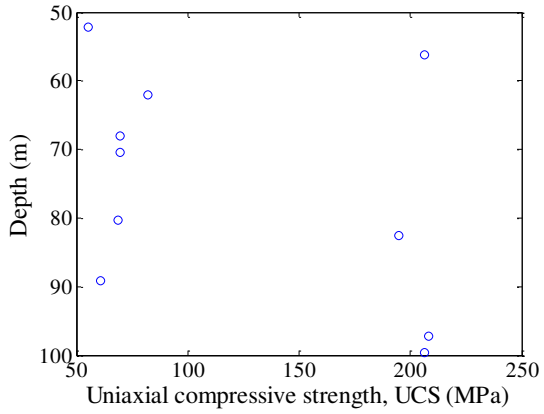

(e) set 5 (sedimentary rock VBH1-3)

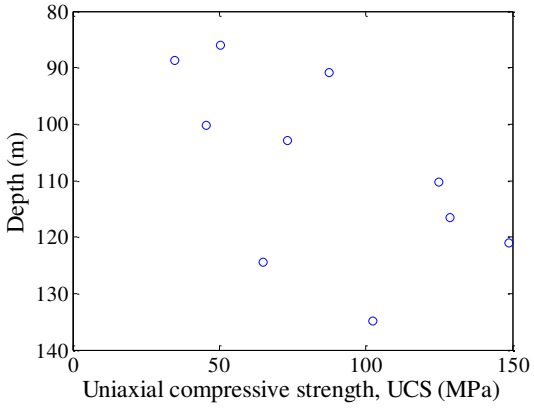

(f) set 6 (sedimentary rock VBH2-1)

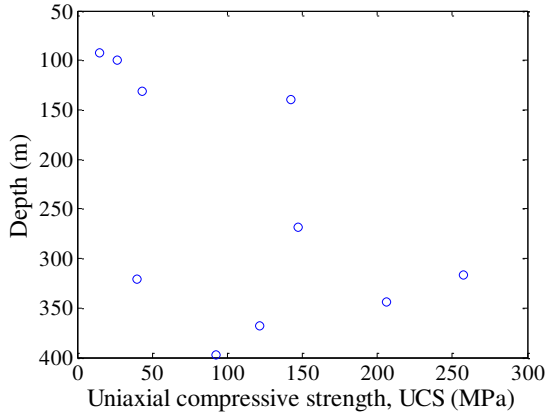

(g) set 7 (sedimentary rock HDD1-1)

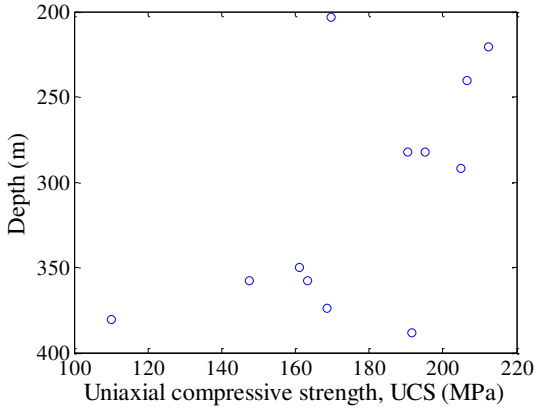

(h) set 8 (igneous rock KLX16A)

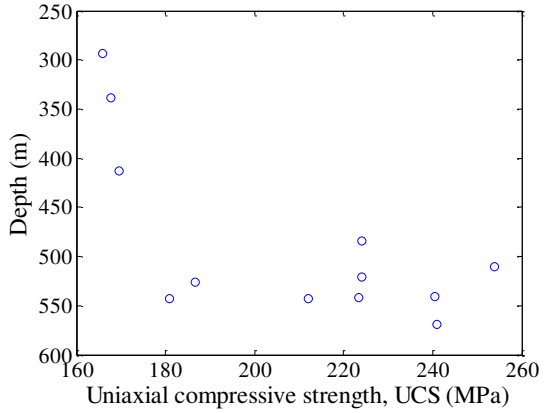

(i) set 9 (igneous rock KLX12A-113)

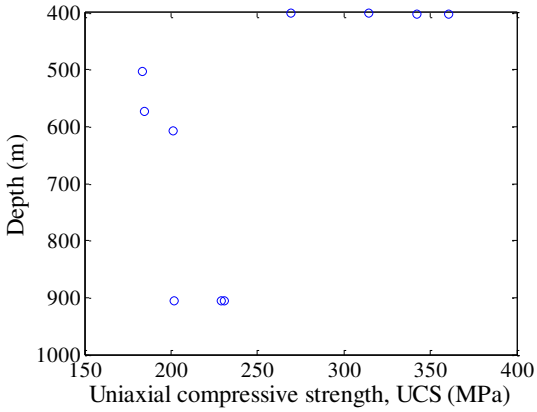

(j) set 10 (igneous rock KLX10-113)

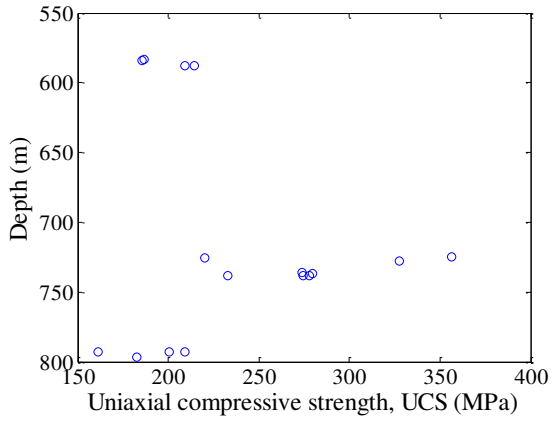

(k) set 11 (igneous rock KLX05-113)

Fig. 7.2. Collected uniaxial compressive strength data

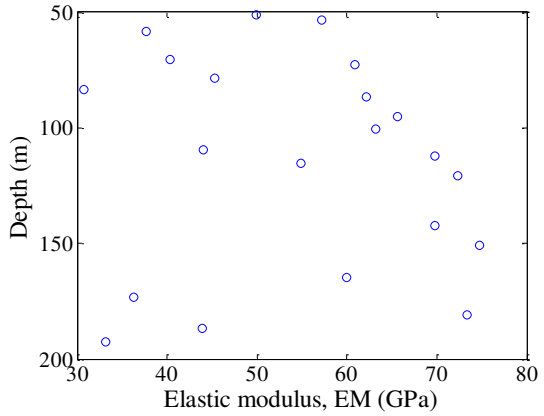

(a) set 1 (sedimentary rock VBH4-3)

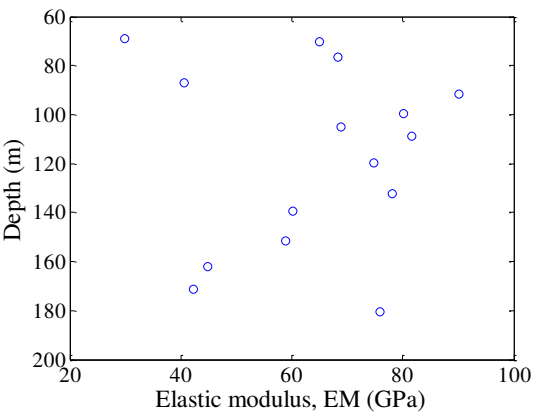

(b) set 2 (sedimentary rock VBH4-1)

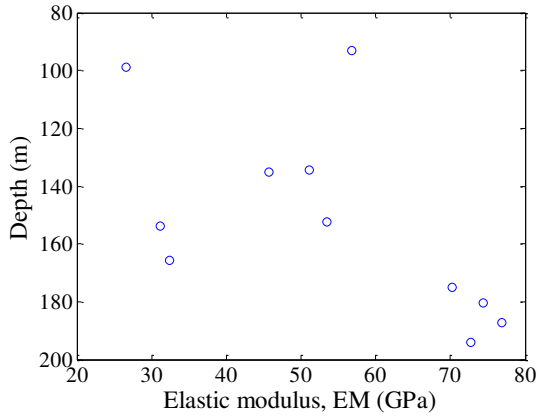

(c) set 3 (sedimentary rock VBH4-2)

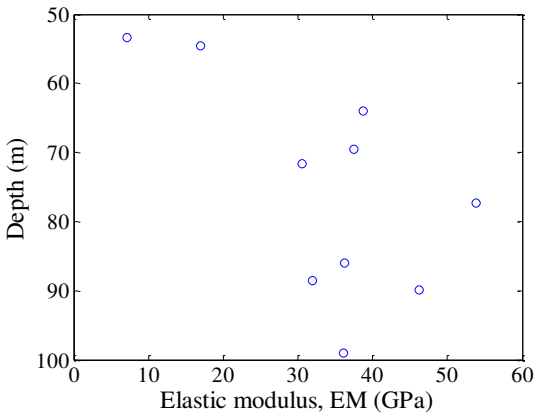

(d) set 4 (sedimentary rock VBH1-1)

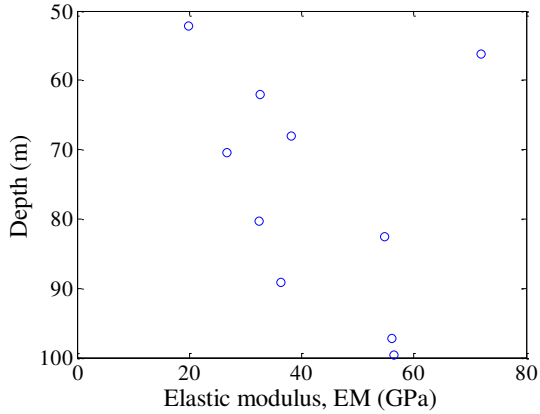

(e) set 5 (sedimentary rock VBH1-3)

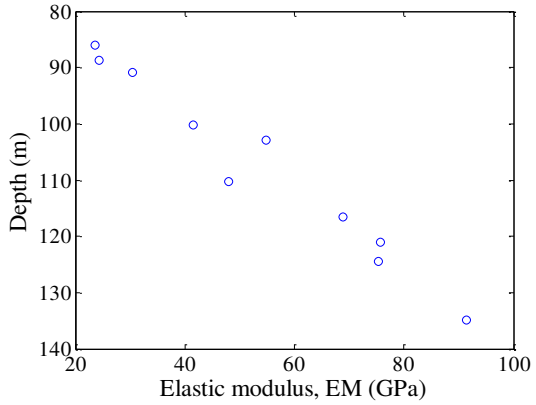

(f) set 6 (sedimentary rock VBH2-1)

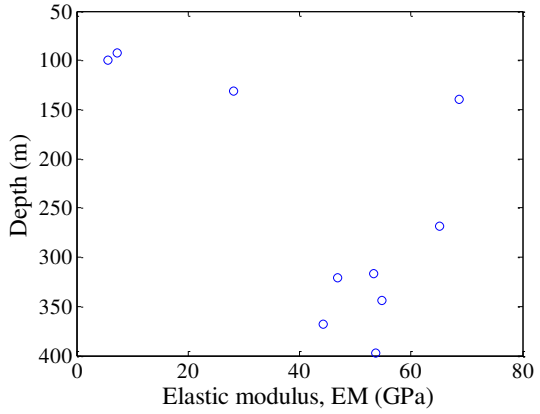

(g) set 7 (sedimentary rock HDD1-1)

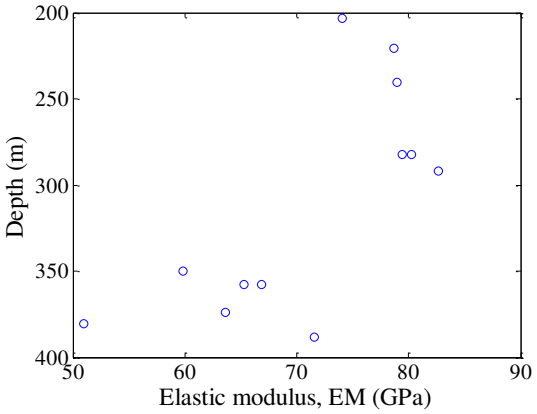

(h) set 8 (igneous rock KLX16A)

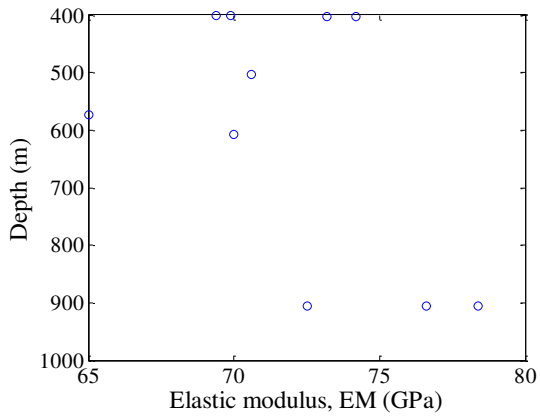

(i) set 9 (igneous rock KLX12A-113)

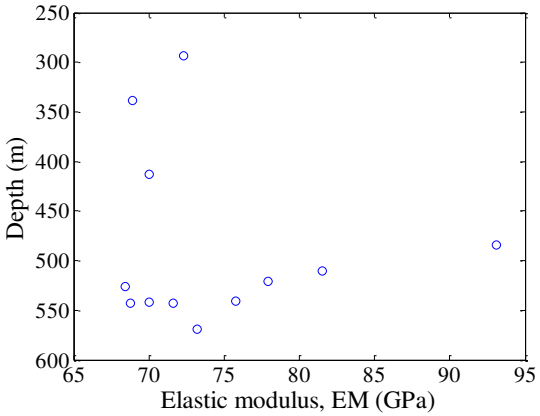

(j) set 10 (igneous rock KLX10-113)

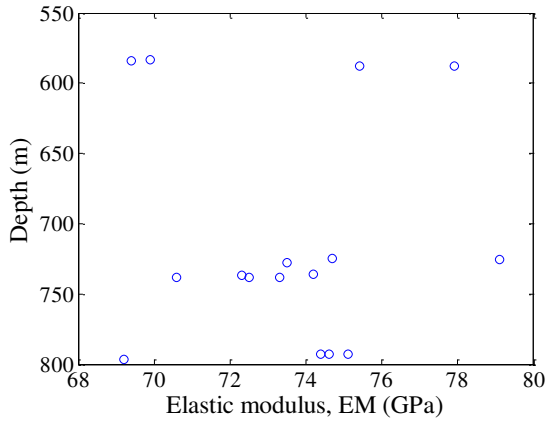

(k) set 11 (igneous rock KLX05-113)

Fig. 7.3. Collected elastic modulus data

7.5 Results for selected autocorrelation model and updated random field parameters for UCS and EM

In this section, the selected most plausible autocorrelation models and associated posterior statistics of the random field parameters for UCS and EM are presented. For the integration via Eq. (7.9), the integration regions with larger likelihood values (i.e. the region around the MPV of random field parameters) are partitioned into denser intervals. The whole integration space is divided into 1,000, 000 parts, i.e.

$n_a \times n_b \times n_\sigma \times n_\theta = 1{,}000{,}000$, where n_a, n_b, n_σ, and n_θ respectively are the numbers of intervals for *a*, *b*, σ and θ. This number ensures the convergence of the evidence. For example, the logarithms of the evidence for the SEACF model, $\ln[P(\hat{Y} \mid M_1)]$, for 1,000, 000 and 7,000,000 intervals respectively are -22.61 and -22.60, the difference between which is insignificant. For evaluating $P(\hat{Y} \mid M_i)$, the prior ranges for the four parameters $[a, b, \sigma, \theta]$ of UCS are respectively set as $a \in [a_i^* - 2.5\text{MPa/m},\ a_i^* + 2.5\text{MPa/m}]$, $b \in [b_i^* - 250\text{MPa}, b_i^* + 250\text{MPa}]$, $\sigma \in$ [0.01 MPa, 150 MPa], and $\theta \in$ [0.01 m, 50 m], where a_i^* and b_i^* are the most probable values of *a* and *b* respectively when the autocorrelation model M_i is used. These bounds are wide enough to produce a consistent solution of the most plausible model because the evidence does not change if wider prior ranges of $[a, b, \sigma, \theta]$ are used, e.g. $[a_i^* - 5\text{MPa/m},\ a_i^* + 5\text{MPa/m}]$, $b \in [b_i^* - 500\text{MPa}, b_i^* + 500\text{MPa}]$, $\sigma \in$ [0.01 MPa, 200 MPa], and $\theta \in$ [0.01 m, 100 m]. In addition, these ranges cover the 95% credible interval defined by the posterior statistics of the random field parameters, indicating that the selected prior ranges are wide enough to consider all the possible values of the random field parameters. Details of the credible interval are illustrated in section 7.5.2. Likewise, the prior ranges for the four parameters $[a, b, \sigma, \theta]$ of EM are set as $a \in [a_i^* - 0.5\text{GPa/m},\ a_i^* + 0.5\text{GPa/m}]$, $b \in [b_i^* - 50\text{GPa},\ b_i^* + 50\text{GPa}]$, $\sigma \in$ [0.01 GPa, 50 GPa], and $\theta \in$ [0.01m, 100m].

7.5.1 Most plausible autocorrelation models for UCS and elastic modulus

The evidence for different autocorrelation models and different sets of UCS data is summarized in Table 7.1. As shown in Table 7.1, the single exponential autocorrelation function has the maximum values of evidence for the two types of rock and all data sets, indicating that the single exponential autocorrelation function is the most plausible model to describe the autocorrelation structure of the UCS of sedimentary and igneous rocks. Table 7.2 summarizes the evidence for different autocorrelation models and different sets of elastic modulus data.

Table 7.1 Logarithms of the evidence for different autocorrelation functions and different sets of UCS data

		M1：Single exponential	M2: Gaussian	M3: Binary Noise	M4: Second-order Markov	M5: Cosine exponential
Sedimentary rock	Set 1	-22.61 [a]	-23.59	-23.36	-23.21	-23.24
	Set 2	-14.40 [a]	-15.12	-14.50	-14.72	-14.65
	Set 3	-8.34 [a]	-9.48	-8.68	-9.05	-8.61
	Set 4	-13.09 [a]	-13.99	-13.72	-13.76	-13.74
	Set 5	-12.83 [a]	-13.31	-13.28	-13.19	-13.38
	Set 6	-10.70 [a]	-12.00	-11.43	-11.70	-11.39
	Set 7	-18.16 [a]	-18.36	-18.39	-18.31	-18.53
Igneous rock	Set 8	-1.57 [a]	-3.44	-2.09	-3.02	-2.09
	Set 9	-0.66 [a]	-2.52	-1.26	-1.98	-1.26
	Set 10	-1.85 [a]	-6.73	-2.45	-4.83	-2.46
	Set 11	-7.32 [a]	-9.19	-8.40	-8.82	-8.23

Note: [a] denotes the maximum value of the $\ln[P(\hat{Y} \mid M_i)]$ for a set of UCS data

Table 7.2 Logarithms of the evidence for different autocorrelation functions and different sets of EM data

		M1：Single exponential	M2: Gaussian	M3: Binary Noise	M4: Second-order Markov	M5: Cosine exponential
Sedimentary rock	Set 1	-11.03 [a]	-11.82	-11.78	-11.67	-11.81
	Set 2	-10.78 [a]	-11.59	-11.46	-11.43	-11.50
	Set 3	-8.25 [a]	-9.75	-9.02	-9.44	-9.02
	Set 4	-8.76 [a]	-10.97	-9.49	-10.53	-9.46
	Set 5	-8.42 [a]	-9.27	-9.05	-9.10	-9.09
	Set 6	1.92 [a]	0.14	1.75	0.44	1.76
	Set 7	-9.37	-10.54	-9.32	-9.79	-9.24 [a]
Igneous rock	Set 8	5.28 [a]	3.47	4.85	3.91	4.89
	Set 9	5.72 [a]	2.68	5.28	3.38	5.33
	Set 10	5.16 [a]	1.49	4.53	2.04	4.54
	Set 11	17.94 [a]	14.38	17.30	15.23	17.34

Note: [a] denotes the maximum value of the $\ln[P(\hat{Y} \mid M_i)]$ for a set of EM data

As shown in Table 7.2, the exponential autocorrelation model also has the maximum evidence for most EM data sets (except for data set 7). As shown by Cao and Wang (2014), the Bayesian model class selection model could identify the most plausible model even when the sampling spacing is large. Since all or most of the data sets have the same optimal autocorrelation function, the single exponential autocorrelation is the most suitable autocorrelation function for the UCS and EM of igneous and sedimentation rocks based on the data sets collected.

7.5.2 Posterior statistics of random field parameters

The posterior means ($\mu_a^*, \mu_b^*, \mu_\sigma^*$ and μ_θ^*) and standard deviations ($\sigma_a^{po}, \sigma_b^{po}, \sigma_\sigma^{po}$ and σ_θ^{po}) for the random field parameters of UCS are summarized in Table 7.3. When calculating the posterior standard deviations, some abnormal values such as extremely large values or infinity are obtained and denoted by "—" in Table 7.3. These abnormal values occur because the diagonal component of the Hessian matrix is equal to or close to 0, resulting in a singular or nearly singular Hessian matrix. To further explore the reason, Fig. 7.4 plots the variation of the likelihood with the scale of fluctuation for set 3 and set 7 of the UCS data.

Table 7.3 Posterior statistics for the random field parameters of UCS

Rock type	Set Number	Posterior MPV (or mean)				Posterior standard deviation			
		μ_a^* / MPa/m	μ_b^* / MPa	μ_σ^* / MPa	μ_θ^* / m	σ_a^{po} / MPa/m	σ_b^{po} / MPa	σ_σ^{po} / MPa	σ_θ^{po} / m
Sedimentary rock	Set 1	-0.12	119.34	56.31	3.40	0.17	24.41	13.95	4.77
	Set 2	0.09	75.28	39.85	8.02	0.24	30.89	11.83	9.18
	Set 3	0.86	-27.23	30.83	5.73	0.23	34.14	8.48	5.98
	Set 4	0.89	3.97	31.21	0.29	0.44	32.48	9.77	5.52
	Set 5	1.28	26.22	67.76	1.16	1.14	84.13	23.90	9.83
	Set 6	1.18	-39.92	32.42	0.13	0.48	50.59	9.45	— [a]
	Set 7	0.30	36.75	85.44	0.22	0.13	29.27	36.58	— [a]
Igneous rock	Set 8	-0.28	264.38	25.73	2.86	0.11	35.39	5.89	2.86
	Set 9	0.24	93.03	22.22	0.84	0.08	36.37	4.70	1.36
	Set 10	-0.07	268.74	50.39	4.14	0.13	78.20	15.81	3.36
	Set 11	0.03	214.20	54.24	0.52	0.16	113.77	12.38	0.50

Note: — [a] means abnormal values are obtained in Bayesian updating, such as extremely large values or infinity

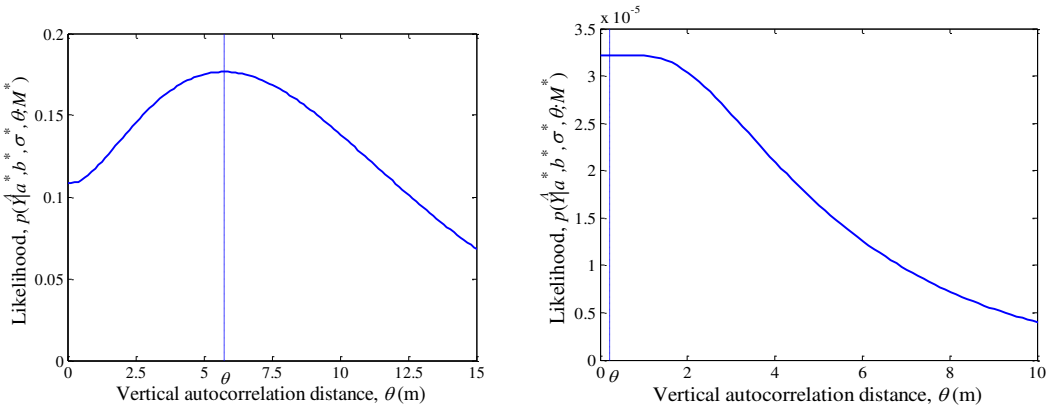

(a) set 3 of UCS data (b) set 7 of UCS data

Fig. 7.4. Variation of the likelihood with scale of fluctuation

The likelihoods in Fig. 7.4 are calculated by setting the values of a, b and σ parameters to their MPVs, i.e. a^*, b^*, and σ^*, and altering the values of θ. As shown in Fig. 7.4, the likelihood may display different trends with the scale of fluctuation for different data sets. For example, there is a peak of the likelihood around the MPV of the scale of fluctuation, θ^*, for UCS data set 3. For this case, the second-order derivative of the objective function, $J(a,b,\sigma,\theta)$ is positive. However, for the set 7 of UCS data in Fig. 7.4 (b), the likelihood is constant around the θ^* and the second-order derivative of the objective function is 0 or nearly 0, resulting in infinite posterior standard deviation of θ. For this case, the results for the posterior PDF of the random field parameters are abandoned.

It can be seen that the scale of fluctuation of UCS ranges from 0.3 m to 8 m and there is no apparent difference between the SoFs for sedimentary rocks and for igneous rocks. Other useful information could also be deduced based on the posterior means and standard deviations of the random field parameters. For example, the posterior coefficient of variation (*COV*) of UCS at various depths are calculated by $COV(z) = \sigma_\sigma^{po} / \mu_{\text{UCS}}^{po} = \sigma_\sigma^{po} / (\mu_a^* z + \mu_b^*)$, where σ_σ^{po} is the posterior standard deviation of σ, and μ_{UCS}^{po}, μ_a^* and μ_b^* are the posterior mean of UCS, a and b. Using this equation, it can be readily calculated that the *COV*s for various sets of UCS data

ranges from 9% to 75%. The interval falls within the ranges summarized by Aladejare and Wang (2017). Apart from *COV*, the credible interval is another useful information in Bayesian statistics. The 95% credible interval of a parameter is a range within which the parameter falls with a probability of 95%. For a normally distributed random variable, the 95% mean-value-centered credible interval is given by $[\mu^* - 1.96\sigma^{po}, \mu^* + 1.96\sigma^{po}]$, where μ^* and σ^{po} respectively are the posterior mean and standard deviation of the parameter. For a lognormally distributed random variable, the 95% mean-value-centered credible interval is given by $[\mu^* / \exp(1.96\sigma_N^{po}), \mu^* \exp(1.96\sigma_N^{po})]$, where $\sigma_N^{po} = \sqrt{\ln(1+(\sigma^{po}/\mu^*)^2)}$ is the posterior standard deviation for the logarithm of the parameter. Assuming the parameters *a* and *b* are normally distributed and σ and θ are lognormally distributed, it can be easily calculated that the 95% credible intervals of *a*, *b*, σ and θ for the set 1 of UCS data respectively are [-0.45 MPa/m, 0.21 MPa/m] and [71.50 MPa, 167.18 MPa], [34.9 MPa, 90.9 MPa] and [0.44 m, 26.26 m]. These intervals fall within the prior range of *a*, *b*, σ and θ, i.e. $a \in [a_i^* - 2.5\text{MPa/m}, a_i^* + 2.5\text{MPa/m}]$ = [-2.62 MPa/m, 2.38MPa/m], $b \in [b_i^* - 250\text{MPa}, b_i^* + 250\text{MPa}]$ = [-130.66 MPa, 369.34 MPa], $\sigma \in [0.01\text{ MPa}, 150\text{ MPa}]$, and $\theta \in [0.01\text{ m}, 50\text{ m}]$. The prior ranges of *a*, *b*, σ and θ are large enough to consider all the possible values of these parameters. The credible intervals of random field parameters for other sets of UCS data also fall within the corresponding prior ranges.

The posterior statistics of random field parameters for the elastic modulus are summarized in Table 7.4. As shown in Table 7.4, the scale of fluctuation for elastic modulus ranges from 0.3 m to 8.4 m. Using the same method as the UCS, it can be easily calculated that the *COV* for the elastic modulus ranges from 4% to 88%. This range also agrees with the results given by Aladejare and Wang (2017). The credible intervals for random field parameters of EM also fall within the corresponding prior ranges.

Table 7.4 Posterior statistics for the random field parameters of EM

Rock type	Set Number	Posterior MPV (or mean)				Posterior standard deviation			
		μ_a^* / GPa/m	μ_b^* / GPa	μ_σ^* / GPa	μ_θ^* / m	σ_a^{po} / GPa/m	σ_b^{po} / GPa	σ_σ^{po} / GPa	σ_θ^{po} / m
Sedimentary rock	Set 1	0.00	55.05	15.17	0.08	—[a]	—[a]	—[a]	—[a]
	Set 2	0.05	58.62	19.91	0.08	0.11	13.70	4.43	—[a]
	Set 3	0.31	7.40	16.58	0.85	0.15	23.06	4.65	6.92
	Set 4	0.64	-15.02	10.65	0.28	0.15	11.13	2.98	13.44
	Set 5	0.54	0.37	12.33	0.13	0.04	1.69	3.37	—[a]
	Set 6	1.40	-96.58	4.34	0.15	0.09	9.18	1.00	—[a]
	Set 7	0.16	1.51	14.29	1.50	0.03	6.43	4.34	2.14
Igneous rock	Set 8	-0.11	103.17	6.82	6.80	0.03	9.97	1.53	5.80
	Set 9	0.02	67.05	6.80	8.35	0.02	11.26	1.68	9.54
	Set 10	0.01	66.86	3.18	0.41	0.01	3.82	0.77	0.50
	Set 11	0.00	71.62	2.77	0.70	0.01	7.77	0.57	0.58

Note: —[a] means abnormal values are obtained in Bayesian updating, such as extremely large values or infinity.

7.6 Summary

Although recognized as an important factor controlling the safety of geotechnical structures, the spatial variability of rock properties is rarely quantified in the literature. This chapter characterizes the autocorrelation structures and scales of fluctuation of two important parameters of intact rocks, i.e. uniaxial compressive strength (UCS) and elastic modulus (EM). UCS and EM data for sedimentary and igneous rocks are used. The autocorrelation structures are selected using a Bayesian model class selection approach and the scales of fluctuation for these two parameters are estimated using a Bayesian updating method. The results show that the autocorrelation structures for UCS and EM could be best described by a single exponential autocorrelation function. The scales of fluctuation for UCS and EM range from 0.3 m to 8.0 m and from 0.3 m to 8.4 m, respectively. These results may serve as guidelines for selecting proper autocorrelation functions and autocorrelation distances for rock properties in the reliability analysis and could also be used as prior information for quantifying the spatial variability of rock properties in a Bayesian framework.

Chapter 8 Summary and Recommendation

This chapter summarizes the major investigations and discussions in previous chapters and provides some recommendations for future research.

8.1 Summary

First, a simple closed-form solution (the Duncan-Fama solution) for circular tunnels in Mohr-Coulomb grounds is used to illustrate various reliability methods, including FORM, direct MCS, LHS, MCS with importance sampling, subset simulation, FOSM and polynomial RSM. This provides the basis for the calculations and discussions in later chapters. For a special case where the design point is far away from the mean value point, the tentative design point for the linear RSM may locate in the unrealistic domain, thus causing a numerical error problem. This problem can be solved by increasing the sampling factor, or by changing the formulation of the performance function, or by using a multiple-step RSM which approximates the limit states in several steps instead of one step. The multiple-step RSM is versatile and suggested to be used to deal with similar numerical error problems.

Next, the reliability analysis of single limit state is extended to system reliability analysis which considers the interaction among different limit states. An iterative closed-form solution for a circular tunnel reinforced by end-anchored rockbolts is used to illustrate the system reliability methods. The bimodal bounds method and the *mvncdf* method are compared for this case study. Results show that the system probability of failure estimated from the *mvncdf* method lies within the lower and upper bounds set by the bimodal bounds method. SORM can be used to refine the FORM reliability indices and to improve the accuracy of the estimated system probability of failure. The influence of the correlation coefficient between the cohesion and friction angle and the influence of the rockbolt installation position on the system probability of failure are discussed. The optimal installation position corresponds to the smallest system probability of failure. A modified hybrid approach using the linear RSM to locate the design point and ANN to approximate the actual

limit state surface is suggested to be used in the system reliability analysis for problems where closed-form solutions are not available. Traditional second-order RSM without cross terms may be inaccurate the suffer from the problem of low convergence rate and the second-order RSM with cross terms may encounter the "false branch" problem. It is shown that the "false branch" problem can be overcome by the importance sampling technique. Comparison with the second-order RSM shows that the proposed approach is efficient, accurate and robust for the system reliability analysis.

Then, how reliability-based design can provide insights to the partial factor design approach is discussed and illustrated using various tunnelling problems. It is shown that FORM is consistent for different but mathematically equivalent limit state functions, which is an advantage over FOSM and PEM. The intuitive expanding ellipsoid perspective and the efficient constrained optimization method help overcome the conceptual and computational barriers for practitioners. Different case studies including structurally-controlled and stress-controlled failure mechanisms are used to show that reliability-based design via FORM can determine the role (resistance or load factor) of input parameters on a case-by-case basis in ways that prescribed partial factors cannot.

An actual underground excavation project, JRC in Singapore, is presented to show how reliability analysis is conducted for a real-life case study. The statistics of the rock engineering properties can be characterized using the site investigation and laboratory test results. The deterministic analysis shows that the estimate of the rock mass Young's modulus has a great influence on the cavern displacement. The longitudinal deformation profile from 3D analysis can be used to determine the stress reduction coefficient for the simplified 2D analysis. For this case, when the support is installed, 70% to 88% of the final displacement has occurred. The monitored displacement is almost zero due to the late installation of the monitoring device and therefore cannot be used to characterize the input parameters for this case. FORM and second-order RSM with cross terms are used to obtain a converged reliability index and design point.

Finally, the autocorrelation structures and scales of fluctuation of two important parameters of intact rocks, i.e. uniaxial compressive strength (UCS) and elastic modulus (EM) are characterized. The autocorrelation structures are selected using a Bayesian model class selection approach and the scales of fluctuation for these two parameters are estimated using a Bayesian updating method. The results show that the autocorrelation structures for UCS and EM could be best described by a single exponential autocorrelation function. The scales of fluctuation for UCS and EM range from 0.3 m to 8.0 m and from 0.3 m to 8.4 m, respectively. These results may serve as guidelines for selecting proper autocorrelation functions and autocorrelation distances for rock properties in the reliability analysis and could also be used as prior information for quantifying the spatial variability of rock properties in a Bayesian framework.

Major academic contributions are summarized as:

- System reliability analysis of tunnelling problems is investigated in detail. A hybrid approach using linear RSM and ANN is proposed to estimate the system probability of failure.
- How reliability-based design (RBD) is linked up with the partial factor design approach and the insights from RBD for rock engineering problems are investigated and discussed.
- Reliability analysis of a real-life project is presented to show the characterization of the statistical information of rock mass properties.
- The autocorrelation structure and scales of fluctuation of intact rock properties are characterized using a large number of actual data. The results show that the autocorrelation structure could be best described by a single exponential autocorrelation function.

8.2 Recommendations for future research

Based on the literature review and the investigation in this thesis, some suggestions for future research are given in this section.

8.2.1 Reliability analysis of structurally-controlled failure problems

There are two instability mechanisms for rock excavations, the stress-controlled and the structurally-controlled instability. From the review of reliability analyses of underground excavation problems, most research concerns the stress-controlled failure in which the rock mass is treated as a continuum. Although the roof wedge problem is analyzed in this thesis, the present research focuses on the stress-controlled failure. For the analysis of rock blocks formed by intersecting discontinuities, uncertainties in the distribution of discontinuities and in strength properties of the discontinuity should be investigated. Deterministic analysis using UDEC and 3DEC and probabilistic analysis of the stability of rock blocks will be covered in the future.

8.2.2 Influence of the spatial variability of rock properties on the stability of underground rock excavations

As shown in Chapter 7, the spatial variability of rock properties can be characterized by the Bayesian approach. Next, the influence of the spatial variability of rock properties on the stability and reliability of rock excavation projects can be investigated.

8.2.3 Transformation uncertainty and model uncertainty

The uncertainty associated with the process from a field parameter to a design parameter is called the transformation uncertainty. It is shown in Chapter 6 that the estimate of the rock mass Young's modulus has a great effect on the cavern displacement. Model uncertainty means the uncertainty of the model output compared with the actual behavior. For example, the FEM output can never accurately predict the actual behavior of geotechnical structures. The transformation and model uncertainties can be discussed for tunnelling problems in the future.

Appendix A List of literature on the reliability analysis of underground excavation problems

Table A.1 summarizes the research work relevant to the reliability analysis of underground excavation problems. The observations of the literature are given in Chapter 2.

Table A.1 List of literature on reliability analysis of underground excavation problems

No	Reference	Problem description	Performance function	Surrogate models and numerical software	Methods for P_f
1	Laso et al. (1995)	Ground-support interaction analysis of a circular tunnel under hydrostatic in situ stress using CCM	Displacement and support capacity	Linear RSM	FOSM, PEM
2	Chen et al. (1997)	A layered roof beam analysis using the beam theory and the stability of a triangular roof prism	Tensile failure of the rock and the stability of the prism	-	FORM
3	Hoek (1998)	Circular tunnel displacement using the Duncan-Fama solution	Displacement	-	MCS
4	Yang et al. (2007)	A closed-form solution is used to calculate the load in the liner	Support capacity	-	MCS
5	Mollon et al (2009b)	Face stability of a tunnel excavated in soils	Tunnel collapse pressure and settlement	Second-order RSM, $FLAC^{3D}$	FORM

Table A.1 List of literature on reliability analysis of underground excavation problems (continued)

No	Reference	Problem description	Performance function	Surrogate models and numerical software	Methods for P_f
6	Mollon et al (2009a)	Tunnel face stability using an improved upper bound limit analysis	Collapse pressure	-	FORM
7	Li and Low (2010)	Circular tunnel displacement and plastic zone size using the Duncan-Fama solution	Plastic zone size and displacement	-	FORM, MCS
8	Cai (2011)	Estimate the mean and standard deviation of the plastic zone size and displacement of the hydropower station with irregular geometries	Plastic zone size and displacement	Phase^2	PEM
9	Su et al. (2011)	Analyze the support pressure using CCM	Support capacity	-	FORM
10	Lü and Low (2011)	Analyze the displacement and plastic zone of two circular tunnels in M-C and H-B grounds and a horseshoe shaped tunnel	Plastic zone size and displacement	Second-order RSM, FLAC^{3D}	FORM, SORM and MCS

Table A.1 List of literature on reliability analysis of underground excavation problems (continued)

No	Reference	Problem description	Performance function	Surrogate models and numerical software	Methods for P_f
11	Lü et al. (2011)	Ground-support interaction analysis of a circular tunnel using CCM	Plastic zone size, displacement and support capacity	Second-order polynomial response surface method	FORM, SORM and MCS
12	Lü et al. (2012)	Ground-support interaction analysis of a circular tunnel using CCM	Plastic zone size, displacement and support capacity	ANN	FORM, SORM and MCS
13	Zhang and Goh (2012)	The global factor of safety calculated from shear reduction method and the percent strain around a horseshoe-shaped tunnel	Factor of safety and limiting percent strain	Polynomial regression model, FLAC^{3D}	FORM
14	Goh and Zhang (2012)	The global factor of safety was calculated for numerous cases with different combinations of the input parameters	Factor of safety	ANN, FLAC^{3D}	FORM
15	Chen (2012)	Stability of the key blocks in a shaft	Stability of key blocks	-	FOSM

Table A.1 List of literature on reliability analysis of underground excavation problems (continued)

No	Reference	Problem description	Performance function	Surrogate models and numerical software	Methods for P_f
16	Lü et al. (2013)	Bimodal bounds method is used to estimate the system P_f of the ground-support interaction problem	Plastic zone size, displacement and support capacity	-	FORM, SORM and MCS
17	Langford and Diederichs (2013)	Analyze the performance of liner for a circular tunnel	Support capacity	Phase^2	PEM
18	Park et al. (2013)	Analyze the rock support failure of a circular rock cavern	Support capacity	FLAC	PEM
19	Zhao et al. (2014)	Two problems are used to verify SVM including the Duncan-Fama solution and a horseshoe shaped tunnel	Tunnel displacement	SVM, Phase^2	FORM
20	Zhang and Goh (2014)	MARS is used to approximate the displacement of a twin cavern case	Displacement and percent strain	MARS, FLAC^{3D}	FORM

Table A.1 List of literature on reliability analysis of underground excavation problems (continued)

No	Reference	Problem description	Performance function	Surrogate models and numerical software	Methods for P_f
21	Zeng and Jimenez (2014)	A linearization approach is used to estimate the system probability of failure for the support-rock interaction using CCM	Support capacity and tunnel displacement	-	FORM
22	Zeng et al. (2014)	Analyze the tunnel face stability problems using the upper bound limit analysis	Collapse pressure	Second-order RSM	FORM, MCS
23	Langford and Diederichs (2015)	Analyze the spalling damage of rock excavations and approximate the performance function over a large parameter space	Spalling initiation condition	Global RSM, Phase^2	FORM
24	Oreste (2015)	Analyze the tunnel-support interaction using CCM	Support capacity	-	MCS
25	Wang et al. (2016a)	Two problems are used to verify the proposed meta-modeling technique including the Duncan-Fama solution and a lined circular tunnel	Tunnel displacement	Augmented radial basis function, ABAQUS	MCS

Table A.1 List of literature on reliability analysis of underground excavation problems (continued)

No	Reference	Problem description	Performance function	Surrogate models and numerical software	Methods for P_f
26	Li et al. (2016)	Uniform design and SVM are combined to analyze the tunnel convergence of three problems	Tunnel displacement	SVM, FLAC	FORM
27	Idris et al. (2016)	Review of the commonly used methods in reliability analysis of tunnels	-	-	-
28	Lü et al. (2017)	Two problems are used to verify the proposed moving least square RSM including the ground-support interaction and a horseshoe shaped tunnel	Support capacity, tunnel displacement and plastic zone size	Moving least square RSM, FLAC^{3D}	FORM, SORM and MCS
29	Su et al. (2017)	Two problems including a soil slope and a tunnel are used to verify the proposed one-dimensional integration method	Tunnel displacement	FLAC	One-dimensional integration method
30	Wang and Li (2017)	The distribution of the tunnel displacement is approximated by SRSM	Tunnel displacement	SRSM	-

Table A.1 List of literature on reliability analysis of underground excavation problems (continued)

No	Reference	Problem description	Performance function	Surrogate models and numerical software	Methods for P_f
31	Napa-Garcia (2017)	Different PEM methods are compared using two circular-tunnel problems	Tunnel displacement	-	PEM
32	Lü et al. (2017)	Design optimization of shotcrete thickness and installation point using CCM	Tunnel displacement and support capacity	Linear RSM	FORM

Appendix B Cross-validation of FORM using different methods in Excel and MATLAB

In this appendix, three different methods or algorithms of FORM are applied to two problems to cross-validate the results using the efficient constrained optimization tool in Excel. Method 1 refers to using the constrained optimization tool Solver in the Excel platform (Low and Tang, 2004; Low and Tang, 2007). Method 2 refers to the traditional or classical iteration approach in the uncorrelated standard random variable space, as elaborated by Ang and Tang (1984), Melchers (1999), Haldar and Mahadevan (2000), for example. Method 3 refers to the constrained optimization approach using the toolbox in MATLAB. The first problem is the Duncan-Fama solution shown in Chapter 3. The second problem is a linear performance function of three random variables with different distributions.

```
function value=Perfunc(x)
% Duncan-Fama solution
% deterministic inputs
    PerF=1; %which performance function is used. 1 represents the plastic zone
    Limit_ratio_plastic=3.0;
    Limit_ratio_disp=0.01;
    pi=0.0;
    Poisson=0.3;
    Radius=2.5;
    Fric_angle=deg2rad(x(1));
    Cohesion=x(2);
    if Cohesion<0
        Cohesion=0.001;
    end
    Young_modu=x(3);
    Insitu_stress=x(4);

    Shear_modu=Young_modu/2/(1+Poisson);
    temp_k=(1+sin(Fric_angle))/(1-sin(Fric_angle));
    sigma_cm=2*Cohesion*cos(Fric_angle)/(1-sin(Fric_angle));
    pi_critical=(2*Insitu_stress-sigma_cm)/(1+temp_k);
    if pi>pi_critical %determine elastic or plastic deformation
        Plastic_ratio=0.0;
        Displacement_ratio=(Insitu_stress-pi)/2/Shear_modu;
    else
        Plastic_ratio=(2*(Insitu_stress*(temp_k-1)+sigma_cm)/((temp_k+1)*((temp_k-
1)*pi+sigma_cm)))^(1/(temp_k-1));
        Displacement_ratio=1/2/Shear_modu*(2*(1-Poisson)*(Insitu_stress-
pi_critical)*Plastic_ratio^2-(1-2*Poisson)*(Insitu_stress-pi));
    end
    if PerF==1
        gx=Limit_ratio_plastic-Plastic_ratio;
    else
        gx=Limit_ratio_disp-Displacement_ratio;  % calculate the performance
function value
    end
    value=gx;
end
```

Fig. B.1. MATLAB code for the Duncan-Fama solution

For the Duncan-Fama solution, the FORM results using Excel Solver (method 1) is shown in Chapter 3. If method 2 is used, the axes of the four original random variables should be rotated to transform the correlated random variables to uncorrelated variables. The orthogonal transformation is used (e.g. Ang and Tang,1984). The calculation of the design point involves iterations. The MATLAB code for the Duncan-Fama solution is shown in Fig. B.1 and the code for the classical iterative approach (method 2) is shown in Fig. B.2. MATLAB also provides a function to conduct the constrained optimization (*fmincon*). The code for the constrained optimization approach using the toolbox in MATLAB is shown in Fig. B.3. All these three methods give the same results (reliability index and design point) as shown in Chapter 3. The pros and cons of these three methods are compared in Chapter 3.

```
muX=[22.85;0.23;373;2.5];
sigmaX=[1.31;0.068;48;0.25];
corre_coeff=[1,-0.5,0,0;-0.5,1,0,0;0,0,1,0;0,0,0,1];
covX=diag(sigmaX)*corre_coeff*diag(sigmaX);
[a,d]=eig(covX);
a(:,[3,4])=a(:,[4,3]);
a(:,[2,4])=a(:,[4,2]);
a(:,[1,2])=a(:,[2,1]);
d=a'*covX*a;
muY=a'*muX; sigmaY=sqrt(diag(d));
x=muX; y=a'*x; normX=eps;
while abs(norm(x)-normX)/normX>1e-6
    increament=0.001;
    for i=1:4
        y_new=y;
        y_new(i)=y_new(i)+increament;
        delta_g(i)=(Perfunc(a*y_new)-Perfunc(a*y))/increament;
    end
    gs=delta_g'.*sigmaY;
    cos_y=-gs/norm(gs);
    beta=(Perfunc(y)+delta_g*(muY-y))/norm(gs);
    y=muY+beta*sigmaY.*cos_y;
    x=a*y;
    beta1=0.01;
    beta2=10.0;
    beta=5.0;
    new_beta=0.0;
    while abs(new_beta-beta)>0.0001
        y_design=muY+beta*cos_y.*sigmaY;
        if Perfunc(a*y_design)>0
            new_beta=0.5*(beta1+beta);
        else
            new_beta=0.5*(beta2+beta);
        end
    end
    x=a*y_design;
end
beta
x
```

Fig. B.2. MATLAB code for the classical iterative approach

```
x0=[22.85;0.23;373;2.5];   % initial starting point
true_DP=[22.998024;0.189326;373.00;2.549328];
%set the options for function 'fmincon'
% return the design point value 'x' and reliability index 'fvar'
options = optimoptions('fmincon');
options = optimoptions(options,'Display', 'off');
options = optimoptions(options,'Algorithm', 'active-set');
[x,fval,exitflag,output,lambda,grad,hessian] = ...
fmincon(@objectfun,x0,[],[],[],[],[],[],@mycon,options);

function [c,ceq]=mycon(x)
    c=[];
    ceq=Perfunc(x);
end

function beta=objectfun(x)
    % set the characteristic values
    muX=[22.85;0.23;373;2.5];
    sigmaX=[1.31;0.068;48;0.25];
    corre_coeff=[1,-0.5,0,0;-0.5,1,0,0;0,0,1,0;0,0,0,1];
    nx=(x-muX)./sigmaX;
    beta=(nx'*inv(corre_coeff)*nx)^0.5;
end
```

Fig. B.3. MATLAB code for the optimization toolbox in MATLAB

For the second problem, the performance function is

$$g(x) = R - G - Q \tag{B.1}$$

where R is the resistance; G is the permanent load effect; Q is the variable load effect. The statistical values of these three random variables, among which there is no correlation, are listed in Table B.1.

Table B.1 Characteristic values for input parameters

	R (kN)	G (kN)	Q (kN)
Distribution	Lognormal	Normal	Extreme value 1
Mean Value	22	10	2
Standard Deviation	2	0.9	0.6

The FORM results using Solver in Excel are shown in Fig. B.4. The reliability index is 4.713 and corresponding design point is (16.710, 11.596, 5.114) by changing the n_i column.

Method 1:

Parameter	x_i*	Correlation matrix [R]			n_i*
R (kN)	16.710	1	0	0	-2.986
G (kN)	11.596	0	1	0	1.773
Q (kN)	5.114	0	0	1	3.186
g(x)	-1E-07	β	4.713	P_f	1.2E-06

Fig. B.4. FORM results using Solver in Excel

```
clear;clc;

muX=[22;10;2];sigmaX=[2;0.9;0.6];   % set characteristic values

% calculate parameters for nonnormal distributions
sLn=sqrt(log(1+(sigmaX(1)/muX(1))^2));
mLn=log(muX(1))-0.5*sLn^2;
aEv=sqrt(6)*sigmaX(3)/pi;
uEv=-psi(1)*aEv-muX(3);

equivmuX=muX;equivsigmaX=sigmaX;
x=muX;normX=eps;
gX=[1;-1;-1];   % gradient of the performance function

while abs(norm(x)-normX)/normX>1e-6
    normX=norm(x);
    norminverseX(1)=norminv(logncdf(x(1),mLn,sLn));

    % calculate equivalent normal distribution values
    equivsigmaX(1)=normpdf(norminverseX(1))/lognpdf(x(1),mLn,sLn);
    equivmuX(1)=x(1)-norminverseX(1)*equivsigmaX(1);
    norminverseX(3)=norminv(1-evcdf(-x(3),uEv,aEv));
    equivsigmaX(3)=normpdf(norminverseX(3))/evpdf(-x(3),uEv,aEv);
    equivmuX(3)=x(3)-norminverseX(3)*equivsigmaX(3);

    gs=gX.*equivsigmaX;
    alfaX=-gs/norm(gs);     % calculate direction cosine
    g=x(1)-x(2)-x(3);
    bbeta=(g+gX'*(equivmuX-x))/norm(gs); % calculate reliability index
    x=equivmuX+bbeta*equivsigmaX.*alfaX;    % calculate design point
end

bbeta
x
```

Fig. B.5. MATLAB code for FORM using traditional iteration procedure

Method 2:

The MATLAB code for the FORM analysis using the iterative procedure is shown in Fig. B.5.

The reliability index is 4.713 and corresponding design point is (16.710, 11.595, 5.115), which are the same as method 1.

Method 3:

The code for the FORM analysis using constrained optimization in MATLAB is shown in Fig. B.6. The explanation of the code is given after the percent sign.

```
clear; clc;
x0=[22;10;2];   % initial starting point

% set the options for optimization function 'fmincon'
options = optimoptions(@fmincon,'Display', 'off');
options = optimoptions(@fmincon,'Algorithm', 'interior-point');

% return the design point value 'xDP' and reliability index 'fvar'
[xDP,fvar]=fmincon(@objecfun,x0,[],[],[],[],[],[],@mycon,options);

function beta=objecfun(x)
    % set the characteristic values
    muX=[22;10;2];
    sigmaX=[2;0.9;0.6];

    % calculate parameters for nonnormal distributions
    sLn=sqrt(log(1+(sigmaX(1)/muX(1))^2));
    mLn=log(muX(1))-0.5*sLn^2;
    aEv=sqrt(6)*sigmaX(3)/pi;
    uEv=-psi(1)*aEv-muX(3);
    equivmuX=muX;equivsigmaX=sigmaX;

    % calculate equivalent normal distribution values
    norminverseX(1)=norminv(logncdf(x(1),mLn,sLn));
    equivsigmaX(1)=normpdf(norminverseX(1))/lognpdf(x(1),mLn,sLn);
    equivmuX(1)=x(1)-norminverseX(1)*equivsigmaX(1);
    norminverseX(3)=norminv(1-evcdf(-x(3),uEv,aEv));
    equivsigmaX(3)=normpdf(norminverseX(3))/evpdf(-x(3),uEv,aEv);
    equivmuX(3)=x(3)-norminverseX(3)*equivsigmaX(3);

    nx=(x-equivmuX)./equivsigmaX;
    beta=norm(nx);
end

function [c,ceq]=mycon(x)
    c=[];
    gx=x(1)-x(2)-x(3);  % calculate the performance function value
    ceq=[gx];
end
```

Fig. B.6. MATLAB code for FORM using constrained optimization

The reliability index is 4.713 and corresponding design point is (16.710, 11.595, 5.115), which are the same as the method 1 and 2.

Above three methods yield the same results, which further validate the results from the constrained optimization using Solver in Excel. The input and output in Excel are straightforward and the use of the Solver is relatively simple, obviating lengthy programming work as shown by the codes in MATLAB. Therefore, FORM using Excel Solver is practical for geotechnical engineers. The advantage of using MATLAB lies in the abundant probability functions and convenient matrix calculations. More advanced reliability analysis can be conducted easily using MATLAB.

Appendix C Iterative closed-form solution for circular tunnels reinforced by rockbolts

Main formulations of the iterative closed-form solution are summarized below when the residue strength of the rock mass equals the peak strength. Details can refer to the Appendix A and B1 in Bobet and Einstein (2011).

The mobilized tensile force T is obtained by

$$T = \frac{E_b A_b}{\rho - r_0}\left[\left(U_r\big|_{r=\rho}^{final} - U_r\big|_{r=\rho}^{initial}\right) - \left(U_r\big|_{r=r_0}^{final} - U_r\big|_{r=r_0}^{initial}\right)\right] \tag{C.1}$$

where E_b is the Young's modulus of the rockbolt; A_b is the cross-section area of the rockbolt; ρ is the rockbolt length plus the tunnel radius r_0; $U_r\big|_{r=\rho}^{final} - U_r\big|_{r=\rho}^{initial}$ calculates the relative displacement of the rockbolt end; $U_r\big|_{r=r_0}^{final} - U_r\big|_{r=r_0}^{initial}$ calculates the relative displacement of the rockbolt head; $\left(U_r\big|_{r=\rho}^{final} - U_r\big|_{r=\rho}^{initial}\right) - \left(U_r\big|_{r=r_0}^{final} - U_r\big|_{r=r_0}^{initial}\right)$ is the extension of the rockbolt.

$U_r\big|_{r=\rho}^{initial}$ and $U_r\big|_{r=r_0}^{initial}$ can be obtained from the Duncan-Fama solution (Duncan Fama, 1993) while $U_r\big|_{r=\rho}^{final}$ and $U_r\big|_{r=r_0}^{final}$ are calculated from a series of equations as follows.

$$\begin{aligned} N_\phi &= \frac{1+\sin\phi}{1-\sin\phi} \\ N_\psi &= \frac{1+\sin\psi}{1-\sin\psi} \\ N_c &= \frac{2c\cos\phi}{1-\sin\phi} \end{aligned} \tag{C.2}$$

$$\begin{aligned} C_1 &= \sigma_0 + \frac{p_0 r_0}{2(1-\nu)\rho} \\ C_2 &= \left\{\frac{N_c}{N_\phi + 1} + \frac{N_\phi - 1}{N_\phi + 1}\left[\sigma_0 + \frac{p_0 r_0}{2(1-\nu)\rho}\right]\right\} r_p^2 \end{aligned} \tag{C.3}$$

$$\left(\frac{r_p}{r_0}\right)^{N_\phi - 1} = \frac{N_\phi - 1}{\left[(N_\phi - 1)(\sigma_i + p_0) + N_c\right](N_\phi + 1)}\left[2\sigma_0 + \frac{p_0 r_0}{2(1-\nu)\rho} - N_c + \frac{N_\phi - 1}{N_\phi + 1}N_c\right] \tag{C.4}$$

where $\phi = \phi_p = \phi_r$ (i.e., peak internal friction angle = residual friction angle); dilation angle is ψ; $c = c_p = c_r$ (i.e., peak cohesion = residual cohesion); r_p is the plastic zone radius; v is the Poisson's ratio of the rock mass; σ_0 is the hydrostatic in situ stress; σ_i is the internal support pressure; p_0 is a value that is to be solved iteratively combined with following equations.

For $r_0 \le r \le r_p$

$$U_r = -Ar^{-N_\psi} - Br^{N_\phi} - Cr \tag{C.5}$$

$$\begin{aligned} A &= \frac{1+\nu}{E}\left[(1-2\nu)C_1 r_p + \frac{C_2}{r_p} - (1-2\nu)\sigma_0 r_p\right] r_p^{N_\psi} \\ B &= \frac{1+\nu}{E}\left(\sigma_i + p_0 + \frac{N_c}{N_\phi - 1}\right)\frac{1 + N_\psi N_\phi - \nu(1+N_\psi)(1+N_\phi)}{N_\phi + N_\psi}\left(\frac{1}{r_0}\right)^{N_\phi - 1} \\ C &= -\frac{(1+\nu)(1-2\nu)}{E}\left(\sigma_0 + \frac{N_c}{N_\phi - 1}\right) \end{aligned} \tag{C.6}$$

For $r_p \le r \le \rho$

$$U_r = -\frac{1+\nu}{E}\left[(1-2\nu)C_1 r + \frac{C_2}{r} - (1-2\nu)\sigma_0 r\right] \tag{C.7}$$

The solution must satisfy the following equation.

$$p_0 = -\frac{E_b A_b}{S_\theta S_z(\rho - r_0)}\left\{\begin{aligned} &\frac{1+\nu}{E}\left[\frac{1-2\nu}{2(1-\nu)}p_0 r_0 + \frac{C_2}{\rho}\right] - \frac{1+\nu}{E}\frac{(N_\phi - 1)\sigma_0 + N_c}{N_\phi + 1}\frac{(r_p^i)^2}{\rho} \\ &-(Ar_0^{-N_\psi} + Br_0^{N_\phi} + Cr_0) + A^i r_0^{-N_\psi} + B^i r_0^{N_\phi} - C^i r_0 \end{aligned}\right\} \tag{C.8}$$

where S_θ and S_z are rockbolt spacings in the circumferential direction and the axial direction; r_p^i is the plastic zone radius prior to reinforcement installation; A^i, B^i, C^i are from the solution where no reinforcement is installed.

The above formulae constitute a system of equations that can be solved by iteration. First, assume a value for p_0. Then r_p is found and other values can be calculated. The new value for p_0 is obtained from Eq. (A.8). This procedure continues until p_0

converges. This iteration process is coded as a function in the Excel that can be used to calculate p_0 automatically.

Appendix D User-defined subroutine of FLAC^{3D} for JRC project

;----------Create a new file, import the finite difference mesh and read in the geometry information for the support----------

```
new
impgrid model_2m2.FLAC3D
table 1 read Heading_start.txt
table 2 read Heading_end.txt
table 3 read Bench1_start.txt
table 4 read Bench1_end.txt
table 5 read Bench2_start.txt
table 6 read Bench2_end.txt
```

;----------Rename the group for the convenience of later excavation------

```
group rock range group 1
group heading range group 4
group bench1 range group 3
group bench2 range group 2
```

;----------Define the input parameters----------

```
def Parameter_setting
        _GSI = 50.0         ;(GSI)
        _mi = 21.0          ;(mi)
        _sigci = 102.0      ;(sigci)
        _Erm = 15600.0      ;(Erm)
        _K0=2.2             ;(K0)
        _mu = 0.25          ;(Poisson's ratio)
        _D = 0.0            ;(Disturbance factor D)

        _bulk_modu = _Erm/(3*(1-2*_mu))  ;(bulk modulus)
        _shear_modu = _Erm/(2*(1+_mu))   ;(shear modulus)

        ;----------calculate the Hoek-Brown paramters----------

        _mb = _mi*EXP((_GSI-100)/(28-14*_D))
        _s = EXP((_GSI-100)/(9-3*_D))
        _a = 0.5+(EXP(-_GSI/15)-EXP(-20.0/3.0))/6.0
        _szz = -3.3             ;(vertical in-situ stress in tunnel section plane)
        _sxx = _szz*_K0         ;(horizontal in-situ stress in plane)
        _syy = -5.839           ;(horizontal in-situ stress out of plane)
```

```
        delzmin=0.75 ;(liner set up)
        lk_=100*((_bulk_modu +(4.0/3.0)*_shear_modu)/delzmin)
end
Parameter_setting

model elastic
prop bulk _bulk_modu shear _shear_modu

;----------------------------------Boundary condition-----------------------------------

fix z range z 69.9 70.1
fix z range z -80.1 -79.9
fix y
fix x range x -70.1 -69.9
fix x range x 69.9 70.1
;---------------------------------Initial condition-----------------------------------
ini sxx _sxx ;grad 0 0 0.0616 range z -80 70
ini syy _syy ;grad 0 0 0.0504 range z -80 70
ini szz _szz ;grad 0 0 0.028 range z -80 70

; ---------------------------------Initial equilibrium ----------------------------------
solve
ini xdisp=0.0
ini ydisp=0.0
ini zdisp=0.0
ini xvel=0.0
ini yvel=0.0
ini zvel=0.0
;----------------------------------Top heading Excavation----------------------------------

model hoekbrown
prop bulk =_bulk_modu shear=_shear_modu hbs=_s hbmb=_mb hba=_a
hbsigci=_sigci hbs3cv=0.0
model null range group heading
step 1
;---------------------------------------Stress reduction-----------------------------------

range name heading group heading
range name rock group rock
def relax_heading
            relax_m=0.2 ; stress relaxation coefficient (0-1)
        p_gp=gp_head
        num_of_gp=0
        loop while p_gp # null
            if inrange('heading',p_gp) = 1 then
                if inrange('rock',p_gp) = 1 then  ; (locate the gp which should
be applied reverse force)
        xf=-gp_xfunbal(p_gp)*relax_m
```

```
            yf=-gp_yfunbal(p_gp)*relax_m
            zf=-gp_zfunbal(p_gp)*relax_m ; (calculate the reversed force)
            pid=gp_id(p_gp)
            command
                apply xforce xf rang id pid
                apply yforce yf rang id pid
                apply zforce zf rang id pid    ; (apply the reversed force)
            endcommand
            num_of_gp=num_of_gp+1
        endif
    endif
    p_gp=gp_next(p_gp)
    endloop
end
relax_heading
solve
;----------------------------Cancel the applied reverse force --------------------------------

def cancel_relax
  p_gp=gp_head
  num_of_gp=0
  loop while p_gp # null
  if inrange('heading',p_gp) = 1 then
      if inrange('rock',p_gp) = 1 then ; (locate the gp to apply reverse force)
            xf=0.0
            yf=0.0
            zf=0.0
            pid=gp_id(p_gp)
            command
                    apply xforce xf rang id pid
                    apply yforce yf rang id pid
                    apply zforce zf rang id pid ;(apply reversed force)
             endcommand
            num_of_gp=num_of_gp+1
      endif
    endif
    p_gp=gp_next(p_gp)
    endloop
end
cancel_relax

;-----------------------------------Install the rockbolts ----------------------------------

def install_heading_rockbolts
    total_num_bolts=table_size(1)
    loop bolt_id (1, total_num_bolts)
            x_coordinate_start=xtable(1,bolt_id)
            z_coordinate_start=ytable(1,bolt_id)
```

```
            x_coordinate_end=xtable(2,bolt_id)
            z_coordinate_end=ytable(2,bolt_id)
            command
                  sel cable id 1 beg x_coordinate_start 1.1 z_coordinate_start & end
                  x_coordinate_end 1.1 z_coordinate_end nseg 5
            endcommand
  endloop
end
install_heading_rockbolts
sel cable id 1 prop emod 50.0e3 ytension 0.35 xcarea 380.0e-6 &
            gr_coh 0.188 gr_per 0.138 gr_k 100.0

;-----------------------------------Install shotcrete-------------------------------------------

sel liner id 1 crossdiag group rock range x -10.1 10.1 y 0.1 2.0 z -0.1 9.1

sel liner id 1 prop isotropic 20.0e3 0.15 thickness 0.08 &
                        cs_nk lk_ cs_sk lk_ cs_scoh 1e20 ;(no slip)

solve
save Top_heading.sav

;-----------------------------------End---------------------------------------------------
```

The above codes only show the top heading excavation. For bench 1 and bench 2 excavation, similar codes can be generated based on the codes for top heading excavation. Therefore, for simplicity, complete codes are not shown here.

References

AASHTO (2012). LRFD Bridge Design Specifications, 6th edition. Washington, DC, American Association of State Highway and Transportation Officials.

Aksoy, C. O., Kantarci, O. and Ozacar, V. (2010), "An example of estimating rock mass deformation around an underground opening using numerical modeling", International Journal of Rock Mechanics and Mining Sciences, Vol. 47, No. 2, pp. 272-278.

Aladejare, A. E. and Wang, Y. (2017), "Evaluation of rock property variability", Georisk: Assessment and Management of Risk for Engineered Systems and Geohazards, Vol. 11, No. 1, pp. 22-41.

Anderson, J. A. (2005), An introduction to Neural Networks, MIT press.

Ang, H. S. and Tang, W. H. (1984), Probabilistic concepts in engineering planning and design, Volume II: Decision, risk, and reliability, John Wiley & Sons, New York.

Asadollahi, P. and Tonon, F. (2010), "Definition of factor of safety for rock blocks", International Journal of Rock Mechanics and Mining Sciences, Vol. 47, No. 8, pp. 1384-1390.

Au, S. K. and Beck, J. L. (2001), "Estimation of small failure probabilities in high dimensions by subset simulation", Probabilistic Engineering Mechanics, Vol. 16, No. 4, pp. 263-277.

Au, S. K., Cao, Z. J. and Wang, Y. (2010), "Implementing advanced Monte Carlo simulation under spreadsheet environment", Structural Safety, Vol. 32, No. 5, pp. 281-292.

Au, S. K., Ching, J. and Beck, J. L. (2007), "Application of subset simulation methods to reliability benchmark problems", Structural Safety, Vol. 29, No. 3, pp. 183-193.

Baecher, G. B. and Christian, J. T. (2003), Reliability and statistics in geotechnical engineering, John Wiley & Sons, San Francisco.

Barton, N. (2002), "Some new Q-value correlations to assist in site characterisation and tunnel design", International Journal of Rock Mechanics and Mining Sciences, Vol. 39, No. 2, pp. 185-216.

Barton, N., Lien, R. and Lunde, J. (1974), "Engineering classification of rock masses for the design of tunnel support", Rock mechanics, Vol. 6, No. 4, pp. 189-236.

Basarir, H. (2008), "Analysis of rock–support interaction using numerical and multiple regression modeling", Canadian Geotechnical Journal, Vol. 45, No. 1, pp. 1-13.

Bieniawski, Z. (1973), "Engineering classification of jointed rock masses", Trans S. Afr. Inst. Civ. Engrs, Vol. 15, No. 12, pp. 335-344.

Bieniawski, Z. T. (1989), Engineering rock mass classifications, John Wiley & Sons, New York.

Bjerager, P. (1988), "Probability Integration by Directional Simulation", Journal of Engineering Mechanics, Vol. 114, No. 8, pp. 1285-1302.

Bobet, A. and Einstein, H. H. (2011), "Tunnel reinforcement with rockbolts", Tunnelling and Underground Space Technology, Vol. 26, No. 1, pp. 100-123.

Bobet, A., Fakhimi, A., Johnson, S., Morris, J., Tonon, F. and Yeung, M. (2009), "Numerical Models in Discontinuous Media: Review of Advances for Rock Mechanics Applications", Journal of Geotechnical and Geoenvironmental Engineering, Vol. 135, No. 11, pp. 1547-1561.

Bond, A. and Harris, A. (2008), Decoding eurocode 7, CRC Press.

Box, G. E. and Wilson, K. (1951), "On the experimental attainment of optimum conditions", Journal of the Royal Statistical Society. Series B (Methodological), Vol. 13, No. 1, pp. 1-45.

Brady, B. H. G. and Brown, E. T. (2006), Rock Mechanics for underground mining, Springer, Dordrecht.

Breitung, K. (1984), "Asymptotic Approximations for Multinormal Integrals", Journal of Engineering Mechanics, Vol. 110, No. 3, pp. 357-366.

Brown, E. T. and Bray, J. (1987), Analytical and computational methods in engineering rock mechanics, Allen & Unwin, London.

Bucher, C. G. and Bourgund, U. (1990), "A fast and efficient response surface approach for structural reliability problems", Structural Safety, Vol. 7, No. 1, pp. 57-66.

Cai, M. (2011), "Rock Mass Characterization and Rock Property Variability Considerations for Tunnel and Cavern Design", Rock Mechanics and Rock Engineering, Vol. 44, No. 4, pp. 379-399.

Cao, Z. and Wang, Y. (2013), “Bayesian approach for probabilistic site characterization using cone penetration tests”. Journal of Geotechnical and Geoenvironmental Engineering, Vol. 139, No. 2, pp.267-76.

Cao, Z. and Wang, Y. (2014), "Bayesian model comparison and selection of spatial correlation functions for soil parameters", Structural Safety, Vol. 49, pp. 10-17.

Carranza-Torres, C. (2004), "Elasto-plastic solution of tunnel problems using the generalized form of the hoek-brown failure criterion", International Journal of Rock Mechanics and Mining Sciences, Vol. 41, Supplement 1, pp. 629-639.

Carranza-Torres, C. (2009), "Analytical and Numerical Study of the Mechanics of Rockbolt Reinforcement around Tunnels in Rock Masses", Rock Mechanics and Rock Engineering, Vol. 42, No. 2, pp. 175-228.

Carranza-Torres, C. and Fairhurst, C. (1999), "The elasto-plastic response of underground excavations in rock masses that satisfy the Hoek–Brown failure criterion", International Journal of Rock Mechanics and Mining Sciences, Vol. 36, No. 6, pp. 777-809.

Chan, C. L. (2012), "Reliability Analysis of Laterally Loaded Single Piles.", Ph.D. Thesis, Nanyang Technological University, Singapore.

Chan, C. L. and Low, B. K. (2012a), "Practical second-order reliability analysis applied to foundation engineering", International Journal for Numerical and Analytical Methods in Geomechanics, Vol. 36, No. 11, pp. 1387-1409.

Chan, C. L. and Low, B. K. (2012b), "Probabilistic analysis of laterally loaded piles using response surface and neural network approaches", Computers and Geotechnics, Vol. 43, pp. 101-110.

Chen, G. (2012), "Probabilistic key block analysis of a mine ventilation shaft stability – a case study", Geomechanics and Geoengineering, Vol. 7, No. 4, pp. 255-262.

Chen, G., Jia, Z. and Ke, J. (1997), "Probabilistic analysis of underground excavation stability", International Journal of Rock Mechanics and Mining Sciences, Vol. 34, No. 3, pp. 51.e51-51.e16.

Chen, X. and Lind, N. (1983), "Fast probability integration by three-parameter normal tail approximation", Structural Safety, Vol. 1, No. 4, pp. 269-276.

Cheng, J. and Li, Q. (2009), "A hybrid artificial neural network method with uniform design for structural optimization", Computational Mechanics, Vol. 44, No. 1, pp. 61-71.

Ching, J., Phoon, K.-K. and Hu, Y.-G. (2009), "Efficient Evaluation of Reliability for Slopes with Circular Slip Surfaces Using Importance Sampling", Journal of Geotechnical and Geoenvironmental Engineering, Vol. 135, No. 6, pp. 768-777.

Ching, J., Wu, S.-S. and Phoon, K.-K. (2015), "Statistical characterization of random field parameters using frequentist and Bayesian approaches", Canadian Geotechnical Journal, Vol. 53, No. 2, pp. 285-298.

Choi, S. K., Grandhi, R. V. and Canfield, R. A. (2007), Reliability-based structural design, Springer, London.

Cornell, C. A. (1967), "Bounds on the reliability of structural systems", Journal of the structural Division, Vol. 93, No. 1, pp. 171-200.

Cundall, P. A. (1971), "A computer model for simulating progressive large scale movements in blocky rock systems", Proc. Symp. Rock Fracture (ISRM), Nancy.

Dasaka, S. M. and Zhang, L. M. (2012), "Spatial variability of in situ weathered soil", Géotechnique, Vol. 62, No. 5, pp. 375-384.

Deng, J. (2006), "Structural reliability analysis for implicit performance function using radial basis function network", International Journal of Solids and Structures, Vol. 43, No. 11–12, pp. 3255-3291.

Der Kiureghian, A., Lin, H. and Hwang, S. (1987), "Second‐Order Reliability Approximations", Journal of Engineering Mechanics, Vol. 113, No. 8, pp. 1208-1225.

Der Kiureghian, A. and Liu, P. (1986), "Structural Reliability under Incomplete Probability Information", Journal of Engineering Mechanics, Vol. 112, No. 1, pp. 85-104.

Ditlevsen, O. (1979), "Narrow reliability bounds for structural systems", Journal of structural mechanics, Vol. 7, No. 4, pp. 453-472.

Duncan Fama, M. (1993). Numerical modelling of yield zones in weak rocks. In: Comprehensive rock engineering. J. A. Hudson editor. Pergamon, Oxford. 2**:** 49-75.

Einstein, H. H. and Baecher, G. B. (1983), "Probabilistic and statistical methods in engineering geology", Rock mechanics and rock engineering, Vol. 16, No. 1, pp. 39-72.

Einstein, H. H. and Schwartz, C. W. (1979), "Simplified analysis for tunnel supports", Journal of Geotechnical and Geoenvironmental Engineering, Vol. 105, No. 4, pp. 499-518.

EN1997-1 (2004). Eurocode 7: Geotechnical design, Part 1: General rules.

Fang, K. T. (1980), "The uniform design: application of number-theoretic methods in experimental design", Acta Math. Appl. Sinica, Vol. 3, No. 4, pp. 363-372.

Friedman, J. H. (1991), "Multivariate adaptive regression splines", The annals of statistics, Vol. 19, No. 1, pp. 1-141.

Goh, A. T. C. (1994), "Seismic Liquefaction Potential Assessed by Neural Networks", Journal of Geotechnical Engineering, Vol. 120, No. 9, pp. 1467-1480.

Goh, A. T. C. (2002), "Probabilistic neural network for evaluating seismic liquefaction potential", Canadian Geotechnical Journal, Vol. 39, No. 1, pp. 219-232.

Goh, A. T. C. and Goh, S. H. (2007), "Support vector machines: Their use in geotechnical engineering as illustrated using seismic liquefaction data", Computers and Geotechnics, Vol. 34, No. 5, pp. 410-421.

Goh, A. T. C. and Kulhawy, F. H. (2003), "Neural network approach to model the limit state surface for reliability analysis", Canadian Geotechnical Journal, Vol. 40, No. 6, pp. 1235-1244.

Goh, A. T. C. and Kulhawy, F. H. (2005), "Reliability assessment of serviceability performance of braced retaining walls using a neural network approach", International Journal for Numerical and Analytical Methods in Geomechanics, Vol. 29, No. 6, pp. 627-642.

Goh, A. T. C. and Zhang, W. G. (2012), "Reliability assessment of stability of underground rock caverns", International Journal of Rock Mechanics and Mining Sciences, Vol. 55, pp. 157-163.

Gravanis, E, Pantelidis, L and Griffiths, DV (2014), “An analytical solution in probabilistic rock slope stability assessment based on random fields”, International Journal of Rock Mechanics and Mining Sciences, Vol. 71, pp.19-24.

Grimstand, E. and Barton, N. (1993), "Updating of the Q system for NMT", Proceedings of the International Symposium on Sprayed Concrete–Modern use of Wet Mix Sprayed Concrete for Underground Support, Fagernes, Norway.

Guan, X. L. and Melchers, R. E. (2001), "Effect of response surface parameter variation on structural reliability estimates", Structural Safety, Vol. 23, No. 4, pp. 429-444.

Hagan, M. T., Demuth, H. B. and Beale, M. H. (1996), Neural network design, Pws Pub, Boston.

Hajiabdolmajid, V., Kaiser, P. K., Martin, C. D. (2002), "Modeling brittle failure of rock", International Journal of Rock Mechanics and Mining Sciences, Vol. 39, pp.731-41.

Haldar, A. and Mahadevan, S. (2000), Probability, reliability, and statistical methods in engineering design., John Wiley, New York.

Harbitz, A. (1986), "An efficient sampling method for probability of failure calculation", Structural Safety, Vol. 3, No. 2, pp. 109-115.

Harrison, J. (2014), "Eurocode 7 and rock engineering: current problems and future opportunities", ISRM Regional Symposium-EUROCK 2014.

Hasofer, A. M. and Lind, N. C. (1974), "Exact and invariant second-moment code format", Journal of the Engineering Mechanics Division, Vol. 100, No. 1, pp. 111-121.

Hoek, E. (1994), "Strength of rock and rock masses", ISRM News Journal, Vol. 2, No. 2, pp. 4-16.

Hoek, E. (1998), "Reliability of Hoek-Brown estimates of rock mass properties and their impact on design", International Journal of Rock Mechanics and Mining Sciences, Vol. 35, No. 1, pp. 63-68.

Hoek, E. (2007), Practical rock engineering. https://www.rocscience.com/documents/hoek/corner/Practical-Rock-Engineering-Full-Text.pdf.

Hoek, E. and Brown, E. T. (1997), "Practical estimates of rock mass strength", International Journal of Rock Mechanics and Mining Sciences, Vol. 34, No. 8, pp. 1165-1186.

Hoek, E., Carranza-Torres, C. and Corkum, B. (2002). Hoek-Brown failure criterion-2002 edition. Proceedings of NARMS-TAC**:** 267-273.

Hoek, E. and Diederichs, M. S. (2006), "Empirical estimation of rock mass modulus", International Journal of Rock Mechanics and Mining Sciences, Vol. 43, No. 2, pp. 203-215.

Hohenbichler, M. and Rackwitz, R. (1988), "Improvement of second-order reliability estimates by importance sampling", Journal of Engineering Mechanics, Vol. 114, No. 12, pp. 2195-2199.

Hong, H. (1999), "Simple approximations for improving second-order reliability estimates", Journal of engineering mechanics, Vol. 125, No. 5, pp. 592-595.

Hornik, K., Stinchcombe, M. and White, H. (1989), "Multilayer feedforward networks are universal approximators", Neural Networks, Vol. 2, No. 5, pp. 359-366.

Hsu, S. -C. and Nelson, P. P. (2006), "Material spatial variability and slope stability for weak rock masses", Journal of Geotechnical and Geoenvironmental Engineering, Vol. 132, No. 2, pp.183-93.

Hykin, S. (1999), Neural Networks: A Comprehensive Foundation., Printice-Hall Inc., New Jersey.

Idris, M. A., Nordlund, E. and Saiang, D. (2016), "Comparison of different probabilistic methods for analyzing stability of underground rock excavations", The Electronic journal of geotechnical engineering, Vol. 21, No. Bund. 21, pp. 6555-6585.

Ji, J. and Low, B. (2012), "Stratified Response Surfaces for System Probabilistic Evaluation of Slopes", Journal of Geotechnical and Geoenvironmental Engineering, Vol. 138, No. 11, pp. 1398-1406.

Jiang, S., Li, D., Cao, Z., Zhou, C. and Phoon, K. (2014), "Efficient System Reliability Analysis of Slope Stability in Spatially Variable Soils Using Monte Carlo Simulation", Journal of Geotechnical and Geoenvironmental Engineering, Vol. 141, No. 2, pp. 04014096.

Jing, L. (2003), "A review of techniques, advances and outstanding issues in numerical modelling for rock mechanics and rock engineering", International Journal of Rock Mechanics and Mining Sciences, Vol. 40, No. 3, pp. 283-353.

Jing, L. and Hudson, J. A. (2002), "Numerical methods in rock mechanics", International Journal of Rock Mechanics and Mining Sciences, Vol. 39, No. 4, pp. 409-427.

JTC (2007). Geotechnical baseline report. Singapore.

JTC (2008). Geotechnical data report. Singapore.

JTC (2010). Geotechnical design report. Singapore.

Juang, C. H. and Chen, C. J. (1999), "CPT-Based Liquefaction Evaluation Using Artificial Neural Networks", Computer-Aided Civil and Infrastructure Engineering, Vol. 14, No. 3, pp. 221-229.

Juang, C. H., Chen, C. J. and Tien, Y.-M. (1999), "Appraising cone penetration test based liquefaction resistance evaluation methods: artificial neural network approach", Canadian Geotechnical Journal, Vol. 36, No. 3, pp. 443-454.

Kaiser, P. K., Diederichs, M. S., Martin, C. D., Sharp, J., Steiner, W. (2000), "Underground works in hard rock tunneling and mining", In: GeoEng2000. Technomic Publication Corporation, pp. 841-926.

Kang, F., Han, S., Salgado, R. and Li, J. (2015), "System probabilistic stability analysis of soil slopes using Gaussian process regression with Latin hypercube sampling", Computers and Geotechnics, Vol. 63, pp. 13-25.

Kar Winn, U. (2016), "Engineering Geological properties of Jurong Formation for Underground Cavern Excavation in Singapore", Confirmation of Candidature Report, Nanyang Technological University, Singapore.

Kirsch, G. (1898), "Die theorie der elastizität und die bedürfnisse der festigkeitslehre", Veit. Deit. Ing., Vol. 42, No. 28, pp. 797-807.

Koutsourelakis, P. S., Pradlwarter, H. J. and Schuëller, G. I. (2004), "Reliability of structures in high dimensions, part I: algorithms and applications", Probabilistic Engineering Mechanics, Vol. 19, No. 4, pp. 409-417.

Köylüoğlu, H. U. and Nielsen, S. R. (1994), "New approximations for SORM integrals", Structural Safety, Vol. 13, No. 4, pp. 235-246.

Lamas, L., Perucho, A. and Alejano, L. (2014), "Some key issues regarding application of Eurocode 7 to rock engineering design", ISRM Regional Symposium-EUROCK 2014.

Langford, J. C. and Diederichs, M. S. (2013), "Reliability based approach to tunnel lining design using a modified point estimate method", International Journal of Rock Mechanics and Mining Sciences, Vol. 60, pp. 263-276.

Langford, J. C. and Diederichs, M. S. (2015), "Reliable Support Design for Excavations in Brittle Rock Using a Global Response Surface Method", Rock Mechanics and Rock Engineering, Vol. 48, No. 2, pp. 669-689.

Laso, E., Lera, M. S. G. and Alarcón, E. (1995), "A level II reliability approach to tunnel support design", Applied Mathematical Modelling, Vol. 19, No. 6, pp. 371-382.

Li, D., Chen, Y., Lu, W. and Zhou, C. (2011), "Stochastic response surface method for reliability analysis of rock slopes involving correlated non-normal variables", Computers and Geotechnics, Vol. 38, No. 1, pp. 58-68.

Li, D. and Wong, L. N. Y. (2013), "Point Load Test on Meta-Sedimentary Rocks and Correlation to UCS and BTS", Rock Mechanics and Rock Engineering, Vol. 46, No. 4, pp. 889-896.

Li, D., Wong, L. N. Y., Liu, G. and Zhang, X. (2012), "Influence of water content and anisotropy on the strength and deformability of low porosity meta-sedimentary rocks under triaxial compression", Engineering Geology, Vol. 126, pp. 46-66.

Li, D-Q, Qi, X-H, Cao, Z-J, Tang, X-S, Zhou, W and Phoon, K-K (2015), “Reliability analysis of strip footing considering spatially variable undrained shear strength that linearly increases with depth”, Soils and Foundations, Vol.55, No. 4, pp. 866-80.

Li, H. Z. and Low, B. K. (2010), "Reliability analysis of circular tunnel under hydrostatic stress field", Computers and Geotechnics, Vol. 37, No. 1-2, pp. 50-58.

Li, L. and Chu, X. (2015), "Multiple response surfaces for slope reliability analysis", International Journal for Numerical and Analytical Methods in Geomechanics, Vol. 39, No. 2, pp. 175-192.

Li, X., Li, X. and Su, Y. (2016), "A hybrid approach combining uniform design and support vector machine to probabilistic tunnel stability assessment", Structural Safety, Vol. 61, pp. 22-42.

Low, B. K. (2007), "Reliability analysis of rock slopes involving correlated nonnormals", International Journal of Rock Mechanics and Mining Sciences, Vol. 44, No. 6, pp. 922-935.

Low, B. K. (2008). Practical reliability approach using spreadsheet. In: Reliability-based design in geotechnical engineering: computations and applications. K. K. Phoon editor. Taylor & Francis**:** 134-168.

Low, B. K. (2014), "FORM, SORM, and spatial modeling in geotechnical engineering", Structural Safety, Vol. 49, pp. 56-64.

Low, B. K. (2015). Reliability-based design: practical procedures, geotechnical examples, and insights. In: Risk and Reliability in Geotechnical Engineering. K. K. Phoon editor. CRC Press**:** 355-393.

Low, B. K. (2017a), "Insights from Reliability-Based Design to Complement Load and Resistance Factor Design Approach", Journal of Geotechnical and Geoenvironmental Engineering, Vol. 143, No. 11, pp. 04017089.

Low, B. K. (2017b), Lead Discusser, Chapter 4, EXCEL-based direct reliability analysis and its potential role to complement Eurocodes. In Joint TC205/TC304 Working Group on "Discussion of statistical/reliability methods for Eurocodes", distributed in ICSMGE2017, Seoul. http://140.112.12.21/issmge/TC205_304_reports/All%20Chapters%20(TC205_TC304).pdf

Low, B. K. and Einstein, H. H. (2013), "Reliability analysis of roof wedges and rockbolt forces in tunnels", Tunnelling and Underground Space Technology, Vol. 38, pp. 1-10.

Low, B. K. and Phoon, K. K. (2015), "Reliability-based design and its complementary role to Eurocode 7 design approach", Computers and Geotechnics, Vol. 65, pp. 30-44.

Low, B. K. and Tang, W. (2007), "Efficient spreadsheet algorithm for First-Order Reliability Method", Journal of Engineering Mechanics, Vol. 133, No. 12, pp. 1378-1387.

Low, B. K. and Tang, W. H. (1997), "Efficient reliability evaluation using spreadsheet", Journal of engineering mechanics, Vol. 123, No. 7, pp. 749-752.

Low, B. K. and Tang, W. H. (2004), "Reliability analysis using object-oriented constrained optimization", Structural Safety, Vol. 26, No. 1, pp. 69-89.

Low, B. K., Zhang, J. and Tang, W. H. (2011), "Efficient system reliability analysis illustrated for a retaining wall and a soil slope", Computers and Geotechnics, Vol. 38, No. 2, pp. 196-204.

Lü, Q., Chan, C. L. and Low, B. K. (2012), "Probabilistic evaluation of ground-support interaction for deep rock excavation using artificial neural network and uniform design", Tunnelling and Underground Space Technology, Vol. 32, pp. 1-18.

Lü, Q., Chan, C. L. and Low, B. K. (2013), "System Reliability Assessment for a Rock Tunnel with Multiple Failure Modes", Rock Mechanics and Rock Engineering, Vol. 46, No. 4, pp. 821-833.

Lü, Q. and Low, B. K. (2011), "Probabilistic analysis of underground rock excavations using response surface method and SORM", Computers and Geotechnics, Vol. 38, No. 8, pp. 1008-1021.

Lü, Q., Sun, H.-Y. and Low, B. K. (2011), "Reliability analysis of ground–support interaction in circular tunnels using the response surface method", International Journal of Rock Mechanics and Mining Sciences, Vol. 48, No. 8, pp. 1329-1343.

Lü, Q., Xiao, Z.-P., Ji, J. and Zheng, J. (2017), "Reliability based design optimization for a rock tunnel support system with multiple failure modes using response surface method", Tunnelling and Underground Space Technology, Vol. 70, pp. 1-10.

Lü, Q., Xiao, Z.-P., Ji, J., Zheng, J. and Shang, Y.-Q. (2017), "Moving least squares method for reliability assessment of rock tunnel excavation considering ground-support interaction", Computers and Geotechnics, Vol. 84, pp. 88-100.

Mahdevari, S., Shirzad Haghighat, H. and Torabi, S. R. (2013), "A dynamically approach based on SVM algorithm for prediction of tunnel convergence during excavation", Tunnelling and Underground Space Technology, Vol. 38, pp. 59-68.

Marinos, P. and Hoek, E. (2000), "GSI: a geologically friendly tool for rock mass strength estimation", ISRM International Symposium.

Martin, C.D. (1997), “The effect of cohesion loss and stress path on brittle rock strength”, Canadian Geotechnical Journal, Vol. 34, pp. 698-725.

McKay, M. D. (1992), "Latin hypercube sampling as a tool in uncertainty analysis of computer models", Proceedings of the 24th conference on Winter simulation, 557-564.

Melchers, R. E. (1989), "Importance sampling in structural systems", Structural Safety, Vol. 6, No. 1, pp. 3-10.

Melchers, R. E. (1999), Structural reliability analysis and prediction. 2nd ed., John Wiley, New York.

Milne, D., Hadjigeorgiou, J. and Pakalnis, R. (1998), "Rock mass characterization for underground hard rock mines", Tunnelling and Underground Space Technology, Vol. 13, No. 4, pp. 383-391.

Möller, S. (2006), "Tunnel induced settlements and structural forces in linings", Ph.D. Thesis, Universität Stuttgart.

Mollon, G., Dias, D. and Soubra, A. (2009a), "Probabilistic Analysis and Design of Circular Tunnels against Face Stability", International Journal of Geomechanics, Vol. 9, No. 6, pp. 237-249.

Mollon, G., Dias, D. and Soubra, A. (2009b), "Probabilistic Analysis of Circular Tunnels in Homogeneous Soil Using Response Surface Methodology", Journal of Geotechnical and Geoenvironmental Engineering, Vol. 135, No. 9, pp. 1314-1325.

Mollon, G., Dias, D. and Soubra, A. (2011), "Probabilistic Analysis of Pressurized Tunnels against Face Stability Using Collocation-Based Stochastic Response Surface Method", Journal of Geotechnical and Geoenvironmental Engineering, Vol. 137, No. 4, pp. 385-397.

Mollon, G., Dias, D. and Soubra, A. (2013), "Range of the Safe Retaining Pressures of a Pressurized Tunnel Face by a Probabilistic Approach", Journal of Geotechnical and Geoenvironmental Engineering, Vol. 139, No. 11, pp. 1954-1967.

Muzeau, J. P. and Lemaire, M. (1997). Reliability Analysis with Implicit Formulations. In: Probabilistic Methods for Structural Design. C. G. Soares editor. Springer Netherlands. 56**:** 141-160.

Myers, R. H. (1971), Response surfaces methodology, Allyn and Bacan Inc, Boston.

Napa-García, G. F., Beck, A. T. and Celestino, T. B. (2017), "Reliability analyses of underground openings with the point estimate method", Tunnelling and Underground Space Technology, Vol. 64, pp. 154-163.

Nelder, J. (1966), "Inverse polynomials, a useful group of multi-factor response functions", Biometrics, Vol. 22, No. 1, pp. 128-141.

Nowak, A. S. and Collins, K. R. (2012), Reliability of structures, CRC Press.

NTU (2013). Final Report of the 2007-2012 Jurong Rock Cavern Research. Singapore, School of Civil & Environmental Engineering, Nanyang Technological University.

Oreste, P. (2005), "A probabilistic design approach for tunnel supports", Computers and Geotechnics, Vol. 32, No. 7, pp. 520-534.

Oreste, P. (2015), "Analysis of the tunnel-support interaction through a probabilistic approach", American Journal of Applied Sciences, Vol. 12, No. 2, pp. 121-129.

Orr, T. L. and Breysse, D. (2008). Eurocode 7 and reliability-based design. In: Reliability-based design in geotechnical engineering, K. K. Phoon editor. Taylor and Francis, Oxon, UK**:** 298-343.

Otter, J. R. H., Cassell, A. C. and Hobbs, R. E. (1966), "Dynamic relaxation", ICE Proceedings, 633-656.

Palmstrom, A. (1995), "RMi-a rock mass characterization system for rock engineering purposes", Ph.D thesis, University of Oslo, Norway.

Palmstrom, A. and Broch, E. (2006), "Use and misuse of rock mass classification systems with particular reference to the Q-system", Tunnelling and Underground Space Technology, Vol. 21, No. 6, pp. 575-593.

Palmstrom, A. and Stille, H. (2007), "Ground behaviour and rock engineering tools for underground excavations", Tunnelling and Underground Space Technology, Vol. 22, No. 4, pp. 363-376.

Pan, X. and Reed, M. (1991), "A coupled distinct element—finite element method for large deformation analysis of rock masses", International Journal of Rock Mechanics and Mining Sciences & Geomechanics Abstracts, Vol. 28, No. 1, pp. 93-99.

Park, D., Kim, H.-M., Ryu, D.-W., Choi, B.-H. and Han, K.-C. (2013), "Probability-based structural design of lined rock caverns to resist high internal gas pressure", Engineering Geology, Vol. 153, pp. 144-151.

Park, D., Kim, H.-M., Ryu, D.-W., Song, W.-K. and Sunwoo, C. (2012), "Application of a point estimate method to the probabilistic limit-state design of underground structures", International Journal of Rock Mechanics and Mining Sciences, Vol. 51, pp. 97-104.

Phoon, K-K and Kulhawy, FH (1999), “Characterization of geotechnical variability”, Canadian Geotechnical Journal, Vol. 36, No. 4, pp.612-24.

Phoon, K-K, Quek, S-T and An, P (2003), “Identification of statistically homogeneous soil layers using modified Bartlett statistics”, Journal of Geotechnical and Geoenvironmental Engineering, Vol. 129, No. 7, pp.649-59.

Rackwitz, R. and Fiessler, B. (1978), "Structural reliability under combined random load sequences", Computers & Structures, Vol. 9, No. 5, pp. 489-494.

Rajashekhar, M. R. and Ellingwood, B. R. (1993), "A new look at the response surface approach for reliability analysis", Structural Safety, Vol. 12, No. 3, pp. 205-220.

Rosenblueth, E. (1975), "Point estimates for probability moments", Proceedings of the National Academy of Sciences, Vol. 72, No. 10, pp. 3812-3814.

Rubinstein, R. Y. and Kroese, D. P. (2011), Simulation and the Monte Carlo method, John Wiley & Sons.

Sakurai, S. (1997), "Lessons learned from field measurements in tunnelling", Tunnelling and Underground Space Technology, Vol. 12, No. 4, pp. 453-460.

Sakurai, S., Akutagawa, S., Takeuchi, K., Shinji, M. and Shimizu, N. (2003), "Back analysis for tunnel engineering as a modern observational method", Tunnelling and Underground Space Technology, Vol. 18, No. 2–3, pp. 185-196.

Sakurai, S. and Takeuchi, K. (1983), "Back analysis of measured displacements of tunnels", Rock Mechanics and Rock Engineering, Vol. 16, No. 3, pp. 173-180.

Samui, P. (2008), "Support vector machine applied to settlement of shallow foundations on cohesionless soils", Computers and Geotechnics, Vol. 35, No. 3, pp. 419-427.

Shahin, M. A., Jaksa, M. B. and Maier, H. R. (2001), "Artificial neural network applications in geotechnical engineering", Australian Geomechanics, Vol. 36, No. 1, pp. 49-62.

Shahin, M. A., Jaksa, M. B. and Maier, H. R. (2008), "State of the art of artificial neural networks in geotechnical engineering", Electronic Journal of Geotechnical Engineering, Vol. 8, pp. 1-26.

Shi, G. (1996), "Simplex integration for manifold method, FEM, DDA and analytical analysis", Proceedings of the first international forum on discontinuous deformation analysis (DDA) and simulations of discontinuous media, Berkeley, CA, 206-263.

Shi, G. H. and Goodman, R. E. (1985), "Two dimensional discontinuous deformation analysis", International Journal for Numerical and Analytical Methods in Geomechanics, Vol. 9, No. 6, pp. 541-556.

Sofianos, A. I., Nomikos, P. and Tsoutrelis, C. E. (1999), "Stability of symmetric wedge formed in the roof of a circular tunnel: nonhydrostatic natural stress field", International Journal of Rock Mechanics and Mining Sciences, Vol. 36, No. 5, pp. 687-691.

Soroosh, A., Foroozan, R. and Asadollahi, P. (2006), "Simulation of 3D effect of excavation face advancement using a neural network trained by numerical models", Tunnelling and Underground Space Technology, Vol. 21, No. 3–4, pp. 375.

Su, Y.-H., Li, X. and Xie, Z.-Y. (2011), "Probabilistic evaluation for the implicit limit-state function of stability of a highway tunnel in China", Tunnelling and Underground Space Technology, Vol. 26, No. 2, pp. 422-434.

Su, Y., Fang, Y., Li, S., Su, Y. and Li, X. (2017), "A one-dimensional integral approach to calculating the failure probability of geotechnical engineering structures", Computers and Geotechnics, Vol. 90, pp. 85-95.

Suykens, J. A. K. and Vandewalle, J. (1999), "Least Squares Support Vector Machine Classifiers", Neural Processing Letters, Vol. 9, No. 3, pp. 293-300.

Tandjiria, V., Teh, C. I. and Low, B. K. (2000), "Reliability analysis of laterally loaded piles using response surface methods", Structural Safety, Vol. 22, No. 4, pp. 335-355.

Tatang, M. A., Pan, W., Prinn, R. G. and McRae, G. J. (1997), "An efficient method for parametric uncertainty analysis of numerical geophysical models", Journal of Geophysical Research: Atmospheres, Vol. 102, No. D18, pp. 21925-21932.

Terzaghi, K. and Peck, R. (1948), Soil Mechanics in Engineering Practice, John Wiley & Sons, New York.

Tritech (2004). Factual Report of Site Investigation at Banyan Basin, Jurong Islands, Volume I, II, III & IV. Singapore.

Tritech (2007). Final Report of Complementary Site Investigation at Banyan Basin, Jurong Islands, Volume I, II & III. Singapore.

Tvedt, L. (1989). Second order reliability by an exact integral. In: Reliability and Optimization of Structural Systems' 88. Springer**:** 377-384.

Tvedt, L. (1990), "Distribution of quadratic forms in normal space-application to structural reliability", Journal of Engineering Mechanics, Vol. 116, No. 6, pp. 1183-1197.

Vapnik, V., Golowich, S. E. and Smola, A. (1997). Support vector method for function approximation, regression estimation, and signal processing. Advances in neural information processing systems 9. M. C. Mozer, M. I. Jordan and T. Petsche, MIT Press**:** 281-287.

Wang, F. and Li, H. (2017), "Stochastic response surface method for reliability problems involving correlated multivariates with non-Gaussian dependence structure: Analysis under incomplete probability information", Computers and Geotechnics, Vol. 89, pp. 22-32.

Wang, Q., Fang, H. and Shen, L. (2016a), "Reliability analysis of tunnels using a metamodeling technique based on augmented radial basis functions", Tunnelling and Underground Space Technology, Vol. 56, pp. 45-53.

Wang, Y. and Aladejare, A. E. (2015), "Selection of site-specific regression model for characterization of uniaxial compressive strength of rock", International Journal of Rock Mechanics and Mining Sciences, Vol. 75, pp. 73-81.

Wang, Y. and Aladejare, A. E. (2016a), "Bayesian characterization of correlation between uniaxial compressive strength and Young's modulus of rock", International Journal of Rock Mechanics and Mining Sciences, Vol. 85, pp. 10-19.

Wang, Y. and Aladejare, A. E. (2016b), "Evaluating Variability and Uncertainty of Geological Strength Index at a Specific Site", Rock Mechanics and Rock Engineering, Vol. 49, No. 9, pp. 3559-3573.

Wang, Y., Au, S.-K. and Cao, Z. (2010a), "Bayesian approach for probabilistic characterization of sand friction angles", Engineering Geology, Vol. 114, No. 3–4, pp. 354-363.

Wang, Y. and Cao, Z. (2013), "Probabilistic characterization of Young's modulus of soil using equivalent samples", Engineering Geology, Vol. 159, pp. 106-118.

Wang, Y., Cao, Z. and Au, S.-K. (2010b), "Efficient Monte Carlo Simulation of parameter sensitivity in probabilistic slope stability analysis", Computers and Geotechnics, Vol. 37, No. 7–8, pp. 1015-1022.

Wang, Y., Cao, Z. and Au, S.-K. (2011), "Practical reliability analysis of slope stability by advanced Monte Carlo simulations in a spreadsheet", Canadian Geotechnical Journal, Vol. 48, No. 1, pp. 162-172.

Wang, Y., Cao, Z. and Li, D. (2016b), "Bayesian perspective on geotechnical variability and site characterization", Engineering Geology, Vol. 203, pp. 117-125.

Wong, L. N. Y., Li, D. and Liu, G. (2013), "Experimental Studies on Permeability of Intact and Singly Jointed Meta-Sedimentary Rocks Under Confining Pressure", Rock Mechanics and Rock Engineering, Vol. 46, No. 1, pp. 107-121.

Wong, L. N. Y. and Wu, Z. (2014), "Application of the numerical manifold method to model progressive failure in rock slopes", Engineering Fracture Mechanics, Vol. 119, pp. 1-20.

Wong, S. M., Hobbs, R. E. and Onof, C. (2005), "An adaptive response surface method for reliability analysis of structures with multiple loading sequences", Structural Safety, Vol. 27, No. 4, pp. 287-308.

Wu, Y.-T. and Wirsching, P. H. (1987), "New algorithm for structural reliability estimation", Journal of Engineering Mechanics, Vol. 113, No. 9, pp. 1319-1336.

Wu, Z. and Wong, L. N. Y. (2012), "Frictional crack initiation and propagation analysis using the numerical manifold method", Computers and Geotechnics, Vol. 39, pp. 38-53.

Xu, B. and Low, B. K. (2006), "Probabilistic Stability Analyses of Embankments Based on Finite-Element Method", Journal of Geotechnical and Geoenvironmental Engineering, Vol. 132, No. 11, pp. 1444-1454.

Yang, C. Y., Chen, W. F. and Xu, M. X. (2007), "Reliability Analysis of Shotcrete Lining during Tunnel Construction", Journal of Construction Engineering and Management, Vol. 133, No. 12, pp. 975-981.

Yuen, K-V (2010), "Bayesian methods for structural dynamics and civil engineering", John Wiley & Sons, Chapter 6, pp. 213-256.

Zeng, P. and Jimenez, R. (2014), "An approximation to the reliability of series geotechnical systems using a linearization approach", Computers and Geotechnics, Vol. 62, , pp. 304-309.

Zeng, P., Senent, S. and Jimenez, R. (2014), "Reliability Analysis of Circular Tunnel Face Stability Obeying Hoek–Brown Failure Criterion Considering Different Distribution Types and Correlation Structures", Journal of Computing in Civil Engineering, Vol. 30, No. 1, pp. 04014126.

Zhang, J., Huang, H. and Phoon, K. (2013a), "Application of the Kriging-based response surface method to the system reliability of soil slopes", Journal of Geotechnical and Geoenvironmental Engineering, Vol. 139, No. 4, pp. 651-655.

Zhang, J., Huang, H. W., Juang, C. H. and Li, D. Q. (2013b), "Extension of Hassan and Wolff method for system reliability analysis of soil slopes", Engineering Geology, Vol. 160, pp. 81-88.

Zhang, J., Zhang, L. M. and Tang, W. H. (2011), "New methods for system reliability analysis of soil slopes", Canadian Geotechnical Journal, Vol. 48, No. 7, pp. 1138-1148.

Zhang, L., Li, D. and Tang, W. H. (2005), "Reliability of bored pile foundations considering bias in failure criteria", Canadian Geotechnical Journal, Vol. 42, No. 4, pp. 1086-1093.

Zhang, L., Tang, W. H. and Ng, C. W. (2001), "Reliability of axially loaded driven pile groups", Journal of Geotechnical and Geoenvironmental Engineering, Vol. 127, No. 12, pp. 1051-1060.

Zhang, L., Tang, W. H., Zhang, L. and Zheng, J. (2004), "Reducing uncertainty of prediction from empirical correlations", Journal of Geotechnical and Geoenvironmental Engineering, Vol. 130, No. 5, pp. 526-534.

Zhang, W. G. (2013), "Probabilistic risk assessment of undergound rock caverns.", Ph.D. Thesis, Nanyang Technological University, Singapore.

Zhang, W. G. and Goh, A. T. C. (2012), "Reliability assessment on ultimate and serviceability limit states and determination of critical factor of safety for underground rock caverns", Tunnelling and Underground Space Technology, Vol. 32, pp. 221-230.

Zhang, W. G. and Goh, A. T. C. (2013), "Multivariate adaptive regression splines for analysis of geotechnical engineering systems", Computers and Geotechnics, Vol. 48, pp. 82-95.

Zhang, W. G. and Goh, A. T. C. (2014), "Multivariate adaptive regression splines model for reliability assessment of serviceability limit state of twin caverns", Geomechanics and Engineering, Vol. 7, No. 4, pp. 431-458.

Zhao, H., Ru, Z., Chang, X., Yin, S. and Li, S. (2014), "Reliability analysis of tunnel using least square support vector machine", Tunnelling and Underground Space Technology, Vol. 41, pp. 14-23.

Zhao, H. B. (2008), "Slope reliability analysis using a support vector machine", Computers and Geotechnics, Vol. 35, No. 3, pp. 459-467.

Zhao, Y.-G. and Ono, T. (1999), "New approximations for SORM: Part 1", Journal of engineering mechanics, Vol. 125, No. 1, pp. 79-85.

Zhu, H. and Zhang, L. M. (2013), "Characterizing geotechnical anisotropic spatial variations using random field theory", Canadian Geotechnical Journal, Vol. 50, No. 7, pp. 723-734.

Zhu, W. S., Sui, B., Li, X. J., Li, S. C. and Wang, W. T. (2008), "A methodology for studying the high wall displacement of large scale underground cavern complexes and it's applications", Tunnelling and Underground Space Technology, Vol. 23, No. 6, pp. 651-664.

Zienkiewicz, O., Kelly, D. and Bettess, P. (1977), "The coupling of the finite element method and boundary solution procedures", International Journal for Numerical Methods in Engineering, Vol. 11, No. 2, pp. 355-375.

Zienkiewicz, O. C. and Morice, P. (1971), The finite element method in engineering science, McGraw-hill, London.